Volume 95, Number 1, January-February 1990
Journal of Research of the National Institute of Standards and Technology

Contents

Articles

News Briefs

Volume 95, Number 1, January–February 1990
Journal of Research of the National Institute of Standards and Technology

[J. Res. Natl. Inst. Stand. Technol. 95, 1 (1990)]

New Program and Directions at the National Institute of Standards and Technology

Volume 95 Number 1 January–February 1990

Donald R. Johnson

National Institute of Standards and Technology,
Gaithersburg, MD 20899

The Trade Act of 1988 created the National Institute of Standards and Technology (NIST) from the National Bureau of Standards (NBS). In addition to explicitly defining and reconfirming the traditional measurement services, the law assigned new responsibilities to NIST to assist U.S. industry in capitalizing on new technologies developed in the U.S. scientific and technical community at a faster rate. This article decribes the new programs being established at NIST to comply with this mandate and the new organizational unit at NIST that brings together the traditional services and these new programs.

Key words: Advanced Technology Program; Clearinghouse for State Technology Programs; Manufacturing Technology Centers; State Technology Extension Program; Technology Services.

Accepted: November 14, 1989

1. Introduction

The rapid loss of competitiveness of American industry in international markets is an extremely serious problem with wide-ranging consequences for the United States' material well-being, security and political influence. Its causes are many, but among them certainly are the slow rate at which new technology is incorporated in commercial products and processes, and the lack of attention paid to manufacturing. There is a clear need to compete in world markets with high-value-added products, incorporating the latest innovations, manufactured in short runs with flexible manufacturing methods. Research, management, and manufacturing methods that support change and innovation are key ingredients needed to enhance our Nation's competitive position.

Many ideas originating in the American scientific and technical community are being commercially exploited in other parts of the world. As a nation, we have been slow to capitalize on new technology developed from America's own intellectual capability. In the past, small and mid-sized companies have led U.S. industry in innovation. Our government must now find ways to help such companies meet the demands of global competition, when the speed with which firms are able to translate innovations into quality commercial products and processes is of utmost importance.

The Omnibus Trade and Competitiveness Act signed into law on August 23, 1988 is the result of policymakers' endeavors to create a new framework and environment that can enhance the rapid commercialization of technology. Among other things the Act created the National Institute of Standards and Technology (NIST) from the National Bureau of Standards (NBS) and assigned to it several new and expanded functions which build on the technical expertise of NBS. NIST will maintain the traditional functions of NBS in support of U.S. industry and will continue to offer the full array of measurement and quality assurance services including calibration services, standard reference materials, standard reference data, and measurement assurance programs.

The NIST resources are still quite modest when compared to research and development expenditures by industry and the federal government, or with the more than $550 million expenditure by the various states for technology development and commercialization. However, the new programs being developed by NIST in response to the new legislative assignments are designed to be collaborative, highly leveraged, and serve as examples to be followed by others with greater resources.

2. New NIST Organizational Unit

A new major organizational unit, Technology Services (TS), was established in NIST to bring together the new assignments, which are mainly extramural, and the traditional NIST (NBS) services which have been, and are now more than ever, an important link in our Nation's efforts to improve its industrial competitiveness. Figure 1 shows the organizational placement of the new unit within NIST. Figure 2 shows the organizational structure of Technology Services in more detail.

3. New Programs

The Act assigns to NIST four new major programs designed to assist private sector initiatives capitalize on technological innovations; advance R&D projects which can be optimized for commercial and industrial applications; and promote shared risks, accelerated development, and pooling of skills necessary to strengthen America's manufacturing skills. The new programs are:

- the Regional Centers for the Transfer of Manufacturing Technology,
- the State Technology Extension Program,
- the Advanced Technology Program,
- the Clearinghouse for State Technology Programs.

3.1 Regional Centers for the Transfer of Manufacturing Technology

The objective of the regional centers is to bring modern automated manufacturing technology to small and mid-sized manufacturing firms. The program focuses on technologies appropriate to firms in a selected geographic region and emphasizes "hands on" experience and "off the shelf" technologies. Three organizations have been selected to become the first NIST Regional Manufacturing Technology Centers: The Great Lakes Manufacturing Technology Center at the Cleveland Advanced Manufacturing Program in Cleveland, Ohio; The Northeast Manufacturing Technology Center at Rensselaer Polytechnic Institute in Troy, New York; and The Southeast Manufacturing Technology Center at the University of South Carolina in Columbia, South Carolina. NIST has now established cooperative working agreements with each of these organizations.

3.2 State Technology Extension Program

The objective of the extension services program is to improve the use of technology, particularly federal technology, by small and mid-sized businesses. A number of federal, state, and local sponsored extension services already exist, but most of the services offered are focused on business assistance rather than technology. In addition, most of the organizations providing extension services do not have sufficient technically trained personnel nor the technical resources needed to help small companies with their technological needs. This NIST program will help to coordinate the state and local extension services with federal technology transfer programs by working with the existing delivery network; provide technology assistance to extension services as appropriate; develop and conduct workshops/seminars on technological issues; and expand the distribution and utilization of NIST services.

3.3 Advanced Technology Program (ATP)

The objective of this program is to accelerate the commercialization of scientific discoveries and manufacturing technologies, particularly by small entrepreneurial firms. This program will provide limited federal funding to encourage and leverage private sources of support for developing generic technology, developing new products from specific projects, and improving existing manufacturing processes.

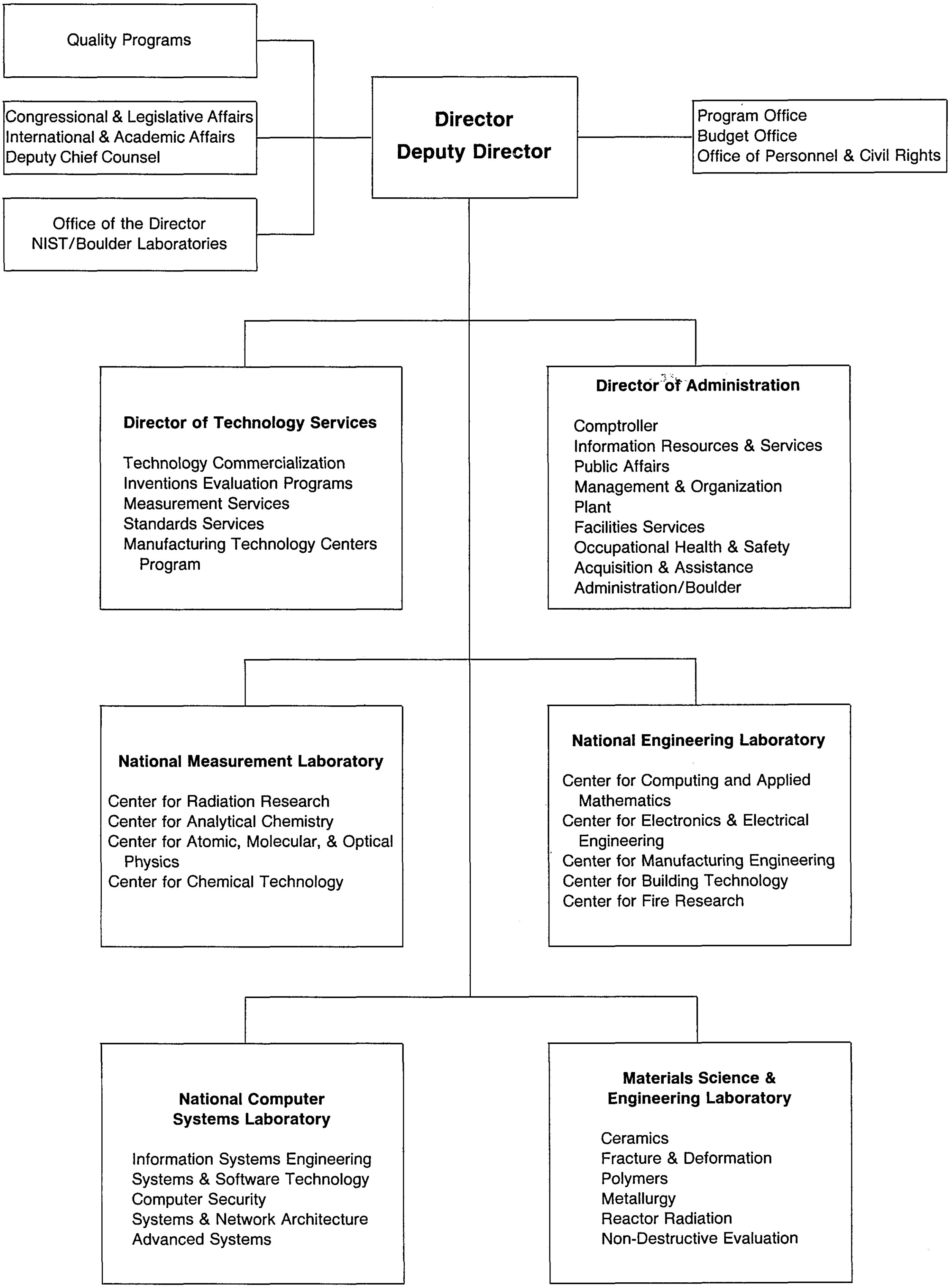

Figure 1. Organizational placement of Technology Services within NIST.

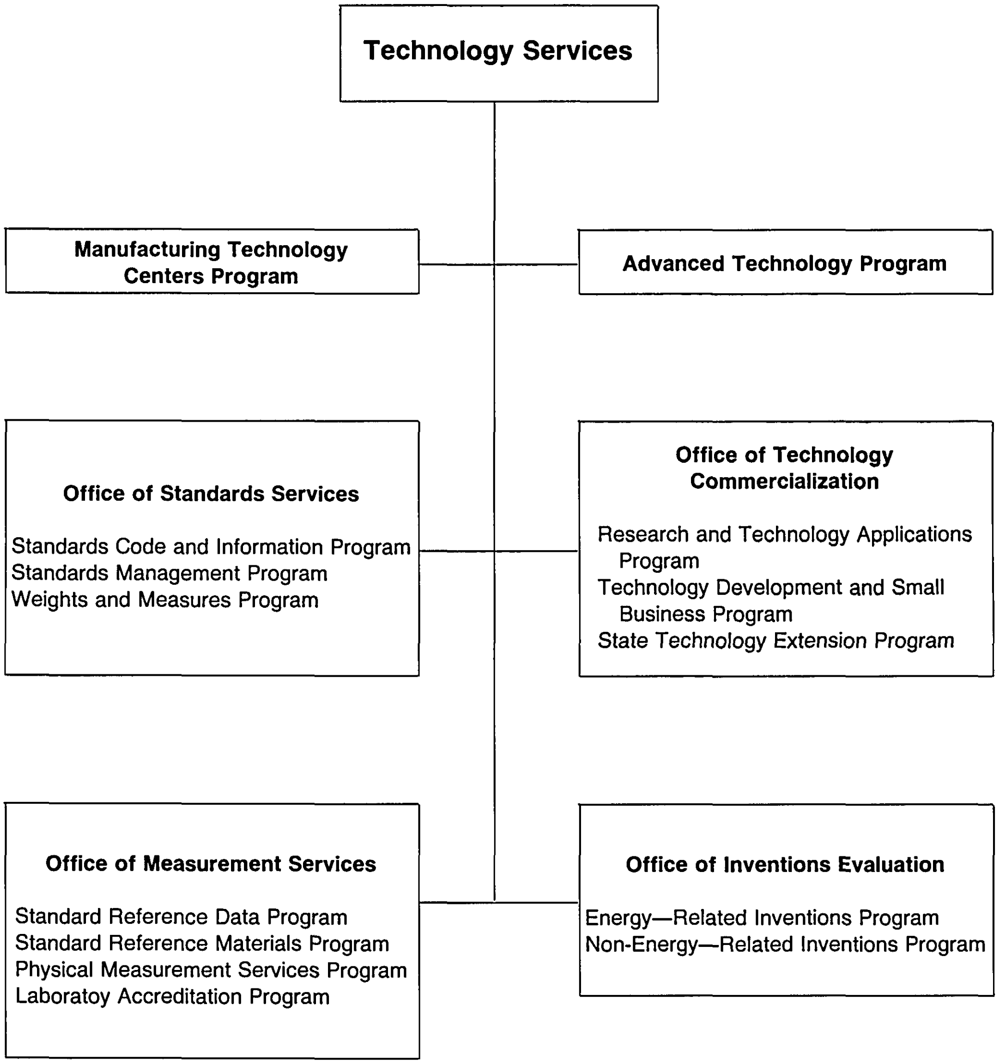

Figure 2. Organizational Structure of Technology Services.

NIST has developed a preliminary ATP program plan that calls for the initiation of eight operating program components (see table 1) that together would:

- •encourage U.S. business to look to the future and to improve their competitive positions through technological innovation,
- •capture greater civilian market potential from existing Federal investment on basic research,
- •systematically vector different aspects of Federal research investments to follow-on funding from state and local governments.

3.4 Clearinghouse for State Technology Programs

The objective of this program is to develop a central base of information on programs already in place and document the results that can be measured as a resource for state and local governments to utilize when deciding on new technology investments. NIST will acquire information through the development of a network of technical contacts within the state and local policy level staff, and through the collection of information on current programs. The clearinghouse will provide the type of information needed at the state and local level by governors, county executives, mayors, and other decision makers as they plan new programs and make policy decisions. The total investment at the state level is large and the influence on the overall direction of U.S. high technology and, hence, the impact on the nation's balance of trade will be substantial. The availability of a quality data base on state technology programs is an essential resource for the decision makers.

Table 1. Advanced Technology Program (ATP) options

- **Emerging Technologies Consortia**
  Provide start-up support for joint R&D ventures to rapidly develop generic technologies having exceptional long-term commerical promise.
- **Manufacturing Research Consortia**
  Provide start-up support for joint R&D ventures to create generic improvements in manufacturing technology or improved productivity and quality control
- **Business-Federal Laboratory Partnership**
  Provide funding matched with private sector funds to extract commercially promising technology from federal labs
- **Business-University Partnership**
  Provide funding matched with private sector funds to extract commercially promising technologies from universities
- **SBIR Phase III Technology Development**
  Provide follow-on support for commercially promising Small Business Innovation Research (SBIR) Phase II Projects
- **Invention Evaluation**
  Provide seed support for highly ranked, commercially promising inventions from extension services program
- **Business-State Partnership**
  Provide leverage funding with state programs to insure local follow-on support for commerically promising projects
- **Prototype Engineering Research**
  Provide support for successfully completed ATP projects with exceptional commerical potential but low private sector funding appeal

4. Conclusion

Our new name, National Institute of Standards and Technology, reflects the broadened role and the new responsibilities. NIST will continue to serve as the Nation's central laboratory for developing and disseminating measurement standards and scientific data for service, engineering, manufacturing, commerce, industry, and education. The combination of our new assignments and the traditional NBS measurement and quality assurance services under the new organizational unit (TS) will enable NIST to focus more effectively on its new purpose, "to assist industry in the development of technology and procedures needed to improve quality, to modernize manufacturing processes, to ensure product reliability, manufacturability, functionality, and cost-effectiveness, and to facilitate the more rapid commercialization... of products based on new scientific discoveries."

About the author: *D. R. Johnson is Director of Technology Services at the National Institute of Standards and Technology in Gaithersburg, MD.*

Volume 95, Number 1, January-February 1990
Journal of Research of the National Institute of Standards and Technology

[J. Res. Natl. Inst. Stand. Technol. 95, 7 (1990)]

Apparatus for Simultaneous Small Angle Neutron Scattering and Steady Shear Viscosity Studies of Polymer Melts and Solutions

Volume 95 Number 1 January-February 1990

Alan I. Nakatani, Hongdoo Kim, and Charles C. Han

National Institute of Standards and Technology,
Gaithersburg, MD 20899

The design and construction of an apparatus for studying the simultaneous small angle neutron scattering (SANS) and steady shear viscosity behavior of polymer melts and concentrated solutions is discussed. Successful operation of the device is demonstrated on a blend of 20 weight percent deuterated polystyrene and 80 weight percent poly(vinylmethylether). The effects of shear on the critical behavior of the blend are observed in the SANS behavior as a function of temperature and shear rate and indicate shear induced mixing behavior for the range of shear rates examined. The steady shear viscosity results alone are insufficient for detecting the transition from one to two phases. The examination of shear effects in polymer blends is important for understanding the critical behavior of binary systems. Technologically, knowledge of the phase behavior of polymer blends under shear are important for the design and improvement of commercial blend processing.

Key words: deuterated polystyrene; phase separation; polymer blends; poly(vinylmethylether); small angle neutron scattering; viscosity.

Accepted: October 3, 1989

1. Introduction

The shear behavior of mixtures near a critical point is of fundamental importance for testing theories of critical behavior. In simple binary fluid systems [1-4], a crossover from non-classical behavior to mean field behavior is expected under the influence of simple shear. Shifts in the critical point on the order of 0.001 K with the application of extremely high shear rates (thousands of reciprocal seconds) have been observed. The temperature control and range of shear rates necessary to examine these small effects in simple fluids is very difficult to achieve.

Polymer blends have displayed mean field behavior under quiescent conditions, and have demonstrated shifts in the critical point on the order of a degree to even tens of degrees with the application of much lower shear rates [5,6]. Therefore, polymer blends are much more amenable to studying the effect of shear on the critical behavior of a mean field system. However, the behavior of polymer blends with shear is not without complications. Different investigators report either shear induced mixing or shear induced demixing behavior. The variation in the results has also spawned a variety of theoretical treatments and predictions for polymer phase behavior during shear. Summaries of various work in this field are given by Rangel-Nafaile et al. [7] and Tirrell [8].

The technological importance of the effect of shear on polymer blends must also be considered. The morphology of polymer blends is directly related to processing conditions. By gaining an understanding of the phase behavior of polymer blends during processing, it may be possible to improve current commercial blends or to develop conditions for the advancement of new polymer blends.

This work will describe an apparatus for studying the simultaneous steady shear viscosity and small angle neutron scattering (SANS) behavior of polymer melts, blends, and concentrated solutions in a controlled, uniform shear geometry. Because of the small wavelength of the incident neutron radiation, concentration fluctuations in sheared-polymer systems on a length scale from a few angstroms to a few hundred angstroms may be obtained with this device. Most previous studies on the shear behavior of polymer blends utilized light-scattering techniques which are only capable of probing concentration fluctuations on the order of 1000 Å. Examination of the fluctuations on a much smaller size scale as well as determining the relationship between the size of the concentration fluctuations and the viscosity behavior is desirable for a microscopic understanding of the system. On the other hand, viscosities of the materials of interest may range from a few poise to millions of poise and phase boundaries for polymer blends range from ambient temperature to over 200 °C, which makes the torque and temperature requirements for the apparatus quite severe. With this in mind, the design and construction of the apparatus will be discussed as well as preliminary data on a blend system of deuterated polystyrene ($M_w=4.4\times10^5$) (440K PSD) and poly(vinylmethylether) ($M_w=1.8\times10^5$) (180K PVME).

2. Experimental

2.1 Apparatus

The SANS shear cell was designed to fit within the constraints of the SANS instrument at NIST (fig. 1). The only limitations to the apparatus are

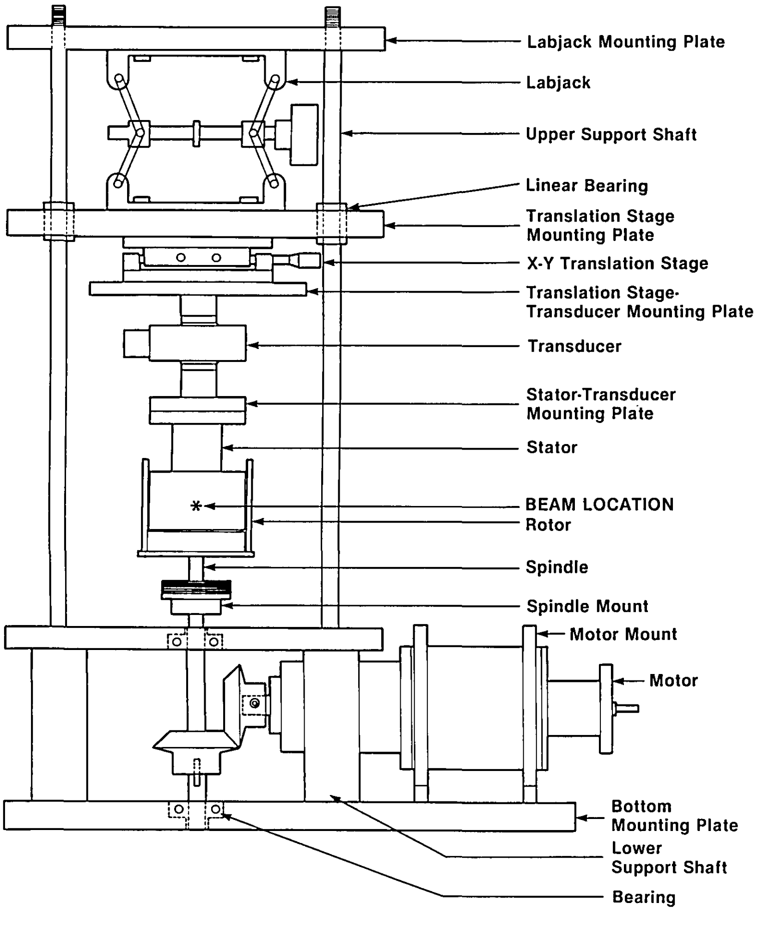

Figure 1. Schematic of SANS shear cell.

transparency to neutrons and a tabletop to beamline distance of 30.48 cm. The apparatus design is similar to that constructed by Lindner and Oberthur [9,10] for use at Institut-Laue Langevin (ILL) in Grenoble, France, with a few important differences. A high torque system with uniform rotor speeds at low shear rates was desirable for studies on concentrated solutions and melts. The SANS shear cell is of couette geometry with an inner radius of the quartz cylinder (rotor) of 4.552 cm. The quartz is bonded with epoxy to an Invar spindle to form the cup. Radial runout tolerances are all less than 0.0013 cm.

The rotor is driven through a set of miter gears by a brushless dc servo motor with an encoder feedback loop and quadrature detection. Two different motors and two different encoders are utilized. The first motor has a 50:1 harmonic speed reducer with a maximum torque of 67 N·m while the second motor has a 4.96:1 helical gear reduction box with a maximum torque of approximately 5 N·m. The two encoders have a resolution of 500 and 2500 pulses per revolution (ppr); the 2500 ppr encoder is particularly useful for extremely slow motor speeds. With this combination of motors and encoders nominal shear rates from 0.02 to 7000 s^{-1} may be attained. Viscosities as high as 1.0×10^6 poise have been successfully examined in the shear cell. The upper limit to the viscosity is determined by the strength of the quartz to Invar bond of the rotor.

The inner cylinder of our device (stator) is unique to the apparatus. Instead of quartz, the stator is constructed from oxygen-free, pure copper. Pure copper has a low neutron cross section and is one of the few metals which can be used successfully as a window material in SANS experiments. The nominal radius of the cylinder at room temperature is 4.506 cm and the height is 5.347 cm. The cylinder has a 3.50-cm diameter hole bored in the transverse direction for the beam path. A thin sheath of copper (0.040-cm thick) is then heat shrunk over the cylinder. Thermal expansion of the cylinder provides a tight fit between the sheath and cylinder (fig. 2). Mechanically, the stator appears as a solid piece of copper; to neutrons the stator is nearly transparent. Copper was utilized instead of quartz to allow for a broader range of temperature control as well as better uniformity and accuracy. Quartz, having a very low thermal conductivity, was not deemed suitable for these purposes. Similar devices [9-11] have a temperature controlling fluid circulating through a quartz stator. Temperature control in our apparatus is achieved by use of four heater cartridges placed in the copper block with PID control of the heater power supply. Additional control is achieved by a secondary electrical heating mantle which surrounds the entire stator/rotor assembly. The control circuit is designed so that the temperature of the external mantle follows the PID controlled temperature of the copper stator. The upper operating temperature is about 170 °C. Alignment of the stator is accomplished by means of a precision x-y stage. Vertical translation of the stator is accomplished using a laboratory jack (Newport Corporation)[1] with extra precision linear ball bushing bearings guiding the x-y translation stage mounting plate on four 3.175-cm diameter, precision-ground rods (straightness tolerance 4.26×10^{-5} cm/cm).

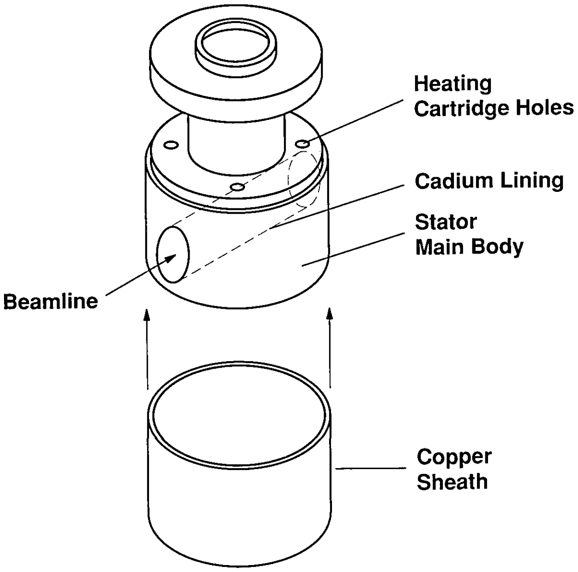

Figure 2. Exploded view of copper stator (drawing not to scale).

The gap between the rotor and stator is nominally 0.5 mm. The exact value was determined based on the linear thermal expansion coefficient of the copper stator. Dimensional changes of the quartz are assumed to be negligible. The bottom of the stator is a truncated 2° cone to reduce edge effects. The shear rate at the bottom is much lower than the shear rate in the gap for a given rotation rate and the contributions to the torque can be neglected.

---

[1] Certain commercial equipment, instruments, or materials are identified in this paper in order to adequately specify the experimental procedure. Such identification does not imply recommendation or endorsement by the National Institute of Standards and Technology, nor does it imply that the materials or equipment identified are necessarily the best available for the purpose.

The transducer, which is connected to the stator, is a combination torque/normal force transducer. The torque component is a static torque transducer with a load capacity of 56.5 N·m and using a digital indicator is accurate to 0.0045 N·m. Higher sensitivity may be achieved by using a chart recorder and monitoring the voltage output of the transducer directly. The thrust component of the transducer is a 2.22×10^3 N capacity load cell. The purpose of this load cell is limited to monitoring thrust on the sample during loading and locating the bottom of the cup.

For a Couette geometry viscometer, the shear rate, $\dot{\gamma}$, and the viscosity, η, are determined as follows [12]:

$$\dot{\gamma}=\omega R_1/(R_2-R_1)$$

$$\eta=T(R_2-R_1)/(2\pi R_1{}^3H\omega)$$

where ω is the angular velocity, R_2 is the inner radius of the quartz cylinder, R_1 is the radius of the copper cylinder, T is the torque, and H is the height of the copper cylinder. Two Newtonian viscosity standards were used from Cannon Instruments, S8000 (238.2 poise at 25 °C) and S30,000 (816.9 poise at 25 °C, 223.1 poise at 40 °C and 103.6 poise at 50 °C) to check the performance of the instrument.

2. Materials

Polystyrene-d_8 (PSD) for this experiment was prepared by anionic polymerization of styrene-d_8 in benzene with butyllithium as an initiator using standard techniques [3]. The PSD was characterized by gel permeation chromatography (GPC) showing $M_w=4.4\times10^5$ and $M_w/M_n=1.28$. Poly(vinylmethylether) (PVME) was polymerized by cationic polymerization in toluene with BF_3-ethyl ether complex as an initiator [14]. The polymer was fractionated in heptane and the fraction utilized in these experiments had a $M_w=1.8\times10^5$ and $M_w/M_n=1.76$ as determined by GPC. The blend composition was 20 weight percent PSD and 80 weight percent PVME corresponding to the critical composition for a PSD/PVME blend [15]. The sample was prepared by dissolving the polymers in toluene and then pouring the solution into the bottom of the rotor and removing the toluene by vacuum in a vacuum oven at 80 °C for 48 h.

3. Results

SANS results were obtained using an incident wavelength of 9 Å at the NIST reactor. Data was collected over a two-dimensional detector and corrected for background and dark current intensity due to electronic noise. Sector averages of the scattered intensity parallel and perpendicular to the flow (horizontal and vertical) were obtained in 10° sectors. Absolute intensity calibration was done with a dry silica gel as a secondary standard, calibrated in terms of a primary vanadium standard.

The 440K PSD/180K PVME blend was studied between 110 °C and 145 °C at shear rates between 0.02 and 3.0 s^{-1}. The optical cloud point at zero shear was 140 °C. Analysis of the zero shear scattering data using a plot of the square of the inverse correlation length versus reciprocal temperature [15] gives a value for the spinodal temperature of 140.6 °C. Torque measurements were obtained during the SANS measurements to give the steady shear viscosity values (fig. 3). At zero shear, the scattering behavior parallel and perpendicular to flow is identical as expected.

At constant temperature, the shear rate dependence of the scattering profiles show some significant differences. In the one phase region (below 140 °C) parallel to flow, the scattering intensity at low q decreases with increasing shear rate. Perpendicular to the flow direction, the scattering profiles are virtually independent of shear rate. An example of the shear rate dependence is shown in figures 4a and 4b for 137.5 °C.

Above 140 °C (near phase separation), the differences in the scattering behavior are much more pronounced. The intensities at low q decrease with increasing shear rate in the parallel direction (fig. 5). Again, no significant changes are observed perpendicular to flow. The solid lines in the figures represent fits to the data using the expression for the structure factor of polymer blends by deGennes using the random phase approximation (RPA) [16]. The fits to the data are good except for the zero shear data in the two-phase region. With the application of shear, the RPA fits still appear reasonable even in the two-phase region. This may reflect the insensitivity of the RPA calculation of $S(q)$ as a function of shear in a three parameter representation.

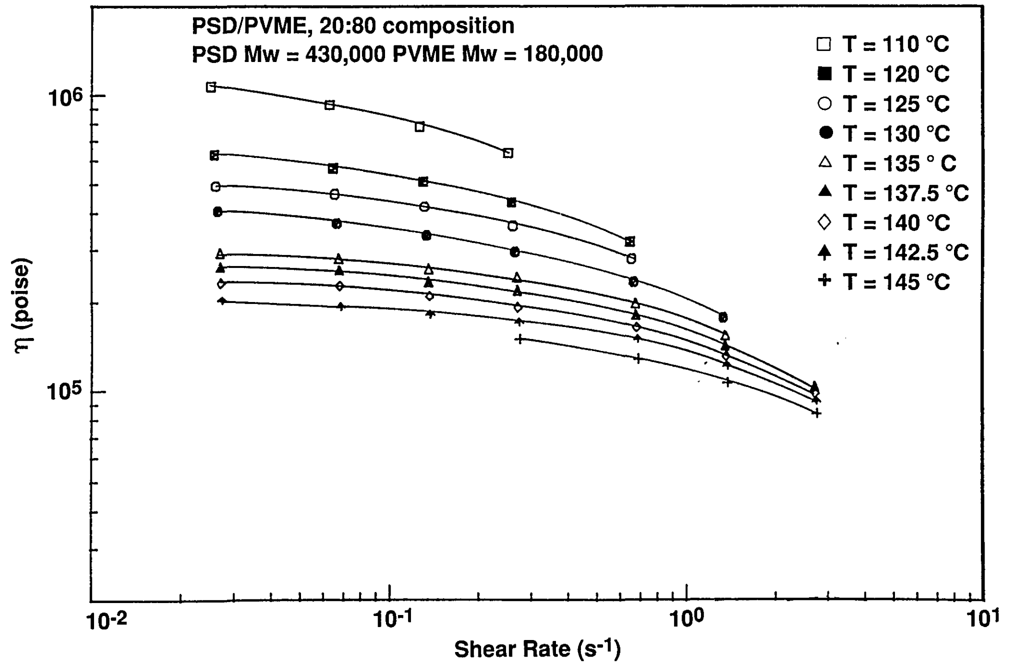

Figure 3. Steady shear viscosity for 20:80 PSD/PVME blend as a function of temperature as measured in the SANS shear cell.

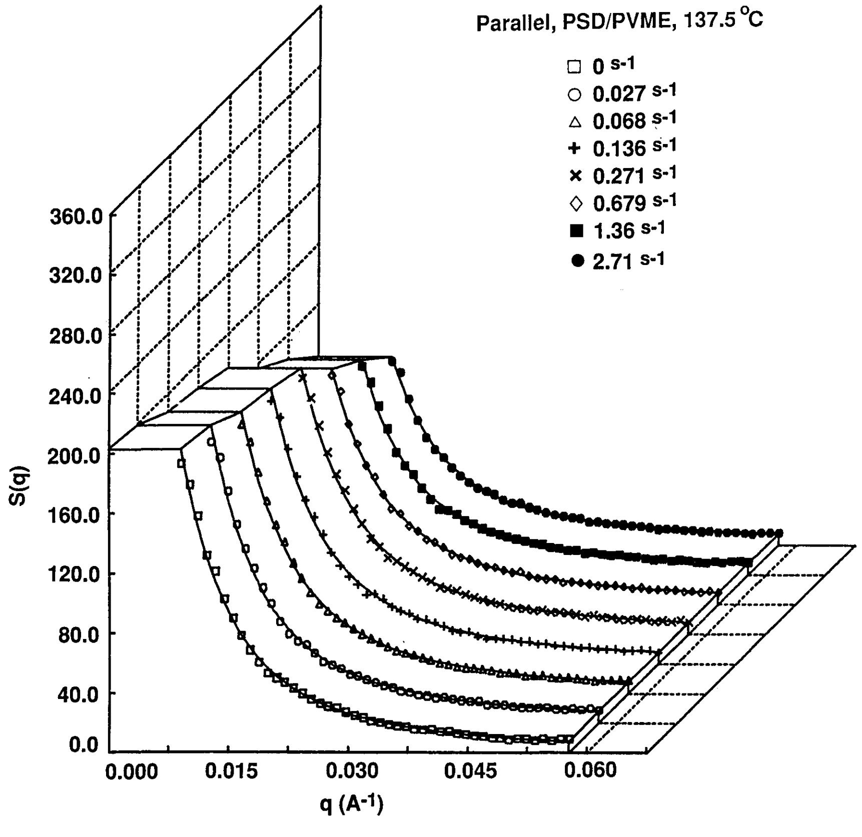

Figure 4a. Scattering intensities as a function of shear rate for a 20:80 blend of $M_w=4.4\times10^5$ PSD and $M_w=1.8\times10^5$ PVME at 137.5 °C. Curves are horizontal sector averages.

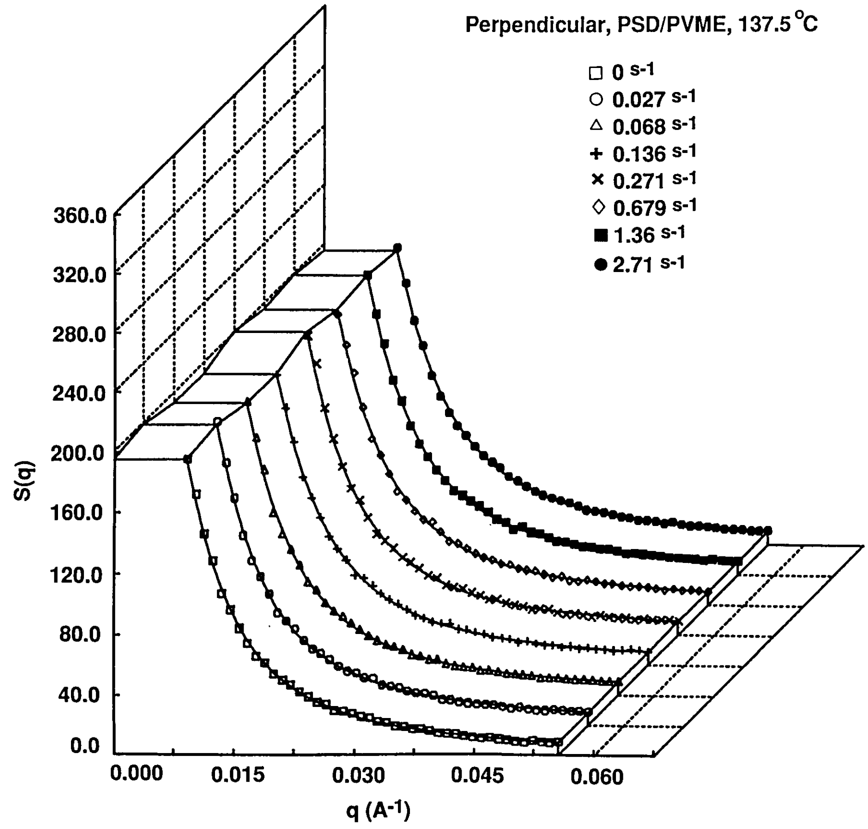

Figure 4b. Scattering intensities as a function of shear rate for a 20:80 blend of $M_w=4.4\times10^5$ PSD and $M_w=1.8\times10^5$ PVME at 137.5 °C. Curves are vertical sector averages. Solid lines represent fits to the RPA function for polymer blends of deGennes.

4. Discussion

The effects of shear on the scattering behavior of polymer blends are quite dramatic parallel to the flow direction. Use of the deGennes RPA function to fit the data may be questionable, therefore discussion on the shear rate dependence of the parameters which are typically extracted from fits to the data such as the polymer/polymer interaction parameter, χ, or the size of the concentration fluctuations, ξ, will not be attempted in this paper. On the basis of SANS studies on quiescent polymer blends [17], the decrease in the scattered intensity parallel to flow may be interpreted as an increase in the miscibility of the two polymers. In agreement with our observations, Pistoor and Binder have predicted that at high shear rates a blend of two different homopolymers would exhibit a lower scattering intensity parallel to the flow direction for simple shear [18]. Results on a polymer/polymer/solvent system using this same apparatus have also shown evidence for shear induced mixing behavior [19].

The steady shear viscosity shows no significant changes as function of temperature through the phase boundary. This is somewhat unexpected since there are many reports in the literature of unusual viscosity behavior in two phase systems [20,21]. More detailed presentations of the SANS and viscosity data and discussion will appear in a subsequent publication.

5. Conclusions

A device for the simultaneous study of the steady shear viscosity and small angle neutron scattering behavior of high viscosity fluids at elevated temperatures has been designed, constructed, and demonstrated to be fully operational. The effects of shear on the critical behavior of polymer blends are dramatic as evidenced by changes in the SANS behavior as a function of temperature and shear rate. The results have qualitatively been interpreted as evidence for shear induced mixing behavior in the PSD/PVME blend examined. The steady shear

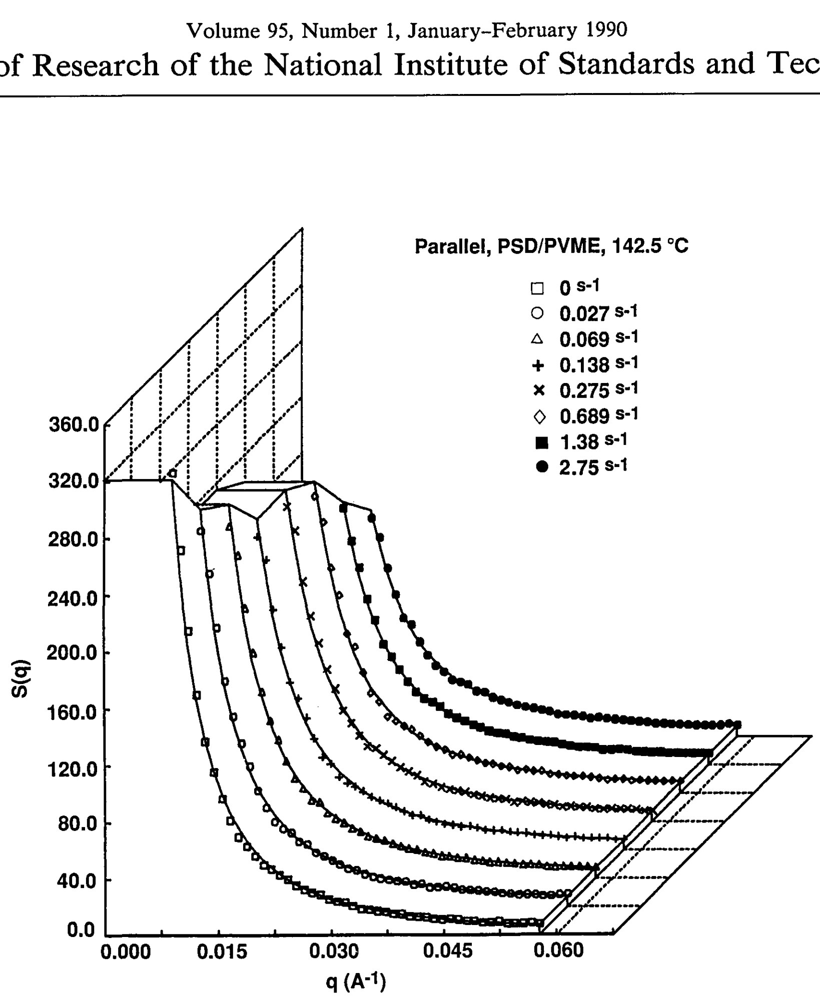

Figure 5. Scattering intensities as a function of shear rate for a 20:80 blend of $M_w=4.4\times10^5$ PSD and $M_w=1.8\times10^5$ PVME at 142.5 °C. Curves are horizontal sector averages. Solid lines represent fits to the RPA function for polymer blends of deGennes.

viscosity behavior alone was not capable of detecting the transition from one phase to two phases.

The successful application of this apparatus to the problem of shear effects in critical phenomena allows us to contemplate future experiments in the areas of single chain behavior under shear in polymer melts as well as examining the shear behavior of a variety of different materials such as liquid crystals and polyelectrolytes by small angle neutron scattering.

6. Acknowledgments

The authors wish to acknowledge the considerable contributions to this work by Dr. Y. Matsushita of Nagoya University for the synthesis of the deuterated polystyrene and Dr. B. Bauer and J. D. Gezelter for the synthesis and characterization of the poly(vinylmethylether).

About the authors: Alan I. Nakatani is a physical scientist and Charles C. Han is a group leader in the Polymers Division at the National Institute of Standards and Technology, Gaithersburg, MD. Hongdoo Kim was a guest scientist and is currently at the Korea Institute of Science and Technology.

7. References

[1] Chan, C. K., Perrot, F., and Beysens, D., Phys. Rev. Lett. **61**, 412 (1988).

[2] Beysens, D., Gbadamassi, M., and Moncef-Bouanz, B., Phys. Rev. A **28**, 2491 (1983).

[3] Onuki, A., Yamazaki, K., and Kawasaki, K., Ann. Phys. **131**, 217 (1981).

[4] Imaeda, T., Onuki, A., and Kawasaki, K., Prog. Theor. Phys. **71**, 16 (1984).

[5] Hashimoto, T., Takebe, T., and Suehiro, S., Polymer J. **2**, 123 (1986).

[6] Hashimoto, T., Takabe, T., and Suehiro, S., J. Chem. Phys. **88**, 5874 (1988).

[7] Rangel-Nafaile, C., Metzner, A. B., and Wissbrun, K., Macromolecules **17**, 1187 (1984).

[8] Tirrell, M., Fluid Phase Equil. **30**, 367 (1986).
[9] Lindner, P., and Oberthur, R. C., Rev. Phys. Appl. **19**, 759 (1984).
[10] Lindner, P., and Oberthur, R. C., Colloid Polym. Sci. **263**, 443 (1985).
[11] Straty, G. C., J. Res. Natl. Inst. Stand Technol. **94**, 259 (1989).
[12] Bird, R. B., Armstrong, R. C., and Hassager, O., Dynamics of Polymeric Liquids, vol. 1, John Wiley and Sons, New York (1977).
[13] Matsushita, Y., Furuhashi, H., Choshi, H., Noda, I., Nagasawa, M., Fujimoto, T., and Han, C. C., Polymer J. **14**, 489 (1982).
[14] Bauer, B., Hanley, B., and Muroga, Y., Polymer Comm. **30**, 19 (1989).
[15] Han, C. C., Bauer, B. J., Clark, J. C., Muroga, Y., Matsushita, Y., Okada, M., Tran-cong, Q., Chang, T., and Sanchez, I. C., Polymer **28**, 2002 (1988).
[16] deGennes, P. G., Scaling Concepts in Polymer Physics, Cornell University Press, Ithaca, New York (1979).
[17] Yang, H., Shibayama, M., Stein, R. S., and Han, C. C, Polymer Bull. **12**, 7 (1984).
[18] Pistoor, N., and Binder, K., Colloid Polym. Sci. **266**, 132 (1988).
[19] Nakatani, A. I., Kim, H., Takahashi, Y., and Han, C. C., Polymer Comm. **30**, 143 (1989).
[20] Roscoe, R., J. Fluid Mech. **28**, 273 (1967).
[21] Chaffey, C. E., Colloid Polm. Sci. **255**, 691 (1977).

Volume 95, Number 1, January–February 1990
Journal of Research of the National Institute of Standards and Technology

[J. Res. Natl. Inst. Stand. Technol. 95, 15 (1990)]

Dynamics of the Bell Prover, II

Volume 95 Number 1 January–February 1990

Fillmer W. Ruegg and Fillmer C. Ruegg

National Institute of Standards and Technology,
Gaithersburg, MD 20899

The bell prover is widely used for gas flowrate measurements by timing a known stroke of the bell as it rises, presumably with a constant speed, from a bath of sealing liquid. A differential equation for the bell motion (from the previous paper of the same title) is used together with the previous equations of motion for the gas and sealing liquid modified here to provide the basis for a computer simulation of the prover performance. Examples of the results of the computations show substantial fluctuations in all of the motions and modified measurement procedures for improved accuracy are discussed. Proposed modifications to the prover itself are shown by the computations to dampen the fluctuations and to improve the measurement accuracy. Only a limited number of changes of the prover design and of the initial conditions were researched for their effect.

Key words: bell prover design; calibration procedures; flow meter calibration; flow rate; gas flow measurement; gas flow standard; prover.

Accepted: October 27, 1989

1. Introduction

The bell prover of figure 1(a) is essentially an ordinary prover which has been modified with parts added in an attempt to provide the basis for an improvement in gasflow measurement accuracy. A porous plug, a heat exchanger, loose metallic-wool (throughout the pipe volume V_b), and thermal insulation are installed in the inlet pipe. These are suggested to help attenuate the fluctuations of pressure that are generated in the bell and also to assure equality of temperature of the bell and of the gas input. A second essential addition consists of two annular orifice plates mounted in the two sealing liquid spaces between the bell and its tank. It's expected that the constricted liquid flow area there will help to attenuate the liquid motion which is shown in the subsequent computations herein to be a major source of flow measurement inaccuracy.

Three other additions of lesser importance are shown in figure 1(a) and these are suggested for use with both the modified and ordinary prover systems. The first is the utilization of a sonic flow nozzle to be placed somewhere in the bottom of the inlet pipe. It will serve to prevent fluctuations in the gas motion that are generated in the bell from feeding back to the meter thereby causing uncertainties in its calibration. A second benefit is that it eliminates the need to include, perhaps, a different pipe volume with the provers tare volume V_i each time a different meter is installed for calibration. A third benefit arises in that the computations that are to follow here will be more likely to represent actual events for this restricted system as compared to the usual large complicated piping system.

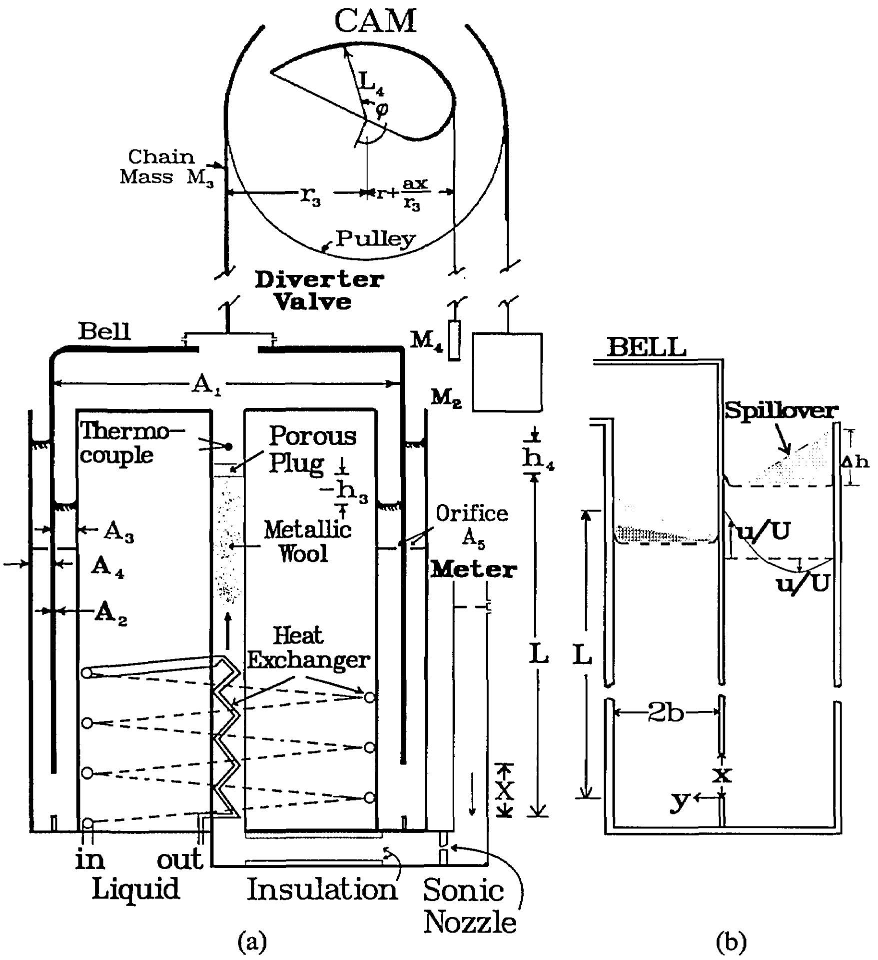

(a) (b)

Figure 1. (a) Schematic drawing of the bell prover. (b) Details of liquid seal and its velocity profile.

More than one nozzle (size) may be needed to be able to cover the full range of flow of any one prover. Other basic requirements are that, at the flow rate of choice, the gas velocity in the nozzle throat be equal to the velocity of sound there, and that the gas at the entry point to bell be at the temperature of the bell. Another concept may prove useful here. Simultaneous measurements of temperature and pressure can be made at the sonic nozzles to calibrate them along with the meter. These calibrated nozzles then should prove useful as secondary flow standards for calibration of meters without the necessity of always exercising the bell prover. A second addition to the ordinary prover should include a thermocouple placed at the exit of the inlet pipe so that it can provide a confirmation that the gas and bell are at equal temperatures all during the measurement stroke of the bell. An average of measurements taken at different times and even places in the bell may not be sufficiently accurate if bell and gas temperatures are not equal.

The third difference between the modified and ordinary prover is in the location and design of the diverter valve. It is placed on top of the bell instead of on that portion of the inlet pipe that is external to the prover's tank. It is proposed that it be an electro-mechanical device designed to be able to remotely select and replicate the stroke time and flow rate history of the gas through the valve. A lateral discharge of the gas from four ports spaced 90° around the new valve will be necessary to avoid a variable and disturbing force on the bell during its upward motion. A rotatable collar or other device with equally spaced and appropriately sized ports together with, possibly, a spring and/or an electric and/or a pneumatic motor to rotate the collar, will be needed to complete the essential parts of the valve. It's not necessary that the new valve be located as shown in figure 1(a), but at that location the initial balance and start-up procedures do not need to differ from that ordinarily used. If it is put on the external pipe of the modified prover some small changes in the initial balance procedure and in the gas flow equations would be needed.

The differential equation of motion for the bell from reference [1], together with modified equations of motion for the gas and sealing liquid, will be used to provide the basis to derive and compare the performance of the two provers.

Special integrals of the Navier-Stokes (NS) equation will be used (for both steady and unsteady motion of the bell in the sealing liquid) to derive the liquid drag forces for use in the bell's equation of motion. Forces connected with entrained liquid and effects not included in the special integrals will be estimated for the same application. The NS equation also provides a justification to treat the motion of the sealing liquid as if it is a "solid" and thus a one-dimensional, second-order differential equation is used for the liquid motion to calculate its effect on the gas volume under the bell.

Each set of differential equations will be subjected to numerical integration using the Runge-Kutta fourth-order method outlined in [2].

2. Equations of Motion

2.1 Gas Motion

The flow measurement process is initiated by a gradual closing of the diverter valve to start the upward motion of the bell from its balanced position. A calculation of the net mass flow into the bell during the stroke of the diverter valve is based on the difference between the initial steady state mass flow out of the valve and the smaller flow out during its stroke. If the ports are rectangular and if the stroke is assumed to be one of constant velocity the orifice port area A_v then can be calculated as $A_v = A_{vi}\ (1-\gamma)$. Here γ is used as t/t_v, the time t from start of the stroke divided by the total stroke time t_v, and A_{vi} is the initial open area. For a constant acceleration stroke, $A_v = A_{vi}\ (1-\gamma^2)$. The latter assumption is used in the subsequent calculations of the flow as its accomplishment seemed to present a simpler valve design problem, and possibly because it would provide a "smoother" acceleration of the bell upward from its float position. A valve might be designed for a still smoother operation to close slowly at both the beginning and end of its stroke, with a port open area represented, for example, by a function such as $A_v = A_{vi}\ (1/2-(1/4)\ \cos^3 \pi\gamma + (3/4)\ \cos\ \pi\gamma)$. The rate of area change with a valve so designed would be $\simeq 0$ at the beginning and end. Effects of valve design on prover performance probably will be researched better by calculations than by experiment.

2.2 The Ordinary Prover

The net mass flow rate into the bell can be written, using the well known equation for the orifice with coefficient of discharge C_D, as

$$\mathrm{d}m/\mathrm{d}t = C_D A_{vi}\ (2\rho_i \Delta P_i)^{1/2} - C_D A_{vi}\ (2\rho\Delta P)^{1/2}\ (1-\gamma^2) \tag{1}$$

where ΔP is $(P-P_a)$ and ΔP_i is $(P_i - P_a)$ and the first term on the right side of eq (1) is the input gas flowrate *FRI*. This rate is to be compared to that established by the calculations from the derived motion of the bell and sealing liquid and for the change of state of the gas in the bell. The mass of gas in the bell and inlet pipe is represented by m and ρ is its density.

The gas law is now used to relate P to the bell and oil motions so that it can be inserted into eq (1). The gas law can be written, using P_i as the initial balance pressure, as

$$(P/P_i) = (mV_t/m_t V)^k = (m/m_t)^k\ (V_t/(V_t + Ax + \Delta V))^k \tag{2}$$

where m_t and V_t are the initial mass and gas volume under the bell and inlet pipe, and Ax is the volume change under the bell due to its motion x from $x=0$. ΔV is the change of gas volume from oil entrainment on the bell as it moves upward plus the volume change caused by motion of the liquid seal. The exponent k may be taken as the ratio of gas specific heats when an apparatus is used that would give adiabatic conditions. For a very small apparatus in which the process might be one of almost constant temperature, k should approach unity. Note here that A is the effective area of a bell prover and is given in [1] as

$$A = A_1 + A_2 A_3/(A_3 + A_4) \tag{3}$$

where A_1 is the interior cross section area of the bell, A_2 the cross section area of the metal of the bell, A_3 and A_4 are the inside and outside horizontal surface areas of the sealing liquid, respectively.

Equation (2) is based first on an assumed uniformity of conditions throughout both volumes V_i and V_b, which allows use of the heat-exchanger but no metallic-wool or porous-plug. Second, the frequency of a Helmholtz resonator built like the bell and inlet pipe was calculated to range from about 8 to 3 times the expected frequency of the pressure pulsations as expected from the motions of the bell. Resonance at the Helmholtz frequency probably will not be observed experimentally.

The gas volume correction for the entrained oil can be derived from eq (9) in reference [1][1] assuming constant pressure (and density) during motion of the bell. Second, if the bell is held stationary while the pressure is changed, the oil seal will move and this also will change the volume of gas under the bell. It is not assumed here that the oil level change will necessarily be such as to maintain equilibrium with the pressure change. Thus ΔV in eq (2) can be written

$$\Delta V=[(A_3-A_4)/(A_3+A_4)]\sum_n \Delta f-A_3(h_3-h_{3,i}) \qquad (4)$$

where the summation indicates the progressive effect starting from the initial balance condition for the bell. The entrained oil volume $\Sigma\Delta f$ is the volume on one side of the bell, and (h_3-h_{3i}) represents the change of sealing liquid level from the initial balance position.

Equation (19a) of [1] gives $\Sigma\Delta f$ (assumed equal to $\Sigma\Delta f_3$ and equal to $\Sigma\Delta f_4$) as

$$\Sigma\Delta f=(4\pi A_1)^{1/2}(Z_3)\,\nu_0^{0.644}\sum_n \dot{x}^{1.644}\Delta t \qquad (5)$$

where Z_3 is a dimensional constant and n is a counter for the number of time intervals in the proposed summation process to replace the integral of eq (19a). Here $\dot{x}$ is the velocity of the bell, and ν_0 is the kinematic viscosity of the sealing oil. $\dot{x}$ has been used in the summation process assuming it adequately represents the quantity $(\dot{x}-\dot{h}_3)$ in eq (19a).

The gas law is used to express the gas density ρ in terms of its pressure in the bell and inlet pipe and then the flow equation (1) can be written

$$\frac{\mathrm{d}m}{\mathrm{d}t}=FRI-C_DA_{vi}\,[2\rho_iP_i(P/P_i)^{1/k}\,(P/P_i-P_a/P_i)]^{1/2}\,(1-\gamma^2). \qquad (6)$$

It should be noted that C_D will be specified as equal to zero at the instant that $\gamma=1$ to simulate a closed diverter valve. Equations (4) and (5) can now be used to insert ΔV into eq (2) for P/P_i which will be used in eq (6) above. These three equations contain numerous terms to be derived subsequently in the discussions of the liquid motions and the equations of motion for the bell.

2.3 The Modified Prover

A computer simulation of the modified prover's performance requires that eq (6) be replaced by two flow rate equations. The first is an equation for the net rate of accumulation of mass in V_b and is expressed as

$$\mathrm{d}m_b/\mathrm{d}t=FRI-FRI(P_b-P)/(P_{bi}-P_i) \qquad (6a)$$

where the second right-hand term represents both the mass rate of flow from the porous plug and also the mass rate entering the space under the bell. Second, the net rate of accumulation of mass m under the bell is

$$\mathrm{d}m/\mathrm{d}t=FRI(P_b-P)/(P_{bi}-P_i)-C_DA_{vi}(2\rho\Delta P)^{1/2}(1-\gamma^2) \qquad (6b)$$

and again C_D should be made equal to zero at the instant γ is specified to equal unity. Note that $(P_{bi}-P_i)$ is the initial pressure drop that is to be specified across the porous plug and that the flow rate through it is proportional to (P_b-P). This requires a plug designed for viscous flow which probably would be more effective than one designed for turbulent flow.

An eq (2a) can now be written similar to eq (2) to derive P as expressed by the equation

$$P/P_i=(m/m_i)^k\,(V_i/(V_i+Ax+\Delta V))^k \qquad (2a)$$

with the reminder that P, m, m_i are for conditions under the bell only. For the specified constant gas temperature in V_b, P_b can be written as

$$P_b=P_{bi}\,m_b/m_{bi}. \qquad (2b)$$

Equations (4) and (5) are used again in the equations above as in those equations for the ordinary prover.

---

[1] Note that the last term of eq (9) in reference [1] has a typographical error. A ratio of densities, not a product, is correct.

2.4 Liquid Motions and Forces

It is intended here to derive the forces on the bell that are associated with the motion of the bell in the sealing liquid. For this purpose some aspects of Couette flow in both steady and unsteady state motion between parallel plates will be discussed. It is also necessary to look at the development of the laminar boundary layer on a flat plate in the event that this could be dominant as to the force it applies to the bell. These considerations might be useful in examining further the forces from oscillatory liquid motion, but these will be ignored as they tend to cancel when both sides of the bell are considered. However, the liquid oscillation would affect the volume of gas under the bell and an attempt will be made to account for this effect. Other force aspects of the liquid motion, such as from entrained oil on the sides of the bell and motion of the oil at its bottom edge are estimated to include them in the bell's motion equation.

2.4.1 Couette Flow I The well-known momentum equation of NS may be used to derive the velocity profile for a fully-developed, steady flow between parallel plates. This condition is practically satisfied if, in figures 1a and 1b, $r >> 2b$ and $(L-x) >> 2b$. These length conditions would limit the influence of the complex flows that exist at the free surface and at the bottom edge of the bell. Thus the applicable equation is written as

$$-\partial P/\rho_0 \partial x + \nu_0 (\partial^2 u/\partial x^2 + \partial^2 u/\partial y^2 + \partial^2 u/\partial z^2)$$

$$= u\,\partial u/\partial x + v \partial u/\partial y + \partial u/\partial t \qquad (7)$$

where y is the distance from the bell's surface, z is along its circumference and u and v are the liquid velocities in the x- and y-directions, respectively, as illustrated in figure 1b. For the specified conditions, the terms $\partial u^2/\partial x^2$, $\partial^2 u/\partial z^2$, $\partial u/\partial x$, v and $\partial u/\partial t$ in eq (7) are all equal to zero. Two boundary conditions, namely that $u = U$ at $y = 0$ (or that the liquid on the bell's surface is carried up with the bell whose velocity is U) and second that $u = 0$ at $y = 2b$ are now used in the integration of eq (7) which gives the profile as follows:

$$u/U = 1 - (1/2bU)(U + [2b^2/\mu_0]\partial P/\partial x)y$$

$$+ (1/2\mu_0 U)(\partial P/\partial x)y^2. \qquad (8)$$

It should be noted that $\partial P/\partial x$ was assumed to be constant across y in the derivation of eq (8).

Equation (8) may now be used to specify a value of $\partial P/\partial x$ such that the liquid up-flow adjacent to the bell is balanced by a down-flow adjacent to the tank wall. Thus, an integration of the flowrate across y derives the volume rate total which, when set to zero, gives $\partial P/\partial x$ as

$$\partial P/\partial x = 3\mu U/2b^2. \qquad (9)$$

The pressure drop along the up-flow as expressed in terms of a liquid head Δh is derived from eq (9) to be equal to $3\mu U(L-x)/2b^2\rho_0 g$. The up-flow must spill over at the free surface to build a liquid head at the tank wall comparable to Δh to provide for the flow down along the tank wall and for its recirculation at the bottom of the bell. When the value of $\partial P/\partial x$ is inserted into eq (8) the velocity profile for zero net flow is found to be

$$u/U = 1 + (3/4)\eta^2 - 2\eta,\ \eta = y/b \text{ and } Q = 0. \qquad (10)$$

Some of these concepts concerning the motion of the sealing liquid are illustrated in figure 1b.

Several interesting features of the flow can now be derived from the velocity profile. First, the velocity gradient at the bell's surface is

$$\partial u/\partial y = -2U/b,\ y = 0 \text{ and } Q = 0 \qquad (11)$$

for calculation of the shear stress there. Second, the volume rate of flow (spillover) carried up by movement of the bell, between the surface and the $u = 0$ point ($y = 2b/3$), is calculated to be equal to

$$Q = 0.296 \ell b U,\ y = 0 \text{ to } y = 2b/3 \qquad (12)$$

for one side of the bell. The quantity ℓ is an average circumference of the bell. Third, this volume rate can be compared to the entrainment rate $\mathrm{d}f/\mathrm{d}t$ of liquid that adheres to the bell as its surface leaves the liquid. Reference [1] gives this rate for a constant bell velocity, $\dot{x}$, as

$$\mathrm{d}f/\mathrm{d}t \simeq Z_3 \ell \nu_0^{0.644} \dot{x}^{1.644}. \qquad (13)$$

For this prover, the entrainment rate ranges from 1.4 to 6 percent of Q in the range of bell velocity researched and discussed in section 3.

The equations of motion will be integrated numerically using a stepwise procedure between time intervals Δt. In a given interval the bell will have velocity $\dot{x} \equiv U$ which will be used to calculate force F_1 on the bell during the interval. Equation (11) gives the velocity gradient and when it is multiplied by μ and the wall areas involved gives F_1 on the two sides of the bell as

$$F_1 = -4\,\mu\,\ell(L-x)U/b. \tag{14}$$

2.4.2 Couette Flow II (a) H. Schlichting [3] in his figure 5.6 and eq 5.24 presents the velocity profile in the fluid between a suddenly accelerated wall and one that is stationary. This "sudden" concept is regarded as applicable here to determine the force on the bell for the integration of the equation of its motion, because the bell velocity changes from interval to interval. His analysis started with two terms of the NS equation, namely the local acceleration term interacting with the friction force. This applies because the convective acceleration and pressure gradient terms are zero in this non-steady, parallel-flow situation.

With that modified NS equation and using appropriate boundary conditions the derived velocity profile is given as a series of complementary error functions (erfc) of the quantities α_1 $[=2b/2(\nu_0 t)^{1/2}]$ and α $[=y/2(\nu_0 t)^{1/2}]$. Partial differentiation (with respect to y) gives the velocity gradient at the moving wall ($y=0$) as

$$\partial u/\partial y = -(\Delta\dot{x}/(\pi\nu_0 t)^{1/2})(1+2\mathrm{e}^{-(2\alpha_1)^2} +2\mathrm{e}^{-(4\alpha_1)^2}\ldots),\ y=0 \tag{15}$$

where $\Delta\dot{x}$ represents the velocity "jump" caused by the "sudden" acceleration. The gradient→∞ as $t\rightarrow 0$, and as $t\rightarrow\infty$, the gradient decays to that for the steady moving wall.

It is proposed here to calculate a time-averaged value of the velocity gradient from $t=0$ to $t=\Delta t$, and to use the "averaged" gradient to calculate force F_2 on the bell. The time-averaged value calculates to be

$$\overline{\left(\frac{\partial u}{\partial y}\right)} = 2\Delta\dot{x}/(\pi\nu_0\Delta t)^{1/2} - 4\Delta\dot{x}\mathrm{e}^{-4b^2/\nu_0\Delta t}/(\pi\nu_0\Delta t)^{1/2}\ldots$$
$$t=0 \text{ to } t=\Delta t \tag{16}$$

where the second and other terms on the right side of eq (16) are negligible for the small values of Δt to be used here. This result is taken as most applicable during the acceleration phase of the motion of the bell. Thus eq (16) leads to

$$F_2 = -4\mu\,\ell X_{\mathrm{WH}}\Delta\dot{x}/(\pi\nu_0\Delta t)^{1/2} \tag{17}$$

(b) The "sudden" concept is also regarded as applicable to estimate the motion of the oil seal (as caused by pressure changes in the bell) and the resultant change of h_3 as used in eq (4) for the volume of gas under the bell. Here it is the oil that is moved suddenly, not the bell. If the velocity of the oil is constant over most of the space between the bell and the walls of the tank, a simple motion equation can be used to estimate $\dot{h}_3$ and h_3 by considering the oil as a solid in motion.

A velocity profile in this "sudden" case is adequately represented (by a single term of a series again for the small time intervals to be used here) as

$$u/\dot{h}_3 \simeq (2/(\pi)^{1/2})\int_{\alpha}^{2\alpha_1-\alpha} \mathrm{e}^{-\eta^2}\mathrm{d}\eta \tag{18}$$

where the approximate equality sign also signifies that $\dot{h}_3$ is not exactly constant across the distance $2b$. The integration limits for η are calculated from α_1 and α as given previously. A numerical integration of eq (18) for values of t assumed equal to integration time intervals Δt to be used here does show an almost constant velocity across practically all of the distance $2b$. Thus, a value of h_3 derived from the "solid" equation of motion should be reduced by a factor derived from an average value of $u/\dot{h}_3$ across the distance $2b$. It should be noted here that the oil motion effect on the gas volume is expected to have most significance while the diverter valve is closing. If the subsequent motion of the bell is at constant velocity the motion of the oil seal should have insignificant influence. Note the big "if" in the previous sentence.

2.4.3 Laminar Boundary Layer A. H. Shapiro [4] presents information on the development of this layer and its velocity profile which was used to estimate its thickness and possible drag force on the bell. It can be shown that the boundary layer thickness quickly becomes comparable to the separation between bell and tank. This would require large and unrealistic pressure gradients in the region such as to void the computations. These and other considerations lead to the conclusion that the laminar layer cannot build up in the apparatus discussed here.

2.4.4 Other Forces (a) Sealing liquid that is entrained on the walls of the bell previously was stated to modify the indicated volume of gas collected. Here the liquid acts to modify the mass of the bell by way of the force of gravity on the liquid. This will be the third non-conservative force F_3 calculated below:

$$F_3 = -2f_3\rho_0 g$$

$$= -2\rho_0 g(4\pi A_1)^{1/2}(Z_3)\,\nu_0^{0.644}\sum_n \dot{x}^{1.644}\Delta t. \qquad (19)$$

(b) Liquid at the bottom edge of the bell is sucked upward by it which creates a drag force there which can be stated as

$$F_4 = -A_2\rho_0\dot{x}^2/2. \qquad (20)$$

2.5 Bell and Liquid Motions

The equation of motion (13) of [1] together with the initial conditions and static balance eqs (14), (15), and (16) of [1] will be used here to set up the second order motion equation for the bell. As indicated in section 2.4.2, it appears that the oil motion can be regarded as the motion of a solid and this basis will be used to set up a second-order differential equation of motion for the oil. These equations, in conjunction with the first-order differential eq (6) for the gas motion, will comprise the system of equations to be handled by numerical integration. For this purpose they will be transformed by the usual procedure into five first-order equations.

For the motion of the bell eq (14) of [1] was used first, here with $x_i = 0$, to calculate h_{4i} at the initial balance condition using an assumed (or specified) value of $(P_i - P_a)$. Second, eqs (15) and (16) of [1] were used to calculate M_3/L_3 (the chain mass per unit of length) so that the cam and buoyancy compensator M_4 could be replaced with the chain compensator. By this means the term involving $\dot{x}^2$ is removed from the bell's equation of motion. The equation thus will be a little simpler. Performance with the chain can be compared later with that of the usual suspension system. Third, eq (13) of [1] then can be simplified further to read as below (after noting that $A_1\ (P_i - P_a) = g\ (M_1 - M_2 - \rho_0 A_2 L) - \rho_0 g A_2 h_{4i}$):

$$(M_1 + M_2 + I/r_3^2)\ddot{x} = -(\rho_0 A_2 - 2M_3/L_3)gx$$

$$+A_1(P - P_i) + \rho_0 g A_2(h_4 - \mathrm{h}_{4i}) + \Sigma F. \qquad (21)$$

All terms above are zero at the initial balance conditions of $x = \Sigma F = 0$ and $h_4 = h_{4,i}$ and $P = P_i$. ΣF designates the sum of the drag forces. Figure 1 locates and defines some of the quantities used. I is the moment of inertia of the pulley.

Two different approaches might be selected to set up the oil motion equation, one regarding the oils on the two sides of the bell as two separate "solids", or by treating the oil as a single "solid" using the assumption that $A_3 = A_4$. For the two "solids" case the equation is quite complicated and contains a product of the oil acceleration and elevation and also its velocity squared. This seems an unwarranted complication at the present time and the single "solid" will be used.

The equation of motion for the single "solid" is derived using the familiar concept that acceleration is given by force per unit mass and that $(h_4 - h_{4i}) \simeq -(h_3 - h_{3i})$, to give

$$\ddot{h}_4 = (P - P_i)/[2\rho_0(L - x)] - g(h_4 - h_{4i})/(L - x)$$

$$-\text{Force Loss}/[\rho_0(A_3 + A_4)(L - x)]. \qquad (22)$$

It should be noted here that the oil mass to be moved is $\rho_0(A_3 + A_4)(L - x)$, and that the term containing h_4 is the liquid's back pressure. The factor 2 (and also unity in the liquid head term) arises from the pressures acting on the assumed area$=(1/2)(A_3 + A_4)$. A "Force Loss" is included in the equation to include the effect of the turn that the oil must make at the bottom of the bell of the ordinary prover. This loss is assumed to be equal to one-half of the velocity pressure, or $(1/2)(1/2)\ \rho_0\dot{h}_4^2$ multiplied by the area A_3, which then gives the last term on the right side of eq (22) above as $(1/8)\dot{h}_4\,|\dot{h}_4|/(L - x)$. The quantity $|\dot{h}_4|$ is used to make the force loss applicable to both flow directions. When the two orifices are installed to constrict the oil flow space down to an area of $(1/2)A_5$ on each side of the bell to modify this part of the prover, a pressure drop will be introduced into the flow there. This drop will arise from the frictional loss of mechanical energy mostly on the downstream side of each constriction. For an area constriction down to about 10 percent, a possibly conservative estimate of the pressure drop would correspond to one velocity head pressure based on the liquid's average velocity in the constricted area. On this bases the last term of eq (22) will be equal to the quantity $(1/2)(A_3 + A_4)^2\ \dot{h}_4|\dot{h}_4|/A_5^2(L - x)$ when the orifices are used.

In the context of the discussion above it should be noted that the "solid" oil motion will have some effect on the ordinary bell by the necessity of making the U-turn there. If it's assumed that the downward motion of the oil pressurizes the "dead" oil space below the bell and acts to help move the bell, the force F_5 can be estimated as

$$F_5 = (1/4)\rho_0\,A_2\,\dot{h}_4^2 \qquad (23)$$

where the above is based on one-half of the velocity pressure. The above force is replaced, for the modified bell, by a suction force on the bottom of the bell as caused by the downward motion of the oil through each orifice constriction. This motion is induced by the upward motion of the bell. As discussed above for a proposed area constriction in the orifice down to 10 percent, one velocity head pressure loss (based on the velocity in the constriction) is probably a conservative estimate. On this basis F_5 for the modified prover is

$$F_5=-(1/2)\,\rho_0 A_2(A_2/A_5)^2\dot{x}^2. \tag{23a}$$

These forces F_5 are introduced as reminders that they and other "end effect" forces exist but probably have small effects.

2.6 Summary of Motion Equations

The gas flow equation (6) for the ordinary prover is

$$\dot{m}=FRI-C_D A_{vi}\,(2\rho_i P_i)^{1/2}\,(P/P_i^{1/k})^{1/2}\,(P/P_i-P_a/P_i)^{1/2}\,(1-\gamma^2) \tag{24}$$

where $C_D=0$ for the condition $\gamma \geqslant 1$ and where the factor $(1-\gamma^2)$ assumes the use of a constant acceleration diverter valve. Equation (24) needs auxiliary eq (2) for P/P_i and eqs (4) and (5) for V/V_t as follows:

$$P/P_i=[m/m_t/(V/V_t)]^k; \tag{25}$$

$$V/V_t=1+Ax/V_t+(Z_1/V_t)\sum_n(\dot{x}^{1.644}\Delta t)+Z_2(A_3/V_t)h_4; \tag{26}$$

where $Z_1=[(A_3-A_4)/(A_3+A_4)]\,(Z_3)\,(4\pi A_1)^{1/2}\,\nu_0^{0.644}$;

Z_2 = a correction factor for lack of oil "solidity";
Z_3 = a constant whose value depends on the system of units that will be used.

Note above that h_4 has replaced $(h_{3i}-h_3)$ because A_3 is assumed equal, in eq (26), to A_4 and that the motion equations when integrated will give $h_4=(h_4-h_{4i})$.

The gas flow eqs (6a) and (6b) for the modified prover are:

$$\dot{m}_b=FRI-FRI\,(P_b/P_i-P/P_i)/(P_{bi}/P_i-1); \tag{24a}$$

and

$$\dot{m}=FRI(P_b/P_i-P/P_i)/(P_{bi}/P_i-1)-C_D A_{vi}[2\rho_i P_i(P/P_i)^{1/k}(P/P_i-P_a/P_i]^{1/2}(1-\gamma^2). \tag{24b}$$

Equations (24a) and (24b) need auxiliary eqs (2a) and (2b) for P/P_i and P_b/P_i, respectively, and eqs (4) and (5) also will be used again in the following equations:

$$P_b/P_i=(P_{bi}/P_i)m_b/m_{bi} \tag{25a}$$

$$P/P_i=[m/m_i/(V/V_i)]^k \tag{25b}$$

$$V/V_i=1+Ax/V_i+(Z_1/V_i)\sum_n(\dot{x}^{1.644}\Delta t)+Z_2(A_3/V_i)h_4 \tag{26a}$$

The equation for the motion of the bell eq (21) is

$$(M_1+M_2+I/r_3^2)\ddot{x}=A_1(P-P_i)-(\rho_0 A_2-2M_3/L_3)gx+\rho_0 g A_2 h_4+\sum_1^5 F \tag{27}$$

which uses individual drag forces, as follows:

$$F_1=-(4\mu\ell/b)(L-x)\dot{x}; \tag{27a}$$

$$F_2=-(4\mu\ell/(\pi\nu_0)^{1/2})(L-x)\Delta\dot{x}/(\Delta t)^{1/2}; \tag{27b}$$

$$F_3=-2\rho_0 g(4\pi A_1)^{1/2}\,(Z_3)\,\nu_0^{.644}\sum_n(\dot{x}^{1.644}\Delta t); \tag{27c}$$

$$F_4=-(1/2)\,\rho_0 A_2\,\dot{x}^2; \tag{27d}$$

$$F_5=(1/2)\,\rho_0\,A_2\,\dot{h}_4^2 \text{ (ordinary prover)} \tag{27e}$$

$$F_5=-(1/2)\,\rho_0 A_2(A_2/A_5)^2\dot{x}^2 \text{ (modified prover).} \tag{27f}$$

The equation of motion eq (22) for the sealing oil in the ordinary prover is

$$\ddot{h}_4=(P-P_i)/[2\rho_0(L-x)]-gh_4/(L-x)-(1/8)\dot{h}_4|\dot{h}_4|/(L-x) \tag{28}$$

and for the modified prover the last term on the right side of eq (28) is specified as equal to $50\dot{h}_4|\dot{h}_4(L-x)$ when A_5 is constructed to be equal to 0.1 (A_3+A_4). With this substitute, last term of eq (28) in place we may label the motion equation for the sealing oil as eq (28a).

Equations (24), (27), and (28) or their (a) and (b) substitutes for the modified prover, comprise the two systems of equations to be integrated numerically by the fourth-order Runge-Kutta method as outlined in [2].

A recapitulation of the main assumptions used in the derivations of the above equations seems advisable. It does not seem advisable at the present time to develop a change to eq (24) to account for a possible non-constant value of C_D. Equations (27b) and (28), and the far right-hand term of eq (26) are based on a special integral of the NS equation for the case of "sudden" motion of the bell and of the sealing liquid. Equation (27a) was derived from the NS eq (7) for steady flow between parallel plates without consideration of end effects. Equation (27e) and the far right-hand term of eq (28) but not for eq (28a) are used as reminders of end effects not fully accounted for. The forces of these "estimated" end effects turned out to have an insignificant effect on the calculated performance of the prover. Except in eqs (27), (26a) and (3), A_3 was assumed equal to A_4 with corresponding assumptions $f_3=f_4$ as in eq (27c) and $-h_3=h_4$ as in eq (28). And, finally, the flow rate into the bell of the ordinary prover is assumed to be constant and unaffected by the probable small changes of state of the gas in V_b.

3. Calculated Results

The numerical integrations of the equations of motion are used to derive the performance of the provers which will be illustrated by various curves showing the motions of the bell and sealing oil and the derived gas pressure and gas volume correction all expressed as a function of the time. (See figs 2 to 5). These figures can give a good qualitative illustration of the performance, but further computations are necessary to derive quantitative evaluations and comparisons of the measurement performance. Equation (2) can be rearranged for this purpose so that the true mass collected can be

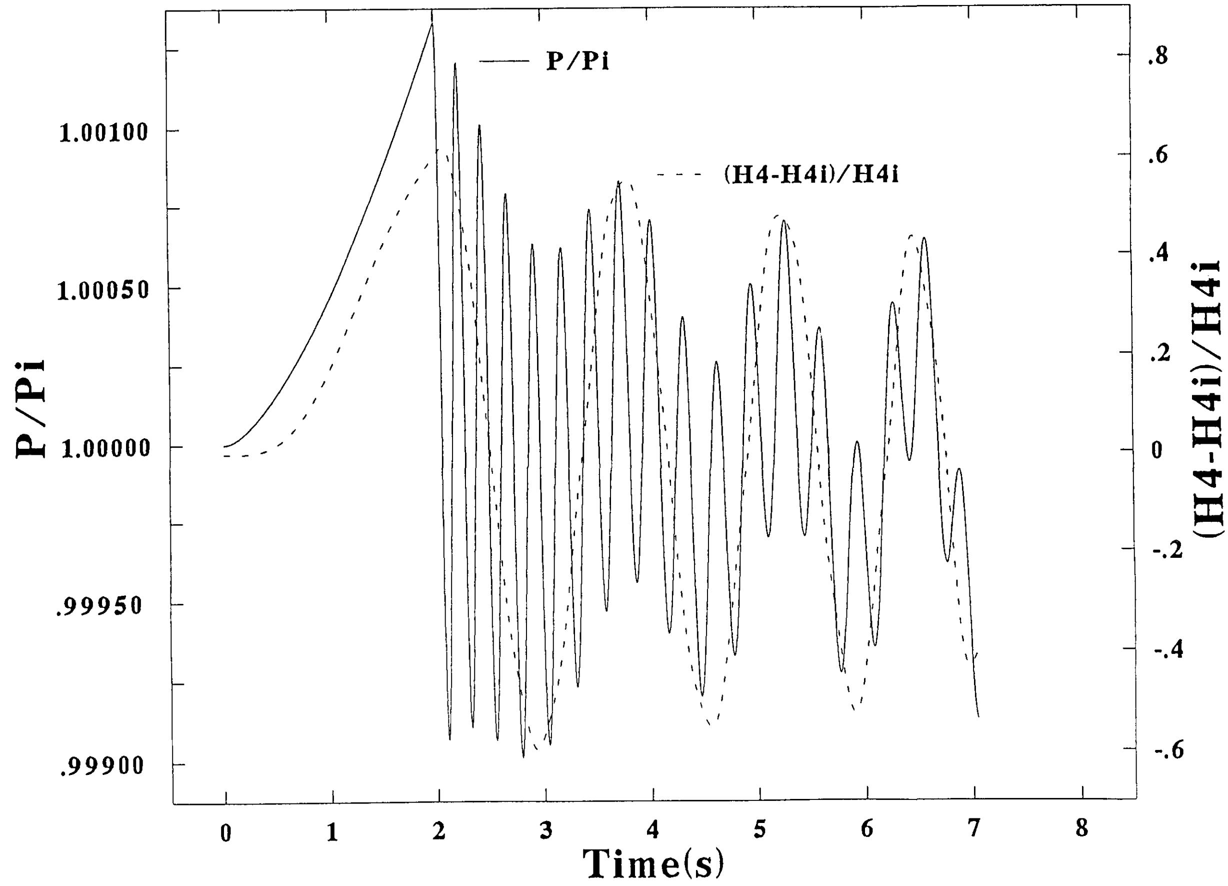

Figure 2. Bell pressure, and height of sealing liquid, plotted vs time. Program HIFLO.

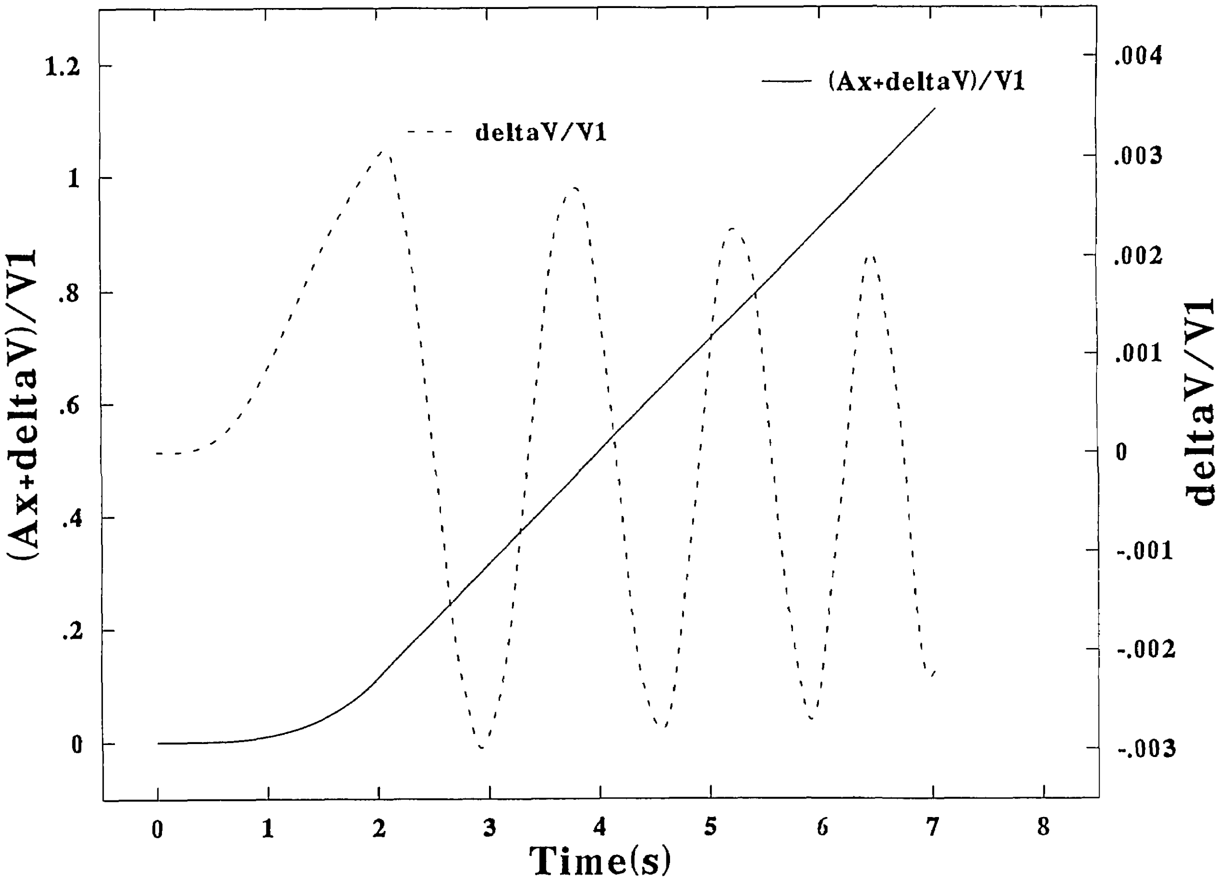

Figure 3. Actual volume of gas collected, and volume correction, plotted vs time. Program HIFLO.

expressed in terms of $\rho_i A\ (x_2-x_1)$ with corrections applied to it for the fluctuations of P and ΔV. Subscripts 1 and 2 are used on x to signify values at the beginning and end of the chosen timing interval, respectively. It seemed preferable to separate the P and ΔV corrections, and to do this the pressure ratio in eq (2) was expressed as very closely equal to $(1+(P-P_i)/kP_i)$. With some use of algebra, eq (2) can be written for the modified prover in the form

$$(m_2-m_1)\simeq\rho_i A(x_2-x_1)\left[1+\frac{\Delta V_2-\Delta V_1}{A(x_2-x_1)}+\frac{(P_2-P_i)(V_i+Ax_2)}{kP_iA(x_2-x_1)}-\frac{(P_1-P_i)(V_i+Ax_1)}{kP_iA(x_2-x_1)}+\frac{(P_{b2}-P_{b1})V_b}{(k=1)P_{bi}A(x_2-x)}\right]. \tag{29}$$

and when the ordinary prover is used $V_b=0$ in the far right-hand term and V_i should be replaced by V_t which is given by (V_i+V_b).

3.1 The Ordinary Prover

Almost complete physical data were available to the authors on a bell prover of nominal capacity V_1 of 5 ft^3 (0.1415851 m^3) and these were used in three computer runs for the first look at the utility of the proposed analytical method. Results of these runs indicate the effectiveness of the integration method as well as demonstrate the size and sources of errors likely to be encountered with the usual laboratory procedures. The prover specifications are listed in table 1 together with data on initial balance conditions, fluid properties and the computer run conditions used in the programs HIFLO and LOFLO. Nominal measured stroke times are 5 and 50 s, respectively, for these two programs.

The two runs at the high rate of flow (nominal collection time of 5 s) were done with different time intervals in the integration process, namely 0.002 and 0.01 s. Rates of flow derived from use of these two integration processes differed by about 0.01 percent. Comparison of other physical variables also showed differences near 0.01 percent. On the bases of this good agreement it was decided to use the 0.01-s time interval for the low (50 s collection) flow rate calculation. It seemed reasonable to expect much larger differences than 0.01 percent between prover performance at the two rates of flow.

Figures (2) and (3) are graphical representations of the calculated results at the high flow rate and figure (4) presents results at the low flow rate. Figure (2) shows a relatively large initial fluctuation of the pressure, about ±46 percent of ΔP_i from P_i with a relatively long period, initially about 1.8 s and decreasing to about 1.1 s. The pressure fluctuation decreases to about ±30 percent of ΔP_i from the mean pressure, but the curve near 7 s shows a hint of a possible increase at that point. Higher frequency fluctuations of the pressure, with periods of about 0.3 s, are also evident. The amplitude of the oil motion as converted from values of h_4 to pressure is about 120 percent of the pressure fluctuation. It is evident that the pressure fluctuations are strongly modulated by the oil fluctuations. It is also

Table 1. Prover specifications and computer run conditions

Prover specifications[a]

A	A_1	A_2	A_3	A_4	ℓ	
.2238913	.2183231	.01189164	.05481303	.06224530	1.678537	SI
2.409936	2.35	.128	.59	.67	5.507	U.S.

M^c	M_1	M_2	$M_3/L_3{}^c$	M_4	I/r_3^{2c}	
94.71400	99.23840	85.45006	5.569795	0	5.032009	SI
6.49	6.8	5.855197	.1163280	0	.3443026	U.S.

b	$V_b{}^c$	$A_5/(A_3+A_4)$	V_1	
0.0175	0.0062	0.1	0.14 m^3	SI
0.0575	0.22	0.1	5 ft^3	U.S.

Initial conditions and fluid properties

L^c	g	P_a	(P_i-P_a)	h_{4i}	$x_i{}^c$	
.82296170	9.8054	101362.1	239.4003	1.344412(10^{-2})	0	SI
2.7	32.17	2117	5	4.410790(10^{-2})	0	U.S.

V_i^c	m_i	k^c	ν_0	μ_0	
2.208728(10^{-2})	3.409868(10^{-2})	1.4	.2006714(10^{-4})	170.453(10^{-4})	SI
0.78	2.336505(10^{-3})	1.4	2.16(10−4)	3.56(10^{-4})	U.S.

ρ_0	ρ_a	ρ_i	$(P_{bi}-P_i)^c$	
850.3685	1.201339	1.204176	$40(P_i-P_a)$	SI
1.65	2.331(10^{-3})	2.336505(10^{-3})	$40(P_i-P_a)$	U.S.

Computer run conditions

Program name	$\dot{m}=FRI$	t_v	Z_2	Δt	$60\dot{m}/\rho_a$	Nominal Collection time, $\rho_a V_1/\dot{m}$	
HIFLO[b]	3.4018341(10^{-2})	2	.95	.002	1.699021	5 s	SI
	2.331(10^{-3})	2	.95	.002	60 scfm	5 s	U.S.
HOLHOG	Same as above	.2	.95	.0002	———same as above———		
LOFLO	3.4018341(10^{-3})	2	.90	.01	.1699021	50 s	SI
	2.331(10^{-4})	2	.90	.01	6 scfm	50 s	U.S.

[a] SI units are kilogram, meter, newton and seconds (MKS). U.S. units are slug, foot, pound-force, seconds.

[b] Program HIFLO was also done with an integration time interval Δt of 0.01 s.

[c] Derived or assumed as probably applicable.

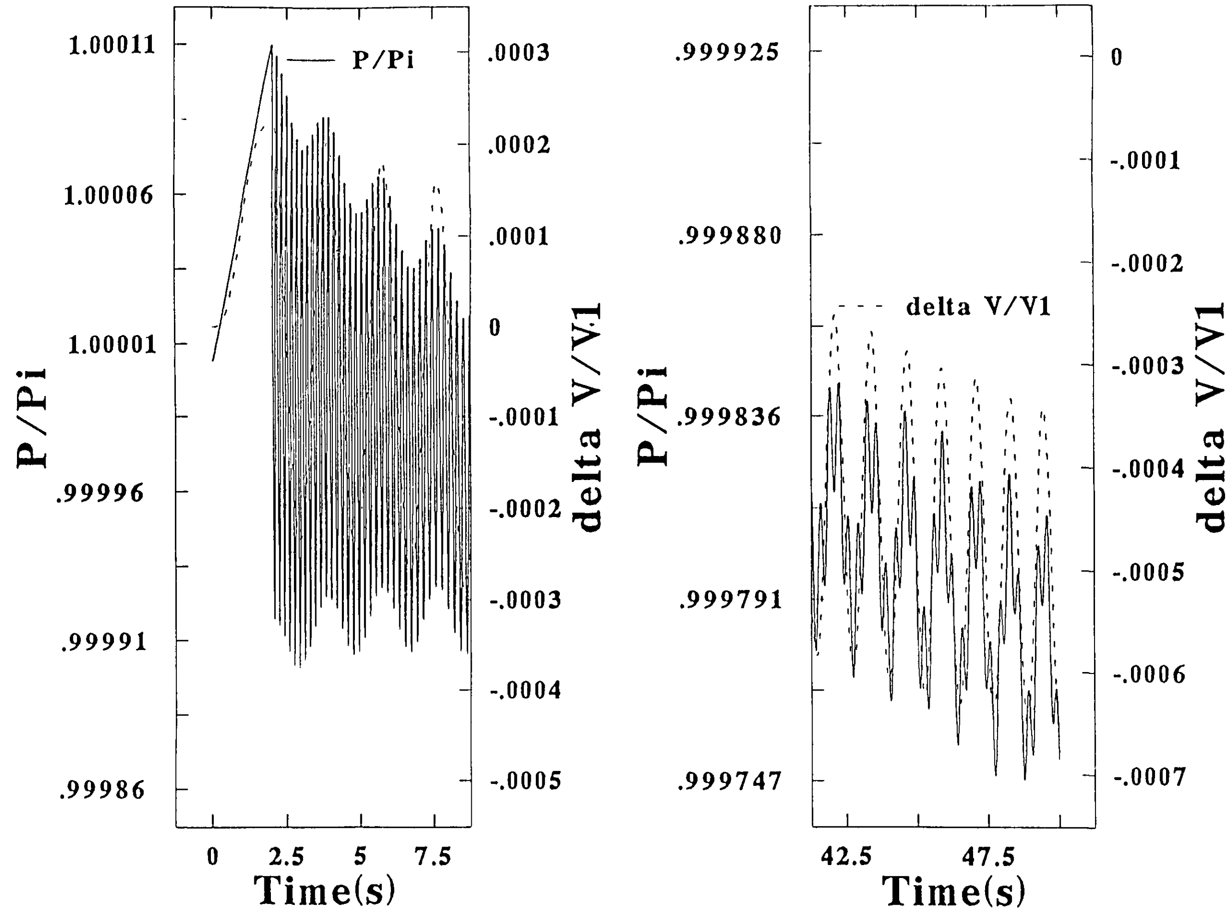

Figure 4. Bell pressure, and gas volume correction, plotted vs time. Program LOFLO.

strongly evident from figures 2 and 3 that the gas volume correction ΔV under the bell fluctuates practically in unison with h_4. This fact suggests that failure to measure h_4 possibly can be the major source of error.

At the low rate of flow figure 4 shows a much smaller initial fluctuation of pressure, about ±4.0 percent of ΔP_i from P_i, and again a relatively long period initially of about 1.8 s which decreases to about 1.4 s. The pressure fluctuation and the pressure level both decrease, the former to ±1.3 percent of ΔP_i about the mean pressure which is about 9 percent of ΔP_i below P_i. These fluctuation amplitudes are about six percent of those at the high rate of flow, as compared to the flowrate ratio of 10 percent. The amplitude of the sealing liquid motion (not shown) begins at about 115 percent of the pressure, but winds up near the end of the measurement stroke at about twice that of the pressure fluctuation. As at the higher flow rate, the gas volume correction (not ordinarily measured) fluctuates practically in unison with h_4 and with the low frequency pressure fluctuations. The high-frequency fluctuations have periods of about 0.19 s which increases to about 0.31 s.

The high frequency motion calculated for the bell can be shown to be real by considering the bell to be vibrating as if suspended from a "spring" which can "replace" the air enclosed in the bell. For the case of the very low values of the pressure fluctuations prevailing here, this concept is sufficiently accurate to derive the "spring constant" on x as equal to $kA_1^2P_i/V$ where V is the volume of air and x is the motion of the bell about a stationary position. The vibration period for this well known case is $2\pi/\{kA_1^2P_i/[V(M_1+M_2+I/r_3^2)]\}^{1/2}$ which calculates to be in the range from 0.2 to 0.4 s. Inclusion of the buoyancy force and damping (drag) forces would not change the calculated period sufficiently to warrant the added complication. Here again these periods are in conformity with those derived from the full motion analysis.

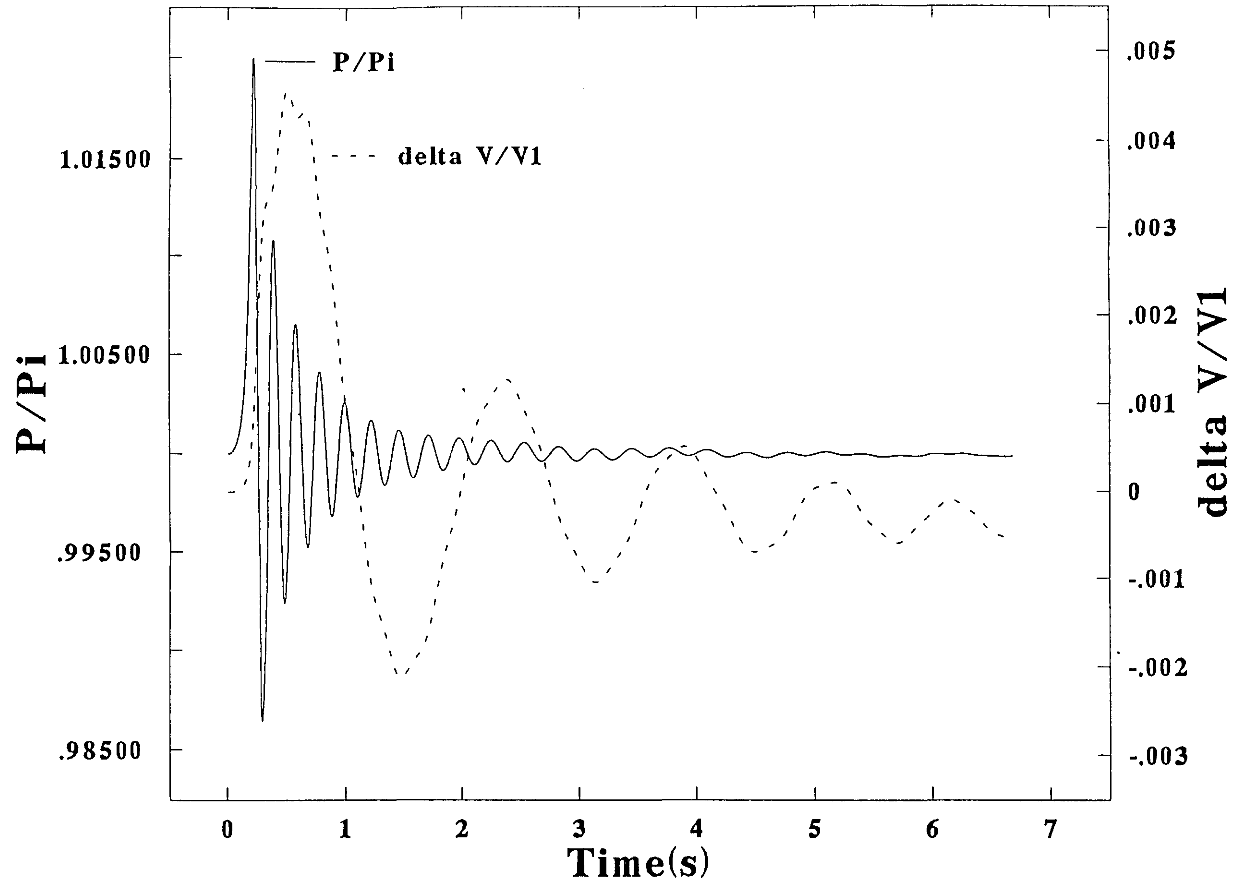

Figure 5. Bell pressure, and gas volume correction, plotted vs time. Program HOLHOG.

An inspection of eq (29) and figures 2, 3, and 4 demonstrates the problems involved with making accurate measurements of the fluctuating physical variables and also the need to correlate those measurements with the timing points used to define the stroke of the bell. It is also evident that various choices and measurement methods can be used to try to derive the various corrections in eq (29) for the true collected mass.

3.1.1 Method 1 If the measurements of P and either Δh_4 (or ΔV) are accurate at any instant and accurately correlated with the bell positions x_1 and x_2, eq (29) provides the true mass.

3.1.2 Method 2 Figure 2 demonstrates that no corrections to $\rho_i A(x_2-x_1)$ are necessary if the initial and final timing points (at 3.36 and 6.2 s, for HIFLO) can be identified by the instrumentation when the variables of $(P-P_i)$ and Δh_4 both equal to zero at both bell positions (a zero-zero criterion). In the more general case (LOFLO, for example) this criterion does not prevail. However, pressure transducers probably are available with capability to follow the low frequency fluctuations of the pressure (as caused by the motion of the oil) with good accuracy especially at the fluctuation mid-points. If the timing points x_1 and x_2 are made to coincide in time with those mid-point pressures, the corrections derived with eq (29) would also be accurate because the mid-points of the ΔV and the ΔP motions are shown here to coincide. These methods should be used but apparently are not because of the practical difficulties. A third procedural compromise, Method 3, is usually used to derive the corrections.

3.1.3 Method 3 Measurements are made with a water manometer to give (what is believed to be) mid-point values of the high-frequency fluctuating pressures (*AFP*) at two preselected, convenient positions x_1 and x_2. These measured *AFP* values are used in eq (29) along with calculated values of ΔV (based on *AFP*) to derive "corrections" to $\rho_i A(x_2-x_1)$. The "worst" timing point choices that can be derived from figures 2 and 4 are used to illustrate in table 2 the errors that might result with use of Method 3. "True" corrections (of Method 1) are also listed for comparison in Table 2.

Table 2. Measurement corrections for worst timing choices

Program	Correction Method	$\Delta(\Delta V)\%$	$\Delta(\Delta P)\%$	$\Delta P_b\%$	% Total, correction	t_1	t_2
HIFLO	1, True	−0.752	−0.072	NA	−0.824	3.73	6.95
HIFLO	3, AFP	−0.196	−0.065	NA	−0.261	3.73	6.95
HIFLO	Remaining error after AFP Correction = −0.563						
LOFLO	1, True	−0.017	−0.060	NA	−0.077	3.8	44.6
LOFLO	3, AFP	−0.053	−0.001	NA	−0.054	3.8	44.6
LOFLO	Remaining error after AFP Correction = −0.023%						
HOLHOG	1, True	−0.138	−0.045	−0.001	−0.184	3.73	6.6
HOLHOG	3, AFP	−0.108	−0.022	−0.001	−0.131	3.73	6.6
HOLHOG	Remaining error after AFP Correction = −0.053%						

For program HIFLO, one "worst" timing point choice would need a very large true correction, while the correction based on values of the *AFP* is only 32 percent of what is actually needed. For a LOFLO "worst" choice, use of the *AFP* gives a correction that is 70 percent of the true correction. The net result is that flow rates based on *AFP* values would be higher than actual by 0.56 and 0.02 percent for the flow rates HIFLO and LOFLO, respectively. It should be noted the corrections for entrained oil on the sides of the bell amounted to −0.013 and −0.003 percent for those two rates. These are not shown above because they are included in the values of ΔV in the true correction procedure [see eq (4)]. It should also be noted that other "worst choices" would give corrections of opposite sign.

There are three suggestions to be made concerning possibilities for improving the instrumentation and/or measurement procedures used with the ordinary prover.

3.1.4 Suggestion 1 Instrumentation problems would probably prevent implementation of the ideal situation in which Method 1 could be effectively used. However, experiments should be conducted to try to overcome these difficulties.

3.1.5 Suggestion 2 It might be possible to implement the zero-zero criterion as described in method 2 to use what is essentially a "correctionless" procedure. Two requirements are necessary for this purpose. First, the prover must be modified to maintain the average of the maximum/minimum pressures, P_m, constant and equal to P_i during the stroke of the bell. Second, an instrument must be available to be able to identify bell positions where the fluctuating values of ΔP and Δh_4 are equal to zero. The first requirement probably can be met by an adjustment of the buoyancy weights (downward by about one and seven percent, respectively, as computed from the pressure curves for HIFLO and LOFLO). This should be and is confirmed if some bell positions, particularly near x_2, can be found where *AFP* values or transducer measured values are equal to P_i. These positions need not necessarily be those that are finally used for the rate measurements.

An instrument which might be used for phase indications of ΔP and Δh_4 is the optical encoder used by G. Kulin, P. Huang, and G. Mattingly [5] to better measure the volumetric displacement of the bell and its velocity. It was mounted on the pulley and it gave (almost) linear vertical motion in the form of electrical pulses. Their temporal traces of the encoder's output voltage displayed fluctuations of the bell's velocity at approximately the same period of about 1.8 s as calculated herein. Some computations for program LOFLO (not shown) demonstrated that maximum bell velocity occurred when both ΔV and values of $(P-P_i)$ both were zero. Therefore, presumably, the encoder's indication of the maximum bell velocity also occurs at the zero-zero condition. This leads to the suggestion that the timing points should be made to coincide with the maximum velocity indications of the optical encoder to try to eliminate the otherwise needed, but in accurate, *AFP* corrections to derive the true mass of gas collected. As an alternative to the above, more attention should be given to fully implement Method 2.

3.1.6 Suggestion 3 It appears to be possible to implement the zero-zero criterion as described in Method 2 using the *AFP* procedure of Method 3 which can be modified to measure the true collected mass of gas. Two modifications appear of possible utility, both needing a constant value of $P_m=P_i$ during the stroke of the bell. The first would use computed motions of Δh_4 (as described herein) to identify and use the bell positions x_1 and x_2 where Δh_4 values are expected to be zero. *AFP* values would then also equal P_i and corrections to

$\rho_i A(x_2-x_1)$ would also equal zero. Results from use of this method could then be compared to results obtained below with the second modified *AFP* procedure.

The second modified *AFP* procedure would utilize a multiplicity of strokes of the bell each with positions x_1 and x_2 systematically moved until both give *AFP* values equal to P_i. P_m must also be maintained equal to P_i with this method (see Suggestion 2). This method is based on the assumption that *AFP* values of pressure fluctuate about P_i with a smaller amplitude than those of the high frequency pressure fluctuations, and with a period of the low frequency fluctuations of Δh_4. It's expected that on average five different strokes of the bell would be needed with x_1 and x_2 each moved each time a distance corresponding to the distance traveled by the bell during 0.05 period of the Δh_4 fluctuation. It's assumed in the experimental situation that the pressure measuring instrument actually does indicate the *AFP* values. If all of these criteria prevail the modified, multiple *AFP* method is also correction less. An advantage of these two procedure modifications is that neither requires apparatus changes.

3.1.7 The Modified Prover Figure 5 presents a graphical picture of the calculated temporal traces for the pressure and gas volume correction as derived in program HOLHOG which was specified to have the same flow rate as in HIFLO. These results show that the modifications made to the prover caused large reductions in the amplitude of the pressure and oil motions (particularly for the latter) as was intended. Each oil orifice had a 10 percent open area, the drop across the Porous Plug was specified as equal to $40\Delta P_i$, and t_v was reduced to 0.2 s (from 2 s as used in HIFLO and LOFLO). These three changes were made simultaneously and "almost" arbitrarily, and hence the name HOLHOG was chosen. Note that ΔV increased by only about 50 percent over that in HIFLO in spite of the 14-fold increase of ΔP at the end of 0.2 s. These larger upsurges, however are subsequently efficiently dampened. Although the frequencies of the motions of ΔV and ΔP are the same as in the ordinary prover, the practically constant phase difference between the two motions is not evident here.

The calculated "worst" corrections for HOLHOG listed in the table above demonstrate that the correction remaining and needed after application of the *AFP* Method 3 is gratifyingly reduced to 0.053 percent from the 0.586 percent needed for the ordinary prover. This possible "worst" result for HOLHOG is improved to a needed remaining correction of only 0.006 percent if a "best" timing choice happens to be made. Phase differences between the ΔV and ΔP motions that change during the stroke of the bell limit suggestions for improvement in methodology to Suggestion 3 above. However, the need for improvement is much, much less than for HIFLO at its worst.

It's appropriate at this point to discuss the "almost" arbitrary group of apparatus changes (specified for HOLHOG) and the problem of setting the initial conditions. As a preliminary to HOLHOG, computations of the effect of the orifice installation alone, and next of the effect of the porous plug alone, indicated that dampening was not effective enough before the bell reached x_1 to make a significant improvement. A third preliminary calculation was done to evaluate the effect of a single change in an initial condition, namely a reduction of t_v from 2 to 0.2 s in program HIFLO. This change produced a two-fold increase in the initial upsurge of ΔV over the already large increase evident in HOLHOG. This large increase illustrates the importance of the initial condition, and second that the orifice effectively dampened the motion of the oil in HOLHOG and especially the initial upsurge motion.

Other changes of initial conditions, such as in the flow rate characteristics of the diverter valve, and changes in the relationship of V_i to V_b to V_1, also could have significant effects on the performance of both provers studied here. This discussion should now revert back to the need to use a motorized and stroke-designed diverter valve as previously suggested herein. This discussion also leads to the conclusion that prover performance cannot be adequately specified until the initial conditions are too.

4. Conclusion

It appears that the equations of motion for the moving elements of the prover system and the procedure used in their numerical integration can produce calculated results which offer a reasonable chance that they can be used to design improvements in the apparatus and measurement procedures. "Dynamic errors" in the measurement of flow rates can arise primarily from the fluctuating motions of the sealing liquid, second from fluctuating velocity of the bell, and third and usually least in magnitude from entrainment of liquid on the bell. Proposed additions to the prover can be used to (1) assure needed equality between gas and bell temperatures and (2) to reduce the amplitude of the fluctuating motions as one way to reduce the magnitude of measurement errors. Three other suggestions for improved measurement procedures include an ideal situation in which pressures and oil motions are accurately measured at any two bell positions of choice. A second more practical suggestion would require that the timing points for the bell motion be properly correlated with indications of the mid-point pressures from a pressure transducer or correlated with indications of the maximums in the fluctuating bell velocity. A third suggestion for improved accuracy entails the utilization of two different approaches both being modifications of that currently in use which relies on manometer reading of the average indications of the high-frequency fluctuating pressures at the two bell positions of choice. Some changes in the initial conditions produced performance changes which emphasizes that blanket performance and accuracy statements cannot be specified unless all initial conditions are also specified.

5. Nomenclature

A = See eq (3), effective bell area
A_1 = Cross-sectional, open area of the bell
A_2 = Horizontal cross-sectional area of the metal wall of the bell
A_3 = Horizontal area of the inside sealing liquid
A_4 = Horizontal area of the outside sealing liquid
A_5 = Sum of orifice open areas in sealing liquid spaces
A_v = Area of ports of the diverter valve
AFP = An average or mid-point values of the fluctuations of P
$2b$ = Separation distance between bell and tank
C_D = Coefficient of discharge for the diverter ports
Δ = Change of
F = Force
FRI = Gas flowrate into the bell $= \dot{m}_i$
f = Volume of entrained oil on one side of the bell
g = Local acceleration of gravity
h_3, h_4 = Sealing liquid elevations with reference to L
Δh = Oil "spillover head"
I = Moment of inertia of the pulley
k = An average ratio of isothermal to adiabatic compressibility—for air between 1.0 and 1.4
L = Sealing liquid depth when $x=0$
L_3 = Length of the chain
ℓ = Circumference of bell
M = Mass of the bell
M_1 = Mass of the bell plus that portion of the chain which is on the same side of the pulley when $x=0$
M_2 = Mass of the counterweight plus its chain weight
M_3 = Mass of the chain
M_4 = Mass for buoyancy compensation (not used here)
m = Mass of the gas in the bell
P_m = Average of the maximum/minimum pressures in the bell
P = Pressure in the bell
P_b = Pressure in the bell inlet pipe of the modified prover
ΔP = Differential pressure
Q = Volume rate of spillover liquid on one side of the bell
s = seconds
t = Time, seconds
t_v = Diverter valve closing interval, seconds
Δt = Integration time interval
t_1 = Time at beginning of timing interval
t_2 = Time at end of timing interval
U = Bell velocity along x, or "freestream" velocity down along X
u = Velocity of sealing liquid to positive x
V_i = Initial volume of gas under the bell only
V = Volume of gas in the bell including V_i or V_t
V_b = Volume of gas in the bell inlet pipe
V_1 = Nominal prover capacity
$V_t = V_i + V_b$
ΔV = Gas volume correction
v = Velocity in the y-direction
x_1 = Bell position at beginning of timing interval
x_2 = Bell position at end of timing interval
x = Bell's movement upward from zero position
y = Distance from bell's surface
z = Distance around circumference of the bell
Z_1 = A group of constants in eq (26a)
Z_2 = A correction factor for lack of oil "solidity"
$Z_3 = 1.09\ \mathrm{m}^{-0.93}\ \mathrm{s}^{1.29}$ (SI) or $0.36\ \mathrm{ft}^{-.93}\ \mathrm{s}^{1.29}$ (U.S.)
$\alpha = y/[2(\nu_0 t)^{1/2}]$
$\alpha_1 = 2b/[2(\nu_0 t)^{1/2}]$
$\gamma = t/t_v$
$\eta = y/b$. Also, value of variable in eq (18)
μ = absolute viscosity of the sealing liquid, force second/length^2
ν_0 = kinematic viscosity of the sealing liquid, length^2/second
ρ = Liquid or gas density

Subscript

a = Ambient condition or air
b = conditions in inlet pipe
i = Initial value, balanced condition
n = Integration time interval counter
o = Liquid
v = Diverter valve

Superscript

$\dot{}$ = First derivative with respect to time
$\ddot{}$ = Second derivative with respect to time

Dimensions Used

slug (= 14.593883 kg)
foot (= 0.3048009 m)
lbf (= 4.4482290 N)
lbf/ft^2 (= 47.880056 N/m^2)

About the authors: Fillmer W. Ruegg is a physicist retired from the Fluid Meters Division at NBS and Fillmer C. Ruegg is a physical scientist in the Analytical Chemistry Division of the National Measurement Laboratory at NIST.

6. References

[1] Ruegg, F. W. and Johnson, D. P., Dynamics of the Bell Prover. Symposium on Flow—Its Measurement and Control In Science and Industry, May 1971.
[2] Carnahan, B., Luther, H., and Wilkes, J., Applied Numerical Methods, John Wiley and Sons, NY (1969).
[3] Schlichting, H., Boundary Layer Theory, McGraw-Hill, NY (1968).
[4] Shapiro, A. H., The Dynamics and Thermo-dynamics of Compressible Fluid Flow, The Ronald Press Co., NY (1954).
[5] Kulin, G., Huang, P. H., and Mattingly, G. E., Medium Flow Rates, Bell Prover Techniques, Natl. Bur. Stand. (U.S.) Spec. Publ. 250 (Aug 1986).

Volume 95, Number 1, January–February 1990
Journal of Research of the National Institute of Standards and Technology

[J. Res. Natl. Inst. Stand. Technol. 95, 33 (1990)]

A Proposed Dynamic Pressure and Temperature Primary Standard

Volume 95 Number 1 January–February 1990

Gregory J. Rosasco, Vern E. Bean, and Wilbur S. Hurst

National Institute of Standards and Technology,
Gaithersburg, MD 20899

Diatomic gas molecules have a fundamental vibrational motion whose frequency is affected by pressure in a simple way. In addition, these molecules have well defined rotational energy levels whose populations provide a reliable measure of the thermodynamic temperature. Since information concerning the frequency of vibration and the relative populations can be determined by laser spectroscopy, the gas molecules themselves can serve as sensors of pressure and temperature. Through measurements under static conditions, the pressure and temperature dependence of the spectra of selected molecules is now understood. As the time required for the spectroscopic measurement can be reduced to nanoseconds, the diatomic gas molecule is an excellent candidate for a dynamic pressure/temperature primary standard. The temporal response in this case will be limited by the equilibration time for the molecules to respond to changes in local thermodynamic variables. Preliminary feasibility studies suggest that by using coherent anti-Stokes Raman spectroscopy we will be able to measure dynamic pressure up to 10^8 Pa and dynamic temperature up to 1500 K with an uncertainty of 5%.

Key words: dynamic calibrations; dynamic sources; molecular transducer; nonlinear optical spectroscopy; pressure; primary standard; Raman spectrum; temperature; transducers.

Accepted: October 13, 1989

1. Introduction

With modern laser diagnostic techniques, it is possible to characterize the pressure (P) and temperature (T) of a gas at the molecular level. The measurement times for these techniques are such that the response to changes in T and P is limited only by the fundamental relaxation and transport processes of the molecular system. This provides the basis for a new approach to the calibration of transducers used in the measurement of dynamical P and T. The essence of dynamic calibrations is the determination of the time dependent response of the transducer, which requires, at a minimum, the application of a stimulus with known time dependence, i.e., a “standard” dynamic source.

If one were to rely on conventional sensors (whose response functions are *not a priori* known) to characterize the dynamic source, an inescapable circularity emerges from the preceding paragraph. Approaches to solution of this problem have traditionally [1] relied on some form of calculable source. In essence, this is a source some properties of which can be determined from accurate measurements, for example of quasi-static values of P and T and time rate of change of position, and whose time dependent P and T is then derived from an appropriate theoretical prescription, e.g., from hydrodynamics for sound propagation or fluid mechanics for shock waves (with appropriate equations of state for isentropic or adiabatic expansions). It must be recognized that every theory relies to some degree on idealizations and that any laboratory realization of a dynamic source is nonideal. Thus, sources of dynamical *P* and *T* cannot be accurately known from theory alone; measurement of the "standard" source always is required.

Ideally, in the maintenance of national standards one seeks to relate the measured quantity to a constant of nature, maintained, for example, in the energy levels of an isolated atom or molecule. We are proposing this type of approach for the development of a "standard" source for dynamic *P* and *T*. The essence of our approach is to combine the very best in calculable generators, fast transducers, and high-speed digital data acquisition systems with a new, fundamental measurement approach. The latter relies on the use of laser-based diagnostic techniques, developed over the past 10 years, to determine the *P* and *T* of the dynamic system. The unique characteristics of the optical techniques are:

- *T* and *P* are derived from measurement of the optical transitions between the atomic or molecular energy levels of the constituents of the dynamic source, i.e., the atoms or molecules are the fundamental transducers of the local *P* and *T* environment

- optical measurements can be accomplished with a single laser pulse of nanosecond duration, with the consequence that the "response time of the transducer" reduces to the equilibration time for the atoms or molecules (in the interaction region) to respond to changes in the local thermodynamic variables

- optical measurements can be accomplished within harsh environments by means of transmitted or reflected laser beams and, for multiple beam techniques, spatial resolution within the source volume can be defined by the regions of overlap of these beams, e.g., mm^3 dimensions.

Our approach relies mainly on the use of nonlinear Raman spectroscopies, since these have consistently been shown to provide useful diagnostic spectra in very short times with high spatial resolution[2]. The spectrum determined with these nonlinear Raman approaches is the simplest, best understood, and most highly characterized of any optical diagnostic technique. Comparisons of spectra observed for systems in known (static) states of *P* and *T* with the predictions of theory provide a high degree of certainty in the use of these data for *P* and *T* measurement.

The purpose of this paper is to describe the nonlinear Raman optical measurements that can provide the new primary standard for dynamical *P* and *T*. This description will include information on the *P* and *T* dependence of the spectrum and a brief consideration of the important elements of a measurement system which can be applied to a dynamic source. For the purposes of this discussion we do not consider the dynamic source in any detail; however, the information we present is considered applicable to a suitably designed shock tube source. The state-of-the-art in optical diagnostics is now at a point where accurate measurement of such a "standard" dynamic source is possible. Accuracy limits of the order of 5% for the metrologically significant range of *P* up to 10^8 Pa and *T* up to 1500 K appear achievable.

In the following, we begin with an operational description of the use of nonlinear Raman spectroscopy for *P* and *T* measurement, drawing from the already established data base on the *T* and *P* dependence of observed spectra. We will then outline the elements of a measurement system for a dynamic source. Areas needing significant instrumental development are included in this discussion. Some questions with regard to the *P* and *T* dependence of the Raman spectrum which need further fundamental research also are highlighted. The presentation style is intended to be descriptive rather than rigorous; for completeness, more detailed information on the *T* and *P* dependence of nonlinear Raman spectra is included in the Appendix.

2. Nonlinear Raman Optical Diagnostics

The proposed approach to measurement of the *T* and *P* of the dynamic source is coherent anti-Stokes Raman spectroscopy (CARS)[3]. In its most simple realizations this technique uses two lasers, termed the pump and the Stokes beams, whose frequency difference is selected to be in resonance with a pure vibrational transition of a diatomic gas molecule contained in the source medium. The nonlinear interaction of the electric fields of these lasers with the molecules of the source medium generates a third, laser-like beam, termed the anti-Stokes beam, which carries the information about the molecular system, in particular about its *T* and *P*.

A useful arrangement of these beams, which provides a high degree of spatial resolution, is shown in figure 1. In this configuration, termed BOXCARS, the interaction volume is defined by the region of overlap of the two pump beams, k_0 (derived from one laser source), and the Stokes beam, k_s. Sample volumes of millimeter and submillimeter dimension are remotely accessible in this arrangement.

The information about the local T and P environment of the molecules in the interaction volume is determined from the spectrum of the generated anti-Stokes beam (designated by k_{as} in fig. 1). The spectrum is obtained by measuring the power of the anti-Stokes beam as a function of the frequency difference between the pump and Stokes lasers. Considering for the moment a static system, a spectrum can be obtained by measuring this power as we change the frequency difference between a tunable narrowband Stokes-laser and a fixed frequency narrowband pump-laser. Since this is simply a power measurement, we can essentially eliminate the use of traditional spectroscopic instruments (e.g., prism or grating spectrometers) and retrieve an undistorted measure of the information imparted by the molecular system. The narrowband Stokes and pump laser sources can readily be made of essentially delta-function-like bandwidth for this application.

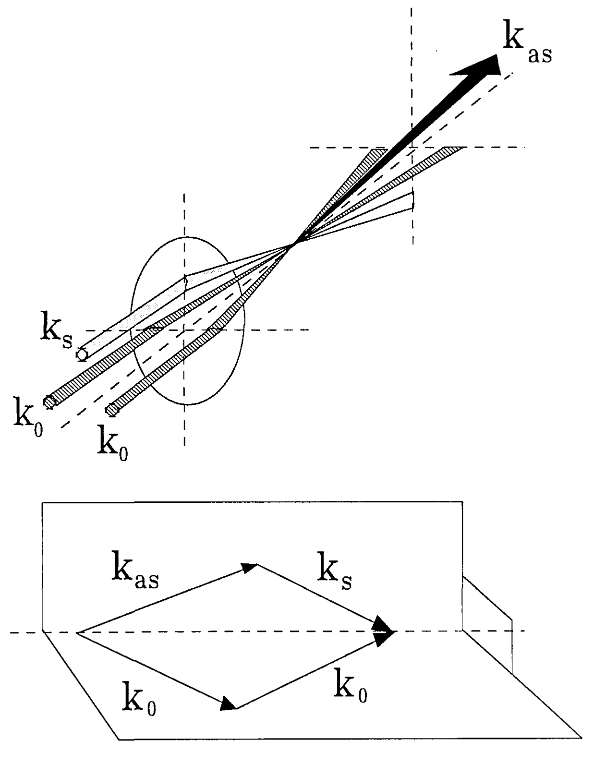

Figure 1. The approximate geometrical arrangement of the pump, (subscript 0), Stokes (subscript s), and generated anti-Stokes (subscript as) beams in a CARS experiment. The sample region is at the intersection of the crossing beams. The phase matching condition for (folded) BOXCARS [11] is indicated.

The special conditions for static systems and narrowband lasers, described in the last paragraph, have been achieved in the laboratory in order to determine the fundamental molecular response, i.e., its spectrum, under known conditions of T and P. This has been accomplished for certain ranges of these variables and for a few selected molecular systems [4]. We will illustrate the basics of spectroscopic T and P determinations by describing spectra derived from these studies.

3. Temperature Dependence of CARS Spectra

In figure 2 we show CARS spectra of pure N_2 as a function of T with the pressure held fixed at 1.0 atm. The horizontal axis is the frequency difference between the pump and Stokes lasers and the vertical axis is the (calculated) power in the anti-Stokes beam (in an unspecified arbitrary unit). These spectra are referred to as vibrational Q-branch spectra, because the optical transition involves a change only in the vibrational quantum state (quantum number v) and no change in rotational state (i.e., no change in the rotational quantum number, J) [5]. The relevant states and modes of motion are schematically illustrated in figure 3.

Returning to figure 2, we see that there are many maxima in the power as a function of frequency difference. Each of these arises from a pure vibrational transition which originates in a different rotational state J. The vibrational frequency depends, to a small degree, on the rotational state because the rotation of the molecule results in a slight stretching of the bond length producing a small change in the forces binding the molecule and a concomitant change in the vibrational frequency. The vibrational frequency (we use the traditional spectroscopic unit cm^{-1}, 1 $\mathrm{cm}^{-1} \simeq 30$ GHz, in the figure) is approximately 2329.91 cm^{-1} for the $J=0$ rotationless state; the value decreases approximately according to $0.01738J(J+1)$, which places the $J=10$ transition at $\simeq 2328.00$ cm^{-1}, less than a 0.1% change. The strength (integrated area) of an individual transition is a function of the population difference between the initial ($v=0$, J) and the final ($v=1$, J) states of the transition. This population

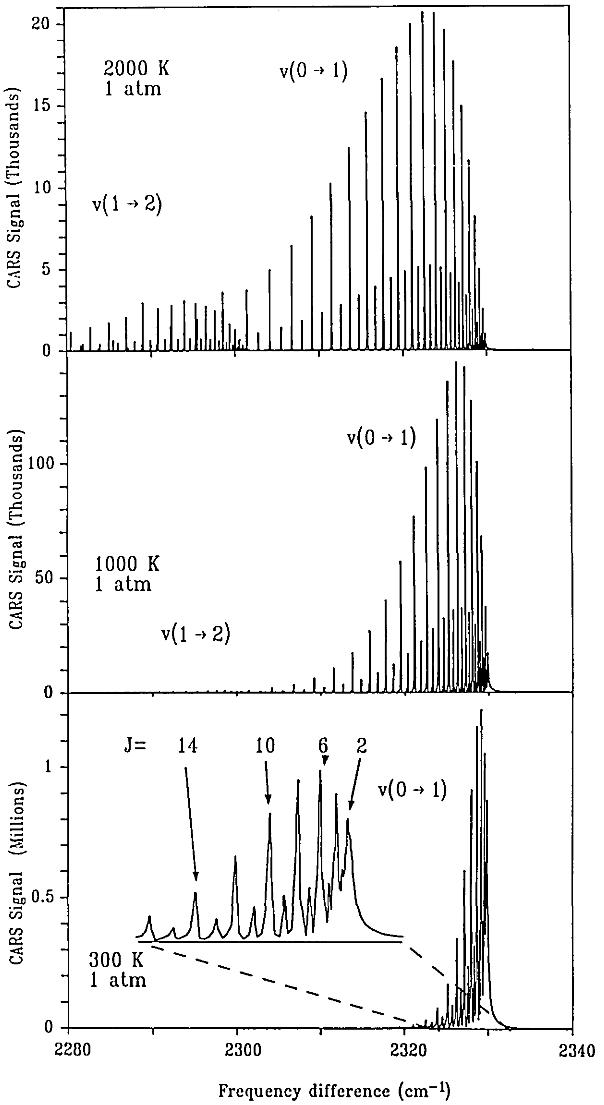

Figure 2. Calculated CARS spectra for the N_2 vibrational Q branch as functions of T for fixed P (=1 atm). The horizontal axis is the frequency difference between the pump and Stokes lasers. The vertical axis is a measure of the CARS power. Although the absolute units of this power are arbitrary, the relative magnitudes as a function of T are accurately represented. Selected transitions and bands of the complete spectrum are indicated. In the bottom panel, the spectral region from $Q(16)$ thru $Q(0)$ is shown on an expanded frequency scale.

dependence in the relative strengths of the transitions as a function of the rotational level, J, is the basis for temperature determination, since for systems in thermodynamic equilibrium the state populations are functions only of the temperature. The vibrational Q-branch spectrum is very useful for measuring T because there are essentially no corrections to apply in order to relate the strength of a fully resolved transition to the population differene and therefore to the T [6]. As is seen in figure 2, the transitions for higher-J states increase in strength with increasing T; this simply mimics the population shifts to higher energy states associated with increasing T.

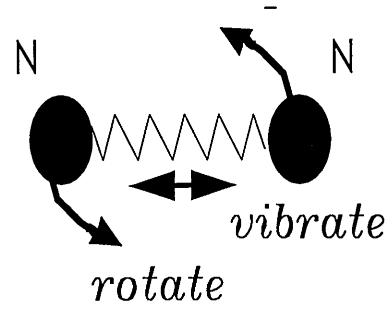

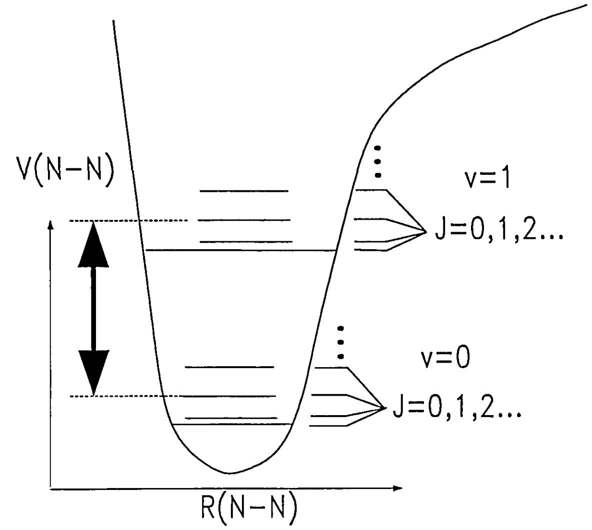

Figure 3. The solid curve schematically represents the potential energy of the ground electronic state versus internuclear separation. Vibrational and rotational energy levels (quantum numbers v and J, respectively) also are indicated (not to scale). A molecular transition, $Q(2)$, associated with the vibrational Q branch is indicated by the arrow.

Strictly speaking, the temperature determined from the relative populations of the rotational levels should be called a "rotational temperature." In like manner, a "vibrational temperature" can be determined from a measurement of the relative populations of the vibrational levels. We observe in the higher-T spectra in figure 2 that there are spectral maxima for transitions labeled $v=1 \rightarrow v=2$. This is a vibrational Q branch which originates in the first excited vibrational level, $v=1$, and terminates in the second excited level, $v=2$. At sufficiently high T there is a significant population in the $v=1$ state and this transition becomes observable. This transition is totally analogous to that discussed above which initiated in the vibrational ground state, $v=0$. Comparison of the integrated areas between the 1→2 and 0→1 transitions gives a measure of the "vibrational temperature." The rotational temperature of the vibrationally excited state also can be determined. The assumption of local thermodynamic equilibrium can thus be tested, since all levels should yield the same thermodynamic temperature in the equilibrium situation.

4. Pressure Dependence of CARS Spectra

First we note that the integrated area of the entire spectrum is a function of the number of molecules with which the intersecting laser beams interact. This feature often is used as a means of measuring species concentration in a diagnostic environment [2,3]. Each molecular species, e.g., N_2, O_2, CO, H_2, etc., has a separate vibrational resonance because the resonant frequency is a sensitive function of the binding forces and the masses of the atoms comprising the molecule. Thus, intercomparison of the areas of these different Q branches can be used as a measure of the relative numbers of each molecule in the sample volume. Because it is very difficult to make accurate measurements of absolute intensity, it has been found that the absolute intensity of a transition is not a good measure of the density or pressure of a sample.

Fortunately, there are good measures of the pressure of a sample which can be recovered from the Q-branch spectrum of some diatomics. We illustrate these by spectra of the Q branch of D_2, which has been extensively studied in our laboratory. Figure 4 presents CARS spectra calculated from results of these experimental studies. The features of primary interest in this figure are the resonance frequencies and widths of the transitions. Figure 4 illustrates the important fact that these transitions change their width (broaden) and their resonance frequency (shift to lower values) with increasing pressure. In the pressure range shown, this broadening and shifting are linear with pressure. For the $Q(1)$ transition of D_2, the broadening rate is 0.0012 cm^{-1}/atm (we use the conventional half width at half peak height as our measure of width) whereas the shift rate is -0.0019 cm^{-1}/atm, i.e., the line shifts more rapidly than it broadens. We see also that the transitions in the D_2 Q-branch spectrum remain isolated, non-overlapped, up to 100 atm. We thus identify a very appealing approach to pressure measurement in that it is tied to the measurement of the frequency positions and widths of molecular transitions.

The situation described above for the D_2 Q branch should be contrasted with the observations of pressure broadening and shifting in the Q branch of N_2. The broadening rates of the N_2 transitions are typically 30–40 times larger than that of the D_2 $Q(1)$ transition. A shifting rate for a N_2 transition is typically 10 times smaller than its broadening rate, thereby making accurate frequency determination less certain with increasing pressure. Additionally, we note that the interline spacing in the N_2 Q branch is approximately 1/60th that of D_2. As a consequence, a transition such as $Q(10)$ would broaden to overlap most of the other transitions shown in figure 2 at a pressure of 100 atm at room temperature. This overlap of transitions leads to important changes in the appearance of the spectrum which are discussed briefly in the Appendix. At this point it suffices to say that the N_2 Q branch involves a complicated spectral distribution function which has the consequence that pressure determinations would generally be less reliable than those derived from the approach based on the Q branch of D_2.

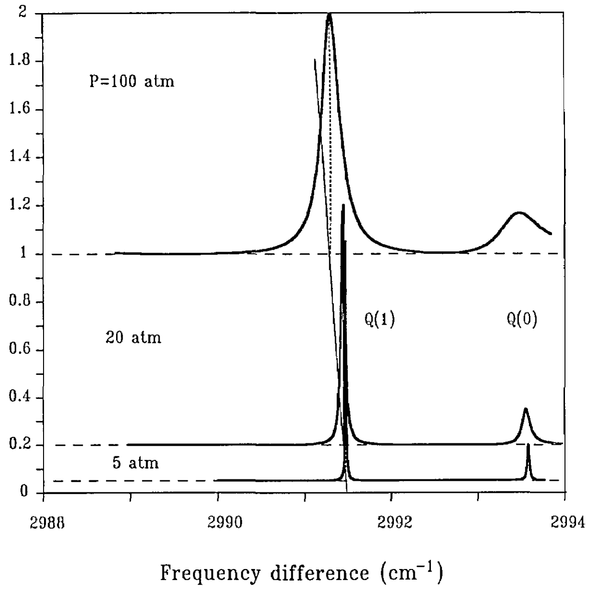

Figure 4. Calculated CARS spectra for the $J=0$ and $J=1$ transitions of the vibrational Q branch of pure D_2 at $T=295$ K. The zero of intensity for each P is shifted by an amount proportional to P. The dotted vertical lines indicate the resonance frequency of the $Q(1)$ line at each P. The solid sloping line drawn through the vertical lines is thus an indication of the linear with P shift of the resonance frequency. At $P=0$ the $Q(0)$ line is at 2993.57 cm^{-1} with the higher J transitions at lower frequencies approximately by the amount $1.056J(J+1)$.

To this point we have restricted consideration to static systems and very high resolution measurements with narrowband lasers. We have displayed the results of careful measurements under known, static conditions of T and P which demonstrate that temperature can be determined by the measurement of the relative intensities of molecular transitions and that pressure can be determined from the positions and widths of molecular transitions. We turn now to discuss briefly the measurement approach required to characterize a dynamic system.

5. Single Shot Diagnostic Measurements

First we point out that we are interested in very rapid measurements, in the range of microseconds or less, in order to characterize the full bandwidth of transducers. Next we note, from the previous discussion, that a relatively large amount of spectral information must be acquired in order to characterize T and P. These requirements of time and spectral range (at relatively high resolution) result in the selection of a technique in which all the spectral elements are measured at once, i.e., a single shot measurement. Single shot measurements are the strong suit of nonlinear Raman diagnostics because we can employ pulsed laser sources and obtain high optical power levels which, by virtue of the inherent nonlinear response of these techniques, results in the generation of strong, readily detected, CARS signals.

The most straightforward approach to single shot measurement is to replace the scanned, narrowband Stokes laser, considered above, with a broadband Stokes laser whose frequency width is sufficient to provide the entire Raman spectrum of interest in a single shot. For example, the entire 60 cm^{-1} region in figure 2 would be measured. We note that a similar spectral bandwidth would be required for temperature measurement via the D_2 Q branch because of the larger interline spacing in the D_2 Q branch, cf. figure 4. The measurement of the spectrum then requires multiple detectors coupled to an instrument which disperses different frequency components in the anti-Stokes beam to the separate spatial locations of the detectors. This combination of a spectrometer and detector we refer to as a multichannel system.

6. Instrument Development

The basic tools for these single shot measurements do exist. The necessary laser systems have been realized in the research laboratory. Adaptation of these to specific diagnostic situations will be required. Similarly, a large variety of spectrometer/detector systems are available and this should allow for reasonably straightforward realization of the specific systems required for our application. Because of the requirements for large spectral ranges and high resolution, noted above, some multiplexing of multichannel systems will be necessary. More details on the instrumentation are discussed in the following.

6.1 Lasers

The basic requirements for the laser sources are well within the state-of-the-art of laser technology. The combination of a single-frequency, pulsed Nd:YAG oscillator with a series of amplifiers and a frequency doubling crystal will provide an adequate Raman pump laser. This laser also will serve as a pumping source for amplifying the required broadband dye laser for the Stokes beam. The oscillator for this Stokes laser will require special design, tailored specifically for the transitions selected for optical characterization of the dynamic source.

6.2 Spectrometer/Detector System

This system also will be tailored to the transitions chosen. It will be unique in that it will have a high resolution (0.001–0.05 cm^{-1}) system for frequency and linewidth determination along with the more conventional low resolution (0.1–0.5 cm^{-1}) channel for temperature determinations. A high resolution multichannel system has not yet been attempted in diagnostic applications. Our ability to selectively add a component such as D_2 to serve as a pressure transducer in the working medium allows us to consider this approach. Incorporating a significant fraction of N_2 in this medium allows for a number of independent checks on the temperature and on the state of thermodynamic equilibrium. Depending on the pressure range, we may be able to determine the temperature from the D_2 spectrum. An approach under consideration is to simultaneously measure the Q branch of D_2 for pressure determination and the pure rotation S branch (transitions within a vibrational state involving a change of $+2$ in the rotational quantum number only) of N_2 to determine the temperature [7].

The discussion in the last few paragraphs indicates one area of the research necessary to develop a standard source of dynamic *P* and *T*. There are additional fundamental studies required to assure accurate knowledge of the *T* and *P* dependence of CARS spectra and ultimately to enable the selection of a measurement approach optimized for application to the dynamic source. We turn now to a brief discussion of these.

7. Fundamental Studies

The most important fundamental question to be answered in this work is the dependence of the spectra of our *specific* dynamic system on *T* and *P*. What is unique and new about the system we propose is that it is by necessity a mixed gas system, for example D_2 contained at low concentrations in N_2. Except for our recent studies (see ref. [4] and below), there is relatively little work on mixed gas systems. Additionally, we are interested in these systems over quite large ranges of *P* and *T*.

There are a number of motivations for the selection of a mixed gas system. First, no one molecule presents all the necessary spectral characteristics which allow an adequate characterization of both *T* and *P*. Of the many single component systems considered, D_2 comes closest to fulfilling this requirement. D_2 provides a good measure of *P* because it has very narrow, isolated lines. This characteristic makes it difficult to simultaneously measure the relative strengths of all the *Q*-branch transitions to obtain an accurate measure of *T*. Furthermore, it is much harder (i.e., it takes much longer) to establish thermodynamic equilibrium for D_2 than it is for N_2 because of the much larger gaps between the energy levels in D_2. Large departures from thermodynamic equilibrium can degrade the performance of a dynamic source and the accuracy of the spectroscopic measurements themselves. The use of pure D_2 has a number of other limitations; for example, a shock tube dynamic source would be very limited in dynamic range by the use of such a light gas. We note also that the cost of running a pure D_2 system would be prohibitive, as also might the potential safety hazards associated with pure D_2 at high pressures or high temperatures.

The use of a mixed gas system is potentially an advantage for pressure measurements. This statement is derived from our observation that mixed gas systems such as D_2:X, with X=He, Ar, and N_2, have a larger shift to width ratio than pure D_2. There remain some fundamental questions in this regard, however, because we have observed line shape asymmetries in the spectrum of D_2:Ar and H_2:Ar [8]. We also know that these asymmetries are functions of *T*. These observations need to be fully understood in order to reliably calibrate *P*; furthermore, these studies must be extended to the D_2:N_2 system. An adequate spectral model and the pertinent molecular parameters must be determined and tested over the complete range of *P* and *T* of interest for the dynamic source.

8. Characterization of the Dynamic Source

8.1 Accuracy Levels in *T* and *P*

The accuracy level for dynamic pressure measurements using the proposed optical/molecular approach is estimated to be approximately 5%. This estimate is based on our ability to measure the widths and shifts of the D_2 *Q*-branch transitions. For the mixed gas systems proposed as standards, the lines shift at least as rapidly than they broaden. Thus our accuracy goals, imply that we can locate the line center to approximately 1/10–1/20th of the line width and that we can make line-width measurements at approximately the 5% level. Achieving these measurement accuracies in a single shot experiment is one of the development goals of this work.

Accuracy in temperature measurements depends on our ability to measure the relative intensities of spectral features associated with different molecular quantum states. In practice, this comes down to comparing an observed spectrum to predicted spectra such as those shown in figure 2. In a single shot experiment this comparison must include the effects of a finite-resolution, spectroscopic instrument function. The accuracy of these comparisons for single shot measurements can be of the order of 5% [3,4]. This is the target level of accuracy for temperature measurements on the dynamic source. The simultaneous and independent measurement of pressure will help eliminate systematic errors in either of these measurements.

8.2 Temporal Evolution

It is important to recognize that the nonlinear laser diagnostic techniques which allow us to obtain a 10 ns "snap-shot" of the local *T* and *P* environment of a molecule, can not easily be extended to provide a continuous-in-time measurement ("movie") of the evolution of *T* and *P* in a dynamic source. These techniques do provide a primary standard which can be used to calibrate measurement approaches which yield good relative measures of T and P with rapid and continuous temporal response. Until this point, we have had no primary standard which could assure the accuracy of these measurements. The primary standard would be used to accurately pin the P and T values at representative points in the temporal evolution of the source during each calibration run. Further, the nonlinear optical techniques would be used to hold the absolute calibration of the source over long periods of use.

9. Conclusions

We have described a new approach to the measurement of T and P of a dynamic source. The measurement is based on the fundamental properties of molecules, specifically on the energies and populations of the vibrational and rotational levels of diatomic gas molecules. The nonlinear optical technique, coherent anti-Stokes Raman spectroscopy (CARS), has been proposed as the method for acquiring the information from the molecular system. This technique has the advantages of very rapid (nanosecond) measurement times, small sampling volumes, and a well understood and verified T- and P-dependent spectrum. The development of this measurement system to provide a reference standard for dynamic calibrations of T up to 1500 K and P up to 10^8 Pa with a 5% accuracy appears highly feasible.

10. Appendix

10.1 Raman Scattering

The Raman spectrum [5] arises from inelastic scattering in which an incident photon of frequency ν_0 is "absorbed," a scattered photon of frequency $\nu_0 \pm \Delta\nu$ is "emitted," and the molecule undergoes a transition among its internal states. The energy difference between the scattered and incident photons, $h\Delta\nu$, is equal to that between the internal states of the scattering molecule. More concisely, Raman scattering, as we will consider it in this discussion, will refer to a two-photon transition originating in the ground electronic state, with intermediate states being far off-resonance, one-photon-allowed electronic transitions. The initial and final states of this transition are molecular vibration-rotation levels in the ground electronic state.

10.2 Nonlinear Optics

The fact that Raman scattering is a two-photon transition makes it essentially a nonlinear optical phenomenon. Many nonlinear Raman spectroscopy techniques simply involve impressing (on the molecules) optical fields corresponding to the two photons of the Raman transition. In the following we will briefly discuss Raman scattering in the context of nonlinear optics [3,9]. In this theory the response of a macroscopic system to an applied electromagnetic field, E, is written in a form such as

$$\Pi \propto \chi^{(1)}E + \chi^{(2)}E{:}E + \chi^{(3)}E{:}E{:}E + \ldots \qquad (1)$$

where Π is the polarization density induced by the action of the fields and $\chi^{(n)}$ is the nth order susceptibility (a tensor of rank $n+1$). The relationship in eq (1) is intended to indicate that we are concerned with vector quantities and that the response of the system involves, in general, all orders of the electric fields. The electromagnetic fields and polarization densities appearing in this expression typically are assumed to be monochromatic (angular frequency ω) plane waves (wave vector k) with the representation

$$E = \sum_i 1/2\, E(\omega_i)\exp(k_i \cdot r - \omega_i t) + \text{c.c.} \qquad (2)$$

(c.c. denotes complex conjugate) with

$$k_i = \frac{n_i \omega_i}{c} \qquad (3)$$

where n_i is the index of refraction and c the speed of light. With this representation of the fields and polarization, the susceptibilities are written as functions of the frequencies of the associated monochromatic components of the field. Nonlinear Raman effects occur when the frequency differences and electric field directions of the applied fields can drive a Raman transition.

10.3 Coherent Anti-Stokes Raman Spectroscopy

In particular, the nonlinear Raman effect known as coherent anti-Stokes Raman spectroscopy (CARS) arises from the 3rd-order terms with electric field components $E_j(\omega_0)$, $E_k(\omega_0)$, and $[E_l(\omega_{as})]^*$ (the j,k,l are spatial indices and the "*" denotes complex conjugate) such that a polarization density at frequency ω_{as} with wave vector K_{as} is generated with the conditions

$$\omega_{as} = 2\omega_0 - \omega_s \tag{4a}$$

and

$$K_{as} = 2k_0 - k_s. \tag{4b}$$

These equations are essentially statements of conservation of energy and momentum. The latter condition indicates that a phase matching geometry must be established between the incident "pump" field (ω_0) and the incident "Stokes" field (ω_s) in order to generate a signal beam, the anti-Stokes component (ω_{as}). The corresponding susceptibility has 2-photon, Raman resonances when

$$\omega_0 - \omega_s = \Delta\omega_{\text{molecular}} \tag{5}$$

with $\Delta\omega_{\text{molecular}}$ being a molecular transition angular frequency ($2\pi\Delta\nu = \Delta\omega_{\text{molecular}}$).

10.4 Raman *Q*-Branch Resonance

For example, the fundamental (i.e., $\nu = 0 \rightarrow \nu = 1$) vibrational *Q* branch is composed of all transitions from the ground to first excited vibrational level without change in rotational quantum number; the molecular transition frequency in this case is

$$\Delta\omega_{\text{molecular}} = \hbar^{-1}[E(\nu = 1, J) - E(\nu = 0, J)]. \tag{6}$$

This relation yields a multiple line spectrum for the *Q* branch because the rotational energy level spacing changes with the vibrational state. The transition frequencies for the vibrational *Q*-branch of a simple diatomic molecule such as N_2, CO, or D_2 can be expressed in terms of familiar molecular constants [5] as

$$\nu(J) \simeq \nu_0 - \alpha_e J(J+1) + \beta_e J^2(J+1)^2 \tag{7}$$

with ν_0 the frequency of the pure vibrational transition between the rotationless ($J = 0$) states and with the α_e and β_e expressing, respectively, the change in the moment of inertia and (lowest order) centrifugal distortion with vibrational state. In keeping with convention, we will express frequency in the spectroscopic unit the wavenumber, cm^{-1}, which is the frequency in Hz divided by the speed of light in cm/s [$\nu/c = \omega/(2\pi c)$].

10.5 CARS Susceptibility

The CARS susceptibility resonance for the isotropic vibrational *Q* branch with laser, Stokes, and anti-Stokes electric field vectors in parallel orientations is defined by the following relations [10]

$$\Pi_1(\omega_{as}) = 3\,\chi^{(3)}_{1111}(-\omega_{as}, \omega_0, \omega_0, -\omega_s)$$

$$[E_1(\omega_0)]^2[E_1(\omega_s)]^* \tag{8}$$

$$\chi^{(3)}_{1111} = \frac{iNc^4}{12\hbar\omega_s^4}\frac{\partial\sigma}{\partial\Omega}S(\omega) + \chi^{\text{NR}} \tag{9}$$

$$S(\omega) = \boldsymbol{l}^{\text{t}}\,(\boldsymbol{G})^{-1}\,\boldsymbol{\Delta\rho_0}\,\boldsymbol{l} \tag{10}$$

$$\boldsymbol{G} = \boldsymbol{G}(\omega) = i\{\omega\,\boldsymbol{I} - \boldsymbol{\omega_J}\} + N\,\boldsymbol{W} \tag{11}$$

$$\omega = \omega_0 - \omega_s \tag{12}$$

$$(\boldsymbol{\omega_J})_{JJ'} = 2\pi c\;\nu(J)\;\delta_{JJ'} \tag{13}$$

$$(\boldsymbol{\Delta\rho_0})_{JJ'} = [\rho_{\text{eq}}(\nu = 1, J) - \rho_{\text{eq}}(\nu = 0, J)]\delta_{JJ'} \tag{14}$$

$$\frac{\partial\sigma}{\partial\Omega} = \frac{\omega_s^4}{c^4}\left|\sum_r\left\{\frac{\mu_{fr}\mu_{ri}}{\hbar(\omega_{ri} - \omega_0)} + \frac{\mu_{fr}\mu_{ri}}{\hbar(\omega_{fr} + \omega_0)}\right\}\right|^2 \tag{15}$$

with N the number density, $\boldsymbol{l}$ a column vector of 1's (superscript "t" signifying transpose), $\boldsymbol{I}$ the unit matrix, $\boldsymbol{\omega_J}$ and $\boldsymbol{\Delta\rho_0}$ diagonal matrices of transition frequencies and (equilibrium) population differences respectively. A nonresonant contribution, χ^{NR}, to the third order susceptibility (see below) is included in eq (9). Equation (10) is a short-hand matrix equation for the frequency dependence of the (Raman) resonant part of the susceptibility which involves the relaxation matrix $\boldsymbol{W}$. This matrix carries all the information about the effects of collisions on the spectrum; we will discuss it later.

10.6 Raman Cross-Section

First we note that eq (15) is an approximate expression for the Raman scattering cross-section. It explicitly shows the two, one-photon dipole matrix elements, μ_{mn}, connecting the initial ($i = \{\nu = 0, J\}$) and final ($f = \{\nu = 1, J\}$) molecular levels via intermediate electronic states, r [the subscripts $\{mn\}$ stand for sets such as $\{ri\}$ or $\{fr\}$ in eq (15)]. This form of the cross-section is used because all photons (laser, Stokes, and, anti-Stokes) satisfy the relation

$$\omega_s < \omega_0 < \omega_{as} \ll \omega_{mn} \tag{16}$$

with

$$\omega_{mn} \equiv \hbar^{-1}[E(m) - E(n)]. \tag{17}$$

As a consequence of these conditions, no denominator in eq (15) is near zero, i.e., we are far from any one photon resonance.

The quantity inside the squared-magnitude symbols in eq (15) is an expression for the optical polarizability matrix element for the transition $\{if\}$. The optical polarizability is a 2nd-rank tensor quantity which, for the systems of interest here, has two irreducible tensor components. These are a scalar, rotationally invariant part of rank zero, and a traceless, symmetric 2nd-rank tensor part, known as the anisotropy. Reference to the "isotropic Q branch" indicates consideration of that part of the interaction associated with the scaler part of the polarizability matrix elements.

The squared-magnitude of the matrix element of the scaler portion of the polarizability is linearly dependent on the vibrational quantum number but essentially independent of the rotational quantum number [6]. As a result, the contribution of an individual $Q(J)$ transition to the isotropic Q branch is almost exactly proportional to the population difference in eq (14).

10.7 Nonresonant Contribution to χ

Reference to eq (11) will show that the contribution of the Raman resonance to the susceptibility has both real and imaginary components. Far off the Raman resonance, when $|\omega-\omega_J|\gg|NW_{J'J}|$ for all $\{J',J\}$, this contribution becomes pure real, cf. eq (9). When one includes all the possible field combinations implicit in eq (1), there are a large variety of far off-resonance two-photon transitions which add together to provide a constant-in-frequency real susceptibility called the nonresonant background. This is the source of χ^{NR} in eq (9).

10.8 CARS Intensity

The polarization density in eq (8) is a source term in Maxwell's equations which are solved to yield the anti-Stokes field. For copropagating (along z), plane wave, linearly polarized (along x) pump and Stokes excitation, the approximate solution is a plane, anti-Stokes wave, with electric field parallel to $x\,(x\equiv 1)$

$$E_x^{\mathrm{as}}=\mathrm{E}(\omega_{\mathrm{as}},z)\exp(k_{\mathrm{as}}z-\omega_{\mathrm{as}}t) \tag{18}$$

$$E(\omega_{\mathrm{as}},z)=\frac{i\pi\omega_{\mathrm{as}}}{2cn_{\mathrm{as}}}\chi^{\mathrm{CARS}}\,[E(\omega_0)]^2[E(\omega_{\mathrm{s}})]^*$$

$$\frac{\sin(\delta kz/2)}{\delta k/2}\,\mathrm{e}^{i\delta kz/2} \tag{19}$$

with

$$\chi^{\mathrm{CARS}}=12\,\chi_{1111} \tag{20}$$

and with

$$\delta k=K_{\mathrm{as}}-k_{\mathrm{as}} \tag{21}$$

expressing the phase matching condition. The wave vectors on the RHS of eq (21) are those of the CARS polarization, eq (4b), and the generated, radiative CARS field, eq (18). The intensity (power density) associated with this field is

$$I(\omega_{\mathrm{as}})=\frac{16\pi^4\omega_{\mathrm{as}}^2}{c^4n_0^2n_{\mathrm{s}}n_{\mathrm{as}}}\left|\chi^{\mathrm{CARS}}\right|^2 I(\omega_{\mathrm{s}})\left(\frac{\sin(\delta kz/2)}{\delta k/2}\right)^2. \tag{22}$$

Equations (18)–(22) involve some idealizations and approximations, such as plane wave excitation and weak field limits, which can easily be removed in the theory or to some extent achieved in the laboratory, or both, see for example reference [3]. These equations do provide a basis for understanding the essential features of the signal generation process, namely, an intensity proportional to: the squared magnitude of a third order nonlinear susceptibility, $\chi(-\omega_{\mathrm{as}},\,\omega_0,\,\omega_0,\,-\omega_{\mathrm{s}})$, the square of the pump intensity, the probe intensity, and a phase matching factor.

10.9 Spatial Resolution and Phase Matching

For systems with $\delta k\simeq 0$, e.g., low density gases, spatial resolution and signal enhancement is achieved simultaneously in the copropagating geometry, discussed above, by using focussed pump and Stokes lasers. Gaussian transverse-mode lasers yield nearly Gaussian anti-Stokes beams generated from spatial volumes of diameter less than the pump focal diameter and with axial distances of the order of $6z_0$, with z_0 the familiar confocal parameter of the focussed pump beam [3]. For a 5-mm diameter (d_0) pump focussed by a 20-cm (f) focussing lens, the approximate dimensions of the sample volume are found from the equations for the focussed beam diameter, $2w_0$,

$$2w_0\simeq\frac{4\lambda_0}{\pi}\frac{f}{d_0}=28\times10^{-4}\ \mathrm{cm} \tag{23}$$

and for the confocal parameter

$$z_0=\frac{\pi w_0^2}{\lambda_0}=0.108\ \mathrm{cm}. \tag{24}$$

Spatial resolution can be enhanced by crossing the pump and Stokes beams, for example as shown in figure 1. The requirements of phase matching for signal enhancement, c.f. eqs (21) and (22), result in the folded BOXCARS [11] arrangement shown in the figure. This arrangement will yield a spatial resolution nearer to the dimensions $2w_0$ and $2z_0$. Since the folded BOXCARS geometry yields good spatial separation of the anti-Stokes beam, this usually is the spectroscopically preferred arrangement. However, many other configurations are possible [2].

10.10 CARS Spectrum

The spectrum results from the frequency dependence of the squared magnitude of χ. From eqs (9) and (10), we can write the general form

$$|\chi|^2=(\chi^{\mathrm{NR}})^2+2\,\chi'_{\mathrm{R}}\,\chi^{\mathrm{NR}}+\chi'^2_{\mathrm{R}}+\chi''^2_{\mathrm{R}} \qquad (25)$$

with the subscript R referring to the (Raman) resonant part of the susceptibility and the prime denoting real and the double prime denoting imaginary part, respectively. If we limit consideration to a single, presumed isolated (our specific meaning for this term will be clarified below) transition, at ω_J, the resonant part of the susceptibility is

$$\chi_{\mathrm{R}} \propto \frac{(\omega-\omega_J)+i\,\Gamma_J}{(\omega-\omega_J)^2+\Gamma_J^2} \qquad (26)$$

with Γ_J the linewidth of the pressure broadened line. The sum of the last two terms in eq (25) yields a Lorentzian lineshape, i.e.,

$$I(\omega) \propto \frac{1}{(\omega-\omega_J)^2+\Gamma_J^2}\,. \qquad (27)$$

The presence of a nonzero nonresonant background leads to asymmetric lineshapes via the second term in eq (25). The first term yields a uniform nonzero signal level which can be dominant if the concentration of the resonant species is low.

10.11 Collisional Line Interference

A transition can be considered isolated if the condition expressed by the relation

$$\sum_{J'\neq J}\frac{W_{J'J}}{(\omega_{J'}-\omega_J)} \ll 1 \qquad (28)$$

is satisfied. The quantity $W_{J'J}$ is an off-diagonal element of the relaxation matrix introduced in eq (11). It is a measure of the rate of collisionally-induced exchange between transitions (see below). Equation (28) simply states that if the rate of exchange between transitions is much smaller than the frequency separation of the transitions, then they can be considered isolated. Conversely, if collisions are mixing lines at a rate commensurate with their separations, we will see line interferences. These are described by the full relaxation matrix equation. The corrections for multiple line spectra which arise when we cannot ignore the nondiagonality of the relaxation matrix in eq (11) are discussed in the following.

10.12 The Relaxation Matrix

10.12.1 Pressure Shift and Broadening In general, the diagonal elements of the relaxation matrix describe the familiar pressure broadening and shifting of spectral lines [12]. Thus, the resonant frequency and linewidth in eq (26) are

$$\omega_J=\Omega_J+\delta_J P \qquad (29)$$

[with the convention that the quantity Ω_J is the zero pressure value derived from accurately known molecular constants, see for example eq (7)] and

$$\Gamma_J=\gamma_J P. \qquad (30)$$

Equations (29) and (30) implicitly define pressure shift and pressure broadening coefficients, δ and γ respectively.

The change and spread of the observed resonance frequency are associated with intermolecular collisions. Encounters with other molecules alter the binding forces and therefore the resonance frequencies of the optically active molecule. In the pressure regimes of our interest, such encounters are limited to binary collision events such that the duration of the encounter is much shorter than the time between collisions. In simplest terms, the shifting coefficient expresses the average rate of collision-induced phase shift of the oscillator. Similarly, the broadening coefficient expresses the rate at which the oscillator is dephased by the collisions.

These effects are expressed as proportional to pressure because the probability per unit time that a collision produces a phase shift in the observed oscillation frequency can be written as the product $N\cdot v_{\mathrm{av}}\cdot\sigma$ of the number density, N (molecule/cm^3), the average velocity, v_{av} (cm/s), and a cross-section, σ (cm^2), appropriate to shifting or broadening for the collision. Such an expression is analogous to that for the collisional momentum transfer which defines the pressure in the gas.

We now turn to consideration of the off-diagonal elements of the relaxation matrix.

10.12.2 Line Mixing and State-to-State Rates In the familiar "impact limit" of collision physics (aspects of which were enumerated in the preceding section, see also ref. [12]), the elements of W are proportional to appropriately averaged products of two scattering ("S-matrix") operators. For molecules such as N_2 and CO, it has been shown that there is very weak dependence of the scattering matrix elements on the vibrational states. This reveals itself in very weak shifting and a line broadening which is independent of vibrational (e.g., 1→2 vs 0→1) or overtone (e.g., 0→2 vs 0→1) branch. The absence of strong vibrational state dependencies in the S-matrix elements yields a relaxation matrix for the isotropic Q branch which can be expressed entirely in terms of state-to-state rates for rotational energy transfer. The off-diagonal element, $W_{J'J}$ for these conditions, is simply the negative of the inelastic rate for a transition from J to J'. In terms of the discussion in the last section, we can see that the occurrence of an inelastic collision terminates the oscillation, i.e., equivalently totally dephases the oscillator. Very little shifting would be expected under these conditions. Thus, the diagonal term, the line broadening coefficient, reduces to the total inelastic rate out of a state J.

Because of the nonzero off-diagonal components, the spectrum resulting from the relaxation matrix equation will show the phenomenon of collisional narrowing of the Q branch with increasing pressure. The important criterion for the narrowing is a rapid rate of rotational energy transfer relative to the frequency difference between the $Q(J)$ transitions, i.e., the relation in eq (28) is not satisfied. Systems such as N_2 and CO show significant narrowing at 1 atm and room temperature, because they have relatively small rotational energy gaps with concomitantly large rates of rotational energy transfer, and small interline spacings within the Q branch. In contrast, the spectra of D_2 displayed in figure 4 can be considered isolated, independent lines. We illustrate the effects of interference in the following.

10.13 Q-Branch Spectra of N_2

Pressure dependent spectra of pure N_2 at room T are shown in figure 5. For comparison, an isolated line model ($W_{J'J}=0$ for $J'\neq J$) for the spectrum at 10 atm is also included in the figure. Clearly, neglect of the collisional interference terms, $W_{J'J}$, would lead to large errors in pressure determinations. The accuracy of theoretically predicted spectra, such as those shown in figure 5, has been tested against spectra measured on samples in the pressure range up to 100 atm and for temperatures from 295 up to 2400 K (the upper limit in T depends on P because of the pressure limits of high-T furnaces and cells), see reference [4].

10.14 Energy Gap Laws for Rotational Energy Transfer

The fundamental basis for calculation of the spectra shown in figure 5 is an energy-gap rate law [13] for the individual state-to-state rates for rotational energy transfer. As discussed above, knowledge of the state-to-state rates allows specification of the entire relaxation matrix and therefore

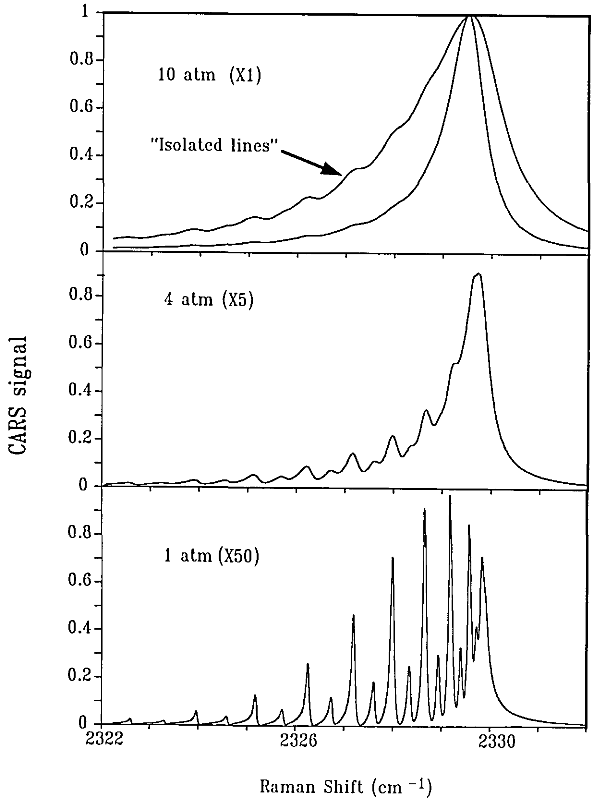

Figure 5. Calculated CARS spectra for the pure N_2 Q branch at 295 K. The intensity at each pressure has been multiplied by the indicated factor and plotted on a unit-normalized scale. An isolated line model which considers only the diagonal elements of the relaxation matrix is included for comparison at 10 atm.

computation of the spectrum [from eqs (9)–(11) and (22)]. The most widely used form of the rate law for specification of the relaxation matrix is the modified exponential gap (MEG) law [14] which parameterizes the upward ($J \rightarrow J'$ with $J < J'$) state-to-state rate according to

$$W_{J'J} = \alpha_0 f(T) \cdot \left(\frac{1 + A\, E(J')/kT\delta'}{1 + A\, E(J')/kT} \right)^2 \cdot \left(\frac{1 + A\, E(J)/kT\delta}{1 + A\, E(J)/kT} \right)^2 \cdot \exp\left(\frac{-\beta\{E(J') - E(J)\}}{kT} \right) \tag{31}$$

with

$$f(T) = \left(\frac{T_0}{T} \right)^{1/2} \frac{1 - \exp(-m)}{1 - \exp(-mT/T_0)} \,. \tag{32}$$

The downward rate is found from the principle of detailed balance, i.e.,

$$\rho_{\mathrm{eq}}(J)\, W_{J'J} = \rho_{\mathrm{eq}}(J')\, W_{J'J} \,. \tag{33}$$

The quantity A is calculated from the Lennard-Jones intermolecular potential parameters for each molecular collision system. The parameters α_0, δ', δ, β, and m are determined from comparisons to accurately measured line broadening coefficients, γ_J, (functions of J and T) and to experimentally determined pressure dependent spectra.

There remain some significant research issues in the prediction of N_2 isotropic Q-branch spectra, such as: some refinement of the rate law model seems important at high temperature [15] and the appropriate spectral and rate law model for situations where N_2 is found in a foreign gas host must be experimentally examined.

10.15 Q-Branch Spectra of the Hydrogens

The state-of-the-art for prediction of the spectrum of molecular systems such as D_2(or H_2):X [X=D_2(or H_2), He, Ar, N_2] is not as fully developed as for N_2:N_2. This situation arises because there is a large vibrational state dependence in the S-matrix elements. Such a vibrational state dependence leads to the addition of a significant "elastic vibrational dephasing," discussed earlier, contribution to the linewidth and line shift in these systems. The elastic vibrational dephasing component, although understood formally from theory, is not easily calculated and does not have a simple predictive basis similar to that just presented for the rotationally inelastic component.

The significance of elastic dephasing for the hydrogens is judged relative to their rotationally inelastic contributions. For the hydrogenic systems, the presence of elastic vibrational dephasing is evidenced by pressure shifting coefficients, δ_J [cf. eq (29)], which are of the order of and often a few times larger than the line broadening coefficients, γ_J [cf. eq (30)]. Because of the large rotational energy gaps in these systems the inelastic portion of the total line broadening is relatively weak (especially for the foreign gas collision partners). Small inelastic rates and large vibrational dephasing both lead to a decrease in the line interference resulting from the solution of eqs (10) and (11). Finally, there is large rotation-vibration interaction in the hydrogens, e.g., α_e in eq (7) is 1.08 for D_2, more than 60 times larger than the α_e of N_2. As a result of all these factors, the hydrogens will display essentially isolated-line type spectra with shift and width measurements yielding good measures of the pressure. The spectra displayed in figure 4 illustrate the pressure sensitivity of the pure gas system, those in figure 6 indicate the potential sensitivity for the D_2:Ar system. The spectra given in this figure are based on actual measurements which to this point have been extended only to 50 atm. Realizing the potential of this system requires more study as we will discuss in the following.

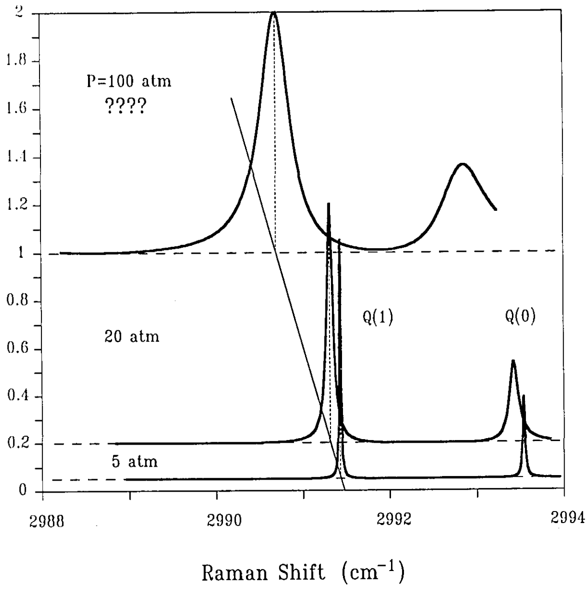

Figure 6. Calculated CARS spectra for the $J=0$ and $J=1$ transitions of D_2 contained at 10% concentration in Ar at 295 K. The spectra are based on experimental measurements which extend only up to 50 atm. The extrapolation to 100 atm is based on the lower pressure data. See caption and compare to figure 4.

The complete J, P, and T dependence of the spectra of $D_2(H_2)$:X is yet to be determined. Some preliminary data on pure H_2 up to 1000 K and 50 atm has been obtained. An empirical fitting law based on the MEG law for the rotationally inelastic contribution and a simple power law in T for scaling the (assumed J independent) vibrational dephasing contribution has been applied with some success to these data. More work is needed for all the systems of interest, in order to have a predictive basis.

In particular there remain some important scientific questions with respect to the foreign gas systems. Recent work has revealed anomalous concentration dependent lineshapes for the D_2(and H_2):Ar system [8]. These anomalies are associated with a large (collision) speed dependence in the cross-sections for line shifting and a small propensity of D_2:Ar collisions to result in speed changes. As a result, the lines are inhomogeneously broadened and rather asymmetric at very low concentrations of the active molecule in the Ar host. More study of the concentration, pressure, and temperature dependence of the D_2:Ar lineshape is required.

10.16 Doppler Broadening

The line broadening, shifting, and interferences discussed above are appropriate to pressure and temperature regimes in which the rate of velocity changing collisions, $N v_{av} \sigma_D$, with σ_D the "diffusion cross-section," is larger than the Doppler width, $\approx |k_0 - k_s| v_{av}$, of the Raman transition. Doppler broadening arises from the free streaming of the molecules, and, at low pressures, it can be used for measurement of translational temperature. For the hydrogens, in particular, this source of line broadening is significant at pressures up to 10 atm at high temperatures, e.g., 1000 K. Research on the D_2:X systems (X=D_2, H_2, He, CH_4, Ar), under conditions where both velocity changing and normal pressure broadening collisions, as discussed above, contribute to the line shape is in progress. A reliable theoretical description appears possible, especially for relatively light collision partners, using a simple diffusion-like model solution to kinetic equations for line formation. However, more work, in particular for the heavy collision partners and high temperatures, remains to be done for these systems.

10.17 Summary

In the above, we have briefly summarized essential aspects of the theory of nonlinear Raman spectroscopy as seen from the viewpoint of one who wishes to apply the technique to temperature and pressure measurements. This has involved some discussion of elements of the theory of spectral line formation for the relevant Raman transitions. Although the level of detail and rigor of this discussion has been limited, the intention is simply to indicate that we have a good understanding of the basic physics which underlies our measurement approach. A great deal of work has gone into building this understanding and developing a reliable predictive basis for temperature and pressure measurements. It is now possible to transfer the static pressure and temperature scale to the molecular level to serve as a primary standard for dynamic P and T.

About the authors: Gregory J. Rosasco, Vern E. Bean, and Wilbur S. Hurst are physicists in the Temperature and Pressure Division of the NIST Center for Chemical Technology.

11. References

[1] Schweppe, J. L., Eichberger, L. C., Muster, D. F., Michaels, E. L., and Paskusz, G. F., Methods for the Dynamic Pressure Calibration of Transducers, National Bureau of Standards Monograph 67, (Government Printing Office, Washington, DC), 1963.

[2] Laser optical diagnostics and nonlinear Raman diagnostics are reviewed in:

Bechtel, J. H., Dash, C. J., and Teets, R. E., "Combustion research with lasers", in Laser Applications, Vol. 5, Ready, J. F., and Erf, R. K., eds., (Academic Press, Inc.), 1984.

Hall, R. J., and Eckbreth, A. C., "Coherent anti-Stokes Raman spectroscopy (CARS): application to combustion diagnostics", in Laser Applications, Vol. 5, Ready, J. F., and Erf, R. K., eds., (Academic Press, Inc.), 1984.

Greenhalgh, D. A., "Quantitative CARS spectroscopy", in Advances in Non-linear Spectroscopy, Clark, R. J. H., and Hester, R. E., eds., (John Wiley and Sons, Ltd), 1988.

Eckbreth, A. C., Laser Diagnostics for Combustion Temperature and Species, (Abacus Press, Cambridge, MA), 1988.

[3] Coherent anti-Stokes Raman spectroscopy is discussed in many recent articles and books, for example:

Druet, S. A. J., and Taran, J.-P., Prog. Quant. Electr. 7, 1 (1981).

Nibler, J. W., and Pubanz, G. A., "Coherent Raman spectroscopy of gases", in Advances in Non-linear Spectroscopy, Clark, R. J. H., and Hester, R. E., eds., (John Wiley and Sons, Ltd), 1988.

Chemical Applications of Nonlinear Raman Spectroscopy, Harvey, A. B., ed. (Academic Press, NY) 1981.

Eesley, G. L., Coherent Raman Spectroscopy, (Pergamon, Oxford), 1981.

[4] The spectra of simple diatomic molecules such as N_2 and CO have been studied by a number of groups, see for example:

Rosasco, G. J., Lempert, W., Hurst, W. S., and Fein, A., Chem. Phys. Lett. **97**, 435 (1983).

Lavorel, B., Millot, G., Saint-Loup, R., Wenger, C., Berger, H., Sala, J. P., Bonamy, J., and Robert, D., J. Phys. (Paris) **47**, 417 (1986).

Rahn, L. A., and Palmer, R. E., J. Opt. Soc. Am. B **3**, 1164 (1986).

Koszykowski, M. L., Rahn, L. A., Palmer, R. E., and Coltrin, M. E., J. Phys. Chem. **91**, 41 (1987).

Rahn, L. A., Palmer, R. E., Koszykowski, M. L., and Greenhalgh, D. A., Chem. Phys. Lett. **133**, 513 (1987).

Rosasco, G. J., Rahn, L. A., Hurst, W. S., Palmer, R. E., Looney, J. P., and Hahn, J. W., Proc. SPIE **912**, 171 (1988).

Rosasco, G. J., Rahn, L. A., Hurst, W. S., Palmer, R. E., and Dohne, S. M., J. Chem. Phys. **90**, 4059 (1989).

Looney, J. P., Rosasco, G. J., Rahn, L. A., Hurst, W. S., and Hahn, J. W., Chem. Phys. Lett. **161**, 232 (1989).

The data base for the hydrogens is more limited with regard to the range of temperature (especially above room temperature) and pressure for which accurate measurements have been reported. Summaries of the applicable measurements are contained in:

Rosasco, G. J., and Hurst, W. S., "The effects of velocity and phase changing collisions on Raman *Q*-branch spectra", in Spectral Line Shapes, Vol. 4, Exton, R. J., ed., (A. Deepak Publishing, Virginia), 1987.

Smyth, K. C., Rosasco, G. J., and Hurst, W. S., J. Chem. Phys. **87**, 1001 (1987).

Rosasco, G. J., May, A. D., Hurst, W. S., Petway, L. B., and Smyth, K. C., J. Chem. Phys. **90**, 2115 (1989).

Farrow, R. L., Rahn, L. A., Sitz, G. O., and Rosasco, G. J., Phys. Rev. Lett. **63**, 746 (1989).

Rahn, L. A., and Rosasco, G. J., submitted to Phys. Rev. A.

[5] Raman spectroscopy is reviewed for diatomic molecules and general gas phase systems in:

Herzberg, G., Molecular Spectra and Molecular Structure I. Spectra of Diatomic Molecules, (D. Van Nostrand Co. Inc.) 1950.

Weber, A., "High resolution Raman studies of gases", in The Raman Effect, Vol. 2, Anderson, A., ed., (Marcel Decker, NY), 1973.

[6] Intensity correction factors for the *Q* branch are given in:

James, T. C., and Klemperer, W. J., Chem. Phys. **31**, 130 (1959).

[7] Recent reports of the use of pure rotational CARS spectra for temperature determinations are given in:

Eckbreth, A. C., and Anderson, T. J., Opt. Lett. **11**, 496 (1986).

Alden, M., Bengtsson, P.-E., and Edner, H., Appl. Opt. **25**, 4493 (1986).

[8] Farrow, R. L., Rahn, L. A., Sitz, G. O., and Rosasco, G. J., Phys. Rev. Lett. **63**, 746 (1989).

[9] In addition to the references in [3], general references on nonlinear optics include:

Yariv, A., Quantum Electronics, Second Edition, (John Wiley and Sons, New York, 1975), Chapters 16 and 18.

Levenson, M. D., Introduction to Nonlinear Laser Spectroscopy, (Academic Press, New York, 1982), Chapter 4.

Shen, Y. R., The Principles of Nonlinear Optics, (John Wiley and Sons, New York, 1984).

[10] The formulae in eqs (8)–(15) are adapted from reference [3].

[11] Shirley, J. A., Hall, R. J., and Eckbreth, A. C., Opt. Lett. **5**, 380 (1980).

[12] Excellent reviews of the fundamentals of spectral line broadening are given in:

Sobel'man, I. I., Introduction to the Theory of Atomic Spectra, (Pergamon Press, Oxford, 1972), Chapter 10.

Fiutak, J., and Van Kranendonk, J., Can. J. Phys. **40**, 1085 (1962); **41**, 21 (1963).

Ben Reuven, A., Adv. Chem. Phys. **33**, 235 (1975).

[13] Brunner, T. A., and Pritchard, D., Adv. Chem. Phys. **50**, 589 (1982).

[14] Koszykowski, M. L., Rahn, L. A., Palmer, R. E., and Coltrin, M. E., J. Phys. Chem. **91**, 41 (1987).

[15] Porter, F. M., Greenhalgh, D. A., Williams, D. R., Baker, C. A., Woyde, M., and Stricker, W., Proceedings of the XIth International Conference on Raman Spectroscopy, London, 1988.

Rahn, L. A., Palmer, R. E., Koszykowski, M. L., and Greenhalgh, D. A., Chem. Phys. Lett. **133**, 513 (1987).

Looney, J. P., Rosasco, G. J., Rahn, L. A., Hurst, W. S., and Hahn, J. W., Chem. Phys. Lett. **161**, 232 (1989).

Volume 95, Number 1, January–February 1990
Journal of Research of the National Institute of Standards and Technology

[J. Res. Natl. Inst. Stand. Technol. 95, 49 (1990)]

Spectroradiometric Determination of the Freezing Temperature of Gold

Volume 95 Number 1 January–February 1990

Klaus D. Mielenz, Robert D. Saunders, Jr., and John B. Shumaker

National Institute of Standards and Technology,
Gaithersburg, MD 20899

A direct spectroradiometric determination of the temperature of freezing gold was performed by measuring the spectral radiances of a gold blackbody relative to those of a laser-irradiated integrating sphere which was calibrated with absolute silicon detectors and an electrically calibrated radiometer. The measurements were performed at three laser wavelengths near 600 nm, and the temperature of the blackbody was calculated by substituting the measured spectral radiances into Planck's radiation formula. The result obtained, $T_{Au}=(1337.33\pm 0.34)$ K, is 0.25 K below the gold-point assignment in the International Practical Temperature Scale of 1968 (IPTS-68) and has been adopted in September 1990 as the new gold-point value in the International Temperature Scale of 1990 (ITS-90). The effect of this change in the gold-point assignment on pyrometric, radiometric, and photometric measurement services provided by the National Institute of Standards and Technology is assessed.

Key words: blackbody; electrically calibrated detectors; integrating spheres; lasers; radiometry; silicon detectors; spectroradiometry; temperature.

Accepted: November 28, 1989

1. Introduction

In this paper, we describe a new spectroradiometric measurement of the freezing temperature of gold based on absolute detector standards. Before describing our measurement, we review the definitions of this temperature in the International Practical Temperature Scale of 1968 (IPTS-68, [1]) and in the International Temperature Scale of 1990 (ITS-90, [2]), assess its significance for pyrometric, radiometric, and photometric measurement services provided by the National Institute of Standards and Technology, and review gold-point measurements performed elsewhere since the adoption of the IPTS-68.

The IPTS-68 allows the realization of temperatures, T_{68}, above the freezing temperature of gold by means of the equation:

$$L_\lambda(T_{68})/L_\lambda(T_{68,\mathrm{Au}})=P(\lambda,T_{68})/P(\lambda,T_{68,\mathrm{Au}}), \qquad (1)$$

where

$$T_{68,\mathrm{Au}}=1337.58 \text{ K} \qquad (2)$$

is the temperature assigned to the gold point; $L_\lambda(T)$ is the spectral radiance [$\mathrm{Wcm^{-3}sr^{-1}}$] at wavelength λ of a blackbody of temperature T [K];

$$P(\lambda,T)=(c_1/n^2\lambda^5)/\{\exp[c_2/n\lambda T]-1\} \qquad (3)$$

is the theoretical blackbody spectral radiance (Planck's radiation formula) for light with air wavelength λ propagating in air with refractive index n; and c_1 and c_2 are the first and second radiation constants. The gold-point temperature given in eq (2) was derived from gas thermometry.

The new ITS-90 was adopted by the International Committee of Weights and Measures (CIPM) in September 1989 [2]. It supersedes the IPTS-68 and incorporates a new value for the freezing temperature of gold which is identical to the one reported in this paper [eq (35), below]. The ITS-90 extends the radiometric temperature definition of eq (1) down to the freezing point of silver, and allows the realization of radiation temperatures in terms of any one of the silver [$T_{90,\mathrm{Ag}}=1234.93$ K], the gold [$T_{90,\mathrm{Au}}=1337.33$ K], or the copper [$T_{90,\mathrm{Cu}}=1357.77$ K] freezing points. The T_{90} values of the silver, gold, and copper points are believed to be self-consistent to such a degree that the substitution of any of them in place of the value of $T_{68,\mathrm{Au}}$ in eq (1) will not result in significant differences in the measured values of T_{90}.

2. Radiometric Significance of the Gold Point

Realizations of the NIST scales of radiance temperature, spectral radiance, spectral irradiance, and photometric quantities, and the transfer of these scales to calibrated lamp standards, have been based on measurement chains derived from gold-point blackbodies for many years [3] ... [6]. Although the instrumentation and procedures used have undergone refinements in the meantime, the IPTS-68 gold-point assignment has remained the starting point for these scale realizations for the past 2 decades. Consequently, the change of the gold-point temperature will affect all of these scales. The magnitude of the scale changes may be estimated as follows.

The realization of radiometric scales in terms of a primary gold-point standard involves measurements at specified wavelengths of the spectral radiance ratios of the gold-point blackbody and other blackbody sources which may then be used as secondary standards over wide temperature and wavelength ranges. The basic measurement equation for these radiance transfers is eq (1), which allows the determination of the temperature of a secondary standard source from the measured radiance ratio $L_\lambda(T)/L_\lambda(T_{\mathrm{Au}})$ and the assigned value of T_{Au}. In the Wien approximation of Planck's radiation formula,

$$P(\lambda,T)\sim(c_1/n^2\lambda^5)\exp(-c_2/n\lambda T), \tag{4}$$

we obtain

$$L_\lambda(T)/L_\lambda(T_{\mathrm{Au}})\sim\exp[(c_2/\lambda)(1/T_{\mathrm{Au}}-1/T)] \tag{5}$$

and, hence, by implicit differentiation with respect to T and T_{Au},

$$\mathrm{d}T/T^2-\mathrm{d}T_{\mathrm{Au}}/T_{\mathrm{Au}}^2\sim 0, \tag{6}$$

if the radiance ratio on the left-hand side of eq (5) has a fixed value. This shows that a radiance temperature T based on a gold-point value T_{Au} will be replaced by $T+\Delta T$, where

$$\Delta T\sim(T/T_{\mathrm{Au}})^2\,\Delta T_{\mathrm{Au}}, \tag{7}$$

on a redefined scale in which T_{Au} is replaced by $T_{\mathrm{Au}}+\Delta T_{\mathrm{Au}}$.

When this result is substituted into the Wien approximation for the spectral radiance of the blackbody at temperature T, we obtain

$$\begin{aligned}\Delta P(\lambda,T)&=[\partial P(\lambda,T)/\partial T]\Delta T\sim P(\lambda,T)\,c_2\,\Delta T/(\lambda T^2)\\&\sim P(\lambda,T)\,c_2\,\Delta T_{\mathrm{Au}}/(\lambda T_{\mathrm{Au}}^2).\end{aligned} \tag{8}$$

Thus, the relative change in spectral radiance due to a change ΔT_{Au} in the gold point is

$$\begin{aligned}\Delta P(\lambda,T)/P(\lambda,T)&\sim c_2\,\Delta T_{\mathrm{Au}}/(\lambda T_{\mathrm{Au}}^2)\\&=1.44\times10^{-2}\,\Delta T_{\mathrm{Au}}/(\lambda T_{\mathrm{Au}}^2),\end{aligned} \tag{9}$$

where T is expressed in kelvins and λ in meters. This result is independent of the temperature of the blackbody and holds for spectral irradiance measurements as well, since radiance/irradiance transfers are based on purely geometrical considerations.

The NIST photometric scales (luminous intensity and luminous flux) are realized and maintained at $T=2856$ K (CIE Source A) by direct comparison with the NIST spectral irradiance scale. The effect of a reassignment of the gold point may be estimated by evaluating eq (9) at the Crova wavelength for Source A ($\lambda=570$ nm) [7]. This gives

$$\Delta Q_{\mathrm{v}}/Q_{\mathrm{v}}=1.41\times10^{-2}\,\Delta T_{\mathrm{Au}}, \tag{10}$$

where ΔT_{Au} is again expressed in kelvins, and Q_{v} denotes a generalized photometric quantity.

From eqs (7), (9), and (10), it can now be estimated that the -0.25 K change in the IPTS-68/ITS-90 gold-point assignments will result in the approximate changes of reported calibration values listed in table 1. Although these changes are well

Table 1. Quoted uncertainties (3σ) of current NIST measurement services for radiation thermometry, radiometry, and photometry and estimated changes in reported values resulting from a −0.25 K reassignment of the gold-point temperature

Quantity	Uncertainty	Change of value
Radiance temperature [4]		
800 °C	±0.5 °C	−0.2 °C
1100	0.6	−0.2
1400	0.8	−0.4
1800	1.3	−0.6
2300	2.0	−0.9
Spectral radiance [3]		
250 nm	±1.6%	−0.8%
350	1.2	−0.6
650	0.6	−0.3
900	0.5	−0.2
1600	0.4	−0.1
2400	0.4	−0.1
Spectral irradiance [5]		
250 nm	±2.3%	−0.8%
350	1.4	−0.6
650	1.0	−0.3
900	1.3	−0.2
1600	1.9	−0.1
2400	6.5	−0.1
Luminous intensity [6]		
2856 K	±1.0%	−0.4%
Luminous flux [6]		
2856 K	±1.4%	−0.4%

within the quoted uncertainties for routine NIST measurement services, they will have an effect to reconcile small discrepancies between radiometric scales that have been observed in recent years. For example: In an intercomparison between independent radiometric scales based on silicon-photodiode physics, gold-point blackbody radiation, and synchrotron radiation, Schaefer, Saunders, and Hughey [8] found that the blackbody scale indicated a spectral irradiance at 600 nm which was about 0.8% higher than the detector scale, and about 1% higher than the synchrotron scale. The −0.25 K adjustment of the gold-point temperature improves the overall agreement of these intercomparisons.

In an international intercomparison of photometric base units, conducted by the Comite Consultatif de Photometrie et Radiometrie (CCPR) in 1985 [9,10], the NIST luminous intensity data were the only ones derived from a gold-point based measurement chain. They fell within the spread of the intercomparison, but were 0.5% higher than the average of the data reported by 14 other national laboratories, all of which had realized the candela with electrically calibrated radiometers. It may be seen from table 1 that the NIST data would have been within 0.1% of the world mean, had the gold-point temperature been 0.25 K lower.

3. Previous Radiometric Determinations of the Gold Point

The first measurement which projected a difference between the thermodynamic temperature of the gold point and its assigned IPTS-68 value was a precision determination of the Stefan-Boltzmann constant which was published by Blevin and Brown [11] of the Australian National Standards Laboratory (NSL) in 1971. Based on the IPTS-68 gold-point assignment their experiment, in which an electrically calibrated radiometer (ECR) was used to measure the spectrally total radiance of a blackbody radiator at the freezing temperature of gold, yielded a result which was about 0.1% lower than the value of the Stefan-Boltzmann constant ($2\pi^5/15h^3c^2$) calculated from the best values of the speed of light, c, and the Planck and Boltzmann constants, h and k. Blevin and Brown suggested that their experiment could be regarded as a radiometric determination of the gold point based on the theoretical value of the Stefan-Boltzmann constant, the corresponding result for the gold point being 1337.27 K, about 0.3 K lower than the IPTS-68 value.

Guildner and Edsinger [12] of the U.S. National Bureau of Standards noted that this result was consistent with their own work, which had revealed that sorption errors in gas thermometry caused a systematic difference between thermodynamic and IPTS-68 temperatures. Assuming that the effects of sorption were approximately linear with wavelength, they predicted that the temperature of freezing gold on the thermodynamic scale will prove to be lower than the value on the IPTS-68 by at least some 0.1 K. They suggested, however, that the IPTS-68 should not be changed without better understanding of the thermodynamic scale, as realized experimentally.

In 1975, Bonhoure [13] of the Bureau International des Poids et Mesures (BIPM) in France reported pyrometric measurements of the temperature differences of variable-temperature blackbodies in the 904 to 1338 K range, one kept at the

IPTS-68 antimony temperature (903.89 K) and the other at selected higher temperatures. Assuming the antimony point to be correct, Bonhoure found that his measurements were in 0.05 K agreement with the IPTS-68 near the gold-point. Andrews and Gu [14] repeated this measurement at the National Physical Laboratory (NPL) of the U.K., using a photon-counting optical pyrometer to compare a gold-point blackbody to a reference source at the antimony point. They, too, concluded that the IPTS-68 gold-point value was not in error.

In the meantime, Guildner and Edsinger [15] had achieved significant improvements of high-temperature gas thermometry and showed that the thermodynamic temperatures from the triple point of water up to 730 K were consistently lower than the IPTS-68 values. Jung [16] of the German Physikalisch-Technische Bundesanstalt (PTB) carried this work further by performing pyrometric measurements at the antimony point relative to a blackbody at a thermodynamic temperature of 729.15 K, as established by gas thermometry. His work showed that the IPTS-68 antimony-point assignment was in fact too high by 0.15 K, thus necessitating numerical corrections to the gold-point values obtained by Bonhoure and by Andrews and Gu. The corrected values, as reported by Tischler and Rebagliati [17] and Hudson et al. [2], respectively, were 1337.20 and 1337.33 K. An expression equivalent to eq (7), above, was used to make the corrections.

Tischler and Rebagliati [17] also recalculated the results of five other researchers who had performed pyrometric measurements of the thermodynamic temperature difference between the silver and gold points between 1973 and 1982. To allow a uniform analysis, Tischler and Rebagliati interpreted all of these measurements as being performed with the silver point as the reference. The five gold-point values so recalculated ranged from 1337.18 to 1337.29 K, their average being 1337.22 K. The silver-point reference temperature assumed was 1234.88 K, a value which is only 0.01 K lower than more recent results obtained by Jones and Tapping [18] and Fischer and Jung [19], and 0.05 K lower then the ITS-90 value[2].

The data described above are summarized in table 2, with uncertainties quoted at the three standard-deviation level. The values given are all lower than the IPTS-68 gold-point assignment.

It should be noted, however, that the only direct determination of the gold point is that by Blevin and Brown [11], which involved absolute radiometric measurements and interpretation of the data obtained in terms of a fundamental law of physics. The others are pyrometric measurements of radiance ratios which relied, directly or indirectly, on the IPTS-68 assignment of the antimony point and agreed with the Blevin and Brown measurement only after allowance was made for an error in the antimony assignment. We conclude that radiometric and pyrometric temperature measurements at higher temperatures are, in themselves, reliable but may be encumbered with uncertainties if they are based on lengthy measurement chains which involve lower-temperature reference points. Our own measurement is similar to the Blevin and Brown experiment in that it is a direct measurement based on absolute radiometry, but differs from it in that we measured the spectral radiance of a gold-point blackbody and used Planck's law to derive its temperature.

Table 2. Results and uncertainties (3σ) of gold-point measurements performed since 1971

Authors	Reference Temperature	Result (K)
Blevin and Brown [11]	None	1337.27±0.4
Bonhoure [13], [17]	Antimony	1337.20±0.5
Andrews and Gu [14], [2]	Antimony	1337.33±0.3
Tischler and Rebagliati [17]	Antimony/Silver	1337.22±0.5

4. Apparatus

4.1 Overview

Our technique consisted of measuring the spectral radiance of a uniform, monochromatic source using two independent radiometric scales established by a standard silicon photodiode and an ECR. As the uniform, monochromatic source we used the exit port of an integrating sphere irradiated by monochromatic laser light near 600 nm. Then, by comparing the spectral radiance of this source to that of a gold-point blackbody with a monochromator-based spectroradiometer, we determined the blackbody radiance and calculated the gold-point temperature from Planck's radiation formula. The use of independent detector standards provided redundancy of the measured data and increased the likelihood of high accuracy and internal consistency of the results.

Figure 1 shows a diagram of the arrangement of the equipment used in these measurements. The three detector systems (silicon diode, ECR, and spectroradiometer) are mounted on a movable

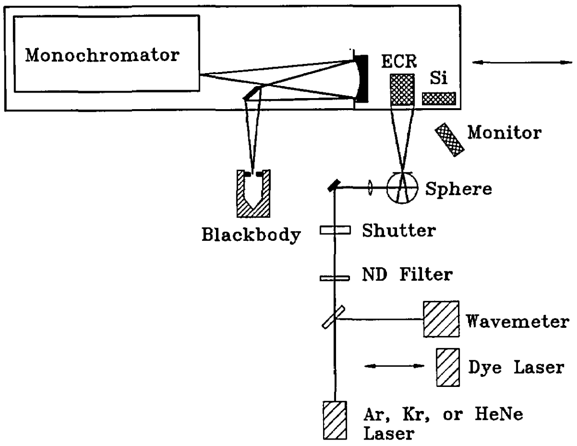

Figure 1. Gold-point measurement apparatus.

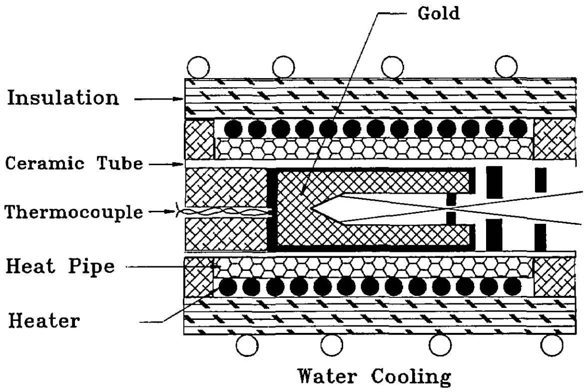

Figure 2. Cross section of heat-pipe blackbody furnace.

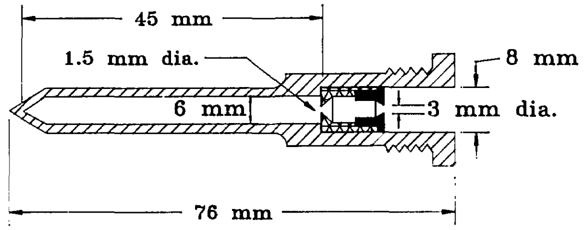

Figure 3. Blackbody inner cavity dimensions.

carriage which permits each of them to be moved into position to view the laser-irradiated integrating sphere. In addition, the carriage can be positioned so that the spectroradiometer views the gold-point blackbody.

Also indicated is a silicon monitor diode which is fixed above the sources and detectors and views the laser sphere from slightly outside the field of view of any of the other detectors. The purpose of this monitor was to compensate for small fluctuations of the laser-sphere source and for the presence of a neutral-density filter which was inserted in the beam for the silicon-diode and spectroradiometer measurements, as described in section 4.7.

Most of the simple operations of the equipment are computer controlled. This includes controlling the blackbody heater current, positioning the movable carriage, operating the spectroradiometer wavelength drive, triggering the simultaneous measurements by the monitor detector and the other detector systems, operating the shutter for dark-current measurements, and setting the integration time for the DVM readings (usually 5 s).

Throughout the discussion which follows, we state numerical estimates of potential sources of systematic error. These estimates are upper limits of systematic errors and will be combined in quadrature with the three-sigma random uncertainties of our measurements.

4.2 Gold-Point Blackbody

The blackbody construction is sketched in figures 2 and 3. The furnace incorporates a cylindrical heat pipe between the electrical heater and the alumina tube which holds the crucible of gold. The crucible and inner cavity are made of graphite, as are many of the rings which limit the viewing cone in front of the crucible and support the thermocouple tube behind the crucible. A slow flow of argon is directed from the back to the front of the furnace within the alumina tube, and fittings on its ends permit maintaining a slight overpressure of argon except when the front shutter is opened for radiance measurements. The front graphite rings are regarded as sacrificial, and after five or ten melt-freeze cycles a few of the outermost rings had generally become partially consumed by oxidation and were replaced.

A microcomputer controls the heater power supply by turning the furnace on, ramping the power up gradually over several hours, and finally alternating power levels to produce melts and freezes which typically last about 45 min each. The thermocouple provides the computer with the necessary continuous information about the state of the furnace which governs the succession of power changes. Spectroradiometric data from a representative melt-freeze cycle are shown in figure 4.

To confirm the radiometric adequacy of the blackbody design, several of the easily changed design parameters were tested by performing spectroradiometric matches between an ultra-stable

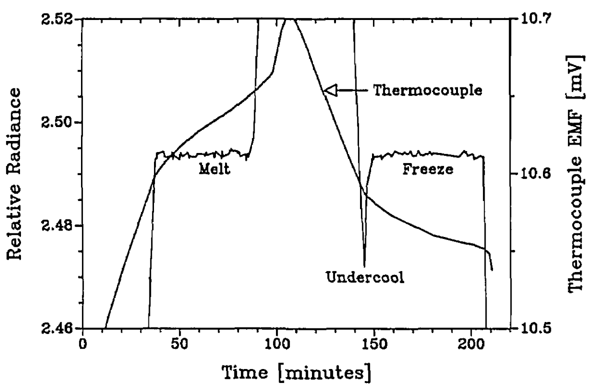

Figure 4. Spectroradiometric blackbody melt and freeze curve (514 nm).

vacuum tungsten strip lamp and the blackbody melts and freezes with modified blackbodies:

(1) Furnaces with different internal diameters were compared. The two designs provided $f/10$ and $f/6.5$ viewing solid angles and crucibles containing 0.7 and 1.3 kg of gold, respectively.

(2) Two different samples of nominally 0.99999 pure gold, acquired at different times, were compared in the smaller furnace, and a third sample in the larger furnace.

(3) Three different inner blackbody cavity openings were compared. Their diameters were 1.0, 1.5, and 2.0 mm.

None of these changes affected the spectral radiance of the cavity within 0.01%. For the measurements reported here, the larger furnace with the crucible containing 1.3 kg of gold and 1.5-mm diameter aperture was used. For the calculation of the gold-point temperature from our spectral radiance measurements and the Planck function, we used an emissivity of $0.9999+0.0001$, calculated from the dimensions of the cavity by Quinn's and Ford's technique [20,21], assuming uniform temperature.

Since heat flows from the outer heat pipe to the inner cavity during melts, and tends to flow from the inside to the outside during freezes, we expected differences in the relative spatial distributions of the blackbody radiance during melts and freezes, as well as changing distributions during the course of a melt or freeze. Relative radiance distributions were measured during melts and freezes carried out for this purpose, by moving the spectroradiometer in 0.6-mm steps across the face of the blackbody furnace, and by raising and lowering the furnace in 1.8-mm steps. Generally, four complete mappings could be acquired during the course of a single melt or freeze. We show in figure 5 examples corresponding to different times during a melt or freeze. In order to eliminate the effect of the change in the distribution during the 10 or 15 min required for each mapping, at each point of the source plane the four spectroradiometer readings obtained during the complete melt or freeze were fitted to a linear function of the time of measurement. Then, "instantaneous" mappings were constructed by interpolation and used in the computation of the spectroradiometer spatial apparatus function correction f_{H} defined in section 5.2.3.

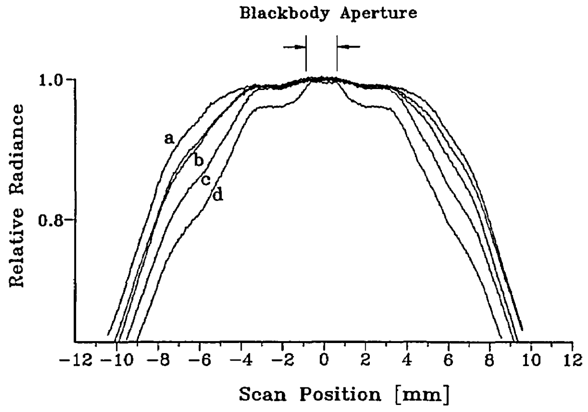

Figure 5. Relative spatial distribution of blackbody radiance (647 nm) at different times during melts and freezes. (a) end of melt (b) beginning and middle of melt (c) beginning of freeze (d) end of freeze.

4.3 Laser Sphere

The laser-sphere source is a 50-mm diameter copper integrating sphere with a 6-mm diameter entrance port located about 120° from a 20-mm diameter exit port. The interior of the sphere is coated with a 3-mm thick layer of compacted Halon (polytetrafluoroethylene) powder [22]. On the outside of the sphere, a single loop of copper cooling water tubing is soldered to each hemisphere.

A 20-W argon ion laser, a 5-mW helium-neon laser, and a 6-W krypton ion laser were used to illuminate the sphere at 514, 633, and 647 nm. The air wavelengths assigned to these laser transitions in Ref. [23] are given in table 3. The power output of the lasers remained stable to better than 1% over several hours, with no further stabilization than the

Table 3. Laser wavelength used in this experiment [19]

Laser	Transition	Air wavelength (μm)
Ar II	$3p^4(^3P)4p(^4D^0_{5/2}) \rightarrow 3p^4(^3P)4s(^2P_{3/2})$	0.514533
HeNe	$2p^5(^2P_{1/2})5s[1/2]^0_1 \rightarrow 2p^5(^2P_{1/2})3p[3/2]_1$	0.63281646
Kr II	$4p^4(^3P)5p(^4P_{5/2}) \rightarrow 4p^4(^3P)5s(^3P_{3/2})$	0.647100

built-in standard power monitoring system of the laser. Since all of our measurements on the laser-sphere were made relative to a simultaneously recorded signal from the monitor detector, this stability was adequate. The helium-neon laser provided too little power for accurate ECR readings, so at 633 nm we only compared silicon-detector and spectroradiometer measurements. The laser beams were directed by a series of plane mirrors through a quarter-wave plate to a lens which focused the beam to a point in the sphere entrance port.

Because the spectroradiometer is sensitive to linear polarization, it was necessary to know the polarization of all sources. The blackbody can safely be assumed to be unpolarized, but we felt less certain about the laser-sphere source since the laser beam is so highly linearly polarized. Consequently, we inserted the quarter-wave plate in the laser beam to convert its linear polarization to circular polarization entering the sphere. Then we measured the linear polarization of the laser-sphere source by the use of a rotating sheet polarizer and, as a polarization indifferent detector, another integrating sphere with a silicon detector in its exit port. With careful attention to alignment, this technique yielded consistent values of 0.0007+0.0003 for the degree of linear polarization of the sphere output. This is sufficiently small, so that we treated the laser-sphere source as unpolarized. We included in our error analysis a polarization uncertainty of ±0.02%, which is the product of the measured degree of polarization of the sphere output and the polarizance of the spectroradiometer (0.3) in the spectral region of interest.

The relative spatial radiance distribution of the laser-sphere source was measured with the spectroradiometer. The exit aperture of the sphere was imaged with a tiltable spherical mirror into the source focal plane of the spectroradiometer. Then, the horizontal scanning capability of the spectroradiometer, coupled with the vertical tilting motion provided by the mirror, permitted a complete mapping of the 255-mm^2 source area in a 1×1 mm grid. Initial attempts to perform this mapping showed a fine structure which depended strongly upon laser beam positioning in the entrance port. This proved to be caused by a fine speckle pattern in the sphere output which we were able to smooth out by rotating one of the plane mirrors to introduce a small, rapid wobble of the beam during the measurements. The spatial distributions thus obtained are reproducible, smooth, and independent of laser alignment and wavelength. In figure 6, we show the distribution at 514 nm.

Since the spectroradiometer views the laser sphere within a larger solid angle (approximately $f/12$) than either the silicon diode ($f/19$) or the ECR ($f/25$), we required that the laser-sphere source be Lambertian. We tested for uniformity of the irradiance field in the detector plane by translating the silicon-diode detector horizontally and vertically in the detector plane and recording the ratio of the signal obtained to that of the monitor detector. The $\cos^4\Theta$ dependence expected for a Lambertian source was obtained to within +0.01% over our largest ($f/12$) viewing angle.

4.4 Spectroradiometer

The spectroradiometer used in our measurements was a Cary-14 prism-grating double monochromator[1]. The fore optics indicated in figure 1 consisted of a plane mirror and a 1-m

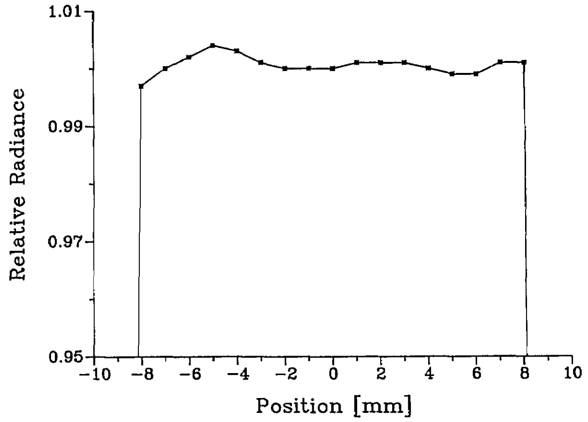

Figure 6. Relative horizontal distribution of laser sphere radiance at exit aperture (514 nm).

---

[1] Certain commercial equipment, instruments, or materials are identified in this paper to specify adequately the experimental procedure. Such identification does not imply recommendation or endorsement by the National Institute of Standards and Technology, nor does it imply that the materials or equipment identified are necessarily the best available for the purpose.

radius-of-curvature spherical mirror. These were positioned to produce 1:1 images of sources on the entrance slit, while keeping the optical axis within less than 3° of the axis of the spherical mirror. A circular aperture stop at the spherical mirror limited the angular field of view of the radiometer to *f*/12 (except in the horizontal direction, in which it was limited to *f*/16 by the internal optics of the monochromator). A polished metal mask containing a 1.0-mm wide by 0.8-mm high rectangular opening was mounted just in front of the entrance slit. Since the slit width used for all measurements was 0.6 mm, the effective field stop of the spectroradiometer system was a rectangle 0.6-mm wide by 0.8-mm high. A telescope focused on the entrance slit mask gave the operator a magnified view of the source image at the slit, to help in the positioning and focusing of sources. In the detector compartment behind the exit slit of the monochromator, a photomultiplier and a small HeNe laser were mounted on an externally positionable sliding platform, so that either can be placed on axis. The photomultiplier is a thermoelectrically cooled, magnetically shielded, end-on, eleven-stage EMI 9658 tube with S-20 response. The laser is used to define the optic axis of the spectroradiometer system for the positioning and orienting of sources.

Measurements of the spectroradiometer slit-scattering function have been described previously [24]. They employed a laser-sphere source and consisted of measurements over a broad range of dye and ion laser wavelengths while the monochromator remained set at a fixed wavelength. These measurements were supplemented by information obtained by scanning the monochromator wavelength setting while viewing a constant ion laser line. An example of the resultant slit-scattering function is shown in figure 7. Using these slit-scattering functions and the definition of eq (31), below, we can calculate the spectral slit width. During the course of the measurements reported here, the slit-scattering function was measured at each wavelength by performing abbreviated monochromator scans which covered only about 10 nm. Consequently, the spectral slit widths calculated from these data were corrected for the truncation of the far wings by multiplying by a factor $1.0025+0.0004$, obtained from the earlier, complete scans by similarly truncating those data. For our nominally 0.6-mm slit widths, we obtained bandwidths in the neighborhood of 2.5 nm. The factor $\sigma(\lambda,\lambda_L)$ in eq (31) causes the slit width to depend on the precise coincidence of the monochromator wavelength, λ, at the laser wavelength, λ_L. The uncertainty of this coincidence ($+0.05$ nm) is included in the composite random uncertainty of our measurements, as discussed in section 6.6.

To measure the spatial apparatus function of the spectroradiometer, we aimed it at the center of the laser-sphere source and mounted a mask containing a 0.3-mm diameter pinhole in the focal plane just in front of that source. Then we recorded the spectroradiometer signal as the mask was translated horizontally and vertically across the source aperture. These traverses were then separately normalized to unity at the center. Examples are shown in figure 8. We found the spatial apparatus function to be essentially independent of wavelength over the spectral range used in our experiment.

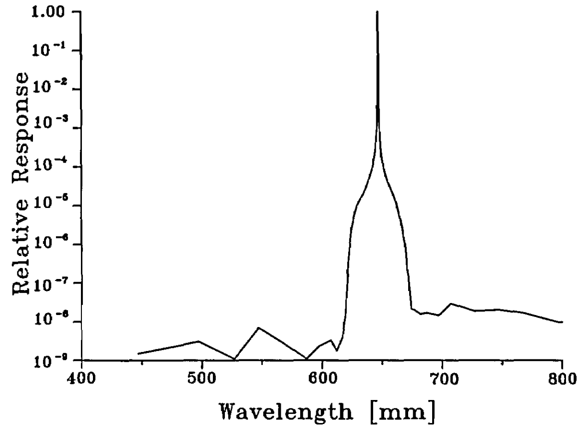

Figure 7. Slit-scattering function of spectroradiometer (647 nm).

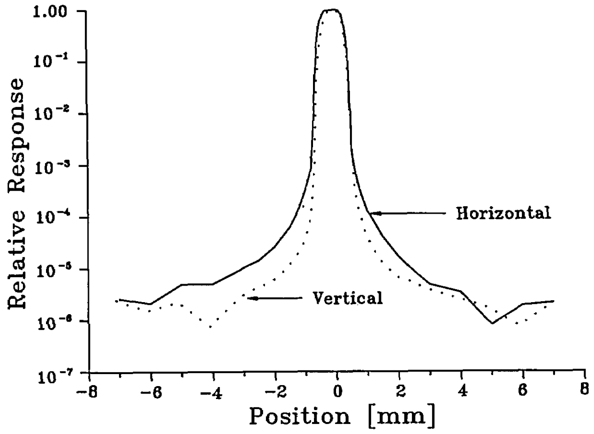

Figure 8. Spatial apparatus function of spectroradiometer (514 nm).

Although our gold-point measurement does not rely on an absolute calibration of the spectroradiometer, the spectral responsivity $R_S(\lambda)$ of the instrument is needed to evaluate the slit-function correction of the measured blackbody radiance [eq (32), below]. We determined $R_S(\lambda)$ with an accuracy sufficient for this purpose by calibrating the spectroradiometer with a standard tungsten-strip lamp. The result of this calibration is shown in figure 9.

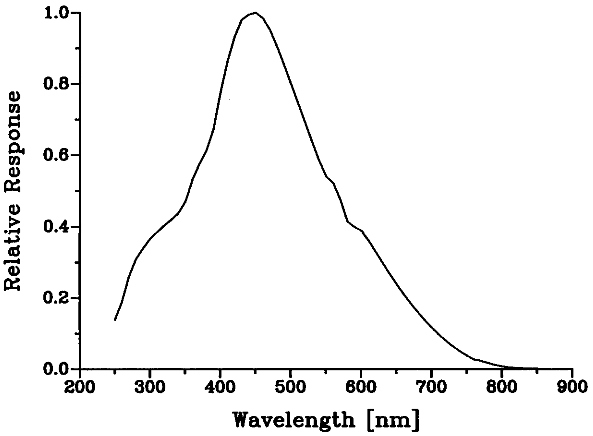

Figure 9. Relative spectral response of spectroradiometer.

4.5 Silicon Diode

The silicon diode detector is a windowless, 1-cm^2, p-n type, Hamamatsu 1337-1010Q diode operated without temperature control. The response of this detector type has been found to be quite independent of temperature at ambient temperatures in the 500 to 700 nm spectral region [25]. The spatial uniformity of the diode response was mapped over a 7×7 mm grid with a 633-nm laser beam and was found to be better than ±0.1%, as shown in figure 10.

The silicon diode was calibrated by senior staff of the NIST Photodetector Metrology Project with a stated three-standard-deviation uncertainty of ±0.2%. This calibration was performed using a monochromator-based spectral response comparator and a high-accuracy, laser-based detector characterization facility. The diode spectral responsivities at 514, 633, and 647 nm were measured by comparison to three fully characterized, absolute QED-200 detector standards. The QED standard is a light-trap configuration of n-p type, UDT UV-100 silicon diodes which, by significantly reducing reflection losses, permits a simplified, accurate self-calibration procedure [26]. During our measurements, we observed no changes in the diode response with respect to the ECR and monitor-diode readings. The overall agreement of the silicon-diode and ECR readings taken at 514 and 647 nm was on the order of 0.05% (see table 7).

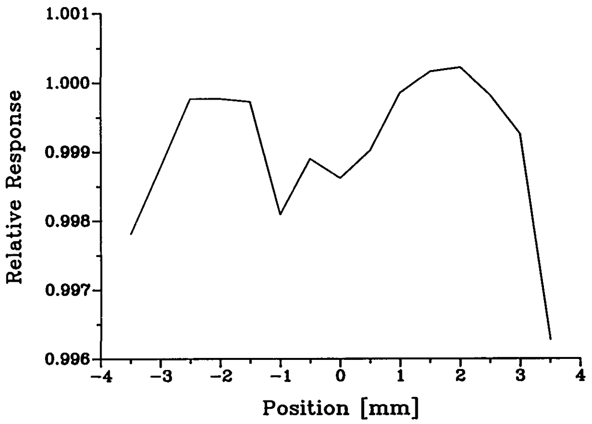

Figure 10. Relative horizontal distribution of silicon-diode responsivity (633 nm).

4.6 Electrically-Calibrated Radiometer

The ECR used was built by the National Institute of Measurement and Testing Technology (NIMTT) of the P.R.C. and is similar to that described in reference [27]. As shown in figures 11 and 12, it has two identical conical copper receivers of 11°19’ half angle, 25-mm length, and 10-mm opening. The heater windings are made of 0.03 mm diameter manganin wire, are uniformly and tightly glued to the insides of the cone, and are coated with black paint and kerosene smoke. The outside of each cone is equipped with a uniform, circular array of 72 nickel-chromium, constantan (type “E”) thermocouples made of 0.1-mm wire. Only one cone is exposed to radiant or electrical heating, respectively, and the thermocouple arrays on the two cones are connected oppositely. In this manner, only the temperature difference of the cones is registered and environmental temperature changes (such as those caused by adiabatic air pressure fluctuations [28]) are largely canceled. The laser-sphere aperture and its distance from the ECR were chosen so that the irradiated and electrically heated portions of the ECR cone were closely matched.

Due to residual differences in the electrical and radiant heating of an ECR, the temperature rise produced by radiant power is not exactly the same as that produced by an equal amount of electrical power. This non-equivalence of electrical and

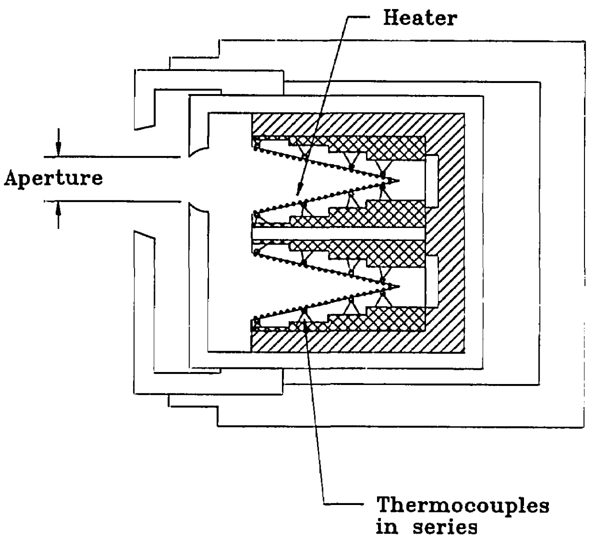

Figure 11. Cross section of ECR.

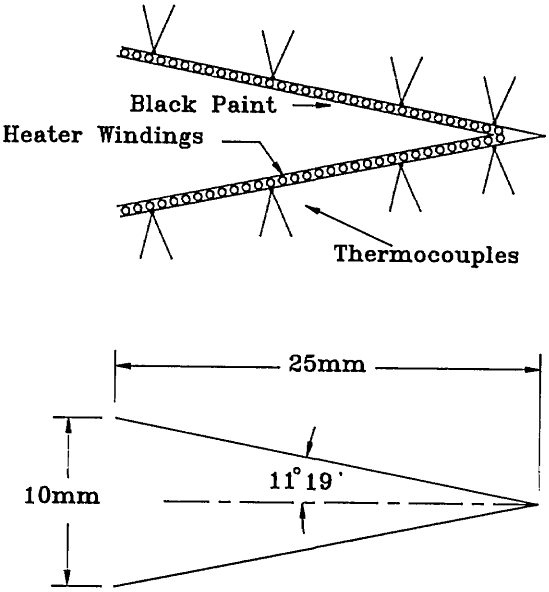

Figure 12. ECR cone details.

radiant heating has been examined in detail by Hengstberger [29]. The determination of the small correction for this non-equivalence is generally a one-time characterization of the ECR, as contrasted with the routine calibration by electrical substitution heating to achieve a thermocouple signal which matches that of an unknown radiant input power. Our characterization of the ECR was based on the equations

$$S_{\mathrm{ECR}}=R_{\mathrm{ECR}}\,P', \tag{11}$$

$$P'=P(1+\kappa-\rho-\eta-\epsilon), \tag{12}$$

where S_{ECR} is the ECR signal (thermocouple EMF), R_{ECR} is its responsivity, P' is the thermal power at the thermocouple hot junctions, P is the total (radiant or electrical) power applied to the ECR, and the remaining quantities are small correction terms:

κ is the environmental heating correction,
ρ is the reflection/emission loss;
η is the air convection/conduction loss,
ϵ is the sum of other losses.

The last term, ϵ, denotes the sum of all losses (such as thermal emission from the back side of the cone) which are identical for radiant and electrical heating and, therefore, do not require a correction. The other correction terms depend on the type of heating and will accordingly be distinguished by subscripts, r and e, so that κ_r denotes radiant case heating, κ_e denotes electrical lead heating, and so on. The characterization of the instrument consists of measuring the six correction terms κ_r, κ_e, ρ_r, ρ_e, η_r, and η_e one at a time in specially designed experiments. To measure κ_r, we covered the ECR aperture with a styrofoam plug and measured the thermopile signals with and without a radiant power P_r falling onto the face of the instrument. The lead heating effect was determined by rearranging the ECR circuitry so that the heat generated by the leads alone could be measured in addition to the heat generated by the heater windings and leads. The reflection/emission loss was measured by irradiating the ECR with a laser beam entering through the small central hole in a spherical mirror which could be rotated to focus the radiation remitted by the ECR back into the receiver cone, or to the side of it. The air convection/conduction correction terms were measured by radiantly and electrically heating the ECR in air and vacuum. These experiments have been described by Geist [30]. The only correction which was measurably non-zero was the air convection/conduction term. It amounted to 0.1%.

To estimate the error caused by spatial non-uniformity of response, we scanned the ECR aperture with a 1-mm diameter, 514-nm laser beam, and also mapped the radiation field produced by the laser sphere at this aperture. The former was found to vary by 0.6% (see fig. 13), and the latter by +0.01%. The corresponding correction factor was evaluated as 0.9998+0.0005.

Since the ECR is presumed to be sensitive in the infrared, it was necessary to determine the contribution which heating of the laser-sphere source

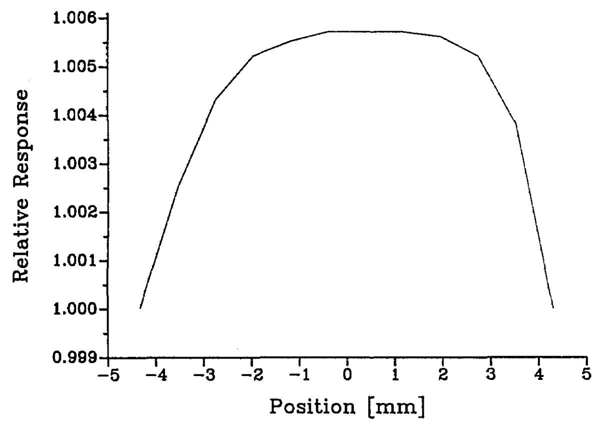

Figure 13. Relative horizontal distribution of ECR responsivity (514 nm).

makes to the ECR signal. This contribution was estimated by measuring the radiation temperature rise of the sphere interior during laser irradiation at 514 nm, using an imaging infrared radiometer. The measured temperature rise was 0.09 K. Hence, the increment in the radiant power received by the ECR was calculated as 0.056 μW, about 0.01% of the 0.4-mW radiant power levels used in our experiment.

The results of these various measurements and their estimated, three-sigma uncertainties are listed in table 4. We applied a 0.1% correction to the ECR responsivities measured by electrical substitution heating and estimated the overall systematic uncertainty of the ECR as 0.2%.

Table 4. Correction factors for ECR spectral responsivity and estimated uncertainties (3σ)

	Factor	Uncertainty (%)
Electrical lead heating	1.0000	0.06
Radiant case heating	1.0000	0.05
Reflection and emission loss	1.0001	0.10
Convection-conduction loss	1.0010	0.10
Non-uniformity of response	0.9998	0.05
Infrared response	1.0001	0.01
Overall correction	1.0010	0.17

4.7 Monitor Diode and Neutral Density Filter

Any measurement of the laser sphere by any of the three detector systems was accompanied by a simultaneous measurement by the monitor detector, followed by dark-current readings obtained by blocking the laser input to the sphere. The ratio of the dark-current corrected detector signal to the dark-current corrected monitor signal was the quantity actually used in the subsequent analysis. As mentioned earlier, this suppressed errors due to fluctuations of laser-sphere output. The monitor diode was an EG&G 444B silicon photodiode. Its response was found to be stable within 0.01% over periods of several hours.

Because the optimal power for ECR measurements is about four orders of magnitude higher than the power level produced by the blackbody, a neutral density filter was inserted in the laser beam when silicon-diode and spectroradiometer readings were taken. The monitor-diode signals obtained with and without the filter provided measurements of the transmittance of this filter, so that our data were automatically adjusted for its presence when ratios were computed.

4.8 Detector Linearity

The linearity of response of the spectroradiometer and silicon detectors was measured with an automated beam conjoiner [31], a flux-addition device. For the range of signal levels and the operating conditions used in these gold-point measurements, we found no correction necessary for departures from strict linearity. The ECR was tested by varying the electric heater power and exhibited no detectable nonlinearity over the small dynamic range in which this instrument was used. We assessed the combined uncertainty due to detector nonlinearities to be less than 0.1%.

4.9 Apertures

The mutual arrangement of the laser-sphere and detector apertures is shown in figure 14. The laser-sphere aperture was oriented perpendicular to the spectroradiometer optic axis by turning on the alignment laser in the spectroradiometer, holding a

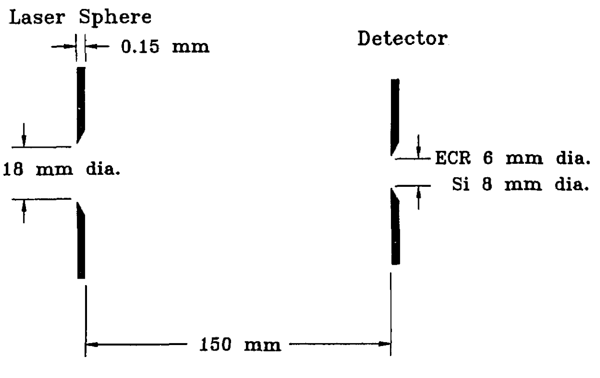

Figure 14. Laser-sphere and detector apertures.

glass microscope slide against the aperture, and adjusting the sphere until the laser beam was reflected by the glass back along itself. In a similar manner, the detector apertures were oriented using an auxiliary HeNe laser mounted on the source table but aimed into the spectroradiometer precisely along the spectroradiometer alignment laser beam. Because of the precision of these alignments, we believe that any error arising from non-parallelism of the apertures is negligible. These co-aligned lasers also provided means of positioning the centers of the detector and sphere apertures in the same horizontal plane, and of determining the spectroradiometer carriage positions at which the detectors are opposite the laser-sphere.

Reflections from the diode surface and from the diode and ECR apertures and mounting hardware could potentially be returned by the sphere aperture or hardware back to the detectors, or be scattered within the sphere and partially returned to the detectors. Although numerical estimates suggested that the errors due to such reflections are exceedingly small, two verification experiments were carried out. In the first, the detectors were covered by black velvet cloth except for the apertures and a narrow sliver at their edges. No detectable (<0.01%) signal differences were observed. In the second, the monitor signal was followed as the detectors were moved into position and away. Again, there was no detectable signal change.

5. Theory

5.1 Simplified Derivation of Measurement Equation

The basic principle of our measurement is best explained by temporarily neglecting small effects arising from the finite bandwidth of the sources and detectors involved, as well as all further effects introduced by their different sizes and spatial radiance distributions. With these simplifications, the spectroradiometer signals obtained at any given wavelength with the gold-point blackbody and laser-sphere sources are given by

$$S_S^{BB}=L_\lambda^{BB}\,\Delta\lambda\,G_S\,R_S, \tag{13}$$

$$S_S^{LS}=L^{LS}\,G_S\,R_S, \tag{14}$$

where $L_\lambda^{BB}\,\Delta\lambda$ and L^{LS}, respectively, are the radiances of the blackbody and the laser sphere, $\Delta\lambda$ is the spectral bandwidth of the spectroradiometer, and G_S and R_S, respectively, denote the geometric extent and the spectral responsivity of the spectroradiometer system. By taking the ratio of eqs (13) and (14), we obtain

$$L_\lambda^{BB}\,\Delta\lambda=(S_S^{BB}/S_S^{LS})\,L^{LS}, \tag{15}$$

thereby eliminating the unknown properties of the spectroradiometer and relying only on the linearity of its response to ensure that this result is accurate. Similar to eq (14), the signal obtained with the silicon-diode or ECR reference detector and the laser sphere is

$$S_D^{LS}=L^{LS}\,G_D\,R_D, \tag{16}$$

where R_D is the spectral responsivity of the detector, and where the geometric extent G_D is given by the standard expression which describes the radiation transfer between circular, parallel, and coaxial apertures with radii r_{LS} and r_D, and separation d [32],

$$G_D=(\pi^2/2)\Big\{(d^2+r_{LS}^2+r_D^2)-[(d^2+r_{LS}^2+r_D^2)^2 - 4r_{LS}^2 r_D^2]^{1/2}\Big\} \tag{17}$$

Combining eqs (15) and (16), we obtain the following approximate result for the spectral radiance of the blackbody in terms of the measured spectroradiometer and reference detector signals, the geometrical parameters of the laser sphere and reference detector arrangement, and the known spectral responsivity of the reference detector,

$$L_{\lambda,0}^{BB}=[S_S^{BB}\,S_D^{LS}/(S_S^{LS}\,\Delta\lambda\,R_D\,G_D)]. \tag{18}$$

The subscript (0) has been affixed to this expression for L_λ^{BB} in order to indicate that it is only an approximation to the full measurement equation. The corrections which must be applied to it for the rigorous reduction of measured data analysis will be derived next.

5.2 Derivation of Correction Factors

5.2.1 Spectroradiometer Signals The rigorous measurement equation describing the spectroradiometer signals obtained when the centers of the blackbody and laser-sphere source are imaged with unit magnification upon the small rectangular entrance slit of the instrument is [33]:

$$S_S(\lambda)=\int\int\int L_\lambda(\lambda',x,y)\, R_S(\lambda')\, \sigma(\lambda,\lambda')\, d\lambda' \cdot H(x,y)\, dx\, dy. \tag{19}$$

Here,

$S_S(\lambda)$ is the spectroradiometer signal;

λ is the wavelength setting of the monochromator and λ' is an arbitrary wavelength;

x and y are cartesian coordinates in the source plane, referred to the source center (0,0);

$L_\lambda(\lambda',x,y)$ is the spectral radiance of the source;

$R_S(\lambda')\, \sigma(\lambda,\lambda')$ is the spectral response of the spectroradiometer to radiation of wavelength λ' when the monochromator is set at λ;

$H(x,y)$ is the relative spatial response of the spectroradiometer to radiation from a source point (x,y) when the instrument is focused at the source center.

The integration in eq (19) and later expressions extends over all wavelengths and over the entire source aperture plane.

The factorization of the spectral response of the instrument into the two factors R_S and σ is uniquely defined if we require that $R_S(\lambda')$ is independent of λ and that the maximum value of $\sigma(\lambda,\lambda')$ is exactly unity. Then $\sigma(\lambda,\lambda')$ is what is commonly known as the slit function shown in figure 7 (or, better, the slit-scattering function to emphasize the fact that the distant wings are due to diffraction and scattering), and $R_S(\lambda')$ is the spectral responsivity of the instrument shown in figure 9, which is dominated by the spectral transmittance of the monochromator and the spectral response of the detector. With perfect imagery, the spatial apparatus function $H(x,y)$ would be a constant everywhere within a 0.6×0.8-mm rectangle and zero elsewhere. However, due to diffraction and scattering from dust and optical imperfections we must allow for the departures from this ideal illustrated by figure 8. We assumed that, like the slit-scattering function, $H(x,y)$ is normalized so that its maximum value is one, although this is not necessary since any such normalization factors will eventually cancel out in our application.

We replace the blackbody spectral radiance by a product of its value at the center and a relative spatial distribution function. The former is expected to be a Planckian function of wavelength. The latter is shown in figure 5. It exhibits a value close to unity over a small (1.5-mm diameter) central circular area, and then decreases to near zero at a radial distance of about 20 mm. Accordingly, we assume

$$L_\lambda(\lambda',x,y)=L_\lambda^{BB}(\lambda')\, \ell_{BB}(x,y), \tag{20}$$

where $\ell_{BB}(0,0)=1$. This factorization of the spectral radiance into separate spectral and spatial factors is an acceptable approximation for the purposes of the integrals in eq (19) because the slit-scattering and spatial apparatus functions are both sharply peaked functions. Thus, the error in this approximation at large distances from the source center or at wavelengths far from the monochromator setting will make a negligible contribution to the value of the integrals. With this approximation to the spectral radiance, we can write the measurement equation for the spectroradiometer viewing the center of the blackbody source as

$$S_S^{BB}(\lambda)=\int L_\lambda^{BB}(\lambda')\, R_S(\lambda')\, \sigma(\lambda,\lambda')\, d\lambda' \cdot\int\int \ell_{BB}(x,y)\, H(x,y)\, dx\, dy. \tag{21}$$

We also assume that the spectral radiance of the blackbody is Planckian, so that

$$L_\lambda^{BB}(\lambda')=\frac{L_\lambda^{BB}(\lambda_L)}{P(\lambda_L,T)}\, P(\lambda',T), \tag{22}$$

where λ_L is the wavelength of the laser-sphere source, T is the blackbody temperature, and $P(\lambda,T)$ is the Planck function defined by eq (3). Thus we rewrite eq (21) as

$$S_S^{BB}(\lambda)=\frac{L_\lambda^{BB}(\lambda_L)}{P(\lambda_L,T)}\int P(\lambda',T)\, R_S(\lambda')\, \sigma(\lambda,\lambda')\, d\lambda' \cdot\int\int \ell_{BB}(x,y)\, H(x,y)\, dx\, dy. \tag{23}$$

In order to estimate the possible error introduced by the approximations of eqs (20) and (22), we modeled the distributions involved by simple analytical functions which permitted the exact evaluation of the integrals in terms of elementary functions. By varying the parameters of these models to correspond in varying degrees to the measured functions, and observing the effect of the product approximation on eq (20), we found that the error is on the order of 0.002%.

We approximate the laser-sphere radiance in eq (19) by

$$L_\lambda(\lambda',x,y)=\delta(\lambda'-\lambda_L)\,L^{LS}(0,0)\,\ell_{LS}(x,y), \qquad (24)$$

where the delta function reflects the fact that the spectral distribution is that of a sharp laser line at wavelength λ_L, and $L^{LS}(0,0)$ is the central radiance of the source. The remaining factor $\ell_{LS}(x,y)$ is the relative spatial radiance distribution of the source shown in figure 6, which is approximately unity over the circular exit aperture of the sphere and zero outside this aperture. By performing the integration over wavelength in eq (19), we obtain

$$S_S^{LS}(\lambda)=R_S(\lambda_L)\,\sigma(\lambda,\lambda_L)\,L^{LS}(0,0)$$
$$\cdot\int\int \ell_{LS}(x,y)\,H(x,y)\,dx\,dy. \qquad (25)$$

5.2.2 Absolute Detector Signals The rigorous measurement equation for the absolute (silicon-diode or ECR) detector signals is [33]

$$S_D^{LS}=\int\int\int\int\int L_\lambda(\lambda',x,y)\,R_D(\lambda')\,d\lambda'$$
$$\cdot\frac{\cos\theta\cdot\cos\theta'}{d^2+(x-x')^2+(y-y')^2}\,dx\,dy\,dx'\,dy'. \qquad (26)$$

In this expression,

S_D^{LS} is the detector signal;

(x,y) and (x',y') refer to parallel cartesian coordinate axes in the source and detector aperture planes, respectively;

θ and θ' are the angles between the normals to these aperture planes and the ray defined by the points (x,y) and (x',y');

d is the distance between the aperture planes;

$L_\lambda(\lambda',x,y)$ is the spectral radiance of the laser-sphere source, assumed directionally uniform (Lambertian) within the small solid angle sampled by the detectors ($f/19$ for the silicon detector and $f/25$ for the ECR);

$R_D(\lambda')$ is the spectral responsivity of the detector.

We assume again that the spectral radiance of the laser-sphere source is given by eq (24). We further assume that in the integrals of eq (26) the relative spatial distribution function can be replaced by its average value,

$$<\ell_{LS}>=\frac{1}{A_{LS}}\cdot\int\int \ell_{LS}(x,y)\,dx\,dy, \qquad (27)$$

and moved outside the integrals. A_{LS} is the laser-sphere aperture area. Thus eq (26) becomes:

$$S_D^{LS}=R_D(\lambda_L)\,L^{LS}(0,0)<\ell_{LS}>$$
$$\cdot\int\int\int\int\frac{\cos\theta\cdot\cos\theta'}{d^2+(x-x')^2+(y-y')^2}\,dx\,dy\,dx'\,dy'. \qquad (28)$$

For the geometry we used, this integral can be evaluated to give

$$S_D^{LS}=R_D(\lambda_L)\,L^{LS}(0,0)<\ell_{LS}>G_D, \qquad (29)$$

where G_D is the geometric extent previously defined by eq (17).

5.2.3 Definition of Correction Factors We can now combine eqs (23), (25), and (29) in order to derive the rigorous analog of the approximate expression (18) for the blackbody spectral radiance. This is accomplished by dividing eq (25) into eq (23), solving for $L_\lambda^{BB}(\lambda_L)$, substituting the result for $L^{LS}(0,0)$ obtained from eq (29), and then multiplying the numerator and denominator by the spectral bandwidth $\Delta\lambda_L$ of the spectroradiometer at λ_L. Thus we obtain

$$L_\lambda^{BB}(\lambda_L)=\frac{S_S^{BB}(\lambda)\,S_D^{LS}(\lambda_L)}{S_S^{LS}(\lambda)\,\Delta\lambda_L\,R_D(\lambda_L)\,G_D}\cdot\frac{f_\sigma f_H}{<\ell_{LS}>}, \qquad (30)$$

where the bandwidth $\Delta\lambda_L$ is defined as the normalized area of the slit-scattering function,

$$\Delta\lambda_L=\frac{\int\sigma(\lambda,\lambda')\,d\lambda'}{\sigma(\lambda,\lambda_L)}. \qquad (31)$$

The left-hand factor in eq (30) is identical to the approximate radiance of eq (18), and the right-hand factor is comprised of three correction terms:

(1) A spectroradiometer slit-scattering function correction, defined as

$$f_\sigma=\frac{P(\lambda_L,T)\,R_S(\lambda_L)\int\sigma(\lambda,\lambda')\,d\lambda'}{\int P(\lambda',T)\,R_S(\lambda')\,\sigma(\lambda,\lambda')\,d\lambda'}. \qquad (32)$$

This factor arises from the different spectroradiometer response to broadband blackbody radiation and monochromatic laser light.

(2) A spatial apparatus function correction, defined as

$$f_{\mathrm{H}}=\frac{\int\int \ell_{\mathrm{LS}}(x,y)\, H(x,y)\, \mathrm{d}x\ \mathrm{d}y}{\int\int \ell_{\mathrm{BB}}(x,y)\, H(x,y)\, \mathrm{d}x\ \mathrm{d}y}. \tag{33}$$

This correction accounts for the different sizes and spatial radiance distributions of blackbody and laser-sphere sources.

(3) A sphere non-uniformity correction, defined as the inverse of the average relative sphere radiance of eq (27). This correction accounts for the fact that the spectroradiometer viewed primarily the center of the sphere aperture, while the silicon and ECR detectors viewed the entire aperture.

5.2.4 Diffraction Effects The theory presented above does not include all diffraction effects which constitute a potential source of error in the physical model leading to eq (30). For the spectroradiometer measurements, diffraction is implicit in the slit-scattering and spatial apparatus functions considered. Diffraction losses at the limiting aperture of the spectroradiometer were eliminated by limiting the field of view, not at the laser sphere or blackbody, but within the spectroradiometer system, so that the effects would cancel when the ratio $S_{\mathrm{S}}^{\mathrm{BB}}/S_{\mathrm{S}}^{\mathrm{LS}}$ in eq (31) is taken. However, for the silicon-detector and ECR measurements, there may be a small diffraction loss caused by the apertures being mounted a few millimeters in front of the detectors themselves. We performed calculations based on the treatment of Steel, De, and Bell [34] and found losses ranging from 0.003% for the silicon detector at 514 nm to 0.02% for the ECR at 647 nm. The upper limit of this range (0.02%) was included in our error analysis.

6. Measurements

6.1 Spectroradiometer Slit-Scattering Function Correction, f_σ

This correction factor was calculated from eq (32) by combining the measured values of the spectroradiometer spectral responsivity $R_{\mathrm{S}}(\lambda)$ (fig. 9) and slit-scattering function $\sigma(\lambda,\lambda')$ (fig. 7) with calculated values of the Planck function $P(\lambda,T)$ [eq (3)] evaluated at the IPTS-68 gold-point temperature, 1337.58 K. For these calculations we used the 0.6-mm slit-scattering functions obtained in our earlier study, because they include far-wing data. Since the slit-scattering function appears in integrals in both the numerator and denominator of f_σ, it tends to cancel and small differences between the functions obtained previously and the current slit-scattering functions are of no consequence. The values of f_σ at the three laser wavelengths fall within the range 0.9999+0.0004.

6.2 Spectroradiometer Spatial Apparatus Function Correction, f_{H}

To compute the value of f_{H} defined by eq (33), we used the normalized horizontal and vertical traverses of the spatial apparatus function of the spectroradiometer shown in figure 8 and the measured spatial radiance distributions of the blackbody and laser-sphere sources shown in figures 5 and 6. These distributions, of course, represent convolutions of the true distributions with the spectroradiometer point-spread function, whereas the functions needed to calculate f_{H} are the true distributions. In the evaluation of the integral in the denominator of eq (33) only the central 1 or 2 mm contribute significantly, and here the effect of convolution is merely a reduction of the apparent radiance by a nearly constant factor (e.g., 0.9997). Consequently, the normalized observed distribution is virtually indistinguishable from the true distribution insofar as the evaluation of the denominator in eq (34) is concerned, and no deconvolution is required. A similar remark applies to the laser-sphere integral appearing in the numerator, although in this case no deconvolution correction would have been expected anyway due to the uniformity of that distribution. The values obtained for f_{H} range from a minimum of 1.0002 at the end of a melt at any wavelength to a maximum of 1.0008 at the end of a freeze at 514 nm. Our final result for f_{H} is the average of all calculated values, $f_{\mathrm{H}}=1.0003+0.0006$, where the uncertainty covers the dependence upon time and wavelength and includes an uncertainty for the contribution of the far wings of the spatial apparatus function, extrapolated beyond ±7 mm.

6.3 Laser-Sphere Nonuniformity Correection, $<\ell_{\mathrm{LS}}>$

The integration of the measured distribution over the laser-sphere source (fig. 6) was performed at all three wavelengths used. The average relative radiance obtained was $<\ell_{\mathrm{LS}}>=1.0022+0.0009$, where the uncertainty is a three-sigma estimate of repeatability.

6.4 Geometric Extent of Absolute Detectors, G_D

For the evaluation of this quantity, eq (17) was used in a simplified form in which the areas of the laser-sphere and detector apertures were used instead of their radii. The aperture dimensions were measured on a movable stage under a microscope calibrated by the Precision Engineering Division of NIST. The microscope was focused on the edge of the aperture being measured, and then the (x,y) coordinates of the stage were recorded as the microscope cross-hairs were positioned at arbitrary intervals of about 5° or 10° around the edge of the aperture. The data points recorded in this way were sufficiently numerous (about 50) that the omission of half of them by using only alternate points resulted in a totally negligible difference in the area determination. The (x,y) coordinate pairs were converted to (r,Θ) coordinate pairs about an origin near the aperture center (chosen so that all r values were equal within 0.01 mm), and the areas were calculated from

$$A=\int_0^{2\pi} r^2 \mathrm{d}\Theta/2 \cong \sum_1^n r_i^2\,(\Theta_{i+1}-\Theta_{i-1})/4, \tag{34}$$

with $\Theta_0 \equiv \Theta_n$ and $\Theta_{n+1} \equiv \Theta_1$. These aperture measurements were repeated two or three times for each aperture by each of two operators with excellent agreement. The values obtained and their repeatabilities (three standard deviations) are given in table 5.

Table 5. Aperture dimensions and distances

Laser-sphere aperture area	(2.5523 ± 0.0013) cm^2
Laser-sphere aperture thickness	(0.015 ± 0.001) cm
Si-detector aperture area	(0.50021 ± 0.00035) cm^2
ECR aperture area	(0.2835 ± 0.0004) cm
Aperture distance	(15.000 ± 0.002) cm
Geometric Extent, G_{Si}	$(5.63843\pm0.00052)\ 10^{-3}$ cm^{2}sr
Geometric Extent, G_{ECR}	$(3.19662\pm0.00049)\ 10^{-3}$ cm^{2}sr

The separation between source and detector apertures was set each morning by holding a parallel-faced gauge block of known length (150.0 mm for most measurements) between the apertures, and adjusting the detector position until both apertures were in light contact with the gauge. In calculating the geometric extents of the two detector systems, we accounted for the fact that the laser-sphere aperture had a thickness of 0.15 mm and was beveled toward the inside of the sphere by using an effective aperture separation of 150.15 mm. The uncertainty in the length of the gauge block was assessed as 0.02 mm, and the possible error due to lack of sharpness of the aperture edges was estimated as 0.01 mm.

6.5 Spectral Radiance Measurements

The measurement of a single blackbody spectral radiance value constituted a day's work which was carried out in accordance with the measurement protocol described below. The measurement was performed in a time-symmetrical fashion, so that possible drifts of the spectroradiometer blackbody signals would be eliminated in part when overall averages were taken. However, no drifts were observed outside of statistical fluctuations. All laser-sphere readings were recorded relative to simultaneously taken monitor-diode readings, so that errors due to small fluctuations of laser-sphere output were minimized and the transmittance of the neutral-density filter was automatically accounted for when it was inserted in the laser beam entering the sphere.

The individual measurement steps performed were:

(1) While the blackbody was heating up to the first melt of the day, the laser was turned on and the separation d between the laser sphere and detector apertures was set as described in section 6.4. The ECR was positioned in front of the laser sphere, and the laser power was adjusted to give readings of approximately 0.4 mW (without neutral density filter).

(2) The ECR was calibrated by applying electrical substitution heating for a duration of 180 s, and then its responsivity R_{ECR} (V/W) was recorded as the ratio of the thermocouple EMF and heating power applied, divided by the ECR correction 1.001.

(3) The ECR was exposed to radiant heating for 180 s, and the relative ECR laser-sphere signal $S_{\mathrm{ECR}}^{\mathrm{LS}}$ was recorded (in V/A) as the ratio of the thermocouple EMF and the monitor-diode reading.

(4) The neutral-density filter was inserted in the beam and the spectroradiometer positioned in front of the laser sphere. The central 10-nm portion of the spectroradiometer slit-scattering function was recorded by scanning the monochromator wavelength drive (514 and 633 nm) or scanning the dye laser (647 nm). The monochromator was set to the

maximum of this scan, where it remained until the measurements were complete for the day. A preliminary value, $\Delta\lambda_0$, of the spectroradiometer bandwidth was calculated from eq (31) by integrating the measured slit-scattering function. This result was corrected for the omitted contribution of the far wings of the slit-scattering function as described in section 4.4.

(5) Once the blackbody was in a melt (or, later, in a freeze), a cycle of three readings was taken repeatedly: the spectroradiometer readings of the blackbody and the laser sphere, and the silicon and monitor diode readings of the sphere. The spectroradiometer blackbody signal S_S^{BB} was recorded as the measured photomultiplier anode current (A). The spectroradiometer and silicon-diode laser-sphere signals, S_S^{LS} and S_{Si}^{LS}, were recorded relative to the monitor-diode readings (in dimensionless units).

(6) During the hour or so following a melt (or freeze) and preceding the subsequent freeze (or melt), the laser sphere was repeatedly measured with the ECR and the silicon and monitor detectors, as described in steps (3) and (5). Generally, two to four melt-freeze cyles were carried out in a day, each time repeating the measurements of step (5).

(7) Following the last freeze of the day, the laser sphere was re-measured with the ECR and the silicon and monitor detectors, the spectroradiometer slit-scattering function was re-measured as in step (4), and the ECR was re-calibrated by electrical substitution as in step (2).

Table 6 gives a representative sample of the average data obtained at 647 nm on a typical day. The table also gives the values of the various other factors needed to calculate the blackbody spectral radiance from eq (30). In the example shown, the silicon-detector and ECR results are 63.319 and 63.395 $\mathrm{Wcm^{-3}sr^{-1}}$, respectively.

6.6 Blackbody Spectral Radiances

The measurement sequence described in section 6.5 was performed five times at each laser wavelength. This gave 10 spectral radiance values, each, at the argon and krypton laser wavelengths, and five values at the helium-neon laser wavelength. The 25 spectral radiance values thus obtained are listed in table 7 and were treated as single measurements for data reduction purposes.

Because our experiment relies on the redundant detector scales established by the silicon diode and the ECR, we verified the mutual agreement of these scales by comparing the differences and the standard deviations of the silicon-diode and ECR values of table 7. As shown at the bottom of the table, the two scales were found to agree within experimental uncertainties.

Table 6. Representative data set obtained at 647.1 nm

ECR responsivity, R_{ECR}	0.267244 V/W
Relative ECR signal, S_{ECR}^{LS}	0.19412 V/W
Spectroradiometer bandwidth (including far wings), $\Delta\lambda$	2.5273×10^{-7} cm
Spectroradiometer blackbody signal, S_S^{BB}	3.17858×10^{-8} A
Relative spectroradiometer laser-sphere signal, S_S^{LS}	0.449073
Relative silicon-diode signal, S_{Si}^{LS}	0.599112
Silicon-diode responsivity, R_{Si}	0.468170 A/W
Silicon-diode geometric extent, G_{Si}	5.63843×10^{-3} cm²sr
ECR geometric extent, G_{ECR}	3.19662×10^{-3} cm²sr
Spectroradiometer slit-scattering correction, f_σ	0.9999
Spectroradiometer apparatus-function correction, f_H	1.0003
Laser-sphere nonuniformity correction, $<\ell_{LS}>$	1.0022
Blackbody spectral radiance (Si), L_λ^{BB}	63.3186 $\mathrm{Wcm^{-3}sr^{-1}}$
Blackbody spectral radiance (ECR), L_λ^{BB}	63.3953 $\mathrm{Wcm^{-3}sr^{-1}}$

Table 7. Measured blackbody spectral radiances ($\mathrm{Wcm^{-3}sr^{-1}}$) and random uncertainties (1σ)

	514.5 nm		632.9 nm	647.1 nm	
	Si	ECR	Si	Si	ECR
	2.7468	2.7523	48.883	63.482	63.484
	2.7576	2.7570	48.621	63.319	63.395
	2.7656	2.7612	48.761	63.192	63.178
	2.7650	2.7605	48.659	63.396	63.379
	2.7653	2.7616	48.696	63.477	63.231
Mean	2.7601	2.7586	48.724	63.373	63.333
Std dev of mean	0.0036 (0.13%)	0.0018 (0.07%)	0.046 (0.09%)	0.054 (0.09%)	0.056 (0.09%)
Difference	0.0015 (0.05%)			0.040 (0.06%)	

The standard deviations of the mean listed in table 7 represent the composite random uncertainties of all of the measurements described in section 6.5. They include the random uncertainties of all detector signals, the calibration of the ECR, the wavelength setting of the spectroradiometer and measurement of its bandwidth, the setting of the aperture distance, the transmittance of the neutral density filter, as well as fluctuations of the blackbody and laser-sphere sources. Since the individual standard deviations are all on the order of 0.1%, our three-sigma estimate of the composite random uncertainty of these measurements is 0.3%.

6.7 Gold-Point Temperature

To find the gold-point temperature T_{Au}, we expressed the theoretical blackbody radiance as the product of Planck's eq (3) and the estimated blackbody emissivity, $\epsilon=0.9999$, of section 4.1. We compared the average measured spectral radiances L_λ^{BB} given in table 7 with the values $\epsilon\, P(\lambda, T_{\mathrm{Au}})$ obtained by substituting trial values of T_{Au}, the laser wavelengths listed in table 3, the refractive indexes of air computed from Edlen's formula [35], and evaluated the radiation constants, $c_1=2hc^2$ and $c_2=hc/k$, in terms of the 1986 values of h, k, and c given by Cohen and Taylor [36]. By varying T_{Au} until the quadrature sum of the weighted differences $[L_\lambda^{\mathrm{BB}}-\epsilon\, P(\lambda, T_{\mathrm{Au}})]/\sigma_\lambda$ (σ_λ being the standard deviations of the mean given in table 7) was minimized, we found $T_{\mathrm{Au}}=1337.334$ K. The relative standard deviation of the mean of this least-squares fit was $\pm 0.056\%$ (relative to radiance). The theoretical blackbody spectral radiances $\epsilon\, P(\lambda, T_{\mathrm{Au}})$ calculated for this temperature and their deviations from the average measured spectral radiances L_λ^{BB} are listed in table 8. These residuals exhibit a small dependence on wavelength which is unexplained, but falls within the combined uncertainty of our measurements.

Table 8. Residuals of least-squares fit for $T_{\mathrm{Au}}=1337.334$ K

Wavelength (nm)	Calculated radiance ($\mathrm{Wcm^{-3}\,sr^{-1}}$)	Residuals Si	Residuals ECR
514.5	2.7561	0.0040	0.0025
632.9	48.736	−0.12	
647.1	63.433	−0.060	−0.100

6.8 Uncertainty

To estimate the uncertainty of this result, we added in quadrature the composite random uncertainty of the blackbody spectral radiance measurements (sec. 6.6), the uncertainty of the least-squares fit (sec. 6.7), and the various systematic uncertainties in excess of 0.01% that have been mentioned in previous sections of this paper. These uncertainties have been collected in table 9, where all of them are given as estimated upper limits of systematic errors or three standard deviations. Their summation in quadrature gives a total uncertainty (relative to radiance) of 0.45%. Hence, the uncertainty of the measured gold-point temperature was estimated from eq (10) as ±0.34 K (at wavelength 600 nm).

Table 9. Estimated uncertainties (3σ) of gold-point measurement (see sections cited in parentheses for details)

Quality	Uncertainty
Composite random uncertainty (6.6)	0.30%
Least-squares fit (6.7)	0.17%
Blackbody emissivity (4.2)	0.01%
Polarization (4.3)	0.02%
Far-wing bandwidth correction (4.4)	0.04%
Detector responsivity [silicon (4.5) or ECR (4.6)]	0.20%
Detector linearity (4.8)	0.10%
Diffraction (5.2.4)	0.02%
Slit-scattering function correction f_σ (6.1)	0.06%
Apparatus function correction f_{H} (6.2)	0.03%
Sphere non-uniformity correction $<\ell_{\mathrm{LS}}>$ (6.3)	0.09%
Geometric extent, G_{D} (6.4)	0.15%
Total radiance uncertainty (added in quadrature)	0.45%
Gold-point temperature uncertainty [from eq (10), at 600 nm]	0.34 K

7. Result

Based on the above, the value

$$T_{\mathrm{Au}}=(1337.33\pm 0.34)\ \mathrm{K} \tag{35}$$

is quoted as the final result of our measurement of the gold-point temperature.[2] This result is in good quantitative agreement with the measurements

---

[2] This value differs from a preliminary value which was reported at an IMEKO Photon-Detector Committee meeting (Braunschweig 1987). The preliminary value was based on an incomplete analysis of the raw data reported in the present paper, and was in error because the refractive index of air (about 1.00027) had not been included in Planck's radiation formula.

described in section 3, above. Our experiment represents the only direct spectroradiometric determination of the gold-point temperature which has been reported so far and, therefore, provides an independent confirmation of these earlier measurements. The value quoted in eq (34) was submitted to the Consultative Commmittee on Thermometry as an official NIST contribution to the ITS-90 and, as noted in section 1, was incorporated into the new scale.

8. Acknowledgments

The following have contributed to this measurement by providing advice and/or calibrations: Jeanne Houston, Donald McSparron, Albert Parr, Martin Reilly, Steve Southworth, and James Walker of NIST; Li Tong Bao of NIMTT, Chengdu, P.R.C.; Klaus Möstl, Jürgen Metzdorf, and Klaus Stock of PTB, Braunschweig, F.R.G.; and Jeffrey Tapping of NML, Sidney, Australia. Their contributions are gratefully acknowledged.

About the authors: Dr. Klaus Mielenz, a physicist, is presently Chief of the Radiometric Physics Division at NIST. Robert Saunders, an optical physicist, is presently the group leader of the Thermal Radiometry Group of the Radiometric Physics Division. John B. Shumaker, a physicist, is a retired group leader from NIST.

9. References

[1] Preston-Thomas, H., Metrologia **12**, 7 (1976).
[2] Proces-Verbaux des Seances du Comite' International des Poids et Measures, (78e Session, octobre 1989), in press.
[3] Walker, J. H., Saunders, R. D., and Hattenburg, A. T., Spectral Radiance Calibrations (NBS Special Publication SP 250-1, U.S. Government Printing Office, Washington DC, 1987).
[4] Waters, W. R., Walker, J. H., and Hattenburg, A. T., Radiance Temperature Calibrations (NBS Special Publication SP 250-7, U.S. Government Printing Office, Washington DC, 1987).
[5] Walker, J. H., Saunders, R. D., Jackson, J. K., and McSparron, D. A., Spectral Irradiance Calibrations (NBS Special Publication SP250-20, U.S. Government Printing Office, Washington DC, 1987).
[6] Booker, R. L., and McSparron, D. A., Photometric Calibrations (NBS Special Publication SP 250-15, U.S. Government Printing Office, Washington DC, 1987).
[7] Walsh, J. W. T., Photometry, Constable & Co., London, (1958), p. 296.
[8] Schaefer, A. R., Saunders, R. D., and Hughey, L. R., Opt. Eng. **25**, 892 (1986).
[9] CCPR, Report of the 11th Session (BIPM 1986).
[10] Mielenz, K. D., J. Res. Natl. Bur. Stand. (U.S.) **92**, 335 (1987).
[11] Blevin, W. R., and Brown, W. J., Metrologia **7**, 15 (1971).
[12] Guildner, L. A., and Edsinger, R. E., J. Res. Natl. Bur. Stand. (U.S.) **77A**, 383 (1973).
[13] Bonhoure, J., Metrologia **11**, 141 (1975).
[14] Andrews, J. W., and Gu, C., BIPM Document CCT/84-39 (1984).
[15] Guildner, L. A., and Edsinger, R. E., J. Res. Natl. Bur. Stand. (U.S.) **80A**, 703 (1976).
[16] Jung, H. J., Metrologia **20**, 67 (1984).
[17] Tischler, M., and Rebagliati, M. J., Metrologia **21**, 93 (1985).
[18] Jones, T. P., and Tapping, J., Metrologia **25**, 41 (1988).
[19] Fischer, J., and Jung, H. J., PTB Mitteilungen **98**, 206 (1988).
[20] Quinn, T. J., Brit. J. Appl. Phys. **18**, 1105 (1967).
[21] Quinn, T. J., and Ford, M. C., Proc. Roy. Soc. (London) **A312**, 31 (1969).
[22] Weidner, V. R., and Hsia, J. J., J. Opt. Soc. Am. **71**, 856 (1981).
[23] Pressley, R. J., (Ed.), CRC Handbook of Lasers, Chemical Rubber Co., Cleveland OH (1971).
[24] Saunders, R. D., and Shumaker, J. B., Appl. Optics **25**, 3710 (1986).
[25] Andor, G., Temperature Dependence of High-Accuracy Photometer Heads, Appl. Opt. **28**, 4733 (1989).
[26] Zalewski, E. F., and Duda, C. R., Appl. Opt. **22**, 2867 (1983).
[27] Gao, Z., Wang, Z., Piao, D., Mao, S., and Yang, C., Metrologia **19**, 85 (1983).
[28] Stock, K. D., Rev. Sci. Instr. **54**, 1708 (1983).
[29] Hengstberger, F., Metrologia **13**, 69 (1977).
[30] Geist, J., Fundamental Principles of Absolute Radiometry etc. (NBS Special Publication 594-1, U.S. Government Printing Office, Washington DC, 1972).
[31] Saunders, R. D., and Shumaker, J. B., Appl. Opt. **23**, 3504 (1984).
[32] Jakob, M., Heat Transfer Vol. 2, Wiley, New York (1965), p.14.
[33] Kostkowski, H. J., and Nicodemus, F. E., Self-Study Manual on Optical Radiation Measurements, Chapter 5 (NBS Technical Note 910-2, U.S. Government Printing Office, Washington DC, 1978).
[34] Steel, W. H., De, M., and Bell, J. A., J. Opt. Soc. Am. **62**, 1099 (1972).
[35] Edlen, B., J. Opt. Soc. Amer. **43**, 339 (1953).
[36] Cohen, E. R., and Taylor, B. N., Rev. Mod. Phys. **59**, 1121 (1987).

Volume 95, Number 1, January-February 1990
Journal of Research of the National Institute of Standards and Technology

[J. Res. Natl. Inst. Stand. Technol. 95, 69 (1990)]

Special Report on the International Temperature Scale of 1990

Report on the 17th Session of the Consultative Committee on Thermometry

Volume 95 Number 1 January-February 1990

B. W. Mangum

National Institute of Standards and Technology,
Gaithersburg, MD 20899

This article summarizes the results of the 17th Session of the Consultative Committee on Thermometry of the International Committee of Weights and Measures (Comité Consultatif de Thermométrie of the Comité International des Poids et Mesures) that met in Sèvres, France, September 12–14, 1989. That session was devoted exclusively to the completion of the International Temperature Scale of 1990, described herein, and to the implications of its adoption.

Key words: CCT; Comité Consultatif de Thermométrie; Consultative Committee on Thermometry; International Temperature Scale of 1990; temperature; temperature scale; thermodynamic temperature; thermometry.

Accepted: **November 4, 1989**

1. Introduction

The Consultative Committee on Thermometry (Comité Consultatif de Thermométrie, CCT) is one of eight Consultative Committees (Comités Consultatifs) of the International Committee of Weights and Measures (Comité International des Poids et Mesures, CIPM). The CIPM is a committee of the General Conference of Weights and Measures (Conférence Générale des Poids et Mesures, CGPM). The eight Consultative Committees (Comités Consultatifs) of the CIPM are:

1. The Comité Consultatif d'Électricité (CCE), established in 1927,
2. The Comité Consultatif de Photométrie et Radiométrie (CCPR), assigned this name in 1971; the previous name was the Comité Consultatif de Photométrie, established in 1933,
3. The Comité Consultatif de Thermométrie (CCT), established in 1937,
4. The Comité Consultatif pour la Définition du Métre (CCDM), established in 1952,
5. The Comité Consultatif pour la Définition de la Seconde (CCDS), established in 1956,
6. The Comité Consultatif pour les Étalons de Mesure des Rayonnements Ionisants (CCEMRI), established in 1958,
7. The Comité Consultatif des Unités (CCU), established in 1964, and
8. The Comité Consultatif pour la Masse et les grandeurs apparentées (CCM), established in 1980.

The CCT is composed presently of members from the following laboratories:

1. Amt für Standardisierung, Messwesen und Warenprüfung [ASMW], Berlin, DDR,
2. Bureau National de Métrologie, Paris, France: Institut National de Métrologie, [INM] du Conservatoire National des Arts et Métiers,
3. Ceskoslovensky Metrologicky Ustav [CSMU], Bratislava, Czechoslovakia,
4. National Research Council [NRC], Ottawa, Canada,

5. CSIRO, Division of Applied Physics [CSIRO], Lindfield, Australia,
6. D. I. Mendeleyev Institute for Metrology [VNIIM], Leningrad, USSR; Physico-Technical and Radio-Technical Measurements Institute (PRMI), Moscow, USSR,
7. National Institute of Metrology [NIM], Beijing, PRC,
8. Istituto di Metrologia G. Colonnetti [IMGC], Turin, Italy
9. Kamerlingh Onnes Laboratorium [KOL], Leiden, The Netherlands,
10. Korea Standards Research Institute [KSRI], Seoul, Korea,
11. National Institute of Standards and Technology [NIST], Gaithersburg, MD, USA
12. National Physical Laboratory [NPL], Teddington, UK,
13. National Research Laboratory of Metrology [NRLM], Ibaraki, Japan,
14. Physikalisch-Technische Bundesanstalt [PTB], Braunschweig, FRG,
15. Van Swinden Laboratorium [VSL], Delft, The Netherlands,
16. Iowa State University, Ames, Iowa, USA, and
17. Bureau International des Poids et Mesures [BIPM], Sèvres, France.

The CCT met September 12–14, 1989 at the Bureau International des Poids et Mesures (BIPM) in its 17th Session [1] and completed the final details of the new temperature scale, the International Temperature Scale of 1990 (ITS-90) [2]. The CCT then recommended to the CIPM at its meeting on September 26–28, 1989 at the BIPM that the ITS-90 be adopted and made the official scale. The CIPM did adopt the new temperature scale at their meeting [3] and the ITS-90 became the official international temperature scale on January 1, 1990, the same date on which changes affecting certain electrical reference standards were implemented [4]. The ITS-90 supersedes the International Practical Temperature Scale of 1968, Amended Edition of 1975 [IPTS-68(75)] [5] and the 1976 Provisional 0.5 K to 30 K Temperature Scale (EPT-76) [6].

The CCT undertook the development of the ITS-90 because of the deficiencies and limitations of the IPTS-68(75) and completed the scale in accordance with Resolution 7 of the 18th Conférence Générale des Poid et Mesures [7], which met in October 1987. The deficiencies and limitations of the IPTS-68(75) included its lower limit of 13.81 K, its inaccuracy relative to thermodynamic temperatures, and its non-uniqueness and irreproducibility, especially in the temperature region from $T_{68}=903.89$ K ($t_{68}=630.74$ °C) to $T_{68}=1337.58$ K ($t_{68}=1064.43$ °C), the region in which the Pt-10%Rh/Pt thermocouple was the standard interpolating instrument.

The ITS-90 extends upward from 0.65 K and temperatures on this scale are in much better agreement with thermodynamic values than are those on the IPTS-68(75) and the EPT-76. The new scale has subranges and alternative definitions in certain ranges that greatly facilitate its use. Furthermore, its continuity, precision, and reproducibility throughout its range are much improved over the corresponding characteristics of the previous scales. The replacement of the thermocouple with the platinum resistance thermometer at temperatures in the range from 630.74 to 961.93 °C of the IPTS-68(75) resulted in the biggest improvement in reproducibility. Also, improvements in radiometric techniques have allowed using the silver freezing point as the reference point for radiation thermometry. This is a lower temperature reference point than was used in the IPTS-68(75).

The change in the temperature scale affects not only technical interests involved directly in thermometry but also those involved with other reference standards, such as electrical standards, if those standards are sensitive to temperature. As examples, standard resistors and standard cells are sensitive to temperature and generally are maintained in constant-temperature environments, at least in national standards laboratories. At the present time, the temperatures of those environments are normally determined with thermometers that have been calibrated on the IPTS-68(75). A given thermodynamic temperature expressed on the ITS-90, however, has a value that is different from that expressed on the IPTS-68(75), as indicated [2,8] in figure 1. A table of differences between temperatures on the ITS-90, T_{90} or t_{90}, and those on the IPTS-68(75), T_{68} or t_{68}, and those on the EPT-76, T_{76}, is given in the text of the ITS-90. Since temperature values expressed on these scales are different, if the temperature of the environment of a reference standard is adjusted so that *its value when expressed on the ITS-90* has the *same value* as had been used on the IPTS-68(75), there will have been a *change* of the thermodynamic temperature and the value of the reference standard will usually change. Of course, one may not want to change the thermodynamic temperature of the reference standard. In that case, the thermodynamic temperature, as expressed on the IPTS-68(75), can simply be expressed on the ITS-90 (a numerical value different

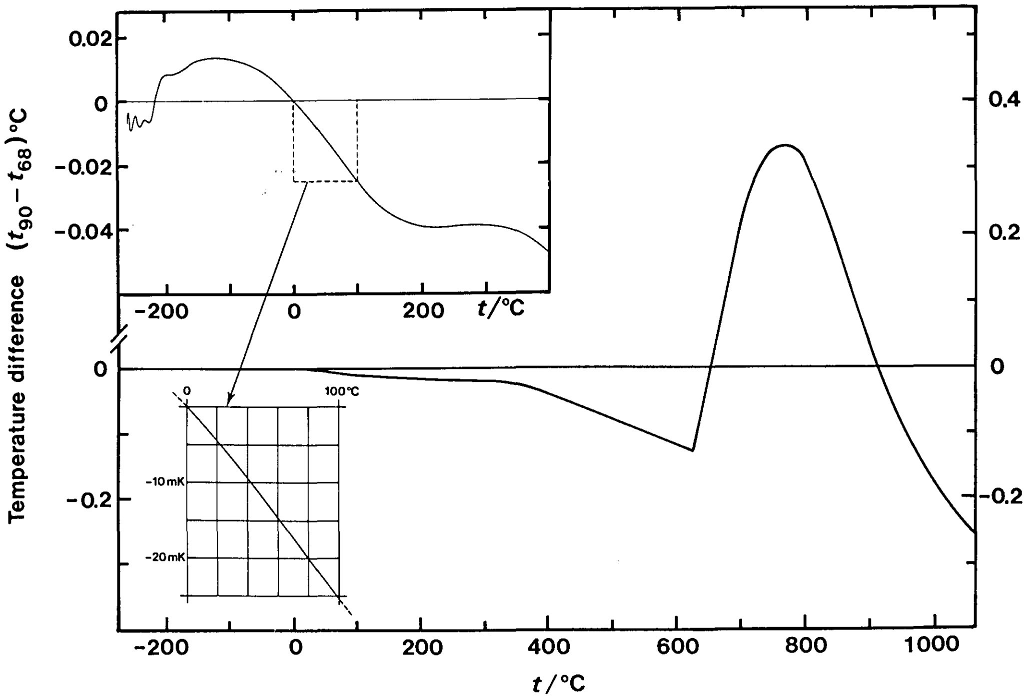

Figure 1. Differences between t_{90} and t_{68} as a function of t_{90} (expressed as t).

from that on the IPTS-68(75)) and the reference standards will be unaffected. For more details on the effects of the change of the temperature scale on electrical standards, see National Institute of Standards and Technology (NIST) Technical Note 1263 [4].

In addition to the effect on reference standards for measurements, all temperature-sensitive properties that are presently expressed on the IPTS-68(75) may be affected and may require changes in values.

For details on realizations and approximations of the ITS-90, see NIST Technical Note 1265 [9].

2. CCT's 17th Session Principal Decisions

2.1 Definition of the ITS-90

The ITS-90 was designed by the CCT in such a manner that temperature values obtained on it do not deviate from the Kelvin thermodynamic temperature values by more than the uncertainties of the latter values at the time the ITS-90 was adopted. Thermodynamic temperature is indicated by the symbol T and has the unit known as the kelvin, symbol K. The size of the kelvin is defined to be 1/273.16 of the thermodynamic temperature of the triple point of water.

Temperatures on the ITS-90 can be expressed in terms of the International Kelvin Temperatures, with the symbol T_{90}, or in terms of the International Celsius Temperatures, with the symbol t_{90}. The unit of the temperature T_{90} is the kelvin, symbol K, and the unit of the temperature t_{90} is the degree Celsius, symbol °C. The relation between T_{90} and t_{90} is:

$$t_{90}/°\mathrm{C}=T_{90}/\mathrm{K}-273.15. \qquad (1)$$

The ITS-90 has alternative definitions of T_{90} in certain temperature ranges and they have equal status. In measurements of the highest precision made at the same temperature, the alternative definitions may yield detectably different temperature values. Also, at any given temperature between defining fixed points, different interpolating thermometers that meet the specifications of the ITS-90 may indicate different temperature values. The magnitude of the differences resulting from these two sources, however, is sufficiently small to be negligible for all practical purposes.

Temperatures on the ITS-90 are defined in terms of equilibrium states of pure substances (defining fixed points), interpolating instruments, and equations that relate the measured property to T_{90}. The defining equilibrium states of the pure substances and the assigned temperatures are listed in table 1.

Table 1. Defining fixed points of the ITS-90

Material[a]	Equilibrium state[b]	Temperature T_{90} (K)	t_{90} (°C)
^{3}He and ^{4}He	VP	3 to 5	−270.15 to −268.15
e-H_2	TP	13.8033	−259.3467
e-H_2 (or He)	VP (or CVGT)	≈17	≈−256.15
e-H_2 (or He)	VP (or CVGT)	≈20.3	≈−252.85
Ne[c]	TP	24.5561	−248.5939
O_2	TP	54.3584	−218.7916
Ar	TP	83.8058	−189.3442
Hg[c]	TP	234.3156	−38.8344
H_2O	TP	273.16	0.01
Ga[c]	MP	302.9146	29.7646
In[c]	FP	429.7485	156.5985
Sn	FP	505.078	231.928
Zn	FP	692.677	419.527
Al[c]	FP	933.473	660.323
Ag	FP	1234.93	961.78
Au	FP	1337.33	1064.18
Cu[c]	FP	1357.77	1084.62

[a] e-H_2 indicates equilibrium hydrogen, that is, hydrogen with the equilibrium distribution of its ortho and para states. Normal hydrogen at room temperture contains 25% para hydrogen and 75% ortho hydrogen.

[b] VP indicates vapor pressure point; CVGT indicates constant volume gas thermometer point; TP indicates triple point (equilibrium temperature at which the solid, liquid and vapor phases coexist); FP indicates freezing point and MP indicates melting point (the FP and the MP are equilibrium temperatures at which the solid and liquid phases coexist under a pressure of 101 325 Pa, one standard atmosphere). The isotopic composition is that naturally occurring.

[c] Previously, these were secondary fixed points.

Table 2. Values of the coefficients A_i, and of the constants A_0, B, and C for the ^{3}He and ^{4}He vapor pressure equations and the temperature range for which each equation is valid

Coef. or constant	^{3}He 0.65 to 3.2 K	^{4}He 1.25 to 2.1768 K	^{4}He 2.1768 to 5.0 K
A_0	1.053 447	1.392 408	3.146 631
A_1	0.980 106	0.527 153	1.357 655
A_2	0.676 380	0.166 756	0.413 923
A_3	0.372 692	0.050 988	0.091 159
A_4	0.151 656	0.026 514	0.016 349
A_5	−0.002 263	0.001 975	0.001 826
A_6	0.006 596	−0.017 976	−0.004 325
A_7	0.088 966	0.005 409	−0.004 973
A_8	−0.004 770	0.013 259	0
A_9	−0.054 943	0	0
B	7.3	5.6	10.3
C	4.3	2.9	1.9

2.1.1 Temperature Range From 0.65 to 5.0 K

Between 0.65 and 3.2 K, the ITS-90 is defined by the vapor pressure-temperature relation of ^{3}He, and between 1.25 and 2.1768 K (the λ point) and between 2.1768 and 5.0 K by the vapor pressure-temperature relations of ^{4}He. T_{90} is defined by the vapor pressure equations of the form:

$$T_{90}/\mathrm{K}=A_0+\sum_{i=1}^{9} A_i[(\ln(p/\mathrm{Pa})-B)/C]^i, \tag{2}$$

with the values of the coefficients A_i, and of the constants A_0, B, and C of the equations being specified, and given in table 2.

2.1.2 Temperature Range From 3.0 to 24.5561 K

Between 3.0 and 24.5561 K, the ITS-90 is defined in terms of the ^{3}He or ^{4}He constant volume gas thermometer (CVGT). The thermometer is calibrated at three temperatures—at the triple point of neon (24.5561 K), at the triple point of equilibrium hydrogen (see footnote a in table 1) (13.8033 K), and at a temperature between 3.0 and 5.0 K, the value of which is determined by using either ^{3}He or ^{4}He vapor pressure thermometry.

For a ^{4}He CVGT used between 4.2 K and the triple point of neon (24.5561 K), T_{90} is defined by the equation:

$$T_{90}=a+bp+cp^2, \tag{3}$$

where p is the CVGT pressure and a, b, and c are coefficients that are determined by calibration at the three specified temperatures, but with the additional requirement that the calibration with the vapor pressure thermometer be made at a temperature between 4.2 and 5.0 K.

For a ^{4}He CVGT used between 3.0 and 4.2 K, and for a ^{3}He CVGT used from 3.0 to 24.5561 K, the non-ideality of the gas must be taken into account, using the appropriate second virial coefficient, $B_4(T_{90})$ or $B_3(T_{90})$. T_{90} is defined in this range by the equation:

$$T_{90}=\frac{a+bp+cp^2}{1+B_x(T_{90})N/V}, \tag{4}$$

where p is the CVGT pressure; a, b, and c are coefficients that are determined from calibration at the three defining temperatures; $B_x(T_{90})$ refers to $B_3(T_{90})$ or $B_4(T_{90})$; and N/V is the gas density in moles per cubic meter in the CVGT bulb. The values of the second virial coefficients at any given temperature are to be calculated according to equations specified in the official document of the ITS-90 (and also in the NIST Technical Note 1265 [9]).

2.1.3 Temperature Range From 13.8033 to 1234.93 K Between 13.8033 K (−259.3467 °C) and 1234.93 K (961.78 °C), the ITS-90 is defined in terms of the specified fixed points given in table 1, by resistance ratios of platinum resistance thermometers (PRTs) obtained by calibration at specified sets of the fixed points, and by reference functions and deviation functions of resistance ratios which relate to T_{90} between the fixed points.

Temperatures on the ITS-90 are expressed in terms of the ratio $W(T_{90})$ of the resistance $R(T_{90})$ at temperature T_{90} and the resistance $R(273.16\text{ K})$ at the triple point of water, i.e.,

$$W(T_{90})=R(T_{90})/R(273.16\text{ K}). \qquad (5)$$

For a PRT to be an acceptable instrument of the ITS-90, its coil must be made from pure platinum and be strain-free. Additionally, the finished PRT must meet one of the following criteria:

$$W(302.9146\text{ K}) \geqslant 1.118\,07 \qquad (6)$$

$$W(234.3156\text{ K}) \leqslant 0.844\,235. \qquad (7)$$

An acceptable PRT that is to be used to the freezing point of silver must meet the following requirement also:

$$W(1234.93\text{ K}) \geqslant 4.2844. \qquad (8)$$

The temperature T_{90} is calculated from the resistance ratio relation:

$$W(T_{90})-W_r(T_{90})=\Delta W(T_{90}), \qquad (9)$$

where $W(T_{90})$ is the observed value, $W_r(T_{90})$ is the value calculated from the reference function, and $\Delta W(T_{90})$ is the deviation of the observed $W(T_{90})$ value of the particular PRT from the reference function value at T_{90}.

There are two reference functions $W_r(T_{90})$, one for the range 13.8033 to 273.16 K and the second for the range 273.15 to 1234.93 K. The deviation $\Delta W(T_{90})$ is obtained as a function of T_{90} for various ranges by calibration at specified fixed points. The form of the deviation function depends upon the temperature range of calibration.

2.1.4 Temperature Subrange From 13.8033 to 273.16 K In the range 13.8033 to 273.16 K, the equation for the reference function $W_r(T_{90})$ as a function of T_{90} is given by:

$$\ln[W_r(T_{90})]=A_0+\sum_{i=1}^{12} A_i\{[\ln(T_{90}/273.16\text{ K}) + 1.5]/1.5\}^i. \qquad (10)$$

The specified inverse of this equation, equivalent to within ±0.000 1 K, is:

$$T_{90}/273.16\text{ K}=B_0+\sum_{i=1}^{15} B_i\left(\frac{[W_r(T_{90})]^{1/6}-0.65}{0.35}\right)^i. \qquad (11)$$

The values of the constants A_0 and B_0 and values of the coefficients A_i and B_i of the two equations are listed in table 3.

Table 3. Values of the coefficients A_i, B_i, C_i, and D_i and of the constants A_0, B_0, C_0, and D_0 in the reference functions, eqs (10) and (18), and in the inverse functions approximating them, given by eqs (11) and (19)

Constant or coefficient	Value	Constant or coefficient	Value
A_0	−2.135 347 29	B_0	0.183 324 722
A_1	3.183 247 20	B_1	0.240 975 303
A_2	−1.801 435 97	B_2	0.209 108 771
A_3	0.717 272 04	B_3	0.190 439 972
A_4	0.503 440 27	B_4	0.142 648 498
A_5	−0.618 993 95	B_5	0.077 993 465
A_6	−0.053 323 22	B_6	0.012 475 611
A_7	0.280 213 62	B_7	−0.032 267 127
A_8	0.107 152 24	B_8	−0.075 291 522
A_9	−0.293 028 65	B_9	−0.056 470 670
A_{10}	0.044 598 72	B_{10}	0.076 201 285
A_{11}	0.118 686 32	B_{11}	0.123 893 204
A_{12}	−0.052 481 34	B_{12}	−0.029 201 193
		B_{13}	−0.091 173 542
		B_{14}	0.001 317 696
		B_{15}	0.026 025 526
C_0	2.781 572 54	D_0	439.932 854
C_1	1.646 509 16	D_1	472.418 020
C_2	−0.137 143 90	D_2	37.684 494
C_3	−0.006 497 67	D_3	7.472 018
C_4	−0.002 344 44	D_4	2.920 828
C_5	0.005 118 68	D_5	0.005 184
C_6	0.001 879 82	D_6	−0.963 864
C_7	−0.002 044 72	D_7	−0.188 732
C_8	−0.000 461 22	D_8	0.191 203
C_9	0.000 457 24	D_9	0.049 025

If the PRT is to be used throughout the range from 13.8033 to 273.16 K, it must be calibrated at the triple points of equilibrium hydrogen (13.8033 K), neon (24.5561 K), oxygen (54.3584 K), argon (83.8058 K), mercury (234.3156 K), and water (273.16 K) and at two additional temperatures very close to 17.0 and 20.3 K. The temperatures of calibration at 17.0 and 20.3 K may be determined by using either a CVGT or the vapor pressure-temperature relation of equilibrium hydrogen. When the CVGT is used, the two temperatures must be within the ranges 16.9 to 17.1 K and 20.2 to 20.4 K, respectively. When the equilibrium hydrogen vapor pressure thermometer is used, the two temperatures must be within the ranges 17.025 to 17.045 K and 20.26 to 20.28 K, respectively. The temperatures of the equilibrium hydrogen vapor pressure thermometer are determined from the values of the hydrogen vapor pressure, p, and the equations:

$$T_{90}/\mathrm{K}-17.035=(p/\mathrm{kPa}-33.3213)/13.32 \qquad (12)$$

$$T_{90}/\mathrm{K}-20.27=(p/\mathrm{kPa}-101.292)/30. \qquad (13)$$

Depending upon the temperature range of application, PRTs may be calibrated from 273.16 K down to 13.8033 K (triple point of equilibrium hydrogen), down to 24.5561 K (triple point of neon), down to 54.3584 K (triple point of oxygen), or down to 83.8058 K (triple point of argon).

The deviation function for calibration in the range 13.8033 to 273.16 K is given by the relation:

$$\Delta W_1(T_{90})=W(T_{90})-W_r(T_{90})=a_1[W(T_{90})-1]$$
$$+b_1[W(T_{90})-1]^2+\sum_{i=1}^{5} c_i[\ln W(T_{90})]^{i+n}, \qquad (14)$$

with $n=2$. The coefficients a_1, b_1, and the five c_i's of the deviation function are obtained by calibration at all of the above eight temperatures, including that at the triple point of water. The values of $W_r(T_{90})$ are obtained from the reference function for this range. Although the official text of the ITS-90 does not assign subscripts to the coefficients a and b, nor does it designate the deviation equations by the symbols $\Delta W_m(T_{90})$, where in eq (14) $m=1$, these designations will be used in this paper for clarity and for ease of reference. In any case, some such terminology must be used in PRT calibration reports and this was chosen for convenience.

2.1.5 Subrange From 24.5561 to 273.16 K The deviation function for calibration in this range is given by the relation:

$$\Delta W_2(T_{90})=W(T_{90})-W_r(T_{90})=a_2[W(T_{90})-1]$$
$$+b_2[W(T_{90})-1]^2+\sum_{i=1}^{3} c_i[\ln W(T_{90})]^{i+n}, \qquad (15)$$

where the exponent n has the value $n=0$. The coefficients a_2, b_2, and c_i of this deviation function are obtained by calibrating the PRT at the triple points of equilibrium hydrogen (13.8033 K), neon (24.5561 K), oxygen (54.3584 K), argon (83.8058 K), mercury (234.3156 K) and water (273.16 K). The values of $W_r(T_{90})$ are obtained from the reference function.

2.1.6 Subrange From 54.3584 to 273.16 K The deviation function for calibration in this range is given by the relation:

$$\Delta W_3(T_{90})=a_3[W(T_{90})-1]+b_3[W(T_{90})-1]^2$$
$$+c_1[\ln W(T_{90})]^{1+n}, \qquad (16)$$

where the exponent n has the value $n=1$. The coefficients a_3, b_3, and c_1 of this deviation function are obtained by calibrating the PRT at the triple points of oxygen (54.3584 K), argon (83.8058 K), mercury (234.3156 K), and water (273.16 K). The values of $W_r(T_{90})$ are obtained from the reference function.

2.1.7 Subrange From 83.8058 to 273.16 K The deviation function for calibration in this range is given by the relation:

$$\Delta W_4(T_{90})=a_4[W(T_{90})-1]$$
$$+b_4[W(T_{90})-1]\ln W(T_{90}). \qquad (17)$$

The coefficients a_4 and b_4 of this deviation function are obtained by calibrating the PRT at the triple points of argon (83.8058 K), mercury (234.3156 K), and water (273.16 K). The values of $W_r(T_{90})$ are obtained from the reference function.

2.1.8 Temperature Subrange From 273.15 to 1234.93 K In the range 273.15 to 1234.93 K, the equation for the reference function $W_r(T_{90})$ is given by:

$$W_r(T_{90})=C_0+\sum_{i=1}^{9} C_i\left(\frac{T_{90}/\mathrm{K}-754.15}{481}\right)^i. \qquad (18)$$

The specified inverse of this equation, equivalent to within ±0.000 13 K, is:

$$T_{90}/\mathrm{K}-273.15=D_0+\sum_{i=1}^{9} D_i\left(\frac{W_r(T_{90})-2.64}{1.64}\right)^i. \qquad (19)$$

The values of the constants C_0 and D_0 and of the coefficients C_i and D_i for these equations are listed in table 3.

If the PRT is to be used over this entire subrange (273.15 to 1234.93 K), it must be calibrated at the triple point of water (273.16 K) and at the freezing points of tin (505.078 K), zinc (692.677 K), aluminum (933.473 K), and silver (1234.93 K).

The deviation function is given by the relation:

$$\Delta W_6(T_{90}) = W(T_{90}) - W_r(T_{90}) = a_6[W(T_{90})-1] + b_6[W(T_{90})-1]^2 + c_6[W(T_{90})-1]^3 + d[W(T_{90}) - W(933.473\ \mathrm{K})]^2. \quad (20)$$

The values of the coefficients a_6, b_6, and c_6 are determined from the measured deviations $\Delta W(T_{90})$ of $W(T_{90})$ from the reference values $W_r(T_{90})$ at the freezing points of tin (505.078 K), zinc (692.677 K) and aluminum (933.473 K). The coefficient d is determined from these values of the coefficients a_6, b_6, and c_6 and the deviation $\Delta W(T_{90})$ of $W(T_{90})$ from the reference value $W_r(T_{90})$ at the freezing point of silver. The coefficient d in this equation is used only for those temperature measurements in the range from the freezing point of aluminum to the freezing point of silver. For temperature measurements below the freezing point of aluminum, $d=0$.

PRTs may be calibrated for use over the whole range (273.15 to 1234.93 K) or for shorter ranges by calibrations at fixed points between 273.15 K and the upper limit of 933.473 K (freezing point of aluminum, 660.323 °C), of 692.677 K (freezing point of zinc, 419.527 °C), of 505.078 K (freezing point of tin, 231.928 °C), of 429.7485 K (freezing point of indium, 156.5985 °C), or of 302.9146 K (melting point of gallium, 29.7646 °C).

2.1.9 Subrange From 273.15 to 933.473 K For application in this range, the PRT is calibrated at the triple point of water (273.16 K), and at the freezing points of tin (505.078 K), zinc (692.677 K), and aluminum (933.473 K). The deviation function is given by the relation:

$$\Delta W_7(T_{90}) = a_7[W(T_{90})-1] + b_7[W(T_{90})-1]^2 + c_7[W(T_{90})-1]^3. \quad (21)$$

The coefficients a_7, b_7, and c_7, identical to a_6, b_6, and c_6, respectively, are determined from the deviations $\Delta W(T_{90})$ of $W(T_{90})$ from the reference values $W_r(T_{90})$ at the freezing points of tin (505.078 K), zinc (692.677 K), and aluminum (933.473 K).

2.1.10 Subrange From 273.15 to 692.677 K For application in this range, the PRT is calibrated at the triple point of water (273.16 K), and at the freezing points of tin (505.078 K) and zinc (692.677 K). The deviation function is given by the relation:

$$\Delta W_8(T_{90}) = a_8[W(T_{90})-1] + b_8[W(T_{90})-1]^2. \quad (22)$$

The coefficients a_8 and b_8 are determined from the deviations $\Delta W(T_{90})$ of $W(T_{90})$ from the reference values $W_r(T_{90})$ at the freezing points of tin (505.078 K) and zinc (692.677 K).

2.1.11 Subrange From 273.15 to 505.078 K For application in this range, the PRT is calibrated at the triple point of water (273.16 K), and at the freezing points of indium (429.7485 K) and tin (505.078 K). The form of the deviation function is the same as that for the subrange 273.15 to 692.677 K, i.e.,

$$\Delta W_9(T_{90}) = a_9[W(T_{90})-1] + b_9[W(T_{90})-1]^2. \quad (23)$$

The coefficients a_9 and b_9 are determined from the deviations $\Delta W(T_{90})$ of $W(T_{90})$ from the reference values $W_r(T_{90})$ at the freezing points of indium (429.7485 K) and tin (505.078 K).

2.1.12 Subrange From 273.15 to 429.7485 K For application in this range, the PRT is calibrated at the triple point of water (273.16 K) and at the freezing point of indium (429.7485 K). The deviation function is:

$$\Delta W_{10}(T_{90}) = a_{10}[W(T_{90})-1]. \quad (24)$$

The coefficient a_{10} is determined from the deviation $\Delta W(T_{90})$ of $W(T_{90})$ from the reference value $W_r(T_{90})$ at the freezing point of indium (429.7485 K).

2.1.13 Subrange From 273.15 to 302.9146 K For application in this range, the PRT is calibrated at the triple point of water (273.16 K) and at the melting point of gallium (302.9146 K). The deviation function is:

$$\Delta W_{11}(T_{90}) = a_{11}[W(T_{90})-1]. \quad (25)$$

The coefficient a_{11} is determined from the deviation $\Delta W(T_{90})$ of $W(T_{90})$ from the reference value $W_r(T_{90})$ at the melting point of gallium (302.9146 K).

2.1.14 Subrange From 234.3156 to 302.9146 K For application in this range, the PRT is calibrated at the triple points of mercury (234.3156 K) and water (273.16 K), and at the melting point of gallium (302.9146 K). The form of the deviation function is the same as that for the subrange 273.15 to 692.677 K, i.e.,

$$\Delta W_5(T_{90})=a_5[W(T_{90})-1]+b_5[W(T_{90})-1]^2. \quad (26)$$

The coefficients a_5 and b_5 are determined from the deviations $\Delta W(T_{90})$ of $W(T_{90})$ from the reference values $W_r(T_{90})$ at the triple point of mercury (234.3156 K) and at the melting point of gallium (302.9146 K). The reference values $W_r(T_{90})$ must be calculated from the relevant reference function, both reference functions being required to cover this range.

2.1.15 Temperature Range Above 1234.93 K At temperatures above 1234.93 K, T_{90} is defined by the relation:

$$\frac{L_\lambda(T_{90})}{L_\lambda[T_{90}(\mathrm{X})]}=\frac{\exp[c_2/\lambda T_{90}(\mathrm{X})]-1}{\exp[c_2/\lambda T_{90}]-1}, \quad (27)$$

in which $L_\lambda(T_{90})$ and $L_\lambda[T_{90}(\mathrm{X})]$ are the spectral concentrations of the radiance of a blackbody at wavelength λ (in vacuum) at T_{90} and at $T_{90}(\mathrm{X})$, respectively. $T_{90}(\mathrm{X})$ refers to either the silver freezing point [$T_{90}(\mathrm{Ag})=1234.93$ K], the gold freezing point [$T_{90}(\mathrm{Au})=1337.33$ K] or the copper freezing point [$T_{90}(\mathrm{Cu})=1357.77$ K]. $c_2=0.014388$ m·K. Although the freezing-point temperature of silver is the junction point of platinum resistance thermometry and radiation thermometry, it is believed that the T_{90} values of the freezing points of silver, gold and copper are sufficiently self-consistent that the use of any one of them as the reference temperature $T_{90}(\mathrm{X})$ will not result in any significant difference in the measured values of T_{90} from what would be obtained if only the silver freezing point were used.

2.2 Recommendations of the CCT

Three recommendations were adopted by the CCT at its 17th Session. These recommendations were considered by the CIPM and Recommendation T1 (1989) of the CCT was adopted as Recommendation 5 (CI-89) of the CIPM. Recommendations T2 (1989) and T3 (1989) of the CCT were noted by the CIPM as CCT recommendations. The CCT recommendations were as follows:

Recommendation T1 (1989)

The International Temperature Scale of 1990

The Comité Consultatif de Thermométrie (CCT) acting in accordance with Resolution 7 of the 18^e CGPM has generated the International Temperature Scale of 1990 (ITS-90) in order to supersede the International Practical Temperature Scale of 1968 (IPTS-68).

The CCT notes that, by comparison with the IPTS-68, the ITS-90

—extends to lower temperatures, down to 0.65 K, and hence also supersedes the EPT-76,

—is in substantially better agreement with corresponding thermodynamic temperatures,

—has much improved continuity, precision, and reproducibility throughout its range and

—has subranges and alternative definitions in certain ranges which greatly facilitate its use.

The CCT also notes that, to accompany the text of the ITS-90 there will be two further documents, the Supplementary Information for the ITS-90 and Techniques for Approximating the ITS-90. These documents will be published by the BIPM and periodically updated.

The CCT recommends

—that on January 1, 1990 the ITS-90 come into force and

—that from this same date the IPTS-68 and the EPT-76 be abrogated.

Recommendation T2 (1989)

Reference Tables for Thermocouples and Industrial Platinum Resistance Thermometers

The Comité Consultatif de Thermométrie,

considering

—that the introduction of the International Temperature Scale of 1990 (ITS-90) will lead to an urgent requirement for new reference tables for both thermocouples and industrial platinum resistance thermometers,

requests its Working Group 2

—to collaborate with national laboratories in the rapid preparation of new reference tables taking into account not only the change from IPTS-68 to ITS-90 but also new information on the behavior of thermocouples and industrial platinum resistance thermometers,

recommends

—that these new tables be used as the basis for new national and international reference tables for thermocouples and industrial platinum resistance thermometers and

—that meanwhile the existing reference tables based upon IPTS-68 should be used in conjunction with the table of differences $T_{90}-T_{68}$ which appears in the ITS-90.

(Note: the table of differences $T_{90}-T_{68}$ referred to here may be obtained also from NIST from the author of this article).

Recommendation T3 (1989)

The Uncertainty Inherent in the Realization of the International Temperature Scale of 1990

The Comité Consultatif de Thermométrie,

considering the requirement for assigning an uncertainty to the numerical value of any temperature on the International Temperature Scale of 1990 (ITS-90),

encourages national laboratories to

a) quantify the uncertainties in the fixed point realizations,

b) quantify the uncertainties resulting from the use of the specified interpolating instruments of ITS-90,

c) develop the mathematical procedures describing the propagation of these uncertainties to any intermediate temperature.

3. Conclusion

Although the uncertainties in the values of thermodynamic temperatures above 100 °C used in the definition of the ITS-90 were larger than desired and larger than had been anticipated a few years ago, the agreement of temperatures on the ITS-90 with thermodynamic temperatures is nevertheless a significant improvement over that of previous scales. The replacement of the thermocouple with the platinum resistance thermometer as the standard instrument of the scale at temperatures in the IPTS-68(75) range from 630.74 to 961.93 °C has improved the reproducibility over that of the IPTS-68(75) significantly. Also, advances in radiometric techniques have improved the precision of measurements in radiation thermometry. The precision of the scale, or what has been called the non-uniqueness of the scale, is significantly improved over that of the IPTS-68(75), as is also the scale's continuity. The extension of the scale downward in temperature to 0.65 K and the use of subranges over which thermometers may be calibrated make the ITS-90 more useful and much more flexible than were the previous scales.

About the author: B. W. Mangum, a physicist, is a Group Leader in the Temperature and Pressure Division of the NIST Center for Chemical Technology and is the NIST representative to the Comité Consultatif de Thermométrie.

4. References

[1] BIPM Com. Cons. Thermométrie **17**, 1989, in press.
[2] The International Temperature Scale of 1990, Metrologia **27**, 3 (1990).
[3] Procès-Verbaux des séances du Comité International des Poids et Mesures, (78^{e} session, octobre 1989), in press.
[4] Belecki, N. B., Dziuba, R. F., Field, B. F., and Taylor, B. N., Guidelines for Implementing the New Representations of the Volt and Ohm Effective January 1, 1990, NIST Technical Note 1263 (June 1989).
[5] The International Temperature Scale of 1968, Amended Edition of 1975, Metrologia **12**, 7 (1976).
[6] The 1976 Provisional 0.5 K to 30 K Temperature Scale, Metrologia **15**, 65 (1979).
[7] Comptes rendus des séances de la dix-huitième Conférence Générale des Poids et Mesures, Resolution 7 (1987).
[8] Quinn, T. J., Metrologia **26**, 69 (1989).
[9] Mangum, B. W., and Furukawa, G. T., Guidelines for Realizing the International Temperature Scale of 1990, NIST Technical Note 1265 (1990), in press.

Volume 95, Number 1, January-February 1990
Journal of Research of the National Institute of Standards and Technology

[J. Res. Natl. Inst. Stand. Technol. **95**, 79 (1990)]

New Assignment of Mass Values and Uncertainties to NIST Working Standards

Volume 95 | Number 1 | January-February 1990

Richard S. Davis

National Institute of Standards and Technology,
Gaithersburg, MD 20899

For some time it had been suspected that values assigned to NIST working standards of mass were some 0.17 mg/kg larger than mass values based on artifacts representing mass in the International System of Units (SI). This relatively small offset, now confirmed, has had minimal scientific or technological significance. The discrepancy was removed on January 1, 1990. We document the history of the discrepancy, the studies which allow its removal, and the methods in place to limit its effect and prevent its recurrence. For routine calibrations, we believe that our working standards now have a long-term stability of 0.033 mg/kg (3σ) with respect to the national prototype kilograms of the United States. We provisionally admit an additional uncertainty of 0.09 mg/kg (3σ), systematic to all NIST mass measurements, which represents the possible offset of our primary standards from standards maintained by the Bureau International des Poids et Mesures (BIPM). This systematic uncertainty may be significantly reduced after analysis of results from the 3rd verification of national prototype kilograms, which is now underway.

Key words: calibration; international standards; kilogram; mass; national standards; SI; standards.

Accepted: January 6, 1990

1. Introduction

The kilogram (kg) is one of the seven base units which form the foundation of the Système International d'Unités or International System of Units, abbreviated SI. Used world wide to express the results of physical measurements, the SI specifies that the kilogram is the unit of mass and that the mass of the International Prototype Kilogram exactly equals 1 kg. The International Prototype referred to in the definition is a cylinder made of an alloy of platinum and iridium and stored at the International Bureau of Weights and Measures (BIPM) in France. The kilogram is thus the only remaining base unit of the SI to rely on an artifact for its definition.

When the SI was established, replicas of the International Prototype were manufactured by the BIPM for use as national prototype kilograms. At long intervals, the national prototypes are returned to the BIPM where their assigned mass is verified by measurements directly traceable to the International Prototype [1]. It was intended by the founders of the SI that the national prototype kilograms would be the primary mass standards within each country. There are, however, several practical difficulties with this scheme. The following discusses the reasons for these difficulties and the steps we have taken to overcome them.

In order for the kilogram unit to be useful, methods must exist to measure multiples and submultiples of 1-kg standards. These methods, when successful, rely on good equipment and sound experimental practice. In addition to these, a calibration service requires rigorous tests to maintain statistical control of the measurement process. At NIST, statistical rigor was introduced in the 1960s through the pioneering work of Pontius and Cameron [2]. Present methods are simply refinements of the system which they established.

The uncertainty of a 1-kg standard, expressed as a dimensionless ratio, propagates directly to mass values of multiples and submultiples derived from the standard. For example, if a kilogram standard has a relative uncertainty of 1 ppm[1], all multiples and submultiples derived from the standard will have an uncertainty component of 1 ppm propagated from the standard. In the field of precision measurement, uncertainty is usually reported at an estimated level of 1 standard deviation. All uncertainties are combined by the root-sum-square (RSS) method according to guidelines recommended by the International Committee for Weights and Measures (CIPM) [3]. In NIST calibration reports, on the other hand, uncertainties are estimated at a level of 3 standard deviations. Furthermore, any uncertainty deemed "systematic" to a series of measurements is added directly to the "random" uncertainties, which are combined by RSS. However, in the rest of this paper, we follow the CIPM recommendations unless otherwise noted.

In addition to the SI, the United States recognizes the U.S. Customary System of units for legal metrology. In this system, the avoirdupois pound (lb) is the unit of mass. It is, by definition, exactly equal to 0.45359237 kg.

2. History of NIST Mass Standards Before 1980

2.1 Primary Mass Standards of Platinum-Iridium

Kilograms K20 and K4 are the two national prototypes of the United States. Kilogram K20 has historically been considered the primary U.S. kilogram standard with K4 being relegated to use as a "check standard." The history of these two artifacts through 1985 has already been documented in a previous report [1]. One important question which remained open in [1] is whether the mass values assigned by BIPM to their working standards have been consistent with the SI definition of mass. The cause for concern was that the embodiment of the SI definition, the International Prototype Kilogram, had not been used since 1946. This situation has changed within the past year as BIPM embarked on only the third calibration of national prototype kilograms since 1889. Preliminary results obtained by BIPM as a part of the 3rd verification confirm the long-term stability of their working standards to within required limits [4].

2.2 Secondary Mass Standards

Platinum-iridium alloy (approximate density 21,500 kg·m^{-3}) is too expensive a material for widespread use. At present, stable alloys of non-magnetic stainless steel (approximate density 8,000 kg·m^{-3}) are usually specified for use as secondary standards. Before such alloys were available, practical standards were typically made of plated brass (approximate density 8,400 kg·m^{-3}). The densities of these alloys assume importance because mass metrology is almost always performed in the ambient air (density ca. 1.2 kg·m^{-3}) using balances which are, in essence, force or torque transducers. The effect of air buoyancy thus becomes a confounding influence which must be removed by correction.

The size of the necessary buoyancy correction relative to the mass of interest is given by:

$$(1-\rho_a/\rho_s)/(1-\rho_a/\rho_x)-1\approx\rho_a(1/\rho_x-1/\rho_s), \qquad (1)$$

where ρ_a = ambient air density
ρ_s = density of the known standard
ρ_x = density of the unknown secondary standard.

Equation (1) makes clear that, when comparing weights of nearly equal density, the importance of the correction is relatively small. Buoyancy corrections are typically 10 ppm between alloys of stainless steel and brass; corrections of less than 5 ppm are typical for comparisons between various alloys of non-magnetic stainless steel. (Specifications for the highest quality analytical weights limit the alloy density to within a narrow range in order to ensure that buoyancy corrections between nominally equal weights will be small.)

By contrast, the buoyancy correction between (i) primary standards of platinum-iridium alloy and (ii) secondary standards of brass or stainless steel typically ranges from 87–97 ppm. In our laboratory, the densities of secondary kilogram standards are determined by hydrostatic weighing. The density of ambient air is now determined from the CIPM-1981 equation-of-state for moist air [5]. The latter requires knowledge of ambient temperature, barometric pressure, relative humidity, and carbon-

---

[1] 1 ppm = 1 part per million = 1×10^{-6}.

dioxide level. A discussion of the accuracy which can be expected from buoyancy corrections in our laboratory is given in [1].

The above considerations dictate that calibrations carried out by NIST on a routine basis be performed with secondary standards having a density near to that of the unknown weight.

2.2.1 N_1 and N_2 Two weights, designated N_1 and N_2, have served as NIST secondary standards of mass since 1965. The weights were fabricated in 1948 of a nickel-chromium alloy having a nominal density of 8,340 kg·m^{-3}, which is close to that of the brass weights which were then in common use. These weights were given an initial calibration in terms of a platinum-iridium prototype (K4) in 1948. They were recalibrated against both K20 and K4 in 1958. The newer calibration gave mass values which were systematically higher by about 0.06 mg/kg. There is no indication in the existing records what, if any, uncertainty was assigned to either calibration. When, in 1965, N_1 and N_2 were placed in service as secondary mass standards, the mass assigned to them was based on selected data from the 1958 series of measurements. Presumably, this decision was made because the 1958 measurements were performed by remote control on a two-pan, Rueprecht balance having a standard deviation below 0.02 mg. By 1965, this device had been replaced by a single-pan balance which was much more convenient to use but which had an inferior standard deviation of about 0.15 mg. Further, remote weighing was not possible on the single-pan balance.

Based on the 1958 measurements, the mass of N_1 and N_2 taken together was calculated to be:

$$R=2\ \text{kg}-10.059\ \text{mg}.$$

The difference in mass between N_1 and N_2 was calculated by pooling a large amount of data:

$$C=-19.476\ \text{mg}.$$

These two numbers, R and C, fix the individual values of each kilogram. The uncertainty in C is largely statistical in nature. It depends almost entirely on the standard deviation of the balance used to compare the mass of N_1 with N_2. Thus its uncertainty could be rigorously assigned. In addition, the significance of any measured change in C could also be determined.

The uncertainty of R was much more problematic. The statistical component of this uncertainty resulting from the balance used in the measurements may, of course, be calculated. There are at least two additional components which increase the uncertainty of R (but not of C):

1. The uncertainty in the accepted mass of K20 with respect to the International Prototype Kilogram.
2. The accuracy of the correction for air buoyancy between the platinum-iridium and the nichrome kilograms.

Rather than base an estimate of these uncertainties on what was considered insufficient metrological data, calibration reports prior to January 1, 1990 state:

"It is assumed that the present 'accepted values' of the two NIST standards at the 1 kilogram level, designated N_1 and N_2, are without error. Estimates of the uncertainty of the accepted values of the NIST standards relative to the International Prototype Kilogram can be provided on request. However, these estimates have no real meaning in either national or international comparison. This is because of the lack of sufficient data to provide a realistic estimate of the uncertainty in the values assigned to the prototype kilograms K20 and K4, particularly in regard to long term, or between-run variability. Changes in the accepted values for the NIST standards at the kilogram level, as and when they occur, will be reported in the scientific papers of the Bureau and will be given wide distribution..."

Except for the change in name of the institution, the above wording had been in place at least since 1967. The reports of that time (and well beyond) also referenced a technical note entitled "The Accepted Values of the NBS Standards at the 1 kg Level and Associated Uncertainty Estimates," to be published at a future date. Unfortunately, this note was never produced. Section 3 of the present paper may therefore be regarded as fulfilling a promise of long standing.

In looking over calibration documentation extending back 25 years, it seems that the original intention was to reserve N_1 and N_2 for calibration of other working standards of similar density. These working standards would be used in routine calibration work and thereby would spare N_1 and N_2 from excessive wear. But the calibration of working standards of 1 kg could only be done on the single-pan balance mentioned above. Thus working standards would be assigned an uncertainty which was large relative to the precision of commercially available balances unless the calibration were based on the average of many measurements. But the latter strategy would no longer spare N_1 and N_2 from excessive use.

Faced with this problem, N_1 and N_2 began to be used as working standards themselves in routine calibrations. They were never cleaned (except for gentle dusting with a brush) in order to prevent discontinuous changes in their mass. It was, of course, recognized that checks must be established to ensure the constancy of the mass assigned to the summation of N_1 and N_2. Two criteria were routinely used.

The first criterion was the constancy of C. A measurement of C was available each time N_1 and N_2 were used. In time, a newer balance of similar design was obtained. This device, which is still in use, has a standard deviation of about 0.035 mg. If values of C were seen to change significantly with time, it would mean that the summation mass of N_1 and N_2 had deviated from its accepted value. This test is effective in checking whether one or the other kilograms has suffered damage since its last use. However, the test fails to detect changes common to both artifacts. Because N_1 and N_2 are virtually identical and receive identical use, such changes cannot be ruled out *a priori*. Thus the constancy of C is not a sufficient test to rule out a change in the summation mass of the two kilograms. A control chart showing values of C over time is given in figure 1. The second criterion is discussed below in section 2.2.2.

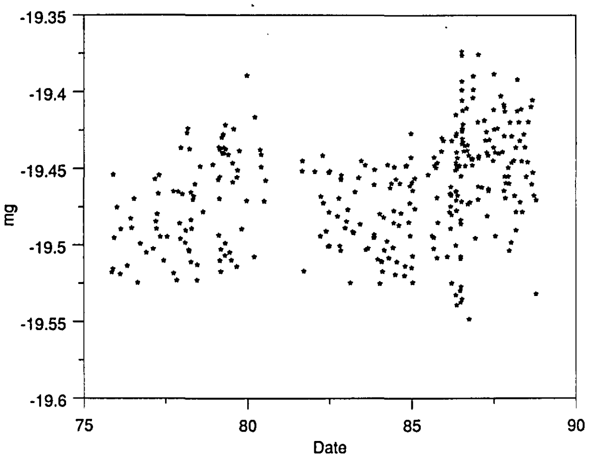

Figure 1. Mass values of N_1-N_2 as a function of time. Measurements were taken on a balance having a standard deviation of 0.035 mg for a single reading.

In 1969, the masses of N_1 and of N_2 were redetermined 10 times with respect to K20 and K4. Measurements were made on a one-pan balance having a standard deviation of 0.14 mg for a single observation. The results of these measurements indicated that N_1 and N_2 were an average of 0.09 mg/kg below their accepted value. However, because the uncertainties propagated from the prototype kilograms and from the correction for air buoyancy could still not be assessed, these data were not used.

2.2.2 100-g Check Standards The second criterion used to monitor the constancy in mass of N_1 and N_2 was the evolution in time of two 100-g "check" standards. A measurement of one or the other of these standards in terms of N_1 and N_2 was obtained each time a routine calibration was performed on a set of weights from 1 kg to 100 g. Such measurements are carried out dozens of times each year. If the mass of the 100-g check standards was seen to change over time, it would be evidence that either their mass or that of N_1 and N_2 was changing. It is unlikely that the mass of the 100-g check standards would change in exact proportion to the mass of the 1-kg working standards. This test suffers, however, from low precision. The statistical precision in the assignment of mass to a 100-g standard is about ten-times lower than the relative precision of mass assigned to 1-kg weights. The reason is simply that all mass comparisons between 1 kg and 100 g are performed on the same balance. One would need to average about 10^2 mass determinations of a 100-g check standard in order to have the same relative precision as one single mass determination of a 1-kg standard.

The 100-g check standard suffers from an additional problem. Since it receives heavy use, its mass can reasonably be expected to decrease with time due to wear. Control charts showing mass values obtained over time for our 100-g check standards, JMC-1 and JMC-2, are given in figure 2. The apparent rapid loss in mass early in the service life of JMC-1 is not unusual. Such behavior is also seen, for instance, in our 1-g check standard where there can be no possibility that the source is instability in 1-kg working standards. Thus the 100-g check standards, while essential to guard against measurement blunders and catastrophic changes in working standards, are themselves susceptible to long-term instability.

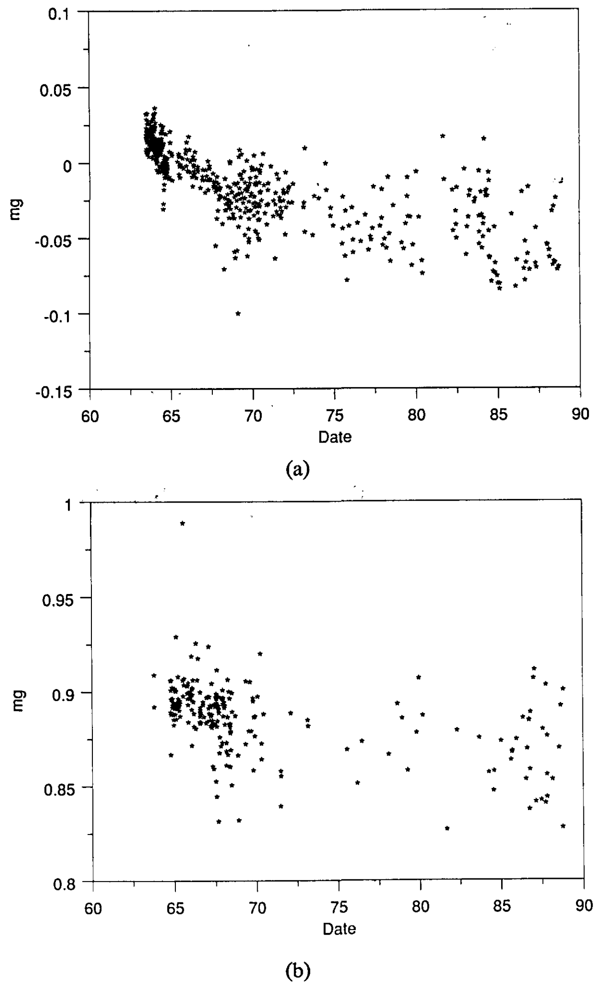

(a)

(b)

Figure 2. Mass values of 100-g check standards JMC-1(a) and JMC-2(b). These values are based on the accepted mass of N_1 and N_2 prior to January 1, 1990.

2.2.3 State Laboratories Each state within the United States maintains a well-equipped laboratory for primary mass metrology, typically placed administratively within the State Department of Agriculture. Training of personnel and many aspects of quality control are coordinated through the NIST Office of Weights and Measures (OWM). The OWM organizes regional round-robin measurements involving State mass-standards of various nominal values. These round-robins also include standards recently calibrated by NIST. An examination of round-robin results for 1-kg masses does not reveal systematic differences between NIST and the States developing over time. But the precision of these comparisons limits conclusions to about 0.5 mg/kg.

2.3 Fundamental Measurements

Some fundamental constants offer a check on the constancy of mass standards. During the 1970s, measurements of the Avogadro constant N_A [6] and the Faraday constant F relied directly on mass values maintained at NIST. These measurements can be compared with related measurements at other laboratories as is done during periodic CODATA adjustments of the fundamental constants [8].

In the case of the NIST determination of the Faraday constant, routine mass calibrations of a 5-g and 3-g working standard were used. It was estimated that the uncertainty in these calibrations was 0.5 ppm (standard error). This estimate contributed less than 10 percent of the combined experimental uncertainty. The Faraday constant has, therefore, little bearing on the present discussion.

This is not true in the case of the Avogadro constant. In order to have their mass values directly traceable to national standards, the experimenters made direct use of K20 and K4. Several calibrations at the 1-kg level were carried out on the newly developed NBS-2 balance [9]. This balance operates under remote control and, at that time, had a standard deviation of less than 0.005 mg. (After initial testing at NBS, the balance was transferred to the BIPM where improved conditions have reduced its standard deviation five-fold.) Unfortunately, N_1 and N_2 were not measured during the experiments, although several stainless-steel kilograms were calibrated in terms of K20 and K4. Two of these kilograms had also been measured against K20 and K4 in 1969 as part of the series of mass determinations which included N_1 and N_2 (see sec. 2.2.1, above). These results were completely consistent with the 1969 measurements and thus raise the question of whether the mass values for N_1 and N_2 dating from 1958 were still appropriate.

3. History of Mass Standards after 1980

About 10 years ago, NIST began a program to tie the mass values disseminated by its calibration services with international standards. It was foreseen that improvements in commercial balance technology and improved precision in measuring critical fundamental constants would soon make this step necessary. In addition, questions of international compatibility of national standards began to be raised at this time. In order to assess the presently accepted values of NIST secondary standards with respect to the SI, four major areas had to be addressed:

1. A meaningful calibration of K20 and K4 with respect to accepted representations of SI standards.
2. A reliable method for making corrections for air buoyancy between primary standards of platinum-iridium and secondary standards of nichrome or stainless steel.
3. A balance which could compare kilogram masses with a precision no worse than 0.005 mg.
4. Demonstration that primary standards could indeed be used periodically to calibrate secondary standards and that mass values so determined did not suffer from serious, unexplainable discontinuities.

We now briefly describe efforts made in these four areas.

3.1 Tie to International Standards

As mentioned in section 2.2.1 above, the main reason given in the past for not basing mass calibrations on routine comparisons with K20 was that the long-term stability of platinum-iridium prototype kilograms had not been rigorously established. One reason for this apparent lack of understanding is the infrequency with which the International Prototype Kilogram is used. The BIPM faces this same problem because it is their job to recertify national prototype kilograms upon request and to provide new national prototype kilograms when required. These activities must be carried out during the long intervals when the International Prototype Kilogram is not accessible.

As described in [1], the BIPM has set in place the following system in which all the mass standards involved are made of platinum-iridium alloy.

Two working standards are used in the calibration of an unknown prototype. The measured difference in mass between the two working standards is used to check that neither has suffered a catastrophic change in mass. The working standards are cleaned at about 15-year intervals. Within these intervals, however, their mass is redetermined periodically against a third kilogram which is reserved for just this use. This third kilogram is cleaned just prior to its use in recalibrating the working standards. Based on the history of the last 40 years, it appears that the BIPM representation of the SI unit of mass is stable to within about 0.02 mg (0.02 ppm). Therefore, it seems a reasonable goal to achieve compatibility with the mass representation currently maintained at the BIPM. These measurements are reported in detail in [1].

3.2 Corrections for Air Buoyancy

In eq (1), the quantity ρ_a is typically determined from an equation-of-state for moist air. The inputs to this equation are temperature, barometric pressure, relative humidity, and ambient level of carbon dioxide. The last of these has relatively little effect. It is obvious that errors in measuring the required experimental input parameters will propagate to the final result. In the 1970s, however, it was appreciated that the equation-of-state itself has great importance and that several such equations were in wide use. Furthermore, it had not yet been demonstrated experimentally that any of the equations-of-state in use were adequate for actual mass comparisons.

At NIST, Jones derived a semi-empirical equation-of-state based on up-to-date data [10]. This equation, with minor changes, was endorsed for use in mass metrology by the CIPM in 1981 [5]. The equation given in [5] is now referred to as the CIPM-81 equation-of-state for moist air and is used for mass metrology by most national laboratories. The NIST began using this equation for international work in 1981. Use of CIPM-81 instead of its predecessor [11] makes a negligible change to routine mass calibrations. As of January 1, 1990, however, CIPM-81 has been adopted for use in all calibration software.

In order to test the efficacy of CIPM-81, it is necessary to determine the mass difference between two nominally equal weights with and without reliance on the equation-of-state. The latter measurement is typically done in vacuum. This type of comparison was done at the Physikalisch-Technische Bundesanstalt (PTB) [12]. Results agreed to within the expected uncertainty, 1×10^{-4} in ρ_a.

It is also necessary to measure the input parameters with sufficient accuracy. In general, this requires the use of transducers whose calibration is checked at frequent intervals by defining instruments. Our capabilities as they existed in 1985 are described in [1]. Since that time, we have improved the accuracy of our measurements of barometric pressure and of relative humidity.

3.3 Improved Balance

The balance used for primary mass metrology must operate by remote control in order to ensure that the weights being compared remain in sufficient equilibrium with the air of the weighing chamber. Schoonover and Keller have demonstrated that severe systematic errors may intrude if the equilibrium constraints are violated [13]. In addition, the balance itself must have sufficiently high precision. We consider the balance to be suitable when either of the two following conditions is met: 1. The contribution of the balance imprecision to the uncertainty of working standards is negligible compared to the imprecision of routine mass calibrations. 2. The imprecision of the balance is negligible compared to typical instabilities of mass standards.

In [1], we described modifications made to an existing balance which allowed it to fulfill the first criterion. Although working reasonably well, we wanted to improve efficiency by fully automating it. In order to make the job of automation more straight forward, the balance was fitted with an electro-magnetic servocontrol system [14]. Introduction of the servocontrol also resulted in a modest improvement in precision [15].

3.4 Stability of Mass Values

It remains to demonstrate that the work undertaken since 1980 has led to an improved representation of the SI unit of mass.

3.4.1 K20 and K4 The most recent mass value for kilogram K20 results from the 1984 calibration at the BIPM [1]. As discussed in [1], the cleaning process at the BIPM removed significant amounts of surface pollution from the two prototypes. (The kilograms had also been cleaned at NIST but by a less effective technique). Since 1984, NIST has adopted the BIPM cleaning method. Values obtained for the difference in mass between K20 and K4 are shown in figure 3. These have standard deviation of 0.0019 mg. We would expect a standard deviation of 0.0013 mg based solely on the observed standard deviation of the balance which was used. The difference is negligible.

3.4.2 N_1 and N_2 Throughout the last 10 years, N_1 and N_2 continued to be used as working standards for routine mass calibrations. In 1982, they were measured against K20 and K4 prior to sending the latter two weights to BIPM for recalibration. The results, calculated after receiving the new BIPM certificate, indicate that the value of $R/2$ was 0.103 mg±0.025 mg below that accepted. The uncertainty is at an estimated level of one standard deviation and is dominated by problems with auxiliary equipment used in measuring air buoyancy. The value of C was found to be -19.474 mg±0.003 mg, consistent with the control chart data shown in figure 2.

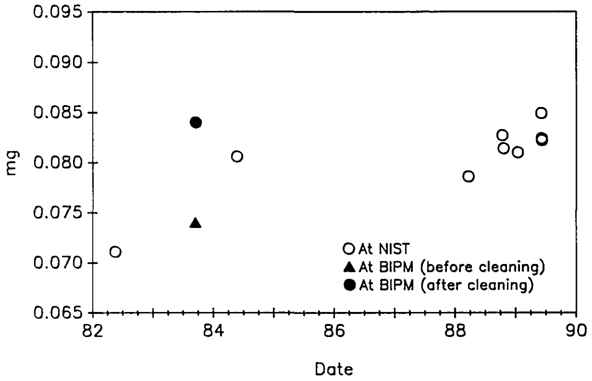

Figure 3. Mass values of K20−K4 as a function of time. Measurements were taken on a balance having a standard deviation of 0.0018 mg for a single reading.

From 1986 to 1988, mass values of N_1 and N_2 were determined three times against K20 and K4 in a more careful series of measurements. Several other stainless-steel kilograms were also involved in the measurements. These are discussed in section 3.4.3, below. It is sufficient to mention at this point that this series of measurements was consistent with the long-term measurements of the other kilograms involved. The results of the 1986–1988 measurements are summarized in table 1. The uncertainty types and the rules for combining uncertainty conform to recommendations of the CIPM [3]. (This reference defines Type A and Type B uncertainties.) Components 2, 4, and 5 will be discussed in more detail in section 3.4.3. In assessing whether the observed change in $R/2$ after 1986 is significant, one must not include Type B components, which we believe to be systematic to all measurements in table 1. It is interesting to note that the observed change in $R/2$ after 1986 is three times greater than the change in C. It is also interesting that the data of figure 1 show a statistically significant variation with time. A linear fit to the data predicts that the value of C in April 1988 was -19.454±0.0028 mg (1 standard deviation), in satisfactory agreement with the measurement shown in table 1.

Table 1. Recent determinations of the masses of kilograms N_1 and N_2 with respect to secondary standards calibrated against K20. The values of C are subject to a measurement uncertainty of 0.0013 mg (1 standard deviation)

Date	$R/2$ $[(N_1+N_2)/2]$	C $[N_1-N_2]$
1986 Aug	1 kg −5.159 mg	−19.440 mg
1987 Nov	1 kg −5.192 mg	−19.451 mg
1988 Apr	1 kg −5.193 mg	−19.447 mg
Accepted values:	1 kg −5.0295 mg	−19.476 mg (1965) −19.454 mg (Apr. 1988)

Uncertainty (1 standard deviation or 68 percent confidence level) for measured values of $R/2$

Component	Type A	Type B
1. Instability of K20 since 1985 BIPM calibration	included in 4	nil
2. Calibration precision of secondary standard	0.0035 mg	nil
3. Correction of secondary standards for air buoyancy	included in 2	0.01 mg
4. Instability of secondary standards	0.0036 mg	nil
5. Calibration precision of $(N_1+N_2)/2$	0.0005 mg	nil
6. Correction of N_1 and N_2 for air buoyancy	nil	0.001 mg
RSS	0.0050 mg	0.010 mg
Combined Type A and B: 0.011 mg		

During this period, several kilograms which were submitted to NIST for calibration were measured against N_1 and N_2 using routine calibration procedures. The test kilograms were also measured against stainless-steel kilograms which are discussed in the next section using our best 1-kg balance. The results were, in all cases, consistent with table 1.

There was now good evidence that the accepted value of $R/2$ was 0.164 mg below the accepted value. Less certain evidence suggests that more than half of this difference had been present since at least 1969 (see sec. 2.2.1). This computes to an average change of order −0.004 ppm/yr.

The standards N_1 and N_2 were again checked in 1989. Although these measurements were not as extensive, they show that the average mass had dropped by another 0.05±0.013 mg (1 standard deviation) with respect to four stainless-steel kilograms reserved for special use. This change thus appears to be real and serves as a warning that N_1 and N_2 are now losing mass at a greatly increased rate. The value of C measured during these measurements had returned to within 0.012 mg of the accepted value.

3.4.3 New Secondary and Working Standards of Mass Kilograms N_1 and N_2 have served as both secondary standards—artifacts of practical density which most accurately represent mass as specified in the SI; and working standards—artifacts of practical density used as standards in routine calibration work. Our intention was to separate these roles by acquisition of new standards, all made of non-magnetic stainless steel. The choice of alloy simply reflects the fact that the highest quality 1-kg weights which are commercially available are now made of stainless steel. Several stainless-steel kilograms were already on hand for use as secondardy standards. Three of these, designated D2, E1, and E2 are about 25 years old. The physical characteristics of all three kilograms are similar; D2 was described in some detail in [1]. We also made use of a newer kilogram, designated CH-1, whose characteristics are also described in [1]. The four artifacts were grouped in pairs: CH-1 and D2 formed one pair while E1 and E2 formed the second pair. When not in use, the pairs were stored in separate containers of different design. The pair E1, E2 was never subjected to any type of cleaning except for gentle dusting with a soft brush. The pair CH-1, D2 was cleaned on various occasions.

The pair CH-1, D2 was compared eight times against primary standards K20 and K4. The mass values of CH-1 resulting from these measurements are shown in figure 4(a). Figure 4(b) shows measurements of the mass difference between CH-1 and D2. Note that results displayed in figure 4(a) include a buoyancy correction of approximately 95 mg while the correction for air buoyancy needed for the results in figure 4(b) was less than 3 mg. Figure 5 shows similar data for the pair E1, E2. In this case, however, the pair CH-1, D2 was used as the standard. The mass value assigned to the standard was the same for all the data shown. Pertinent statistical parameters are summarized in table 2. The outlying point in the mass difference of CH-1 and D2 was repeatable. Because the difference returned to its previous values upon recleaning the two kilograms, we assume the outlying value was due to some type of surface contamination. At any

Table 2. Statistical parameters inferred from measurements of secondary standards

Mass of:	s_{total}	DF	s_{w}	s_{b}	DF
CH-1	0.0085 mg	8	0.0013 mg		
CH-1−D2	0.0052 mg	18	0.0013 mg	0.0036 mg	16.9
E1	0.0015 mg	4	0.0011 mg	0.0011 mg	2.5
E1−E2	0.0016 mg	9	0.0013 mg	0.0009 mg	4.2

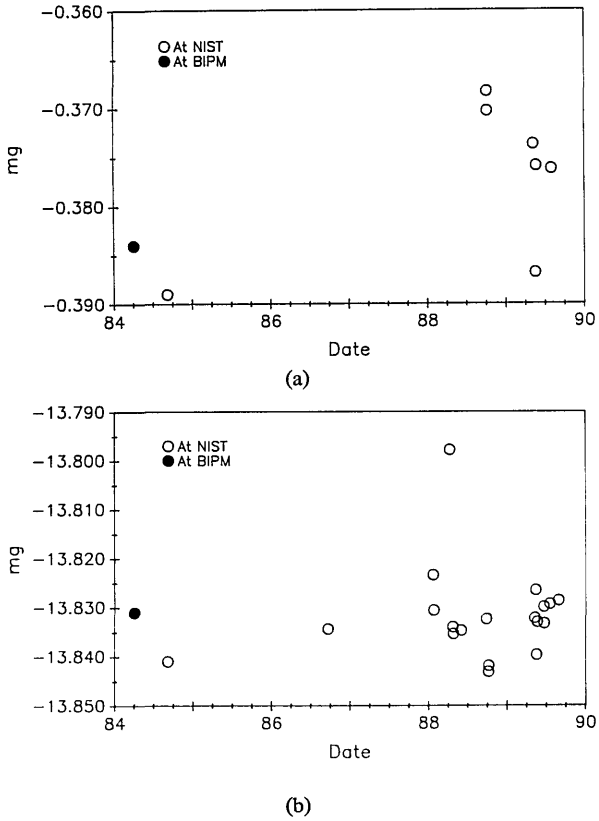

(a)

(b)

Figure 4. (a) Mass of CH-1 as a function of time. These values are based on direct comparison with K20. The balance used has a standard deviation of 0.0018 mg for a single reading. (b) Mass of CH-1−D2 as a function of time using the same balance as in (a). There is one outlying point which has been excluded in the data analysis.

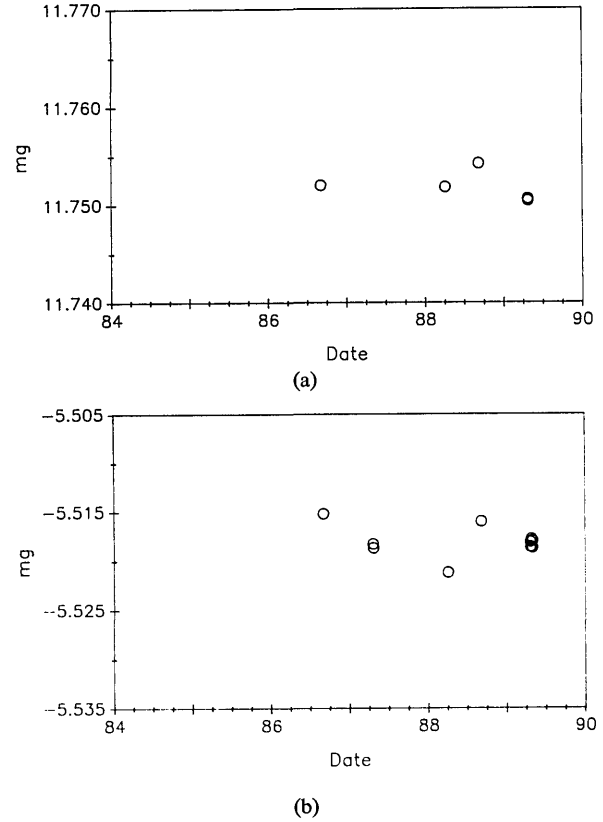

(a)

(b)

Figure 5. (a) Mass of E1 as a function of time. These values are based on direct comparison with CH-1 and D2. The balance used has a standard deviation of 0.0018 mg for a single reading. (b) Mass of E1−E2 as a function of time using the same balance as in (a).

rate, the outlying point is not included in the calculations for table 2.

In table 2, s_{total} is the estimated standard deviation of the data shown in figures 4 and 5. The number of degrees of freedom in this estimate is given in the next column. The quantity s_{w} refers to the "within-group" standard deviation—that component of the observed standard deviation which can be attributed to the balance precision. This number is pooled from a great many measurements and thus has a large number of degrees of freedom. The "between-group" standard deviation, s_{b}, is a measure of increased variability seen over long time periods. This quantity is calculated from the others in the table. The estimated number of degrees of freedom [16] in s_{b} is given in the last column. A full discussion of these parameters as well as their treatment in the context of mass calibrations has been given by Croarkin [17]. It is interesting to note that the data of figure 2, when subjected to the same analysis, indicate that s_b for these measurements is 0.0116 mg [17].

The Croarkin model is not sufficient to model direct comparisons of CH-1 and D2 with K20 and K4. This is because uncertainties in buoyancy corrections have little effect on measured differences between weights of the same density but have large effects on measured differences between weights of different density. While the transducers used to measure the parameters of temperature, pressure, relative humidity, and carbon-dioxide level have excellent short-term precision, slow drifting between recalibration leads to an additional "between group" uncertainty. If the error model of [17] is extended to include buoyancy effects, the data of table 2 can be used to compute an additional parameter $s_p = 0.007$ mg (DF=3.9). This parameter characterizes daily variability in the measured mass difference between a kilogram of platinum-iridium and a kilogram of stainless steel due solely to measurement of the air buoyancy correction.

Although based on somewhat limited data, it seems that E1 and E2, kilograms of the identical alloy and which are never cleaned, have a more stable mass than CH-1 and D2. This is a curious result in the sense that mass values for E1 and E2 are based on direct comparison with CH-1 and D2. In these comparisons, it is assumed that the summation mass of CH-1 and D2 is the average of all recent measurements which are in statistical control. The evidence thus suggests that this average is a better estimate of the mass of CH-1 and D2 than, for instance, the most recently obtained values.

As mentioned in the introduction to this section, it was envisioned that use of N_1 and N_2 as working standards would be superseded by stainless-steel kilograms. These would have a nominal density of 8000 kg·m^{-3}. In 1985, six such kilograms, identical to CH-1, were obtained for this purpose. They are marked 1,2,...,6 but for purposes of discussion we shall refer to them as C1, C2,...,C6. Until January 1988, these six kilograms were used extensively for various cleaning studies. Now, however, they will be used as working standards as described below in section 4.

4. Summary of the Change on January 1, 1990

Beginning on January 1, 1990, the mass values assigned to working standards of the NIST calibration service are based on a calibration chain which starts with mass values assigned to NIST primary standards K20 and K4 by the BIPM, continues with mass values assigned to secondary standards CH-1 and D2 with direct reference to K20 and K4, and finally to working standards C1, C2,...,C6 by direct reference to CH-1 and D2.

4.1 Effect on Industry and Technology

An Ad Hoc Committee of the National Conference of Standards Laboratories (NCSL) was formed in order to help assess industrial and technological implications of the actions contemplated for January 1, 1990. Members of the Committee include representatives from civilian and military standards laboratories, balance manufacturers, and weight manufacturers. All were asked to estimate the impact which a change of roughly 0.15 mg/kg would have on their programs. The members could not identify a single instance where such a change would affect a manufactured product or a critical measurement. Virtually all concerned, however, recognized that a change of this magnitude could be noticeable within their metrology laboratory. This is not surprising since typical NIST calibrations give an uncertainty of about 0.075 mg (3 standard deviations) for calibrations of 1-kg standards and users of these standards often have balances of comparable precision to our own.

In recent years, calibrations for primary national laboratories of other countries have been carried out using secondary standards CH-1 and D2 with assigned values based directly on measurements against K20. These measurements are not, therefore, in need of correction.

4.2 Implementation

Based on the data shown in section 3.4.2, it is clear that, by 1988, mass values assigned to NIST working standards were some 0.164 mg/kg higher than our best estimate of their actual value (that is, the value directly traceable to the representation of the SI unit of mass). At the beginning of the decade, the discrepancy was about 0.10 mg/kg. There is evidence that, between 1988 and 1989, the discrepancy grew still greater.

In early 1988, and based on the data available to that point, it was decided to assign new mass values to NIST working standards on January 1, 1990. On the same date, the new quality-control procedures designed to keep mass values assigned to NIST working standards closely tied to the SI representation of mass would be in place. Various standards organizations were informed of these intentions by letter. The letter also stated that the new mass values would be of the order of 0.15 ppm lower than the present values. Also in 1988, the NCSL Ad Hoc Committee was established to help in the implementation of the change. The target date of January 1, 1990 was chosen to coincide with the date on which international changes in the representations of the SI volt, ohm, and kelvin would be implemented. Guidelines developed by the Ad Hoc Committee are given in the Appendix.

These guidelines treat the discrepancy between the accepted mass of NIST working standards and the mass traceable to SI representations as equal in magnitude to 0.17 mg/kg (0.17 ppm) throughout the decade from 1980 through 1989. Based on data presented above, we see that this is an oversimplification. Our best data, taken between 1986 and 1988, give the discrepancy as 0.164 mg/kg. Less accurate data, however, suggest that the discrepancy grew slowly throughout the decade and then increased rapidly in the last year. A time-dependent correction algorithm with time-dependent uncertainty could, of course, be devised based on these data. The complexity of applying such an algorithm combined with its trivial scientific or technological benefit made this course unwise. Instead we recommend correction of −0.17 mg/kg made to NIST calibration certificates dated during the 1980s. This, we believe, will provide sufficient continuity with certificates issued after January 1, 1990.

The BIPM is conducting the 3rd verification of national prototype kilograms. When this exercise is completed (perhaps in 2 years) we will have a much better idea of the internal stability of BIPM standards and the stability of these standards with respect to the national prototype kilograms. For the present, we estimate that the mass values used by NIST in its calibrations represent SI values as maintained by the BIPM to within 0.03 mg/kg or 0.03 ppm (1 standard deviation). This uncertainty will not be included in NIST calibration reports except to say that it is systematic to all mass measurements.

5. Future Plans

We plan to participate in the 3rd verification of national prototype kilograms being organized by the BIPM. Consequently, in early 1990, we will send our national prototype (K20) to BIPM for a lengthy set of comparisons.

We plan to recalibrate our working standards in terms of secondary standards CH-1 and D2 at approximately 6-month intervals. The working standards will not, initially, be cleaned although the secondary standards will. We foresee calibrating the secondary standards in terms of our primary standards K20 and K4 at about 2-year intervals. Based on the data presented above, we believe this procedure will permit us to know the mass ratio between our working standards and our primary standards to within 0.01 ppm (1 standard deviation) at all times. As noted at the end of the previous section, this uncertainty does not include possible discrepancies between NIST standards and those of the BIPM. We tentatively set the latter uncertainty at 0.03 ppm (1 standard deviation).

It would be helpful to have a balance of 1-kg capacity and a standard deviation of order 0.005 mg for use in routine calibration work. Such a device would help compensate for the fact that, since January 1, 1990, we are formally recognizing that our working standards are subject to uncertainty.

A major goal of the new quality-control system is to improve international compatibility regarding practical mass standards. We are, therefore, seeking to promote international comparisons of stainless-steel mass standards in order to ascertain the degree of compatibility among various industrialized countries.

In conclusion, we note that a system of metrology ultimately based on an artifact standard will necessarily have shortcomings. Over a long enough period of time, mass differences between any two artifact standards will be unstable; the estimated standard deviation based on the complete data record will diverge. If the mass of one of the artifacts is arbitrarily assumed to be constant, its actual instability will in time be revealed by measurements of true physical constants. While there has as yet been no such revelation [18], modern technology may soon be expected to put the present definition of the SI kilogram to a severe test.

6. Appendix. Notice of Change in the Unit of Mass Traceable to The National Institute of Standards and Technology

On January 1, 1990 the unit of mass as disseminated by the National Institute of Standards and Technology (NIST) will shift by 0.17 mg/kg (0.17

ppm). This small shift will bring the unit of mass traceable to NIST into better agreement with international standards. Since the avoirdupois pound is defined as 0.45359237 kg, pound masses traceable to NIST will also be affected to the same extent (0.17 μlb/lb, or 0.17 ppm).

Most people will be unaffected by this small change so that continued traceability to NIST can be maintained without taking any action. Unaffected users will be those whose mass standards are assigned an uncertainty greater than 1 mg/kg or 1μlb/lb (1 ppm). Included in the *un*affected list are:

1. Analytical weights certified to be within any of the tolerances prescribed by NIST/NBS or ASTM/ANSI or to any OIML tolerance except E_1.
2. Direct-reading balances and scales.
3. Any analytical weights which have been assigned an uncertainty greater than 1 mg/kg or 1 μlb/lb (1 ppm). [This will typically include all weights greater than 2 kg or less than 20 g which were calibrated by NIST/NBS (see table A1). In some special cases, however, NIST calibrations at weight denominations other than those shown in table A1 may have an uncertainty lower than 1 mg/kg.]

Traceability to NIST of the above three categories is unaffected by the change which will take effect on January 1, 1990. No action need be taken. In addition, any calibration certificate dated January 1, 1990 or later already has any necessary changes incorporated.

Table A1. Typically, action need be taken only for these nominal values of weights *and* only if the assigned uncertainty is below the value given. Although this table shows weight denominations most likely to require correction, denominations which may require correction are not necessarily limited to those shown

Nominal mass	Uncertainty	Nominal mass	Uncertainty
2 kg	2.00 mg	50 lb	50 μlb
1 kg	1.00 mg	30 lb	30 μlb
		20 lb	20 μlb
500 g	0.50 mg	10 lb	10 μlb
300 g	0.30 mg		
200 g	0.20 mg	5 lb	5 μlb
100 g	0.10 mg	3 lb	3 μlb
		2 lb	2 μlb
50 g	0.05 mg	1 lb	1 μlb
30 g	0.03 mg		
20 g	0.02 mg	0.5 lb	0.5 μlb
		0.3 lb	0.3 μlb
		0.2 lb	0.2 μlb

Weights which will be affected by the change which will take effect on January 1, 1990 are all those which do not fall into category 3 above and, in addition, whose calibration certificate bears a date before January 1, 1990. Affected weights are those which have an assigned calibration uncertainty of less than 1 mg/kg (1 ppm). Based on typical NIST calibration reports, these will generally be weights with denominations between 2 kg and 20 g or 5 lb and 0.2 lb. Other denominations may be affected in special cases, however.

The following actions will be necessary in order to maintain traceability to NIST for the affected weights:

a. Weights whose calibration certificate bears a date after January 1, 1980 and before January 1, 1990.

   After January 1, 1990 the mass of each affected weight should be *reduced* by 0.17 mg/kg (0.17 ppm) as shown in table A2. This applies both to the true mass and the apparent mass. The uncertainty stated in the report remains the same.

   (Alternatively, the mass values stated in the calibration certificate may remain uncorrected provided the stated uncertainty is increased by 0.17 mg/kg).

b. Weight sets whose calibration certificate bears a date before January 1, 1980 but which have been subjected to a surveillance test within the 10 years preceding January 1, 1990. (An example of a surveillance report

Table A2. Corrections to apply to calibrations dated between January 1, 1980 and January 1, 1990. The denominations shown are those of table A1

Nominal mass	Correction	Nominal mass	Correction
2 kg	−0.3400 mg	50 lb	−8.500 μlb
1 kg	−0.1700 mg	30 lb	−5.100 μlb
		20 lb	−3.400 μlb
500 g	−0.0850 mg	10 lb	−1.700 μlb
300 g	−0.0510 mg		
200 g	−0.0340 mg	5 lb	−0.850 μlb
100 g	−0.0170 mg	3 lb	−0.510 μlb
		2 lb	−0.340 μlb
50 g	−0.0085 mg	1 lb	−0.170 μlb
30 g	−0.0051 mg		
20 g	−0.0034 mg	0.5 lb	−0.085 μlb
		0.3 lb	−0.051 μlb
		0.2 lb	−0.034 μlb

issued by NIST is shown at the end of this Appendix.

After January 1, 1990 the mass of each affected weight should be *reduced* by 0.17 mg/kg (0.17 ppm) as shown in table A2. This applies both to the true mass and the apparent mass. The assertions of the surveillance report will remain in effect.

(Alternatively, the mass values stated in the calibration certificate may remain uncorrected provided the stated uncertainty is increased by 0.17 mg/kg).

c. Weights whose calibration certificate bears a date before January 1, 1980 and which have had no surveillance test subsequent to January 1, 1980.

After January 1, 1990 the uncertainty assigned to each affected weight should be increased by 0.17 mg/kg (0.17 ppm) until a new calibration or surveillance test is performed.

Sample Surveillance Report Issued by NIST

April 1, 1987

In reply refer to: 731/12345

Company XYZ
1 Metrology Blvd.
Grovers Corner, NJ 00000
Attention: J. Doe

Subject: Recalibration of Mass Standards previously calibrated under NBS Test No. 00/G00000 (copy attached)

Items: Nine (9) Mass Standards: 100 g – 1 g

The above items have been intercompared in sums. The differences as measured have been compared with the differences computed from the value under G00000. One or more of the items have been checked against national standards. The results of this test indicate that there is no significant change since the last calibration. This test assures the continuing accuracy of the values under G00000.

Sincerely,

Richard S. Davis
Group Leader, Mass Group
Center for Manufacturing Engineering

Attachment

7. Acknowledgments

Many colleagues at NIST have assisted in one or more areas of the above work. Dr. Joe D. Simmons first directed that the work be done. Mr. Randall Schoonover and Mr. Jerry Keller provided historical information and much useful advice. Mr. Henry Oppermann of the Office of Weights and Measures shared historical data with the author. Mrs. Ruth Varner and Mrs. M. Carroll Croarkin provided computational help and welcome advice on statistical questions.

The National Conference of Standards Laboratories aided materially by organizing an Ad Hoc Committee under their aegis. Committee members helped assess the technological implications of the changes discussed above and recommended methods of implementation of those changes.

The staff of the BIPM provided calibrations of NIST mass standards and cooperated fully in detailed explanations of their calibration process.

About the author: Richard S. Davis is a physicist in the NIST Center for Manufacturing Engineering.

8. References

[1] Davis, R. S., J. Res. Natl. Bur. Stand. (U.S.) **90**, 263 (1985).
[2] See for instance, Pontius, P. E., and Cameron, J. M., Realistic Uncertainties and the Mass Measurement Process, Natl. Bur. Stand. (U.S.) Monograph 103, August 1967.
[3] Giacomo, P., Metrologia **17**, 73 (1981).
[4] Comité International des Poids et Mesures, Document CIPM/89-9.
[5] Giacomo, P., Metrologia **18**, 33 (1982).
[6] Deslattes, R. D., in Proceedings of course LXVIII Metrology and Fundamental Constants, Summer School of Physics—Enrico Fermi, Varenna Italy (1976), Soc. Italiana di Fisica, Bologna (1980) p. 38.
[7] Bower, V. E., Davis, R. S., Murphy, T. J., Paulsen, P. J., Gramlich, J. W., and Powell, L. J., J. Res. Natl. Bur. Stand. (U.S.) **87**, 21 (1982).
[8] Cohen, E. R., and Taylor, B. N., Rev. Mod. Phys. **59**, 1121 (1987).
[9] Almer, H. E., J. Res. Natl. Bur. Stand. (U.S.) **76C**, 1 (1972).
[10] Jones, F. E., J. Res. Natl. Bur. Stand. (U.S.) **83**, 419 (1978).
[11] Varner, R. N., and Raybold, R. C., National Bureau of Standards Mass Calibration Computer Software, Natl. Bur. Stand. (U.S.) Tech. Note 1127, July 1980.
[12] Balhorn, R., PTB-Mitteilungen **93**, 303 (1983).
[13] Schoonover, R. M., and Keller, J., in Report of the 68th National Conference on Weights and Measures 1983, Natl. Bur. Stand. (U.S.) Special Publ. 663 (1983) p. 39.
[14] The basic design of the servo system is given in: Schoonover, R. M., and Taylor, J. E., An Investigation of a user-operated mass calibration package, Natl. Inst. Stand. Technol. Report NISTIR 88-3876 (1988).
[15] Davis, R. S., Comité Consultatif pour la Masse et les Grandeurs Apparentées, Document CCM/88-8 (1988).
[16] Brownlee, K. A., Statistical Theory and Methodology in Science and Engineering, John Wiley and Sons, Inc., New York (1965) p. 300.
[17] Croarkin, C., Metrologia **26**, 107 (1989).
[18] Davis, R. S., Metrologia **26**, 75 (1989).

Volume 95, Number 1, January–February 1990
Journal of Research of the National Institute of Standards and Technology

[J. Res. Natl. Inst. Stand. Technol. 95, 93 (1990)]

Observation and an Explanation of Breakdown of the Quantum Hall Effect

Volume 95 Number 1 January–February 1990

M. E. Cage, D. Y. Yu, and G. Marullo Reedtz

National Institute of Standards and Technology,
Gaithersburg, MD 20899

We observe a spatially localized breakdown of the nearly dissipationless quantum Hall effect into a set of discrete dissipative states in wide, high-quality GaAs/AlGaAs samples. The phenomenon can be explained by an extension of the quasi-elastic inter-Landau level scattering model of Eaves and Sheard.

Key words: acoustic phonon; breakdown of the dissipationless state; inter-Landau level scattering; population inversion; quantum Hall effect; two-dimensional electron gas.

Accepted: January 29, 1990

1. Introduction

The integral quantum Hall resistance [1] $R_H(i)=V_H(i)/I_x=h/(e^2i)$ is observed when the longitudinal resistance $R_x=V_x/I_x$ of the two-dimensional electron gas is very small. Here $V_H(i)$ is the Hall voltage of the ith plateau, i is an integer, and I_x is the current through the sample. There is a critical current I_c above which R_x rapidly increases by several orders of magnitude [2,3]. R_x becomes finite as one approaches the critical current. This is referred to as breakdown.

We present results of a breakdown experiment in which sets of discrete V_x signals are observed. We propose an explanation based on an extension of the quasi-elastic inter-Landau level scattering (QUILLS) mechanism of Eaves and Sheard [4].

2. The Experiment

Our samples [3] were GaAs/$Al_xGa_{1-x}As$ heterostructures grown by molecular beam epitaxy with $x=0.29$. The samples are designated as GaAs(7) and GaAs(8). They have zero magnetic field mobilities of ~100,000 cm^2/(V·s) at 4.2 K. They exhibit excellent integral quantum Hall effect properties. The inset of figure 1 shows the geometry of the samples. They are 4.6 mm long and 0.4 mm wide. Contact was made to the two-dimensional electron gas at points 1, 2, 3, and 4, as well as the source S and the drain D.

An important feature of the GaAs(7) sample is that the breakdown occurs somewhere within the longitudinal shaded region between the middle Hall probe pair 3,4 and the outer Hall probe pair 1,2 of figure 1, but not within the transverse region of either Hall probe pair. This crucial fact can be explained by examining figure 1. The minimum V_x signal, $V_x^{\min}$, measured between probe pairs 2 and 4, increases by a factor of 10^7 between $I_x=25$ μA and $I_x=370$ μA, but the quantized Hall resistance R_H for the $i=4$ plateau decreases by only one part in 10^7 for probe pair 3,4 at 370 μA, and by only six parts in 10^7 for probe pair 1,2. These changes in R_H are only about 0.01% of what was expected from

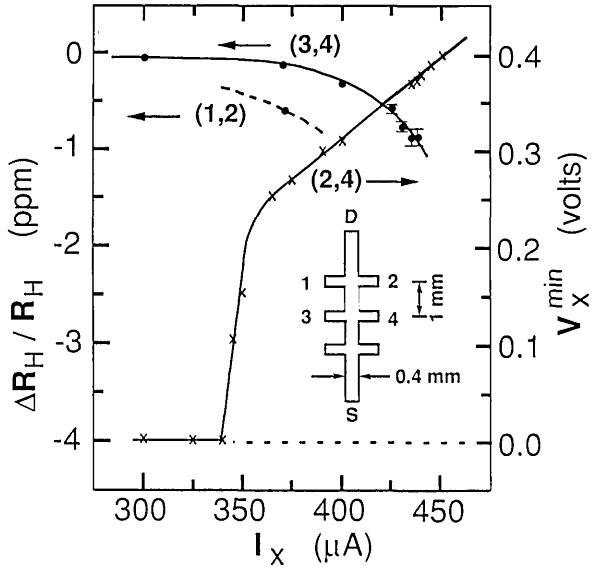

Figure 1. Current dependence of $\Delta R_H/R_H$ and $V_x^{\min}$ for the $i=4$ plateau of the GaAs(7) sample at 1.2 K. The inset shows the sample geometry.

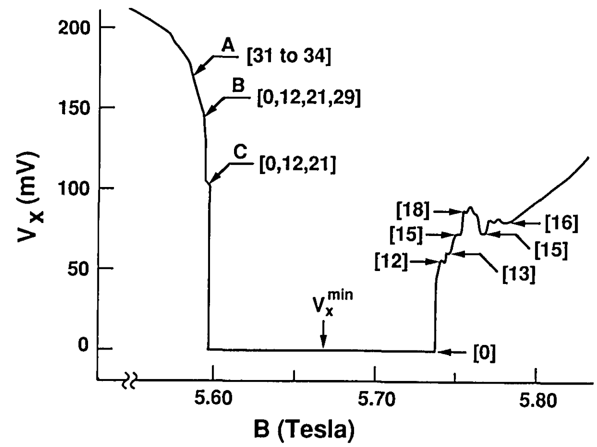

Figure 2. Time-averaged V_x signals for the $i=4$ plateau of GaAs(7) at 1.2 K and 300 μA. The number of inter-Landau level transitions ($N'-N$) is indicated in brackets.

the mixing of V_x into V_H due to the known misalignment of the Hall probes. We therefore know the general region where the breakdown occurs, and that the $i=4$ Hall resistance is accurately quantized on both sides of the spacial breakdown region.

The critical current at which $V_x^{\min}$ starts to rise abruptly is $I_c=340$ μA. Figure 2 shows a V_x vs B curve for GaAs(7) at $I_x=300$ μA, well below that critical current. This curve exhibits reproducible structures. Figure 3, (a) and (b), respectively, show digital oscilloscope displays of the time-dependence and time-averaged distributions of the values of V_x obtained at points A, B, and C of figure 2. There are clearly distinct dc voltage levels and switching between levels. Figure 3 clearly shows that the character of these levels changes with magnetic field. Also, V_x is in only one state at any given time. It remains in that state until electrical noise or other noise processes induces it to switch to another state. Similar switching between dc voltage levels occurs in the GaAs(8) sample. The V_x curve of figure 2 masks this switching by displaying time-averaged values of these dc voltage levels.

We make an initial attempt to interpret our observations by using a modified version of the QUILLS model of Eaves and Sheard [4] because that is a model which seems to provide a satisfactory explanation. Eaves and Sheard used their model to interpret the experimental data of Bliek et al. [5] who made breakdown measurements on GaAs/AlGaAs samples in which Hall potential probe sets were placed on either side of a 1 μm wide constriction. Their V_x vs B curves show features similar to our data, and their Hall voltages were also quantized. Our samples have no geometrical constriction; they are instead 400 μm wide. But we propose that the nearly dissipationless conduction channel is very narrow in our samples as the critical current is approached, and that the conduction channel becomes entirely pinched-off and dissipative above the critical current. Our samples therefore may have effective geometries similar to those of Bliek et al. [5] near breakdown. We assume the global current-carrying equipotentials of the percolation model [6], as strongly suggested by experiments which measured the potential distribution across quantum Hall devices [7].

3. The QUILLS Model

To explain our data we first extend the QUILLS model of Eaves and Sheard [4] to include transitions between non-contiguous Landau levels. Particles of positive charge q and reduced mass m^* (0.068 times the free electron mass in GaAs) move with velocity v_x in the positive x direction through a constriction of average length L_x and average width L_y as shown in figure 4. The quantities L_x and L_y can be less than the length L and width W of a geometrical constriction. The average electric field within the constriction and the average mag-

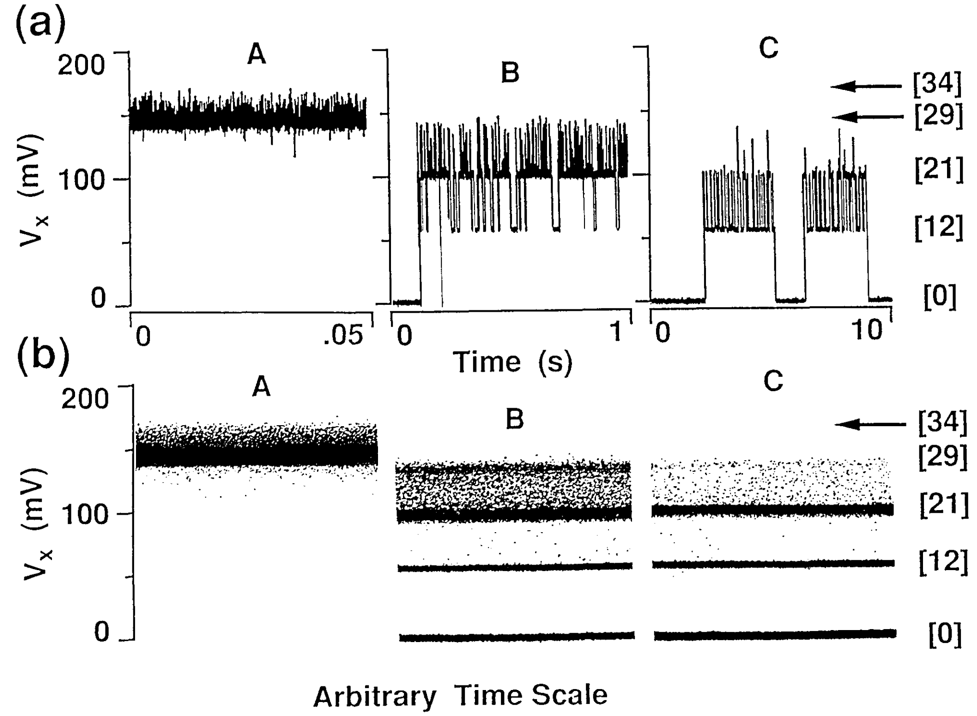

Figure 3. (a) Digital oscilloscope recordings of the time-dependent V_x signals at the positions labeled A, B, and C in figure 2. (b) Digital oscilloscope recordings of the time-averaged distribution of the values of V_x at the positions A, B, and C.

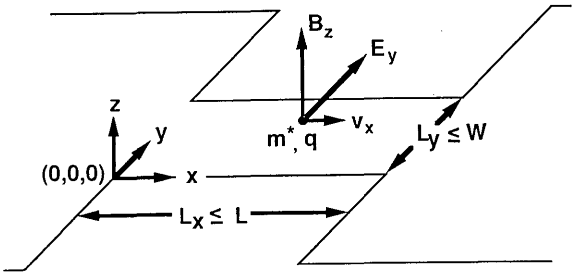

Figure 4. Motion of a charged particle through a constriction. The dynamical length and width L_x and L_y may be smaller than the physical length and width L and W.

netic field is E_y and B_z, respectively. Therefore, $v_x = E_y/B_z$. The Hamiltonian for this system, neglecting spin-splitting and scattering, is $\hat{H} = (1/2m^*)(\hat{p} - qA)^2 + qV_y$ in SI units, where $\hat{p}$ is the momentum operator $-i\hbar\nabla$, A is the magnetic vector potential and $V_y = -yE_y$. Using the Landau gauge $A_x = -yB_z$ and $A_y = A_z = 0$, one obtains the normalized eigenfuctions ψ and energy eigenvalues $\mathscr{E}$ to Schodinger's equation $\hat{H}\psi = \mathscr{E}\psi$:

$$\psi_{N,k_x}(x,\xi) = \frac{1}{(L_x)^{1/2}} e^{ik_x x} \frac{1}{(2^N N!)^{1/2}} \frac{1}{(\pi)^{1/4}} e^{-\xi^2/2} H_N(\xi)$$

$$\psi_{N,k_x}(x,\xi) = \frac{1}{(L_x)^{1/2}} e^{ik_x x} \Phi_N(\xi)$$

$$\mathscr{E}_N(y_0) = (N + \frac{1}{2})\hbar\omega_c - qy_0E_y + \frac{1}{2}m^*v_x^2,$$

where N is the Landau level number, $\omega_c = qB_z/m^*$ is the cyclotron angular frequency, $\ell_B = (\hbar/qB_z)^{1/2}$ is the magnetic length, $y_0 = (v_x/\omega_c - \ell_B^2 k_x)$ is the y coordinate of the center of motion of each cyclotron orbital, $k_x = 2\pi N_k/L_x$ is the x component of the wavevector of a cyclotron orbital state (N,N_k), N_k is the integer quantum number of the wavevector of that state, $\xi = (y - y_0)/\ell_B$, and $H_N(\xi)$ is a Hermite polynomial.

Figure 5 shows the energy eigenvalues for Landau level N as a function of y. The slope of the lines is $-qE_y$. The eigenvalues are equally spaced, with separation $\Delta y_0 = 2\pi\ell_B^2/L_x$. The maximum number of allowed extended states (N,N_k) is $(qB_z/h)L_xL_y$ for level N. The total number of allowed extended states per unit area is $n_s = i(qB_z/h)$.

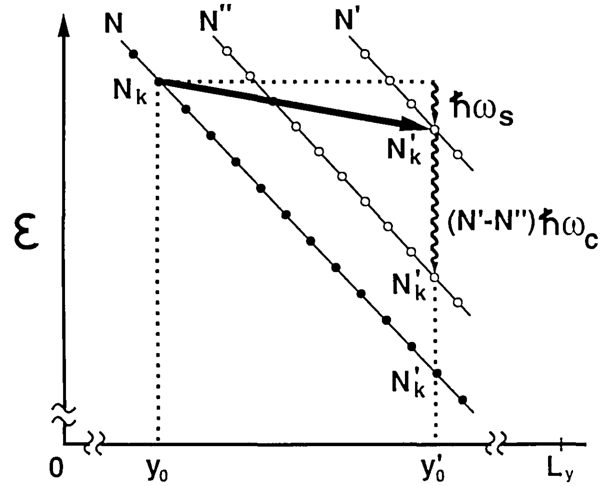

Figure 5. Total energy eigenvalues $\mathscr{E}_N$ as a function of position y across the constriction for each Landau level N. Every eigenvalue of level N has a unique quantum number N_k. The figure shows a QUILLS transition from level N to N' and an associated acoustic phonon. The decay, either directly down to level N or through an intermediate level N'', and its associated optical phonon, are also shown.

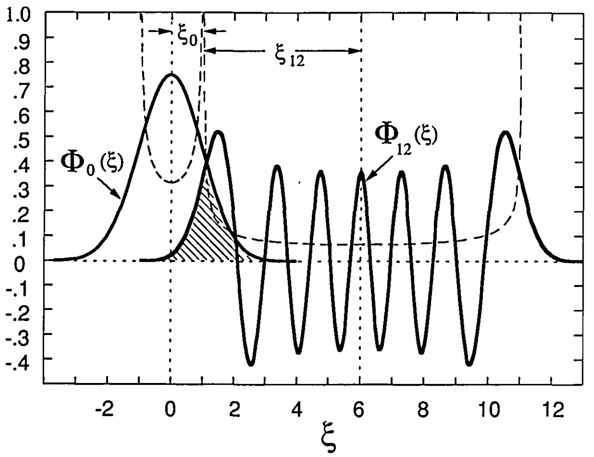

Figure 6. The wavefunctions $\Phi_0(\xi)$ and $\Phi_{12}(\xi)$, shown overlapping at the classical harmonic oscillator separations ξ_0 and ξ_{12}. The dashed lines represent the classical harmonic oscillator probability distributions.

If L_y becomes small enough and E_y large enough then it may be possible for a particle to make a transition from state (N,N_k) to an empty state (N',N_k') at a lower total energy, as shown in figure 5. The particle moves across the sample in this model from position y_0 to y_0'. Energy and momentum must be conserved in the transition. Therefore, an acoustic phonon of wavevector

$$K_x=\frac{2\pi}{L_x}(N_k-N_k')=\frac{\omega_c}{(v_x-v_s)}(N'-N) \tag{1}$$

and energy $\mathscr{E}_{\text{phonon}}=\hbar\omega_s=\hbar v_s K_x$ is emitted in the x direction, where v_s is the velocity of sound in that medium ($\sim 2.47\times10^3$ m/s in GaAs[8]).

Only transitions in which the ratio $(y_0'-y_0)L_x/(2\pi\ell_B^2)$ is an integer number (N_k-N_k') are allowed. One can obtain an equation for (N_k-N_k') by estimating the value of $(y_0'-y_0)$. This is accomplished by noting that the spatial extent of $\psi_{N,k_x}(x,\xi)$ or $\Phi_N(\xi)$ is approximated well by the amplitude of motion of a classical harmonic oscillator: $A_N=\ell_B\sqrt{2N+1}$. Transitions can commence when the wavefunctions just begin to significantly overlap:

$$(y_0'-y_0)\approx(A_N+A_N')=\ell_B\xi_{c\ell}^{N,N'} \tag{2}$$

where $\xi_{c\ell}^{N,N'}=\sqrt{2N+1}+\sqrt{2N'+1}$. Figure 6 shows such an overlap between $\Phi_0(\xi)$ and $\Phi_{12}(\xi)$. Thus

$$(N_k-N_k')\approx\frac{L_x}{2\pi\ell_B}\xi_{c\ell}^{N,N'}. \tag{3}$$

There is another condition for the transition: $(N'-N)$ must also be an integer. From conservation of energy, the electric field $E_y=V_H/L_y$ is

$$E_y=[(N'-N)\hbar\omega_c+\hbar\omega_s]/q(y_0'-y_0). \tag{4}$$

The simultaneous integer conditions (N_k-N_k') and $(N'-N)$, given by eqs (3) and (4), occur only at particular values of the current and magnetic field. There may be many intervening Landau levels between N and N' in which these conditions are not satisfied. Notice that the filled states of Landau level N are at a higher total energy than those of the unoccupied N' level. The large Hall electric field E_y has induced a population inversion for QUILLS transitions.

After the particles make the N to N' QUILLS transitions they then decay, by optical phonon emission [9], back down to the original Landau level N, either directly or by cascading through intermediate levels N'', as shown in figure 5. The optical phonon transitions probably occur just outside of the constriction. One can calculate the voltage signal V_x from the electrical power dissipated, $P=I_x^2R_x=I_xV_x$, when the particles return to the lowest Landau level during the average time taken to traverse the constriction:

$$V_x=\frac{1}{q}\frac{n'}{n_s}[(N'-N)\hbar\omega_c+\hbar\omega_s], \tag{5}$$

where $I_x = qn_s v_x L_y$, and n'/n_s is the fraction of conducting particles that make the transition. We assume both spin states can undergo transitions. Therefore N is 0 and $n'/n_s \leqslant 1$ for the $i=2$ plateau. N is either 0 or 1 and $n'/n_s \leqslant 1/2$ for the $i=4$ plateau. If all the electrons make the transition, then n'/n_s is 1 and 1/2 for the $i=2$ and 4 plateaus.

4. Analysis of Our Data

We next apply this QUILLS model to our V_x vs B data at 300 μA. Equation (5) is used first to obtain the values of $(N'-N)$ by ignoring the small term $\hbar\omega_s$. The electric field E_y is then calculated from eqs (4) and (2) for specific values of V_x and B_z. E_y ranges between $1.6\text{-}3.9\times10^6$ V/m across the quantized Hall resistance plateau. The constriction width $L_y = V_H/E_y = I_x R_H/E_y$ varies between 0.5-1.2 μm across the plateau, and is narrower on either side of the $V_x \approx 0$ region. The range of $v_x = E_y/B_z$ is $2.8\text{-}7.0\times10^5$ m/s across the plateau, and v_x is $\sim 200 v_s$. Also, $\hbar\omega_s = \hbar v_s K_x$, calculated from eq (1), is $\sim 0.5\%$ of $(N'-N)\hbar\omega_c$. The dissipation of the QUILLS transitions is therefore very small indeed. The current density $J_x = I_x/L_y = E_y/(h/4q^2)$ varies between 240-600 A/m. This is an astonishingly large number compared with that found in [5], but the current has a better opportunity of finding a dissipationless path in wide high-quality samples. Also, $qV_H \approx 200\hbar\omega_c$. This is very large compared with our deduced $(N'-N)\hbar\omega_c$ values, and is in an entirely different regime than that of Kirtley et al. [10] who found small integer values of $qV_H/\hbar\omega_c$. $(N_k - N'_k)$ is the only quantity that can not be deduced from the data because the length of the constriction L_x is unknown. If L_x is assumed to be comparable to the width, i.e., about 1 μm, then $(N_k - N'_k) \approx 90$ from eq (3). Finally, eq (5) predicts that the quantity $(n_s/n')(m^*/\hbar)V_x/[(N'-N)B_z]$ should be nearly equal to 1. This quantity is within 3% of 1 for the $(N'-N)$ transitions shown in figure 2, and is within our experimental accuracy. All of the electrons in Landau level N apparently make the transition to level N'.

Multiple values of V_x sometimes occur at certain values of B_z, as for example at points B and C of figures 2 and 3. In such cases the above equations yield a different value of L_y for each value of V_x. A more realistic approach in those situations is to use the smallest value of L_y obtained from the largest value of V_x for that magnetic field. The values of L_y and E_y are then constant for all QUILLS transitions observed at a given B_z and I_x. With these assumptions, the values of $\xi^{N,N'}$ for the smaller V_x transitions are then less than the classical values $\sqrt{2N+1}+\sqrt{2N'+1}$. This presents no problem because the overlap integral between $\Phi_N(\xi)$ and $\Phi_{N'}(\xi')$ becomes somewhat larger inside of the classical value and then falls off slowly over a wide region as $\xi^{N,N'}$ is reduced.

The features labeled with the $(N'-N)$ values 12, 13, 15, 16, and 18 on the right hand side of the V_x curve of figure 2 have very stable single-valued signals. This is not always the case; for example, we see switching about the $(N'-N)=12$ transition at position C and about the $(N'-N)=21$ transition at position B. We believe that the switching is noise-induced.

We clearly observe discrete levels of V_x in figure 3. It is difficult to understand why the overlap of the rather broad wavefunctions and the integer requirements of the apparently large values of $(N'-N)$ and $(N_k - N'_k)$ would by themselves lead to preferential N to N' inter-Landau level transitions. An additional, unaccounted selection mechanism may be present.

One has to be careful about the definition of critical current. For example, in our experiment V_x is large and there appears to always be dissipation at points B and C in figure 2. However, when looking at the discrete voltage states of those points in figure 3 we see that for one of those states ($V_x \approx 0$) the dissipation is negligible. Therefore the critical current has not yet been exceeded.

5. Discussion

Our interpretation of the QUILLS model for breakdown is consistent with the experiment of Bliek et al. [5], who made physical constrictions of order 1 μm width and 10μm length. They observed step-like structures in their V_x vs B curves and empirically found equations for the quantized values of R_x at those steps and for the magnetic field values at which the structures occur. The empirical number $n_L = L_x(2qB_z/h)^{1/2}$ of Bliek et al. [5] corresponds to $n_L = (N_k - N'_k)(4\pi)^{1/2}/\xi_{c\ell}^{N,N'}$ in our formulation, whereas Eaves and Sheard [4] predicted that $n_L = (N_k - N'_k)$. The equation $R_x = n_R(n_L/n_O)(h/2e^2)$ of [5] corresponds to our interpretation of QUILLS if $n_R = (n'/n_s)\xi_{c\ell}^{N,N'}/(\pi)^{1/2}$ and $n_0 = n_s L_x L_y$. Eaves and Sheard [4] predict that n_R is an integer number. Neither n_L nor n_R are integers in our formulation.

In our interpretation of the data of Bliek et al. [5] the values of $(N'-N)$ vary between 3 and 13 for their $i=2$ plateau assuming, as they did, that their V_x signal is not a time average of several Landau level transitions. They obtained values of n_R between 2 and 19. We find that the effective constriction of their sample L_y varies between about 0.2–0.5 μm, significantly less than the 1 μm physical width. If L_x equals the physical 10.3 μm length L, then (N_k-N_k') ranges between about 650–990. L_x is probably much less than L, yielding smaller values of (N_k-N_k'). Bliek et al. [5] found that n_L varied between 528 and 607.

Sachrajda et al. [11] also used samples with a narrow constriction. They observed structures having the same triangular behavior as that of the critical current versus magnetic field plot of Bliek et al. [12]. They believed that this behavior did not agree with the QUILLS model. But we find from our data that the conduction channel narrows on either side of $V_x \approx 0$, and because less current is required in a narrower channel to obtain the same electric field, our results show that the QUILLS model is consistent with that behavior.

It has been proposed [13,14] that breakdown is due to emission of phonons in a manner analogous to the Cherenkov effect if $v_x > v_s$. In the QUILLS interpretation of our data $v_x \approx 200 v_s$ and the Cherenkov angle $\theta_c = \cos^{-1}(v_s/v_c)$ varies between 89.5° and 89.8°. The dissipative voltage V_x can be very small even when the velocity v_x is apparently quite large. The experiment of Bliek et al. [5] provides excellent proof that this may indeed be the case. Figure 1 of their paper shows that V_x has structures on the sides of the $i=2$ plateau and goes to zero in the center of the plateau for $I_x = 45$ μA, $L_y \approx 1$ μm, and $B_z \approx 6.4$ T. Therefore, $v_x = E_y/B_z = (I_x R_H)/(L_y B_z) \approx 36.7 v_s$, and yet V_x still goes to zero.

We have considered the acoustic phonon emission to be collimated in the x direction. However, the electron gas has a probability distribution in the z direction that extends over an interval Δz which is about 50 Å in GaAs/AlGaAs. Therefore the acoustic phonons may have $K_z \sim 1/\Delta z$ components which are about 35% of the magnitude of the K_x component in our experiment for the $(N'-N)=12$ transition. Phonon emission in the x-z plane would not have a significant effect on the results of this paper, but it might preclude the possibility of spontaneously emitted phonons stimulating the other phonons to make population-inverted QUILLS transitions in a manner analogous to photon emission of lasers.

6. Conclusions

We have observed spatially localized breakdown of the nearly dissipationless quantum Hall effect into a discrete set of dissipative states, and have interpreted these observations in terms of the QUILLS model. Theoretical analyses of QUILLS transition rates, similar to [13], and optical phonon decay rates would be very useful in determining the validity of QUILLS. Direct observation of the acoustic phonons would confirm the QUILLS process. There are other interesting features that could be studied: the decay process; the quantum heater property of R_x; and the fact that two crossed resistances, R_H and R_x, are both quantized. We suggest that QUILLS transitions may be the dominant breakdown mechanism in high-quality integral quantum Hall effect samples, and that the discrete V_x signals are indicators of those transitions.

7. Acknowledgments

The authors thank A. C. Gossard who made the MBE-grown GaAs/AlGaAs heterostructures and D. C. Tsui who did the photolithography and ohmic contacting. The authors also thank C. T. Van Degrift, S. M. Girvin, E. R. Williams, R. S. Davis, B. N. Taylor, A. F. Clark, K. C. Lee, and R. E. Elmquist for their discussions and comments. This work was partially supported by the Calibration Coordination Group of the Department of Defense, the Naval Strategic System Programs Office, and Sandia National Laboratories.

About the authors: Marvin E. Cage is a physicist in the Electricity Division of the NIST Center for Electronics and Electrical Engineering. Dingyi Yu is a physicist from the Shanghai University of Science and Technology, Shanghai, China and is a guest researcher at NIST. Giancarlo Marullo Reedtz is a physicist at the Galileo Ferraris National Electrotechnical Institute, Turin, Italy and was a guest researcher at NIST.

8. References

[1] von Klitzing, K., Dorda, G., and Pepper, M., Phys. Rev. Lett. **45**, 494 (1980).

[2] Ebert, G., von Klitzing, K., Ploog, K., and Weimann, G., J. Phys. C **16**, 5441 (1983).

[3] Cage, M. E., Dziuba, R. F., Field, B. F., Williams, E. R., Girvin, S. M., Gossard, A. C., Tsui, D. C., and Wagner, R. J., Phys. Rev. Lett. **51**, 1374 (1983).

[4] Eaves, L., and Sheard, F. W., Semicond. Sci. Technol. **1**, 346, (1986).

[5] Bliek, L., Hein, G., Kose, V., Niemeyer, J., Weimann, G., and Schlapp, W., Proc. Intern. Conf. on the Application of High Magnetic Fields in Semiconductor Physics, ed. by Landwehr, G., Springer-Verlag, Berlin, **71**, (1987), p. 113.

[6] Kazarinov, R. F., and Luryi, S., Phys. Rev. B **25**, 7626 (1982).

[7] Ebert, G., von Klitzing, K., and Weimann, G., J. Phys. C **18**, L257 (1985); Zheng, H. Z., Tsui, D. C., and Chang, A. M. Phys. Rev. B **32**, 5505 (1985).

[8] McSkimin, H. J., Jayaraman, A., and Andreatch, P., J. Appl. Phys. **38**, 2362 (1967).

[9] Slater, G. W., and Tremblay, A.-M. S. Phys. Rev. B **29**, 2289 (1984).

[10] Kirtley, J. R., Schlesinger, Z., Theis, T. N., Milliken, F. P., Wright, S. L., and Pallmateer, L. F., Phys. Rev. B **34**, 5414 (1986).

[11] Sachrajda, A. S., Landheer, D., Boulet, R., and Moore, T., Phys. Rev. B **39**, 10460 (1989).

[12] Bliek, L., Braun, E., Hein, G., Kose, V., Niemeyer, J., Weimann, G., and Schlapp, W., Semicond. Sci. Technol. **1**, 110 (1986).

[13] Heinonen, O., Taylor, P. L., and Girvin, S. M., Phys. Rev. B **30**, 3016 (1984).

[14] Streda, P., and von Klitzing, K., J. Phys. B **59**, 379 (1985).

News Briefs

General Developments

STANDARDS FOR OLDER ERW PIPE NOT WARRANTED

Special standards for the inspection and operation of pipelines with older steel pipe made by electric resistance welding (ERW) are not warranted due to the very low number of annual failures said NIST in a special report to Congress. However, NIST recommends periodic hydrostatic testing in critical risk locations to eliminate large flaws, and the use of damage control systems with pressure and flow monitoring sensors, remote control valves, and product containment structures. The recommendations were made after a review of failures in approximately 575,000 miles of natural gas and hazardous liquid transmission lines. The assessment was made after a 1988 pipeline failure in Maries County, MO, that resulted in a spill of more than 800,000 gallons of crude oil. NIST was asked to conduct an independent assessment of the metallurgical analysis of the failed pipe and to consider whether special standards should apply to the inspection of older pipelines, and to make specific recommendations. For a copy of An Assessment of the Performance and Reliability of Older ERW Pipelines (NISTIR 89-4136), send a self-addressed mailing label to: Public Information Division, NIST, A903 Administration Bldg., Gaithersburg, MD 20899; telephone: 301/975-2762.

FIRST OSI/ISDN TRIAL SUCCESSFUL

A recent trial combining two major communications technologies was pronounced "successful" by NIST. NIST initiated the trial, held at Mather Air Force Base in California, to determine whether Integrated Services Digital Network (ISDN) technology should be included in version two of the Government Open Systems Interconnection (OSI) Profile (GOSIP). Products from five different vendors were included. After August 1990, federal agencies must use the GOSIP specifications in procuring certain networking or telecommunications products. NIST is proposing to revise GOSIP to include ISDN functions as well as several new applications. Before doing so, the institute wanted to be sure that ISDN can support OSI applications.

NEW DATABASE WILL COMPILE OSI TEST RESULTS

In a move to speed the development and use of commercial networking products in industry and government, NIST and partners from private industry are developing a computerized database of commercial products that have implemented successfully the Open Systems Interconnection (OSI) standards and are interoperable. The participating vendors will test their products using OSINET, an experimental computer network coordinated by NIST. In approximately 3 months, users will have free, on-line access to the results. For further information on the OSINET Testing and Registration Service, write to Gerard Mulvenna, NIST, B217 Technology Bldg., Gaithersburg, MD 20899.

IMPROVING PURITY OF DIODE LASERS

Using optical feedback and electronic techniques, NIST scientists have achieved a 10,000-fold improvement in the color purity of commercial diode lasers. Typical diode lasers have spectral linewidths—the range of colors emitted—that are tens of megahertz wide; NIST scientists obtained linewidths of less than 1 kHz. The techniques also automatically stabilize the laser's oscillation frequency. The narrow linewidths and frequency stabilization make the diode lasers, which have low cost and high efficiency, attractive for applications in high-resolution spectroscopy and precision measurements.

Narrow laser linewidth will also be a key feature in the next generation of lightwave communication technologies. Additional studies involving modification of the diode lasers—such as changes in the antireflective coatings—will be undertaken. Two papers outlining some of the techniques are available from Jo Emery, NIST, Division 104, Boulder, CO 80303; telephone: 303/497-3237.

TWO-WAY TIME TRANSFERS BY SATELLITE

The use of geostationary, commercial communication satellites is a cost-effective way of comparing or synchronizing distant clocks at the highest levels of precision and accuracy. Equipment costs are low, satellite space is abundant, and data reduction is simple. For about $100 per week in satellite lease charges, a precision of 0.5 ns is obtainable. Three recent technical papers authored or coauthored by NIST scientists discuss the fundamentals of two-way time transfers, time transfers between North America and Europe, and NIST-U.S. Naval Observatory experience in two-way time transfer over approximately 2 years. For copies of these papers, contact Jo Emery, NIST, Division 104, Boulder, CO 80303; telephone: 303/497-3237.

NEW INSTRUMENT IMPROVES TRACE METAL ANALYSIS

A chelation ion chromatographic instrument that allows new levels of speed, accuracy, and precision for trace metal analysis has been developed by NIST and private industry. With the system, analytical measurements that would be impossible by traditional ion chromatographic methods can be made on complex samples. The technique separates "transition metals"—nickel or copper, for example—from specimens such as human and plant tissue, body fluids, and environmental samples. The system permits analysis of transition elements at levels as low as parts per billion, and it is 10 to 100 times faster than conventional open-column methods. Research with the instrument so far has concentrated on analysis of biological and biomedical samples with a goal of determining factors such as whether toxic levels of nickel or vanadium are present in human tissues exposed to fossil fuel emissions. One potential advantage of the system is that it allows ultra-trace (nanogram-level) analyses to be made in laboratories designed for only trace (microgram-level) analyses, thus eliminating some expensive and tedious clean room procedures.

VOLUMES VII AND VIII OF PHASE DIAGRAMS FOR CERAMISTS COMPLETED

The data input, evaluation, and typesetting of the seventh and eighth volumes in the series Phase Diagrams for Ceramists have been completed. Production of the series of publications is a joint effort of NIST and the American Ceramic Society. ACerS employees work in the data center under the direct supervision of Ceramics Division personnel, collecting published papers containing phase diagrams, maintaining a bibliographic database, digitizing the diagrams, and entering them in a graphics database. The diagrams and references are evaluated by contributing editors outside NIST who provide commentaries. The bibliography, commentary texts, and digitized diagrams form a large computer database which is the basis of the published volumes and of computer databases currently being considered for dissemination to users.

The final editing steps, computer-typesetting of the text material, pagination, and index generation are all performed at NIST. Each volume contains about 1,000 diagrams. The diagrams in Volume VII comprise a variety of salt systems, largely halides and oxyanions of the halogens, but also covering sulfates, nitrates, hydroxides, carbonates, etc. The chemical systems included in Volume VIII include oxide and salt systems containing water studied under high pressures.

LABORATORY TESTING OF ULTRASONIC SYSTEM FOR ROLL-BY INSPECTION OF RAILROAD WHEELS

An ultrasonic system for roll-by inspection of railroad wheels currently is undergoing extensive laboratory testing. The system consists of: a transducer embedded in the head of a rail; analog electronics for generation and reception of ultrasonic signals; digital electronics for signal processing; and a lap-top computer for data collection and storage.

The transducer generates and receives signals propagating in the tread of a railroad wheel as the wheel rolls by. The signals are of two types: echoes from defects, and signals traveling completely around the wheel (round-trip signals). The digital electronics record peak amplitudes and arrival times of both echoes and round-trip signals. These data are put into a microcontroller, where the effects of attenuation in the wheel are compensated for, as well as any variability in coupling the ultrasonic signals between the transducer and the wheel. An algorithm programmed in the microcontroller will then predict the size of any defects in the tread and decide whether the defect is above or below critical size.

NEUTRON SCATTERING STUDY OF CHROMATOGRAPHIC SURFACES

Surface-modified silica is an important material for chromatographic separation processes. A prime example of this is the bonding of trimethylsilyl (TMS) groups to silica surface oxygens via the reaction of trimethylchlorosilane with surface silanol groups. As a result, the affinity of the silica surface is changed from hydrophilic to hydrophobic. In order to more fully understand the nature of this surface modification, a collaborative effort among scientists at NIST was undertaken to characterize the bonding of TMS adsorbates to silica substrates.

The TMS vibrational spectra in the range 0-230 meV were obtained as a function of temperature by incoherent inelastic neutron scattering (IINS). The spectra exhibited similar, identifiable features: intense peaks at approximately 2.5 and 20 meV due to the trimethylsilyl and methyl torsional modes, respectively; weak features between 30 and 80 meV due to the different skeletal modes; more pronounced peaks between 80 and 120 meV due mainly to the Si-C-H bending modes; and higher-energy peaks at approximately 160 and 180 meV due to the H-C-H bending modes. Acceptable spectral fits by normal coordinate analysis indicated the presence of significant intramolecular interactions.

The temperature dependence of the broadening of IINS vibrational features and quasielastic neutron scattering spectra between 4 and 300 K confirmed that rapid trimethylsilyl group rotational motions were present at 80 K and below, with the methyl group rotational motions (observable at higher temperatures) already virtually frozen out at this temperature.

This work is part of a long-term program in which the particular sensitivity of neutron-scattering to hydrogen dynamics is utilized to elucidate adsorption/absorption-related phenomena.

NIST DEVELOPS TRITIUM (HT) GENERATION SYSTEM FOR TESTING ATMOSPHERIC HT MONITORS

NIST chemists have developed a stable tritium generation system for use in testing monitors designed to determine tritium in the atmosphere. Tritium, a radioactive isotope of hydrogen with a 12-year half life, is present in trace concentrations in the atmosphere, primarily as a result of the atmospheric testing of nuclear weapons in the 1960s. These measurements are needed to establish a known baseline for atmospheric tritium.

Molecular hydrogen in the form of HT, i.e., a molecule containing one atom of normal hydrogen and one atom of tritium, is a useful monitor for tracing atmospheric processes. The tritium generation system produces HT in air at concentrations from 1 to 10 times the current background level (about 8×10^{-10} microcuries per liter of air). This is accomplished by precise mixing of two controlled gas flows, one from an argon-tritium mixture of known radioactivity concentration, and the other from a stream of clean tritium-free air. The system has a total output flow of about 1 L/min, and was designed and evaluated to test atmospheric HT monitors that have an input flow of less than 0.85 L/min.

QUANTUM BEHAVIOR OF ULTRACOLD ATOMIC COLLISIONS

Over the past several years scientists at NIST have improved techniques for cooling and trapping small samples of neutral atoms at temperatures less than 1 mK. Recent theoretical work has shown under what conditions atomic collision rates can limit the density and lifetime of cold neutral atom traps. This work indicates that atoms colliding with very low energy do not act like classical "billiard balls." Rather, their quantum wave-like nature strongly affects the collision rate coefficients. Criteria was developed to determine the characteristic temperature for the onset of quantum threshold behavior as temperature approaches zero. This characteristic temperature is strongly dependent on the atomic mass and the strength of the interatomic forces. It is greater than 1 K for light H atoms, but drops to 300 μK for heavy Cs atoms, in the range of most trap experiments. Methods were developed to calculate the quantum threshold behavior of low-temperature rate coefficients and has obtained simple formulas for estimating their magnitudes. One conclusion is that, even though velocities are very small, collision rates can be as large or larger than typical values at room temperature.

GROUP FORMED TO DEMONSTRATE WORLDWIDE INTEROPERABILITY OF OSI STANDARDS

Established by National Computer System Laboratory (NCSL) in 1984, OSINET is a cooperative government/industry research network which fosters the development, promotion, and use of commercial open system interconnection (OSI) products. At a meeting in Sydney, Australia, OSINET representatives met with delegates from four other regional networks to form a cooperative association called OSIone. The purpose of the new group is to demonstrate to the international business community the worldwide interoperability available in products built in accordance with international OSI standards. OSIone includes representatives from regional networks in Europe (EurOSInet), Japan (INTAPnet), Singapore (OSNET), and Australia (OSIcom).

To present the new technology to a large potential customer base, OSIone intends to build a library of demonstration scripts which will enable public exhibitions to be held in all OSIone regions with a minimum of preparation. Also planned are major exhibitions in regions represented by one OSIone organization with satellite demonstrations and support by the other OSIone membership. A CeBIT '90 event in Hanover, West Germany, in March 1990, will launch the OSIone, with demonstrations in other OSIone regions to be scheduled in the following 18 months. The demonstrations will focus initially on the needs of the international users of message handling systems but will be enhanced to cover the full spectrum of OSI applications.

ENHANCEMENT OF INFORMATION RESOURCE DICTIONARY SYSTEM (IRDS) STANDARD PROPOSED

A draft American National Standard for an IRDS services interface that was developed with NCSL assistance currently is undergoing public review. The services interface is being considered as an extension of Federal Information Processing Standard (FIPS) 156, Information Resource Dictionary System, which specifies two user interfaces: the command language and the panel interface. The proposed services interface addresses the additional need for a programmatic interface through which software external to the IRDS can populate, access, and maintain the contents of an IRDS dictionary and its schema.

The services interface will enable an IRDS to be used as a database of information resource descriptions by a wide variety of software tools that are employed in the management of information resources. Any programming language or system that provides an external call mechanism and that supports character, integer, and real data types can use the services interface. Some examples of external software that could make use of the provided services are programming language compilers directly extracting data definitions; SQL and NDL database management systems maintaining database definitions; computer-aided software engineering tools; information locator/retrieval systems; application development systems; text editors; report writers; and open system interconnection systems maintaining directory information.

THEORETICAL STUDY OF SUPERCONDUCTOR MAGNETIZATION COMPLETED

NIST scientists have completed a theoretical study on the magnetization of infinite long type-II superconducting wires having rectangular cross section. The work shows that the equations for magnetization as a function of field may be simplified, by taking different limits, to equations for simple geometries (slab and cylinder) or equations for constant J_c (Bean model). A useful result is that, even for the Kim model for critical-current density (J_c) as a function of magnetic field, J_c may be deduced from magnetization measurements for any of these geometries. The work is based on critical-state theory and the Kim model. The theoretically derived hysteresis loops of magnetization versus field resemble experimental data for both traditional and high-temperature superconductors.

MODELS FOR HIGH DOPING AND CARRIER DENSITIES IN GALLIUM ARSENIDE CONFIRMED

NIST scientists recently completed calculations to determine the modifications to the conduction and valence bands of gallium arsenide (GaAs) that occur as a result of either high doping, high carrier densities, or both, conditions encountered in practical devices. These results now have been confirmed by two groups. Prof. M. S. Lundstrom at Purdue University has utilized the NIST-predicted asymmetry between the effects of dopant ions in n- and p-type GaAs to make more efficient solar cells and bipolar transistors. His team's experimental results show reasonable numerical agreement with the NIST model data. Prof. A. Compaan at the University of Toledo has made photoluminescence measurements on heavily doped n-type GaAs that are in good agreement with the NIST predictions. In charge-neutral material the ionized dopant and carrier densities are equal, and the band states are shifted in energy because of the interaction of the carriers with the dopant ions and with each other. There is a distortion of the band shapes, and entirely new functions for the densities of electron states result. These NIST results are important to device modelers and designers.

HIGH-CURRENT, WIDEBAND TRANSCONDUCTANCE AMPLIFIER DEVELOPED

To meet an increasing number of requests to NIST for a variety of calibrations at higher currents and higher frequencies than were previously available, a high-current, wideband transconductance amplifier has been developed. Three companies have already expressed interest in developing commercial versions. The amplifier provides a stable output current up to 35 A rms at 100 kHz with an output compliance voltage of 5 V rms. The 3-dB bandwidth is 1 MHz, and the gain instability is less than ±10 ppm/min. Although commercial transconductance amplifiers exist that can deliver currents well in excess of 35 A, available instruments are limited to a few kHz at these high current levels and are not sufficiently stable for many calibration applications for which the amplifier is to be used. These include calibrating thermal current converters, precision current sources, ammeters, current transformers, and shunts, including ac/dc difference determinations on high-current, wideband shunts.

AC VOLTAGE LABORATORY INTERCOMPARISON TESTS CONDUCTED USING NIST-DEVELOPED DSS

NIST scientists recently conducted an ac voltage intercomparison to determine the consistency of ac voltage measurements made at various industry and government standards laboratories. The transport standard used for the evaluation was a division-developed digitally synthesized sinusoidal voltage source (DSS) whose rms value is calculated by measuring the dc level of each of the steps used to synthesize the sine wave. The DSS principle provides an alternative to the conventional thermal voltage converter as a dc to ac reference. The uncertainty of the calculated voltage at 7 V rms is typically within ±10 ppm from 15 Hz to 7.8 kHz. Preliminary measurements made at each of the participating laboratories agree with the calculated value to within ±20 ppm, a result which is interpreted as showing that at 7 V, in the low audio-frequency range, the ac voltage measurement capability at these laboratories (using various techniques) is near the state of the art.

CONSORTIUM FORMED TO FUND NIST DEVELOPMENT OF MIMIC METROLOGY

NIST has formed with industry and other government participants a consortium that is providing funds for NIST development of the metrology required for the production and application of microwave monolithic integrated circuits (MIMICs). MIMICs are needed to exploit microwave and millimeter-wave technology in civilian fields as diverse as direct television broadcast by satellite and on-board radar for alerting operators of automobiles and other vehicles of potential collisions. MIMICs are also needed for advanced military communications, countermeasures, and radar systems.

The goals of the consortium are to involve the major U.S. companies and government organizations that fabricate and test MIMICs in the development of test methods and protocols that would make available selected on-chip measurements and lead to dramatic reductions in testing costs. The methods are necessary to provide a practical technology for defense electronics, to remove a major barrier to civilian commercial applications, and to improve the U.S. competitive position. At its first formal meeting, the Board of Directors selected three initial projects: thermal characterization of gallium arsenide integrated circuits, traceability for on-wafer S-parameter measurements, and improvement of/traceability for on-wafer noise measurements.

NIST PARTICIPATES IN MASS FIRE EXPERIMENT

In a jointly supported project by various U.S. and Canadian agencies, NIST participated in a mass fire experiment outside of Chapleau, Ontario, about 400 miles northwest of Toronto. An objective of NIST's participation in this study is to assess predictive models describing mass fires in order to better evaluate the consequences of urban conflagrations. In this experiment, a prescribed burn, or designed fire ignition by jelled gasoline dropped from a helicopter, created concentric ring fires over portions of the 400 hectare (or approximately 1,000 acres) tract of harvested forest debris. The initial fire spread in discrete patches over a region of about 50 hectares and caused a plume to rise to approximately 15,000 to 20,000 ft. A condensation cumulus cloud formed and later a small thunderstorm resulted downwind. Flames on the ground reached a maximum of approximately 40 ft. The multi-agency project team made measurements of the temperatures, velocities, and combustion-product concentrations of the fire and set up tower mounted video cameras that recorded ground conditions in the fire. NIST plans to work with some of the data to develop a dynamic estimate of the energy release rate of the fire and the region undergoing active combustion. The results will be used to compare predicted fire induced ground velocities with measured values.

THREE CASE STUDIES RELEASED ON QUALITY STRATEGY

The Malcolm Baldrige National Quality Award Office has released three case studies on total quality management prepared by the award's first-year winners. The reports, available from NIST, are titled: "The Motorola Story"; "Performance Leadership Through Total Quality: A Case Study in Quality Improvement (Westinghouse)"; and "The Development of the Globe Metallurgical Quality System." According to Curt W. Reimann, director of the Baldrige Quality Award Office, "The reports offer some of the finest examples of quality practices today. Together they make a major contribution to the literature on how the award's rigorous criteria apply to companies practicing total quality management. They should also serve as a guide for implementing total quality management at corporations for many years to come." The reports are avaialable from the Malcolm Baldrige National Quality Award Office, NIST, A1123 Administration Bldg., Gaithersburg, MD 20899. Requests should be accompanied by a self-addressed, stamped 12.5"×9.5" envelope with $1.45 postage affixed.

STUDY ON NATIONAL PROGRAMS IN MATERIALS PUBLISHED

Materials experts from industry, universities, and government argue in a new report that the national programs of other nations in technology development, related to materials science and engineering, have made Europe and Japan fully competitive, and in some cases, able to surpass the United States. The study on national comparisons was conducted by Panel 3 of the Committee on Materials Science and Engineering (COMMSE) commissioned by the National Research Council. The report by Panel 3, deals with many facets of materials science and engineering as practiced in the United States and other countries. It contains information from a survey of national programs for science and technology and materials science and engineering, and it elaborates on the administrative structures to carry out research and development. For a copy of the report by Panel 3, International Cooperation and Competition in Materials Science and Engineering (NISTIR 89-4041), send a self-addressed mailing label to Samuel Schneider, NIST, B309 Materials Building, Gaithersburg, MD 20899; telephone: 301/975-5657.

NEW APPLICATION OF AN ION-EXCHANGE MEMBRANE

Efficient methods to separate and purify bioproducts are an important factor in a commercially successful biotechnology. One attractive, low-energy approach to bioseparation is membrane-based separation. In a recent paper, NIST researchers report on the successful use of perfluorosulfonic acid (PFSA) membranes for isolating amino acids—used in products from food additives to pharmaceuticals— from aqueous solutions. "We have cast a thin PFSA film on a porous support and obtained greatly increased fluxes of amino acids. In addition, the composite membrane exhibited good mechanical strength because of the support film," they report. Further research is needed before PFSA can be used commercially. For a copy of the paper, contact Jo Emery, NIST, Division 104, Boulder, CO 80303; telephone: 303/497-3237. Ask for paper no. 50-89.

NIST WORK CITED BY NOBEL COMMITTEE

When the Royal Swedish Academy of Sciences announced the Nobel Prize in Physics in October 1989, for research related to atomic clocks, they cited work at NIST's Boulder, CO, laboratories. Norman F. Ramsey of Harvard University received the prize for discovering the theoretical basis for current cesium atomic clocks; Hans G. Dehmelt of the University of Washington and Wolfgang Paul of the University of Bonn shared the Nobel for developing the ion trap technique which makes it possible to study a single electron or a single ion with extreme precision. In referring to the latter work, the Nobel committee said "this opened the way to a new kind of spectroscopy, which has been further refined and applied particularly at the National Institute of Standards and Technology ... in Boulder, Colorado." Researchers in NIST's Time and Frequency Division are doing research based on this technique which could some day result in atomic clocks that will neither gain nor lose a second in 10 billion years, or roughly the age of the universe. Professor Ramsey also has close ties with NIST. He has been a member of the NIST statutory Visiting Committee and in the 1986-87 academic year he was a visiting fellow at the Joint Institute for Laboratory Astrophysics (JILA) and is currently a Fellow-Adjoint at JILA. JILA is a cooperative research effort between NIST and the University of Colorado.

TWO NEW NIST PRECISION MEASUREMENT GRANTS AWARDED FOR FY 90

Since 1970, NIST has awarded Precision Measurement Grants to scientists in academic institutions, primarily for experimental work in precision measurement and fundamental constants areas important to the science of measurement. NIST sponsors these grants to promote and encourage fundamental research in the field of measurement science in U.S. colleges and universities, and to foster contacts between NIST scientists and those researchers in the academic community who are actively engaged in such work.

Two new $30,000 NIST Precision Measurement Grants have been awarded for fiscal year 1990. The recipients are Steven Chu of Stanford University and Edward E. Eyler of the University of Delaware. The recipients were selected from among an initial group of 20 candidates by both an outside advisory committee.

Chu's project, "Precision Optical Spectroscopy of Positronium," will determine the 1 $^3S-$ 2 ^3S interval in positronium (Ps, the e^+e^- atom) via two photon laser spectroscopy with a relative uncertainty approaching 1 part in 10^{10}, thereby providing one of the best tests of the two-body problem in quantum electrodynamics. Agreement between theory and experiment at this level can be used to set an upper limit (at the same level) on the particle-antiparticle mass difference of the electron and positron, thus critically testing the CPT theorem (charge conjugation, space inversion or parity, and time reversal invariance).

Eyler's project, "Far Ultraviolet Spectroscopy with Single-Frequency Lasers," will develop and characterize intense tunable single frequency laser sources in selected regions of the far ultraviolet (50-200 nm) suitable for precision two-photon spectroscopy. The lasers will be used to measure the 1 $^1S-2$ ^1S interval in atomic helium with an accuracy approaching 6 parts in 10^9, thereby providing a precise experimental test of recent calculations of Lamb shift and relativistic corrections in the groundstate of helium and establishing a much improved set of calibration lines for vacuum ultraviolet spectroscopy in this region.

LASER-DRIVEN REACTIONS ON SEMICONDUCTOR SURFACES

Chemical reactions at semiconductor surfaces play a central role in the fabrication of electronic circuit components. In recent years, there has been a great deal of interest in the use of lasers to initiate and control these surface reactions. In order to evaluate processing alternatives for the future, it is critical to understand the underlying principles of optical excitations that are presently used to selectively induce reactions.

Recent NIST work has addressed the reaction mechanism and desorption dynamics involved in the optically driven removal of NO from silicon. These experiments have demonstrated that the carriers generated within the semiconductor during the optical excitation process are directly responsible for the desorption of adsorbed NO.

In these experiments, laser radiation above the band gap of the semiconductor is incident on an adsorbate-covered sample. As a result of the excitation of the substrate, a small fraction of adsorbed NO is ejected from the surface. Using a second laser to detect the desorbed NO, it is possible to characterize the energy content of the removed species. While the laser-induced temperature rise of the substrate is negligible (<1 K), it has been determined that the energy of the ejected NO deviates substantially from predictions of equilibrium theory. The temperature characterizing the kinetic energy exceeds the surface temperature by a factor of 10 and the vibrational temperature varies from 10 to 30 times the surface temperature as the NO coverage is increased. The other degrees of freedom of the desorbed NO have substantially less energy than the vibrations and translations.

FEDERAL INFORMATION PROCESSING STANDARD (FIPS) FOR ELECTRONIC DATA INTERCHANGE (EDI) PROPOSED

National Computer Systems Laboratory (NCSL) has proposed a new FIPS adopting national and international standards for EDI for use by federal agencies. This FIPS will adopt families of standards known as X12 and EDIFACT, which were developed by Accredited Standards Committee X12 on EDI and by the United Nations Economic Commission for Europe, Working Party (Four) on Facilitation of International Trade Procedures.

In electronic data interchange, information traditionally conveyed on paper documents is provided in an electronic format according to established rules and procedures. The formatted data may be transmitted to one or more recipients over telecommunications lines or physically transported on storage media.

The data on each type of document are transmitted together as a standard formatted message type or "transaction set." Underlying standards, integral to the use of the message type standards, define data types, data elements, data segments, and message transmission envelopes. The message type standards together with the underlying standards form a family of interconnected standards that must be treated together as a whole. The standardization of message formats, and of data segments and elements within the messages, makes possible the formulation, decomposition, and processing of the messages by computer.

NIST INITIATES "DESIGN FOR QUALITY" COURSE

NIST scientists have developed and initiated a course for engineers on design for quality. The importance of designed experimentation—a systematic and rigorous plan for conducting an empirical investigation—is gaining increasing appreciation in the scientific and engineering communities. NIST has a unique vantage point, founded in measurement science, for disseminating the technology of designed experiments to engineers. Widespread development and use of this technology are dominant reasons for Japanese breakthroughs in quality engineering.

The course runs over several days and covers specific designs for three classes of engineering problems: 1) how to determine if a scientific/engineering modification has significantly improved the response; 2) how to ferret out systematically the most important factors from a large number of potential factors; and 3) how to converge to an optimal operating condition starting from a "best guess" setting. The course is being given in the fall of 1989 for NIST staff and in the spring of 1990 for engineers from local industry. The course is a feature of NIST's effort to support industry in its pursuit of quality and productivity goals.

CEMENT MICROSTRUCTURE MODEL USED BY MICHIGAN STATE UNIVERSITY

The cement microstructure model, developed by NIST to simulate the development of microstructure as cement reacts with water, is the first model to be installed on the NIST Cementitious Materials Modeling Laboratory, a computer facility designed for mathematical modeling of cementitious materials. The modeling laboratory is associated with the Northwestern University Center for the Science and Technology of Advanced Cement-Based Materials and can be remotely accessed by researchers. Other models dealing with the hydration, microstructure, properties, and performance of cement-based materials will be added to the modeling laboratory.

TWO U.S. COMPANIES RECEIVE TOP QUALITY AWARD

Milliken & Company and Xerox Corporation's Business Products and Systems, two U.S. manufacturing companies, received the 1989 Malcolm Baldrige National Quality Award on November 2 for superior quality in their management systems. President Bush, who presented the awards, praised the two companies for "leading the resurgence in American business leadership." Improvements in quality and service by American companies are "national priorities as never before," Bush said. The award, named after former Commerce Secretary Malcolm Baldrige, was established by legislation passed in August 1987. It promotes national awareness about the importance of improving total quality management and recognizes quality achievements of U.S. companies. The 1988 winners were Motorola Inc., the Commercial Nuclear Fuel Division of Westinghouse Electric Corp., and Globe Metallurgical Inc. The award is managed by NIST, with the active involvement of the private sector. For information on applying for the award, contact the Malcolm Baldrige National Quality Award Office, NIST, A1123 Administration Building, Gaithersburg, MD 20899.

COPPER REDUCES TOXICITY OF BURNING POLYURETHANE

Adding a minute amount of copper to flexible polyurethane foam, widely used as padding in upholstered furniture, can reduce the toxicity of smoke during a fire, say researchers at the NIST Center for Fire Research. Hydrogen cyanide (HCN), a colorless, highly toxic gas, is among the toxicants that can be produced when nitrogen-containing materials—such as polyurethane foam—burn. NIST researchers found that adding as little as 0.1 percent of copper to the foam significantly reduced both the atmospheric concentration of hydrogen cyanide and the toxicity of the smoke. For several years, the project has been sponsored partially by the International Copper Association Ltd. In the upcoming year, the Society of the Plastics Industry also will be lending support. According to the National Fire Protection Association, each year in the United States about 1,600 people die in 70,000 fires that begin with a cigarette that is dropped onto furniture, the bulk of which contains polyurethane foam. Overall, about 6,000 people die in fires in the United States each year. Most of these deaths are due to smoke inhalation and not to burns.

LOOKING AT WAYS TO ASSESS STRUCTURAL PERFORMANCE

Reliable, economical devices are needed to measure the behavior of structures during events such as earthquakes or strong winds or to assess the day-to-day condition of a structure. At present field measuring devices tend to be costly and need almost constant monitoring as well as frequent equipment servicing and calibration. In some cases, they produce questionable data or malfunction during critical events such as earthquakes. In a meeting held last fall, experts from around the world convened at NIST to discuss these problems and some new materials and improved technology that could have a dramatic impact on the reliability and versatility of measurement devices. In addition, the experts formulated recommendations for future research. A report, Sensors and Measurement Techniques for Assessing Structural Performance—Proceedings of an International Workshop (NISTIR 89-4153), is available from the National Technical Information Service, Springfield, VA 22161. Order by PB#89-235865 for $15.95 prepaid.

ACCURATE GAUGING OF FOOD COMPONENTS IS AIM OF RMs

Scientists are continually striving to make accurate measurements of nutrients and contaminants in food samples. But they need standards to ensure the reliability of instruments and analytical methods—preferably standards containing a variety of foods representative of an American diet. A reference material (RM) now available from NIST offers just such a dietary composite complete with values for a variety of nutritional and potentially toxic components. The material contains listed concentrations of 17 elements—potassium, sodium, iron, zinc, and selenium, to name a few—as well as ash, fat, protein, total sugar, and starch. Food chemists can analyze the RM as they would any food sample and compare their results with the numbers provided. The material, known as Mixed Diet (RM 8431A), is available for $114 from the Office of Standard Reference Materials, NIST, B311 Chemistry Building, Gaithersburg, MD 20899; telephone: 301/975-6776.

QUALITY CONTROL NEEDED FOR LONG-LASTING CONCRETE

In a study for the U.S. Nuclear Regulatory Commission (NRC), researchers at NIST are attempting to determine if concrete can be formulated to last up to 500 years. The NRC is responsible for developing a strategy for storing low-level radioactive waste. One approach being considered by NRC involves storing radioactive wastes in underground concrete vaults that will be required to last 500 years. NIST analyzed the major degradation processes likely to affect the vaults and recommended ways to predict the service life of concrete. Based on available knowledge, says NIST, it seems likely that concrete can be formulated which should have a service life of 500 years in the expected environments. NIST cautions that such a lifetime can be achieved only if the concrete materials meet carefully defined specifications and good construction practices are followed. Service Life of Concrete (NISTIR 89-4086) is available from the National Technical Information Service, Springfield, VA 22161. Order by PB#89-215362/AS for $21.95 prepaid.

WEIGHTS AND MEASURES HANDBOOKS REVISED

Two handbooks have been revised by NIST to reflect changes adopted at the 74th Annual Meeting of the National Conference on Weights and Measures (NCWM) held in Seattle, WA. NCWM is an organization of state, county, and city weights and measures enforcement officials, which was established in 1905. NIST, which is a non-regulatory agency, provides technical support to NCWM through its Office of Weights and Measures.

NIST Handbook 44-1990. The major changes to NIST Handbook 44-1990, *Specifications, Tolerances, and Other Technical Requirements for Weighing and Measuring Devices,* include a revised section on liquid measuring devices that establishes a requirement for equipment capable of computing the cash/credit pricing of retail motor fuel. NCWM also adopted a specification permitting the use of electronic data audit trails as security seals for electronic devices that are to be considered the equivalent to the physical sealing of other devices with lead and wire seals or pressure-sensitive seals.

NIST Handbook 130-1990. A new regulation was adopted for the maximum allowable variation (MAV) for polyethylene sheeting. Individual packages of poly sheeting cannot be short weight or short in thickness by more than an MAV of 4 percent of the labeled weight or thickness. NIST Handbook 130-1990., *Uniform Laws and Regulations,* also has a revision to the Uniform Regulation for the Method of Sale of Commodities that covers stuffed items such as meat, fish, seafood, and poultry as combination foods. The quantity representation may be in terms of the total weight of the product or combination, and a quantity representation need not be made for each element provided that a statement listing the ingredients in order of their predominance by weight is shown on the label. This handbook also contains a new method of sale requirement for home liquid oxygen used for respiration. A ticket must be provided showing the weight of the cylinder before filling, after filling, and the net weight of the oxygen delivered.

Copies of the handbooks are available from the Superintendent of Documents, U.S. Government Printing Office, Washington, DC 20402. Order Handbook 44-1990 by stock no. 003-00302964-5, $16 prepaid, and Handbook 130-1990 by stock no. 003-003-02962-9, $10 prepaid.

INTERNATIONAL TEMPERATURE SCALE OF 1990 ADOPTED

A new temperature scale, the International Temperature Scale of 1990 (ITS-90), was formally adopted by the Comitê International des Poids et Mesures (CIPM) meeting September 26-28, 1989, at the Bureau International des Poids et Mesures (BIPM). The new temperature scale incorporates important advances developed at NIST to improve the accuracy of temperature measurements common in industrial process technologies and to extend the internationally recognized temperature scale to lower temperatures that are increasingly essential to emerging technologies. The ITS-90 became the official international temperature scale on January 1, 1990, the same date changes affecting the use of some practical/electrical units were implemented. This new scale supersedes the present scales, the International Practical Temperature Scale of 1968 (IPTS-68) and the 1976 Provisional 0.5 K to 30 K Temperature Scale (EPT-76). The ITS-90 extends upward from 0.65 K, and temperatures on this scale, compared with those on the IPTS-68, are in much better agreement with thermodynamic values. The new scale has subranges and alternative definitions in certain ranges that greatly facilitate its use, and it has much improved continuity, precision, and reproducibility throughout its ranges. NIST scientists have worked with industrial users through the National Conference of Standards Laboratories to assure that U.S. industry can meet the new temperature-related requirements of international trade.

NIST PUBLISHES GOVERNMENT OPEN SYSTEMS INTERCONNECTION PROFILE (GOSIP) USERS' GUIDE

To assist federal agencies in planning for the introduction of GOSIP-compliant products into the workplace, NIST has published Special Publication 500-163, Government Open Systems Interconnection Profile Users' Guide. GOSIP was issued as a Federal Information Processing Standard in August 1988 and becomes mandatory for use in federal procurements after August 15, 1990. For use by federal procurement specialists, technical specialists, and managers, the guide provides tutorial information on Open Systems Interconnection (OSI) protocols as well as information on OSI registration, OSI procurement, GOSIP technical evaluation, and GOSIP transition strategies.

CONTINUOUS SPEECH DATABASE DEVELOPED

In collaboration with industry, NIST has developed a continuous speech database in CD-ROM (compact disk-read only memory) format. The database consists of a corpus of recorded speech for use in designing and evaluating algorithms for continuous speech recognition. Speaker-independent, speaker-adaptive, and speaker-dependent recognition modes are accommodated. The corpus, a collection of recorded speech, contains oral readings of sentences from a 1000-word language model of a naval resource management task built around existing interactive database and graphics programs.

The first two in a series of four disks are available for sale by the National Technical Information Service, with the balance of the corpus to be released shortly.

FEDERAL INFORMATION PROCESSING STANDARD (FIPS) PROPOSED FOR FIBER DISTRIBUTED DATA INTERFACE (FDDI)

A new FIPS adopting voluntary industry standards for FDDI has been proposed for federal agency use. The FDDI is a layered standard for a 100 Mbits fiber optic token ring local area network (LAN). The FDDI network allows up to 500 stations connected by up to 200 km of fiber and is particularly suited as a "backbone" network interconnecting other, lower data-rate LANs. It also supports applications inherently requiring high bandwidth, such as image processing with engineering workstations and connecting storage servers to powerful computers as well as other applications whose size and data transfer requirements exceed the capacity of other LANs.

NIST TEST SYSTEM PROVIDES NEW CAPABILITIES FOR NONDESTRUCTIVE EVALUATION OF POWER TRANSISTORS

A new NIST nondestructive test system for power transistors that can accommodate up to 100 A and switch up to 2000 V has been applied to two major NASA programs, the space shuttle transportation system and the Hubble space telescope. The system responds to the need to evaluate new power transistors developed during the last decade. The NASA applications are for the gyroscope controller of the space telescope and for the main engine controller of the space shuttle. NIST offers documentation sufficient to build the system, including photographs, a complete circuit description, and a circuit diagram. In the system's normal mode of operation, the transistor under test is placed in series with an inductive load and turned on for a period of time needed to obtain a selected collector or drain current. When the transistor is turned off, its collector voltage increases abruptly. As this voltage increases, the system senses the onset of breakdown and quickly shunts the transistor to prevent it from being destroyed. In addition to providing voltage breakdown points, the system has provision for viewing current and voltage waveforms on an oscilloscope or capturing them in a transient digitizer.

MBE SYSTEM OPERATIONAL

NIST's molecular-beam epitaxy (MBE) laboratory is now operational. NIST scientists have completed testing the system and carrying out qualification growth-rate and doping calibration runs for gallium arsenide. This primary MBE system is dedicated to growing III-V compound semiconductors and has the capability to grow layers of gallium arsenide, aluminum arsenide, and indium arsenide of controlled thicknesses on a substrate.

Device structures that can be grown in the MBE system include heterojunction bipolar transistors, field-effect transistors, resonant tunnel diodes, and high-electron-mobility transistors (HEMTs), used in millimeter-wave and microwave circuits. HEMT devices have already been grown. In addition, NIST will fabricate quantum-Hall-effect devices for new resistance standards from material grown in the MBE system. Another planned use is in the development of methods and Standard Reference Materials for the determination of dopant concentration and the mole fraction of aluminum in aluminum arsenide.

SYSTEM FOR ON-MACHINE FAST PART PROBING DEVELOPED BY NIST

As part of a quality-in-automation project, NIST has developed a system that allows fast on-machine part probing using touch-trigger probes. On-machine part probing is used for process-intermittent measurements of the part being made on a machine tool. The information from such measurements is used to modify the cutting process parameters to achieve better part accuracy or for statistical process control. Probing cycles currently implemented by machine-tool controllers use slow feed rates of about 5 in/min and are slow in transferring the data to external medium, usually via RS-232 serial interfaces. The time spent for this kind of gauging operation reduces available machining time. The new system is based on a single-chip microcomputer. When this system is inserted between the machine feedback system and the controller, it allows probing with feed rates up to at least 100 in/min and uses parallel interfaces to transfer data to a PC for analysis. With this system, the probing time is reduced by a factor of three.

HEARING ANNOUNCED ON FEDERAL ROLE IN STANDARDS

Whether or not the U.S. standards systems, as they now exist, adequately serve the nation's trading needs in today's international markets will be the topic of a special public hearing on April 3, 1990. Marketing, manufacturing, engineering, and design professionals are invited to testify at the NIST-sponsored hearing. They will be asked to comment on what the U.S. role should be in international standards, describe any problems associated with the acceptance of U.S. products in foreign markets, assess the current situation, and provide suggestions for improvement, especially regarding mechanisms for coordination of U.S. participation in international standards activities. Information and comments will be used to make recommendations to the Secretary of Commerce to improve the effectiveness of U.S. participation in international standards-related activities. A written request to participate in the hearing should be submitted by March 22, 1990, to Dr. Stanley I. Warshaw, Office of Standards Services, NIST, A603 Administration Building, Gaithersburg, MD 20899; telephone: 301/975-4000. The hearing will be held at 9:30 a.m. in the auditorium of the Department of Commerce in Washington, DC. Individuals unable to attend may submit written comments to Warshaw.

Calibration Services

IMPROVED DIGITAL AC VOLTAGE SOURCE DEVELOPED

NIST researchers have developed an instrument that provides a portable digitally synthesized ac voltage source with many potential applications, including the calibration of high-accuracy digital voltmeters. As a calibration tool, the instrument, known as NIST DSS-3, is an improvement over other voltage sources. Commercially available digitally synthesized sources were not designed to be used as voltage standards for calibrations, and analog voltage standards are about 10 times less accurate. The NIST instrument also can be used to evaluate thermal voltage converter-based measurement systems and for on-line ac voltage calibration of automatic test equipment. Because it refers ac voltage to dc voltage standards, the instrument may be calibrated in the user's laboratory with dc standards only. This saves the cost of sending the instrument out for calibration. Future revisions to the instrument may include integrating faster components (digital-to-analog converters, switches, and amplifiers) and digital signal processing chips into the instrument's design.

OXYGEN CALIBRATION FACTOR ADOPTED INTERNATIONALLY

The accuracy of measuring oxygen in silicon wafers, which is tightly specified by integrated circuit manufacturers when they buy silicon, has been improved substantially by the recent adoption around the world of the results of an international interlaboratory experiment in which NIST was a participating laboratory. NIST's role was to manage the conduct of the experiment and carry out the complete data analysis. The value determined by the experiment is the calibration factor used to calculate the interstitial oxygen content of silicon from room-temperature infrared absorption measurements. The ASTM, the Deutsches Institut fur Normung in West Germany, and the Japan Electronics Industry Development Association (JEIDA) have now each accepted that result and are revising their standard measurement methods to reflect the change; JEIDA is reissuing certificates for its reference materials (primarily distributed in Japan). The accuracy of the new result is 3 percent, while previously used values were only accurate to about 10 percent at best. Producers of silicon wafers thus are now better able to meet their customers' needs. Since the new result has been accepted throughout the free world, differences in measurements resulting from the use of one standard method by the producer and another by the purchaser should not arise, and a potential nontariff barrier to international trade is avoided.

NIST ANNOUNCES MILLIMETER-WAVE SERVICES

In response to industry needs, NIST has expanded the theory and practice of its antenna near-field scanning method by establishing antenna measurement services at millimeter-wave frequencies (above 30 GHz). Services are now offered for antenna gain and polarization to 65 GHz and for antenna pattern to 50 GHz. The new services use planar scanning, in which a well-characterized measurement probe scans across a plane at a fixed distance from the plane of the antenna. At higher operational frequencies, the errors in the computed far-field pattern introduced by errors in probe position become more significant. NIST has developed special software programs to correct the final results, once the positional error has been determined over the scanning plane. To arrange for a calibration, contact Allen Newell, telephone: 303/497-3743 or Kathy Hillen, NIST, Div. 723.10, Boulder, CO 80303; telephone: 303/497-3753. Copies of paper 46-89, which describes these services, can be obtained from Jo Emery, NIST, Div. 104, Boulder, CO 80303; telephone: 303/497-3237.

Standard Reference Materials

NIST ANNOUNCES CHARPY V-NOTCH IMPACT TEST PROGRAM

The most widely used standard for predicting the behavior of steel used in structures and other products has been transferred to NIST from the U.S. Army Materials Technology Laboratory, Watertown, MA. NIST will continue worldwide service with certified standard reference materials (SRMs) and impact test machine evaluations for the Charpy V-notch test. Each SRM unit consists of five identical V-notched blocks, 10×10×54 mm in size and a questionnaire on the impact machine. After the five test blocks are broken, the 10 halves are sent with the questionnaire to the NIST Fracture and Deformation Division, Boulder, CO. The broken specimens are then examined to verify that proper procedures have been followed, and then the performance of the test machine may be certified. SRM 2092, Certified Low-Energy Samples for Charpy V-Notch Test Machines with an average fracture energy between 11 and 15 ft/lb, and SRM 2096, Certified High-Energy Samples for Charpy V-Notch Test Machines with an average fracture energy between 66 and 78 ft/lb, are available for $150 per each SRM set from the Office of Standard Reference Materials, NIST, B311 Chemistry Building, Gaithersburg, MD 20899; telephone: 301/975-OSRM (6776).

Standard Reference Data

MIPROPS PROGRAM NOW AVAILABLE ONLINE, WORLDWIDE

A computer program for calculating the thermophyscial properties of 12 important organic and inorganic industrial fluids, developed by NIST, now is available worldwide to subscribers of STN International (Scientific and Technical Network), an online private sector retrieval service. MIPROPS is designed for use in performing quick calculations on the properties of helium, argon, oxygen, nitrogen, hydrogen, and nitrogen trifluoride as well as the hydrocarbons, methane, ethane, ethylene, propane, isobutane, and normal butane. The new online program is based on NBS Standard Reference Database 12, *Interactive FORTRAN Programs to Calculate Thermophysical Properties of Fluids, MIPROPS, 1986.* For information on the availability of MIPROPS through STN, or MIPROPS for lease on a computer-readable magnetic tape or floppy disk, contact the Office of Standard Reference Data, NIST, A323 Physics Building, Gaithersburg, MD 20899; telephone: 301/975-2208.

EXAMINING HALOGENATED HYDROCARBONS

Since fully halogenated chlorofluorocarbons (CFCs) have proven destructive to the Earth's ozone layer, scientists worldwide are on an intensive search for suitable substitutes for CFCs as refrigerants. NIST researchers have prepared two new papers as part of the science and technology review that will form the basis for a reassessment of the Montreal Protocol, which limits the production of certain CFCs. The papers examine thermophysical property data of halogenated hydrocarbons as possible substitutes. These data are needed to determine whether halogenated hydrocarbons will best serve as replacements for the many uses of CFCs. One paper examines nine halogenated hydrocarbons and finds a mixed bag with property data "ranging from well-documented, high-accuracy measurements from published sources to completely undocumented values listed on anonymous data sheets." The second paper sets out criteria for the ideal refrigerant and notes that hydrofluorcarbons (HFCs) and hydrochlorofluorocarbons (HCFCs) "remaining as the most promising coincidates for replacement working fluids." For copies of the papers, contact Jo Emery, NIST, Division 104, Boulder, CO 80303; telephone: 303/497-3237. Ask for papers no. 48-89.

EDUCATIONAL VERSION OF DIPPR DATABASE AVAILABLE

A special educational version of DIPPR (Design Institute for Physical Property Data) Data Compilation of Pure Compounds, 1989, is available for chemistry students on diskette or tape. The new database provides students with quick access to important information on the behavior of substances and their reactions under various pressures and temperatures. It contains evaluated data on 39 properties for 100 chemical compounds most frequently used in classroom exercises. For the chemicals selected, data are provided on their thermodynamic, physical, and transport properties. Designed specifically as a teaching tool; the database is not for research use because of the limited number of available chemicals. *NIST Standard Reference Database 11A, DIPPR, Student (Educational) Data Compilation of Pure Compound Properties, 1989* is available for $75 from the Office of Standard Reference Data, NIST, A323 Physics Building, Gaithersburg, MD 20899; telephone: 301/975-2208.

X-RAY PHOTOELECTRON SPECTROSCOPY DATABASE RELEASED

A new standard reference database is available for surface scientists, tribologists, and analytical chemists using x-ray photoelectron methods to analyze surfaces of materials to determine wear, friction, and resistance to corrosion, *NIST Standard Reference Database 20, X-Ray Photoelectron Spectroscopy* gives easy access to critically evaluated photoelectron and Auger spectral data on more than 13,000 measurements from the literature through 1985. The "user-friendly" program allows for searches on photoelectron and Auger lines as well as chemical shifts to be made by element, line energy, and other variables. Users can easily identify unknown measured lines by matching them to previous measurements. The database is designed for personal computers (PCs) and runs on any MS-DOS or PC-DOS computer using a 2.1 or later disk operating system, It is available on a 3-1/2 or 5-1/4-in floppy disk that requires 5 megabytes of storage space. The database is available for $495 from the Office of Standard Reference Data, NIST, A323 Physics Building, Gaithersburg, MD 20899; telephone: 301/975-2208.

STANDARD REFERENCE DATA PUBLISHES COMPILATION OF OCTANOL-WATER PARTITION COEFFICIENTS

A critical compilation of octanol-water partition coefficients for 611 organic compounds appears in the latest issue of the Journal of Physical and Chemical Reference Data. This quantity, which is a measure of the way a chemical compound distributes itself between water and octanol, has been found to correlate well with the biological activity of many toxic substances and drugs. The correlation results from the similarity of octanol to the lipids which form an important part of the cells of animal organisms. Thus the octanol-water partition coefficient allows one to estimate how much of a substance will be transferred from the bloodstream to the body cells, where damage can occur if the substance is toxic (or beneficial effects can result if the substance is a pharmaceutical). For this reason, such data are widely used in modeling the fate of environmental pollutants, designing new drugs, and many similar applications.

The new compilation represents the most careful evaluation of this property to date. Data from 265 references were evaluated, and recommended values, including uncertainties, are given for all compounds. This database provides a sound foundation for developing predictive methods for more complex substances for which measurements have not been made. The compilation is expected to get wide use by chemists, biologists, and environmental scientists.